Tuning the steric and electronic parameters of mixed-donor palladium(II) complexes: coordination chemistry, substitution kinetics and biological activities

By

Reinner Ochola Omondi

Submitted in partial fulfilment of the academic requirements for the degree of **Doctor of Philosophy in Chemistry** in the College of Agriculture, Engineering and Science,

School of Chemistry and Physics, University of KwaZulu-Natal,

Pietermaritzburg Campus, South Africa

Supervisor: Prof Stephen Ojwach

June 2021

DECLARATION

I, Reinner Omondi declare that the thesis, tuning the steric and electronic parameters of mixed-donor palladium(II) complexes: coordination chemistry, substitution kinetics and biological activities reports on research results of my own work, carried out in the School of Chemistry and Physics, University of KwaZulu-Natal, Pietermaritzburg campus. Where use of others has been made, it is duly accredited through reference citations. The thesis has not been submitted for the award of any qualification at any other University.

Signed: ……[redacted]…… Date: …….30/06/2021……

Reinner Omondi

As the supervisor of the candidate, I have approved the submission of this PhD thesis for examination.

Signed: [redacted] … Date: ……30/06/2021……

Prof Stephen Ojwach

DEDICATION

This work is dedicated to the memory of my late father, Peter Omondi (1960-2017).

Dear Dad in heaven, you will never be goodbye, for you have left your heart with us. While God has you in His keeping, we have you in our hearts. You left us with a memory of courage which the years can but increase. We will always remember thee. And here is why. You were the best example of what a man should be. Teaching us the value of integrity, honesty and hard work. We wonder if we ever thanked you enough for all the sacrifices you made for us.

Truly, no one can fill the empty place you left behind.

Together again we will be, all in God's time.

"For we are strangers before thee,

and sojourners, as were all our fathers."

-1 CHRONICLES 29:15

ACKNOWLEDGMENTS

Firstly, this work would not have been possible by any means without the favour, strength and grace of God. Secondly, I wish to express my heartfelt appreciation to Prof Stephen Ojwach for his exemplary supervisory role, profound knowledge in chemistry, informative and instructive comments on this study. My most humble and sincere thanks to Prof Deogratius Jaganyi for his advices, guidance, and valuable suggestions, and tremendous support throughout the study period. Warm acknowledgement to Dr. Amos Fatokun from Liverpool John Moores University for his assistance with the anticancer studies.

Thirdly, I sincerely acknowledge financial support from the University of KwaZulu-Natal, and National Research Foundation (NRF-South Africa, CPRR-98938), without which all these could not have been possible. To the academic and technical staff in the School of Chemistry and Physics, University of KwaZulu-Natal, thank you for your support. To my colleagues in the Kinetics and Catalysis Research Group, thank you for your support, friendship and the great moments we shared.

Finally, I wish to express my deepest gratitude to my family who supported and encouraged me, despite thousands of kilometres between us. To my mom, Benter Omondi and my siblings, Webber, Benard, and Denilson Omondi, without your encouragement and inspiration, I might never have travelled down this road. To my extraordinary wife Sheilah Omondi, your unwavering love and continued support throughout this journey cannot be measured in mere words. My debt also extends to my children, Fabian and Nolwazi Omondi, for their enduring and untiring love.

PREFACE

This thesis is organised in seven chapter as follows: **Chapter 1** reviews relevant literature on Pt(II)/(IV), Pd(II), Ru(II)/(III), and Au(III) complexes towards, ligand substitution kinetics, DNA/BSA interactions and cytotoxicity. The correlations on kinetic reactivity, DNA interactions, protein binding (BSA), and anti-tumour properties of these complexes are discussed. The chapter has been published in *Inorganica Chimica Acta,* **2020**, 119883. **Chapter 2** covers the methods, instrumentations, synthetic procedures and analytical data for the Pd(II) complexes. The chapter also entails application procedures, electrochemistry, computational studies, substitution kinetics, DNA/BSA interactions, and cytotoxicity of the complexes.

Chapter 3 focuses on the role of remote heteroatoms on substitution kinetics patterns, DNA interactions and cytotoxicity of Pd(II) complexes. The chapter reports on the synthesis, characterisation, substitution kinetics and *in vitro* biological activities of tridentate bis(benzazole) Pd(II) complexes. Computational studies, density functional theory (DFT) and molecular dockings were executed to rationalise the acquired experimental data. The findings of this chapter have been published in *Journal of Inorganic Biochemistry*, 2020, 111156.

Chapter 4 evaluates the *trans*-influence of the heteroatoms on the carrier ligand(s) on kinetic substitution patterns, DNA/BSA binding propensities, and cytotoxic effects of Pd(II) complexes. The chapter details the synthesis, structural characterisation, ligand substitution kinetics of Pd(II) complexes of bridged-bis(pyrazolyl) ligands and their biological applications. In particular DFT simulations were conducted to account for the observed experimental trends.

Chapter 5 concerns the role of π-conjugation on the coordination behaviour, kinetic reactivity, DNA/BSA interactions, and cytotoxic effects of Pd(II) complexes. The chapter deals with the synthesis, molecular structures of tridentate carboxamide Pd(II) complexes and their substitution kinetic behaviours and biological properties. The stability of the complexes in aqua and DMSO media were determined using both UV-Vis and ^{1}H NMR spectroscopies. Electrochemistry studies was performed to determine the electronic properties of the complexes. DFT computations were executed to explain the experimental data.

Chapter 6 is centred on the electronic and steric (ring size) effects of the spectator ligand(s) on the substitution behaviours, DNA/BSA interactions, and anti-proliferative activities of Pd(II) complexes. The chapter presents the synthesis, characterisation and biological activities of Pd(II) complexes bearing CNC and SNS pincer-type ligands. Density functional theory (DFT) computations were carried out to rationalise the experimental data e activities of the complexes. Finally, the general conclusions on the key findings of this study and future prospects are given in **Chapter 7**.

RESEARCH OUTPUTS

This thesis is based on the following original publications.

1. Reinner O. Omondi, Stephen O. Ojwach, Deogratius Jaganyi. Review of comparative studies of cytotoxic activities of Pt(II), Pd(II), Ru (II)/(III) and Au(III) complexes, their kinetics of ligand substitution reactions and DNA/BSA interactions. *Inorganica Chimica Acta*, 512 (**2020**) 119883.
2. Reinner O. Omondi, Rajesh Bellam, Stephen O. Ojwach, Deogratius Jaganyi, Amos A. Fatokun. Palladium(II) complexes of tridentate bis(benzazole) ligands: Structural, substitution kinetics, DNA interactions and cytotoxicity studies. *Journal of Inorganic Biochem*istry, 210 (**2020**) 111156.
3. Reinner O. Omondi, Nicole RS. Sibuyi, Deogratius Jaganyi, Mervin Meyer, Stephen O. Ojwach. Role of π-conjugation on the coordination behaviour, substitution kinetics, DNA/BSA interactions, and *in vitro* cytotoxicity of carboxamide palladium(II) complexes. *Dalton Tranactions*, 50 (**2021**) 8127.
4. Reinner O. Omondi, Deogratius Jaganyi, Amos A. Fatokun Stephen O. Ojwach, Exploring the influence of trans-heteroatoms on the substitution kinetics, DNA/BSA interactions, and cytotoxicity activities of palladium(II) complexes of pincer ligands, (Manuscript submitted to *ChemMedChem*).
5. Reinner O. Omondi, Deogratius Jaganyi, Amos A. Fatokun Stephen O. Ojwach. Electronic and ring size effects of CNC and SNS pincer-type ligands on kinetic of ligand substitution reactions, DNA/BSA interactions, and cytotoxicity of their palladium(II) complexes, (Manuscript under preparation to be submitted to the *New Journal of Chemistry*).

ABSTRACT

Reactions of 2,6-bis(benzimidazol-2-yl)pyridine (**L_1**), 2,6-bis(benzoxazol-2-yl)pyridine (**L_2**), and 2,6-bis(benzothiazol-2-yl)pyridine (**L_3**) with $[Pd(NCMe)_2Cl_2]$ in the presence of $NaBF_4$ afforded the corresponding Pd(II) complexes, $[Pd(\mathbf{L_1})Cl]BF_4$, **PdL_1**; $[Pd(\mathbf{L_2})Cl]BF_4$, **PdL_2**; $[Pd(\mathbf{L_3})Cl]BF_4$, **PdL_3**; respectively, while reaction of bis[(1H-benzimidazol-2-yl)methyl]amine (**L_4**) with $[Pd(NCMe)_2Cl_2]$ afforded complex $[Pd(\mathbf{L_4})Cl]Cl$, **PdL_4**. Characterisation of the complexes was accomplished using NMR, IR, MS, elemental analyses and single crystal X-ray crystallography. Ligand substitution kinetics of these complexes by biological nucleophiles thiourea (**Tu**), L-methionine (**L-Met**) and guanosine 5′-diphosphate disodium salt (**5-GMP**) were examined under *pseudo*-first order conditions. The reactivity of the complexes decreased in the order: **PdL_1** > **PdL_2** > **PdL_3** > **PdL_4**, ascribed to electronic effects. Density functional theory (DFT) supported this trend. Studies of interaction of the Pd(II) complexes with calf thymus DNA (CT-DNA) revealed strong binding affinities *via* intercalative binding mode. Molecular docking studies established associative non-covalent interactions between the Pd complexes and DNA. The *in vitro* cytotoxic activities of **PdL_1**-**PdL_4** were assessed in cancer cell lines HeLa and MRC5-SV2 and a normal cell line MRC-5, using 3-(4,5-Dimethyl-2-thiazolyl)-2,5-diphenyl-2H-tetrazolium bromide (MTT) assay. **PdL_1** exhibited cytotoxic potency and selectivity against HeLa cell that was comparable to cisplatin's. Complex **PdL_1**, unlike cisplatin, did not significantly induce caspase-dependent apoptosis.

Treatment of 2,6-bis[(1H-pyrazol-1-yl)methyl]pyridine (**L_5**), bis[2-(1H-pyrazol-1-yl)ethyl]amine (**L_6**), bis[2-(1H-pyrazol-1-yl)ethyl]ether (**L_7**), bis[2-(1H-prazol-1-yl)ethyl]sulphide (**L_8**) with $[PdCl_2(NCMe)]_2$ in the presence of $NaBF_4$ led to the formation of the respective Pd(II) complexes, $[Pd(\mathbf{L_5})Cl]BF_4$ (**PdL_5**), $[Pd(\mathbf{L_6})Cl]BF_4$ (**PdL_6**), $[Pd(\mathbf{L_7})Cl]BF_4$ (**PdL_7**), $[Pd(\mathbf{L_8})Cl]BF_4$ (**PdL_8**) in moderate to high yields. The complexes were structurally characterised using NMR spectroscopy, mass spectrometry, elemental analysis, and single crystal X-ray crystallography. The solid-state structures of complexes **PdL_5**-**PdL_8** confirmed a tridentate coordination mode, with one chloro ligand completing

the coordination sphere to afford square planar complexes. The substitution kinetics of the complexes with the biological nucleophiles thiourea (**Tu**), L-methionine (**L-Met**) and guanosine 5′-diphosphate disodium salt (**5'-GMP**) follow the order; **PdL_6** < **PdL_7** < **PdL_8**, and **PdL_6 < PdL_5**. The kinetic reactivity is dependent on the electronic effects of the spectator ligand(s), and the trend is supported by the DFT electronic descriptors. The interaction of the complexes with calf thymus (CT-DNA), and bovine serum albumin (BSA) suggest intercalation mode of interaction, and the order of their interactions is consistent with the kinetic reactivity. The complexes exhibited lower cytotoxic effects in comparison to cisplatin against the proliferation of HeLa cancer cells.

The carboxamide complexes, [Pd(**L_9**)Cl] (**PdL_9**); [Pd(**L_{10}**)Cl] (**PdL_{10}**); [Pd(**L_{11}**)Cl] (**PdL_{11}**); and [Pd(**L_{12}**)Cl] (**PdL_{12}**) were prepared by reacting the corresponding ligands *N*-(pyridin-2-ylmethyl)pyrazine-2-carboxamide (**L_9**), *N*-(quinolin-8-yl)pyrazine-2-carboxamide (**L_{10}**), *N*-(quinolin-8-yl)picolinamide (**L_{11}**) and *N*-(quinolin-8-yl)quinoline-2-carboxamide (**L_{12}**) with $[PdCl_2(NCMe)]_2$. Structural characterisation of the compounds was achieved by NMR and FT-IR spectroscopies, elemental analyses and single crystal X-ray crystallography. The solid-state structures of complexes **PdL_{10}**-**PdL_{12}** established the formation of one tridentate ligand unit, and Cl atom around Pd(II) ion, giving a square planar geometry. Electrochemical investigations of **PdL_9**-**PdL_{12}** showed irreversible one-electron oxidation reactions. Kinetics reactivity of the complexes towards bio-molecules; thiourea (**Tu**), L-methionine (**L-Met**) and guanosine 5′-diphosphate disodium salt (**5'-GMP**) decreased in the order: **PdL_9** > **PdL_{10}** > **PdL_{11}** > **PdL_{12}**, in tandem with the density functional theory (DFT) data. The complexes bind favourably to calf thymus (CT-DNA), and bovine serum albumin (BSA), and the order of their interactions agree with the substitution kinetics trends. The *in vitro* cytotoxic activities of **PdL_9**-**PdL_{12}** were examined in cancer cell lines A549, PC-3, HT-29, Caco-2, and HeLa, and a normal cell line, KMST-6. Overall, **PdL_9** and **PdL_{11}** displayed potent cytotoxic effects on A549, PC-3 HT-29 and Caco-2 comparable to cisplatin. All the investigated complexes exhibited lower toxicity on normal cells than cisplatin.

Complexes [Pd(**L$_{13}$**)Cl]BF_4 (**PdL$_{13}$**), [Pd(**L$_{14}$**)Cl]BF_4 (**PdL$_{14}$**), [Pd(**L$_{15}$**)Cl]BF_4 (**PdL$_{15}$**) and [Pd(**L$_{16}$**)Cl]BF_4 (**PdL$_{16}$**) were derived from the reactions of the precursor $PdCl_2(NCCH_3)_2$ with ligands 2,6-bis(3-methylimidazolium-1-yl)pyridine dibromide (**L$_{13}$**), 2,6-bis(3-ethylimidazolium-1-yl)pyridine dibromide (**L$_{14}$**), 2,6-bis(1-methylimidazole-2-thione)pyridine (**L$_{15}$**), and 2,6-bis(1-ethylimidazole-2-thione)pyridine (**L$_{16}$**), respectively. The compounds were fully characterised by ^1H, ^{13}C NMR and IR spectroscopy, mass spectrometry, elemental analyses, as well as single crystal X-ray crystallography. The solid state structure of **PdL$_{14}$** established the formation of one tridentate ligand unit, and Cl atom around Pd(II) ion, giving a distorted square planar geometry. Kinetic reactivity of the complexes with the nucleophiles thiourea (**Tu**), L-methionine (**L-Met**) and guanosine 5′-diphosphate disodium salt (**5-GMP**) decreased in the order: **PdL$_{13}$** > **PdL$_{14}$** > **PdL$_{15}$** > **PdL$_{16}$**. The reactivity of the complexes was largely dependent on the electronic and steric effects of the chelate ligands. Density functional theory (DFT) simulations showed that alkyl substituents on the spectator ligand(s) and the size of the chelate chelate rings have a direct electronic (σ-donor capacity) and steric (ring size) significance on the substitution kinetics patterns. The interactions of the complexes with Calf thymus DNA (CT-DNA), and bovine serum albumin (BSA) binding titrations revealed strong and favourable binding. The *in vitro* antiproliferative activities of complexes **PdL$_{13}$-PdL$_{16}$** on cervical cancer (HeLa) cell line, indicated lower cytotoxic effects than cisplatin.

TABLE OF CONTENTS

Table of Contents

LIST OF FIGURES

LIST OF SCHEMES

LIST OF TABLES

ABBREVIATIONS AND SYMBOLS

d	Doublet
J	Coupling constant
m	Multiplet
s	Singlet
t	Triplet
δ	Chemical shift
mg	miligram(s)
mL	millilitres
mmol	millimoles
Å	Angstrom
eV	Electronvolt
K	kelvin
kJ	Kilojoules
DCM	Dichloromethane
DMSO	Dimethyl sulfoxide
MS	Mass spectrometry
TOF	Turn over frequency
ESI	Electron spray ionization
IR	Infrared spectroscopy

MHz	Megahertz
NMR	Nuclear Magnetic Resonance
ppm	Parts per million
CV	Cyclic voltammetry
SWV	Square wave voltammetry
DFT	Density functional theory
B3LYP	Hybrid Becke, 3-parameter, Lee-yang-Parr
HOMO	Highest occupied molecular orbital
LUMO	Lowest unoccupied molecular orbital
k_{obs}	Observed pseudo first-order constant
k_2	Second order rate constant
NBO	Natural bond orbital
Nu	Nucleophile
Tu	Thiourea
L-Met	L-methionine
5’-GMP	Guanosine 5′-diphosphate disodium salt
$\Delta H^{\neq}$	Enthalpy of activation
$\Delta S^{\neq}$	Entropy of activation
$\Delta G^{\neq}$	Gibbs free energy of activation
DNA	Deoxyribonucleic acid

MTT	3-(4,5-dimethyl-2-thiazolyl)-2,5-diphenyl-2Htetrazolium bromide
IC_{50}	Concentration of a compound that induces 50% of growth inhibition of cells compared to untreated cells

CHAPTER 1

The role of substitution kinetics on DNA/BSA interactions, and cytotoxic activities of Pt(II), Pd(II), Ru(II)/(III), and Au(III) complexes

1.1 Introductory remarks

Transition metal-based drugs offer diversity in the chemical modification of ligands to fine-tune their bio-activity [1-4]. Based on the variable oxidation states, wide range of coordination numbers of these compounds, careful manipulation of these parameters can lead to the design of new compounds with unique biological properties. Following the seminal discovery of the cisplatin, as an effective metallo-based anti-cancer agent, a number of related platinum compounds have been designed and evaluated as anti-cancer agents [5-8]. Besides cisplatin, platinum based drugs such as oxaliplatin, carboplatin, nedaplatin, heptaplatin and lobaplatin have been approved as current chemotherapeutic agents (Figure 1.1) [9, 10].

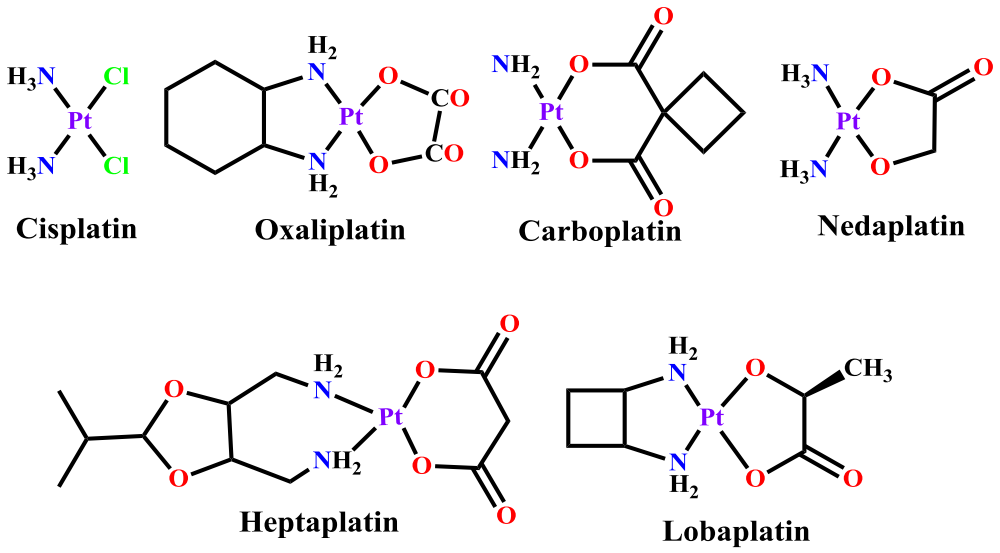

Figure 1.1: Platinum complexes currently being used in the treatment of cancer [9, 10].

These drugs are employed in the treatment of a number of tumours, including lung, colorectal, lymphomas, testicular, cervical, bladder, head and neck cancers [9, 10]. To date, besides platinum-based compounds, other metals such as palladium, ruthenium, and gold have also been evaluated as anti-neoplastic agents [11-15]. Some of the non-platinum based compounds that have found their way in human clinical trials are shown in Figure 1.2 [16-19].

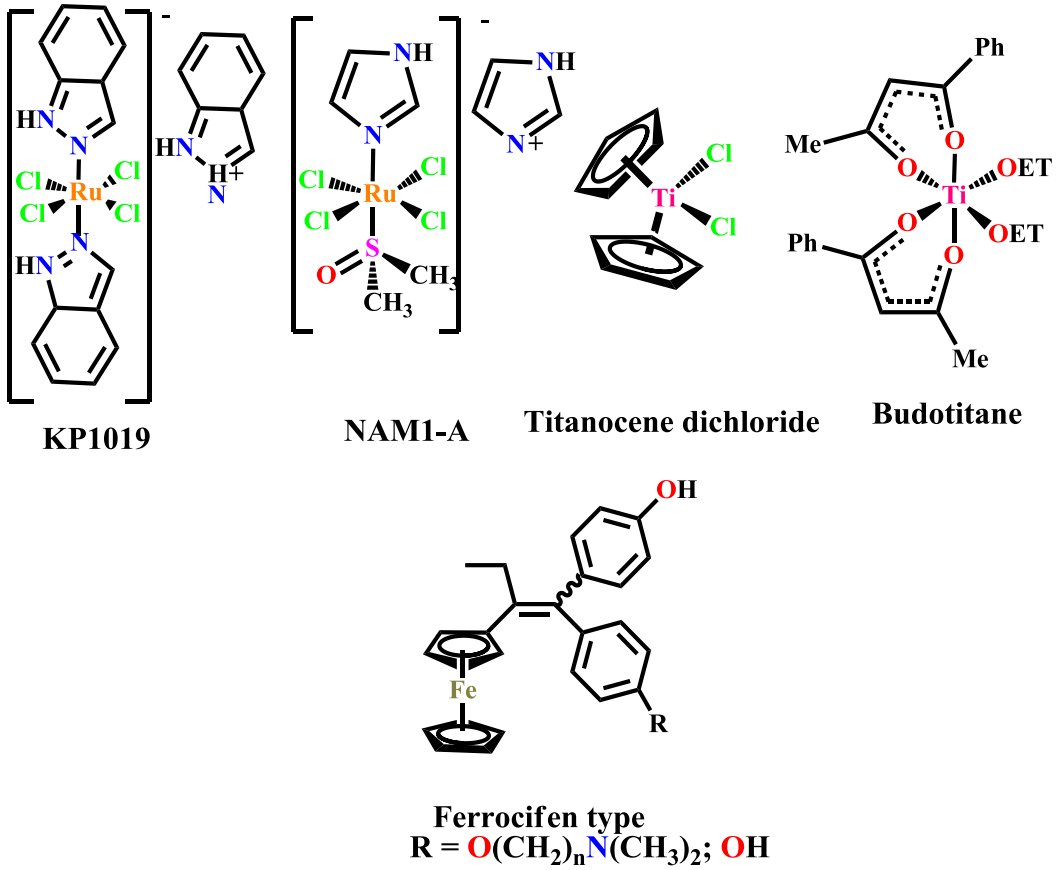

Figure 1.2: Non-platinum based compounds currently undergoing clinical trials [16-19].

The mode of action of metal-based drug design is mostly believed to occur *via* binding to the DNA molecule, thus hindering the synthesis and replication of the DNA, leading to cell death [20-22], Figure 1.3. For some metal-based drugs, for instance, NAMI, Ru-based drug, the mode of action is known to be through binding to the proteins [23] as illustrated in Figure 1.4. In addition, serum albumin which is the most abundant protein in plasma, is one of the most important transport proteins and is responsible

for the distribution of metal-based drugs in the body. As such, studies on the interactions of biologically active complexes with proteins give useful information on the structural features that determine the overall drug distribution, excretion, toxicity and activity [24]. Thus in the design of viable and effective metal-based drugs, proper understanding of the kinetics of substitution reactions and DNA/BSA interaction is of utmost significance. In this chapter, we thus present an overview of the results reported to date on the kinetics of ligand substitution reactions and DNA/BSA interactions, as well as cytotoxicity of the metal complexes. It is believed that the data presented herein will provide some insights and the possible use of kinetics and DNA/BSA binding studies as tools for rational design and development metal-based anti-cancer drugs.

1.2. Mechanism of action of metal-based drugs

For a better understanding of the mechanisms of action of the metal-based drugs and role of kinetics of ligand subsititution, this section gives the elementary steps involved in the drug uptake and metabolism, with specific reference to cisplatin and ruthenium-based complexes. Despite the discovery of metal-based drugs over 60 years ago, their precise mechanism of action is still unclear and elusive.

1.2.1 Mechanism of action of cisplatin

In cancer chemotherapy, cisplatin is administered intravenously mainly due to its poor water solubility [25]. The physiological concentration of chloride in the blood and extracellular body fluids is high enough to prevent the aquation of the compound [26]. The neutral complex, $[Pt(NH_3)_2Cl_2]$, enters the cell *via* cell membrane either by active uptake or passive diffusion mechanisms (Figure 1.3). Inside the cytoplasm, the concentration of chloride is 3-20% of the 100 mM chloride concentration in the bloodstream [27], consequently the drug undergoes hydrolysis to give a mono-aqua complex [*cis*-$[Pt(NH_3)_2(OH_2)Cl]^+$. Further substitution of the remaining chloride ligand leads to the formation of a

di aqua molecule *cis*-$[Pt(NH_3)_2(OH_2)_2]^{2+}$. These activated complexes i.e. the mono and di aqua species bind are more reactive towards the nucleobases in the DNA structure, with a predilection for nucleophilic N7-sites on purine bases (with guanine being the most preferred over adenine). The possible binding modes include functional binding to a single purine base (sequence **a**, Figure 1.3, monohydrated complex binding) and intra- and interstrand bifunctional binding (sequence **b**, Figure 1.3, dihydrated complex), [27-30]. Due to the cis position of the leaving groups, intrastrand cross-links between the the two nucleopbases are the most preferred (sequence **c**, Figure 1.3).

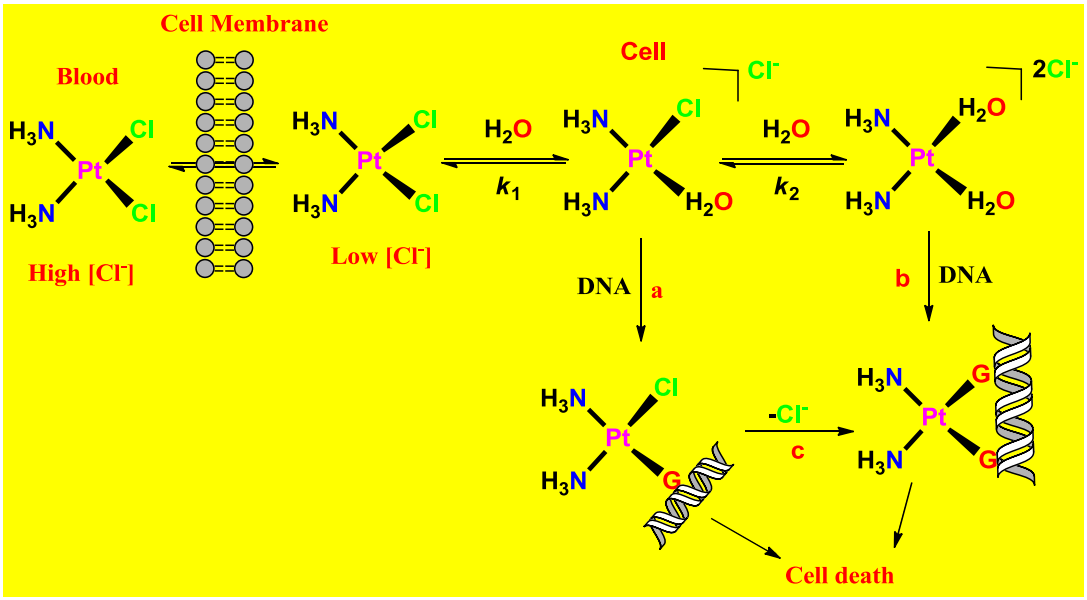

Figure 1.3: Intracellular hydrolysis and bio-activation of cisplatin in aqueous solution leading to binding at DNA in the cell nucleus and two proposed possible mechanism involving the mono and di-aquated species.

1.2.2 Postulated mode of mechanism of ruthenium-based drugs

The ruthenium-based drugs are administered as relatively inert Ru(III) species. The Ru(III) complexes mimic iron and hence are transported by coordinating to serum transferrin and albumin proteins [31, 32]. These proteins promote efficient uptake of iron for metabolic purposes. Since cancer cells have higher affinity for iron, they have increased number of transferrin receptors situated on their cell surfaces

than the normal cells, thus sequestering most of the circulating metal loaded transferrin (Figure 1.4, inset). This increases the selectivity of the drug as it bypasses the healthy cells and gets absorbed into the cancer cells [33], resulting in minimal toxicity [34]. Significantly, Ru(III) complexes do not necessarily replace the iron within these proteins, but are transported simultaneously. Cancer cells are known to have low pH and oxygen concentration, and considerable amounts of biological reducing agents such as glutathione (GSH). This promotes reduction of Ru(III) to the more kinetically labile Ru(II) species [33], (Figure 1.4). Thus the drug is administered as a less active, non-toxic Ru(III) compound, which is easily activated in the cancer cell [35] to form bifunctional intrastand adduct on double-helical DNA, leading to termination of the RNA synthesis. When the active Ru(II) compound leaves the low oxygen environment, it is re-oxidised to the Ru(III) by biological oxidants [36]. This proposed pathway is supported by NMR investigations of KP1019 that demonstrate that in the presence of cellular reducing agents, such as glutathione, the Ru(III) metal centre undergoes reduction to Ru(II) [37, 38]. However, unlike other Ru-based drugs, NAMI-A undergoes rapid extracellular hydrolysis, losing all its orginal ligands, and the resulting "naked" Ru(III) ions interact with proteins through the carboxylate group of glutathione or imidazole of histidine [23], (Figure 1.4). The mechanism explains why NAMI-A displays robust antimetastatic activity with negligible cytotoxicity.

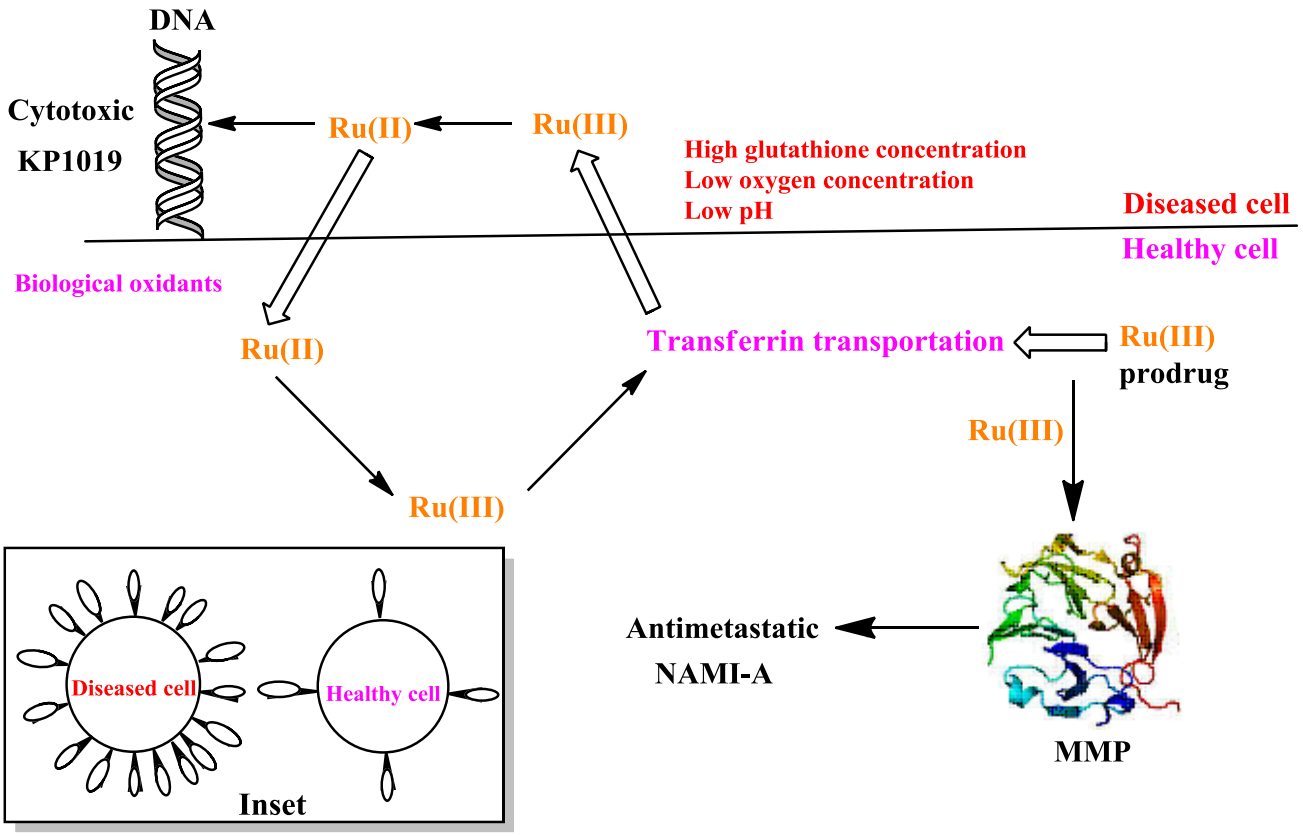

Figure 1.4: The mode of action of ruthenium complexes; insert, transferrin receptors on healthy and cancer cells (MMP = matrix metalloproteinases).

1.3. Substitution kinetics of clinically approved drugs

The cytotoxicity of metal-based drugs is thought to be related to the rate of substitution of the labile ligands by water molecules or other relevant biological nucleophiles. Miller and House [39-42], have performed extensive investigations on the first hydration of cisplatin at physiological pH in both basic and acidic solutions and rate constants (k_1) of (0.2-1) x 10^{-4} s^{-1} have been obtained. Previously, Knox *et al.*, [43] calculated the rate constants for the aquation of cisplatin and carboplatin, from their half-life in chloride-free phosphate buffer, pH 7 at 310 K and the values of 8.0 x 10^{-5} and 7.2 x 10^{-7} s^{-1} respectively were found. The results from the study indicated that the rate constant for the aquation of carboplatin is 100-fold slower compared to cisplatin. Carboplatin has a retention half-life of 30 h, compared to 1.5-3.6 h for cisplatin, hence it presents reduced side-effects [44]. Literature is replete with similar studies that show the rate constant, k_1, for the aquation of carboplatin ranging from 5.0 x 10^{-7}

to 1.0 x 10^{-9} s^{-1} at 310 K, [45-47] and according to a research investigation by Canovese *et al.*,[45] carboplatin is very stable and can remain in water for up to two months. In a similar study it has been found that the UV-Vis spectrum of carboplatin in water remains constant for several days at 298 K. Nevertheless, on the addition of dilute perchloric acid the spectrum of the final product resembles that of a fresh solution of *cis*-$[Pt(NH_3)_2(OH_2)_2]^{2+}$ [48]. These studies have suggested that the slower rate of substitution of carboplatin is likely to hinder aquation as a means of activating the drug in the cytosol. In light of this, a number of proposals such as direct interactions with DNA, enzymatic activation or reactions with sulfur nucleophiles have been suggested to account for the activity of carboplatin [46, 49]. The slower hydrolytic exchange of carboplatin chelating ligand contributes to its lower biological efficacy.

Similar to carboplatin, the aquation reaction of oxaliplatin, in a 10 mM HEPES buffer, pH 7 at 310K is much slower than that of cisplatin, with a rate constant of 1.2 x 10^{-6} s^{-1} [50]. The study shows that the hydration of oxaliplatin proceeds in two steps. The first step which is the ring opening step, takes place at a half-life of 16 min. In the second step, the oxalate ligand is lost at a half-life of 92 min. Hence, the first rate constant, k_1 (ring opening step) is virtually six times faster than the second rate constant, k_2 which involves the loss of the oxalato ligand. In another research study, the hydration reactions of oxaliplatin has been examined in aqueous medium under neutral and acidic condition using density functional theory (DFT) and conductor-like dielectric continuum model (CPCM) approach to obtain a detailed mode of action of the drug [51]. The analysis agrees well with the experimental data, that the hydrolysis reaction in the neutral media is much slower than the acid counterpart. The hydrolysis reactions of nedaplatin and lobaplatin have also been examined under neutral and acidic conditions using DFT coupled with CPCM. The studies revealed that the mode of action of the drugs is similar to that of oxaliplatin [51, 52].

1.4. Correlative studies on the kinetics of ligand substitution reactions, DNA/BSA interactions and cytotoxic activity of metal-based complexes

Even though a number of potential targets for metal-based drugs have been reported, it is generally believed that cellular DNA is the most likely biological target. Binding of a drug to DNA is likely to interfere with the DNA replications mechanisms, thus triggering cell death [53]. The key elements linked to effective interactions of the metal-based drugs with the DNA, include aquation, kinetic inertness of the drug to biomolecular nucleophiles, and efficient transport to the target through the blood plasma [54]. In this context, this section seeks to determine if some correlations exist between the kinetics of the substitution reactions of metal-based drugs to their DNA/BSA binding abilities and cytotoxic effects.

1.4.1 Platinum(II)/(IV) complexes

Since the discovery of cisplatin in 1969, the use platinum-based drugs in cancer treatment has gained a significant interest [55-60]. Platinum complexes demonstrate similar metal-ligand exchange kinetics as the division of the diseased cells, which makes them suitable to supress mitosis process. Moreover, these compounds are capable of forming thermodynamically stable bonds with the N-donor ligands in the DNA helix, hindering DNA replication and thus promoting cell death [61, 62]. For instance, Zhao and colleagues [63] explored the hydrolytic and antitumour behaviour of Pt(IV) complexes of *N*-isopropyl-*1R,2R*-diaminocyclohexane ligand with different R groups (where R = CH_3, **1** and $CHCl_2$, **2**, Figure 1.5). Generally, Pt(IV) complexes are known to be kinetically inert, and can resist hydrolysis prior to entering the cancer cells. It is assumed that Pt(IV) complexes act as prodrugs and undergo reduction in the cytoplasm to form the active Pt(II) species [64]. Nonetheless, complexes **1** and **2** undergo fast hydrolysis due to the strong σ-donor ability of the N-isopropyl-*1R,2R*-diaminocyclohexane moiety. It was observed that complex **2** hydrolyses relatively quicker under biological conditions (pH 7.4 and 37.5°C) than complex **1**, with the values of (60.2 ± 5.5) x 10^4 and (1.26 ± 0.13) x 10^4 s^{-1},

respectively (Table 1.1). Complex **2** demonstrates better cytotoxic activity than complex **1** against HCT-116, HePG-2 and A549 cell lines, reflecting a positive correlation between hydration kinetics and cytotoxicity. Even though complex **2** is more labile than **1**, its timescale of hydrolysis should be long enough to allow the complex to reach the target site, before being activated.

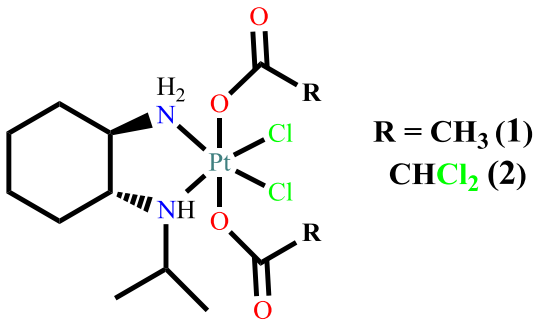

Figure 1.5: Monuclear Pt(IV) complexes of *N*-isopropyl-*1R,2R*-diaminocyclohexane ligand which display positive correlation between hydrolysis reactions and cytotoxic effect [63].

In a follow-up work, Ćoćić and others [65] found that steric influence of the chelating ligands, affect the interactions of mononuclear Pt(II) complexes with biologically relevant nucleophiles, thiourea (**Tu**), L-cysteine (**L-Cys**), L-methionine (**L-Met**) and guanosine 5'-monophosphate (**5'-GMP**). The evaluated complexes were of the form, [Pt(H_2L^{tBu})Cl]Cl **3**, and [Pt(Me_2L^{tBu})Cl]Cl **4** (where H_2L^{tBu} = 2,6-bis(5-(tert-butyl)-1H-pyrazol-3-yl)pyridine and Me_2L^{tBu} = 2,6-bis(5-(tert-butyl)-1-methyl-1H-pyrazol-3-yl)pyridine (Figure 1.6). For instance, the rate constants, k_2, of complexes **3** and **4** with thiourea nucleophile were obtained as 1.225 ± 0.004 and 0.935 ± 0.002 M^{-1} s^{-1} respectively (Table 1.1). The slower reactivity of **4** was assigned to the presence of the methyl substituents on the nitrogen atoms that increases steric crowding at the Pt(II) centre, thus blockng the entry of the incoming nucleophile to the reaction metal centre. In line with the kinetic lability, complex **3** strongly and favourably binds to CT-DNA and BSA protein relative to that of **4** as presented in Table 1.1. The anti-proliferative efficacy of complexes **3** and **4** on HeLa, PANC-1 and MRC-5 cancer cell lines reveals that complex **3** exerts a more

promising growth inhibitory effect than complex **4** against the studied cancer cell lines (Table 1.1), a trend that correlates well with the high kinetic reactivity and greater DNA/BSA binding constants for complex **3**. The higher rate constants and BSA binding abilities of complex **3**, relative to complex **4** , show that the Pt-S adduct functions as a drug reservoir, delivering the active species of **3** to the DNA, facilitating facile DNA interactions. The reasoning is well-supported by the better DNA binding constant and growth inhibitory of complex **3**. However, complex **3** is non selective on the studied cancer cell lines, when compared to complex **4**. For example the selectivity index (SI) of complex **3** is < 2 on both HeLa and MRC-5, while the SI values of complex **4** are 2.78 and < 2 on HeLa and MRC-5 after 24 h, respectively. Notaby, SI values < 2 demonstrate non-selective nature of the complexes.

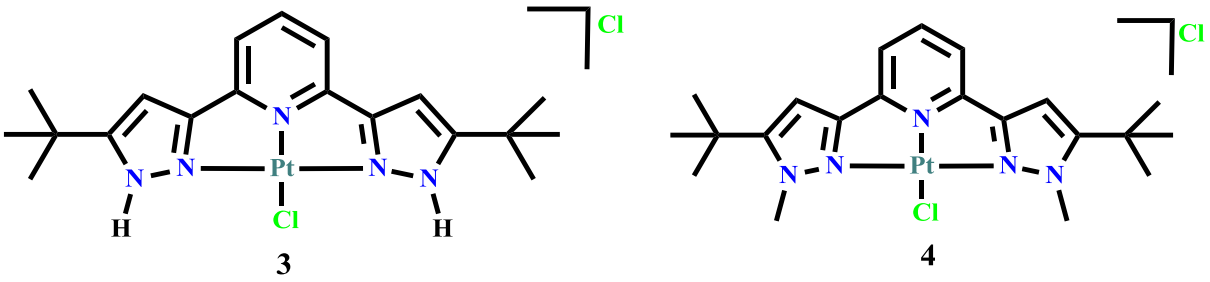

Figure 1.6: Mononuclear (pyrazolyl)pyridine Pt(II) complexes showing a positive correlation between the rates of substitution kinetics reactions and DNA/BSA affinities and cytotoxicity [65].

Jaganyi and co-workers [66] recently studied the effects of methyl groups and extended π-conjugation on the substitution kinetics, DNA/BSA interactions and *in vitro* cytotoxicity of mononuclear Pt(II) complexes anchored on 2,3-di(2-pyridyl)quinoxaline ligands. The investigated complexes were, $[Pt(bpq)Cl_2]$ (bpq is 2,3-di(2-pyridyl)quinoxaline) **5**, $[Pt(dmbpq)Cl_2]$ (dmbpq is 6,7-dimethyl-2,3-di(2-pyridyl)quinoxaline) **6**, and $[Pt(bbq)Cl_2]$ (bbq is 2,3-bis(2'pyriyl)benzo[g] quinoxaline) **7** (Figure 1.7). The rate of substitution reactions of the aquated complexes with the S-donor nucleophiles, thiourea (**Tu**), 1,3-dimethyl-2-thiourea (**Dmtu**), and 1,1,3,3-tetra methyl-2-thiourea (**Tmtu**) is in the order **5** < **6** < **7** (Table 1.1). The lability of the aqua ligands is influenced by *trans* σ-effects of methyl groups. The

binding strengths of the complexes towards DNA and BSA follows the same order **5** < **6** < **7** (Table 1.1), indicating a positive correlation between kinetics of ligand substitution reactions and DNA/BSA interactions. In addition, the *in vitro* MTT cytotoxicity of complexes **5**, **6** and **7** towards HepG2 cell line are 15.7 ± 1.6, 14.9 ± 1.4, and 17.9 ± 2.0 μM, respectively (Table 1.1), showing no correlation between kinetic reactivity and cytotoxicity. The lower cytotoxic effect of **7** may be due to the non-specific deactivation by the other biomolecules in cytoplasma, since it is the the most kinetically labile among the three compounds. This data thus represent a classical example of the complexity in relating kinetic lability to biological activity. While kinetic lability is essential for the aquation and transportation of the complexes in the cytoplasm, highly labile systems have the potential to undergo deactivation by other non-target biomolecules [67]. A potent drug should be able to reach the site of action in sufficient concentration and in a timely manner.

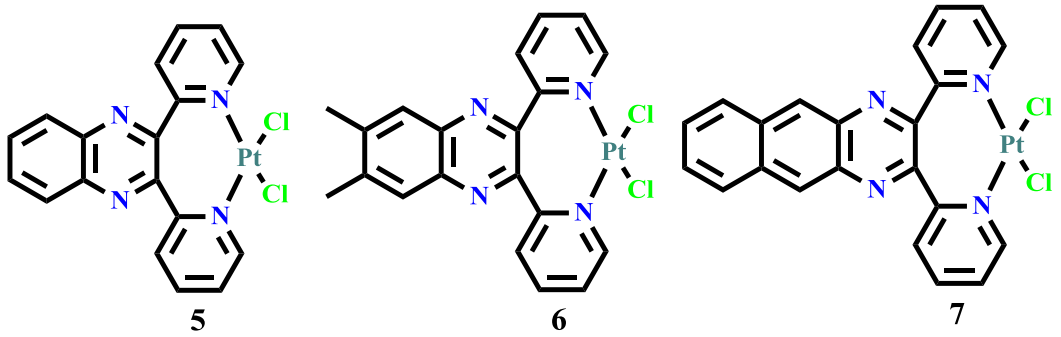

Figure 1.7: Mononuclear Pt(II) complexes supported on 2,3-di(2-pyridyl)quinoxaline ligands. The complexes exhibit positive correlation between substitution kinetics and DNA/BSA interactions. However, the complexes show no correlation between kinetic reactivity and cytotoxicity [66].

The work of Bugarčić and colleagues [68, 69] has demonstrated that the introduction of a bridged pyrazine ligand between two metal centres may confer profound influence on the reactivity and cytotoxic properties of the dinuclear Pt(II) complexes of the type [{trans-$Pt(NH_3)_2Cl\}_2$(μ-pyrazine)]$(ClO_4)_2$, **8**, [{trans-$Pt(NH_3)_2Cl\}_2$(μ-4,4′-bipyridyl)]$(ClO_4)_2$·DMF, **9**, and [{trans-

$Pt(NH_3)_2Cl\}_2(\mu$-1,2-bis(4-pyridyl)ethane)$](ClO_4)_2$, **10**, as shown in Figure 1.8. The rate of reactivity of the complexes with the biologically relevant ligands, **Tu**, **GSH**, and **5′-GMP** decreases in the order **8** > **9** > **10**. For example, with reference to **Tu**, complexes **8**, **9** and **10** display varied rate constants of (1.56 ± 0.07) x 10^4, (1.30 ± 0.07) x10^4, and (8.0 ± 0.40) x 10^3 M^{-1} s^{-1}, respectively (Table 1.1). The close proximity of the two Pt metal atoms in **8** facilitates electronic communication between the two Pt(II) centres and thus rendering the metal centre more electrophilic. The cytotoxic potency of **8-10** in MSC cell line, presents a significant activity of 4.3 μM, for **9** and 5.6 μM, for **10**. Consistent with the results of Jaganyi and co-workers, the minimal cytotoxic effect for complex **8** (IC_{50} = 250 μM) may be linked to its higher kinetic lability, and hence more susceptible to competition from S-donor and N-donors other than the molecular target DNA.

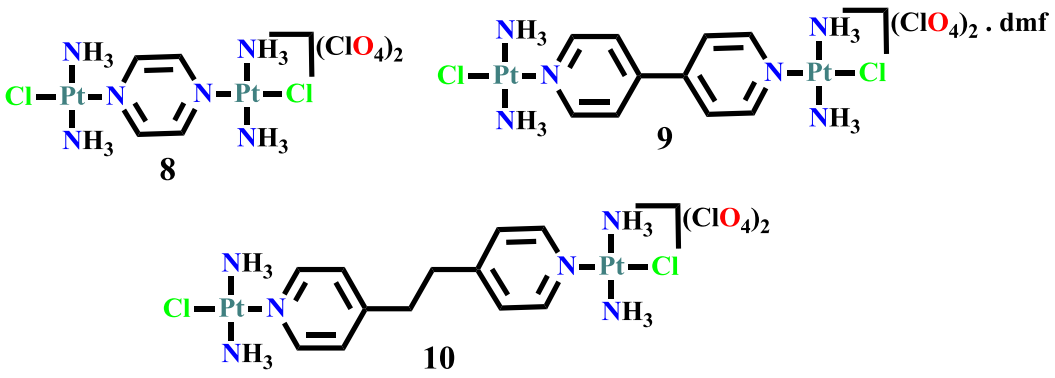

Figure 1.8: Mono-dinuclear bridged Pt(II) complexes indicating no correlation between the rates of substitution kinetics and cytotoxic effects [68, 69].

Table 1.1: A summary of the correlative studies of substitution kinetics reactions, DNA/BSA interactions and cytotoxic activities of mononuclear and dinuclear Pt(II)/Pt(IV) complexes

Complex	Kinetics reactions (s^{-1} or M^{-1} s^{-1})	DNA binding, K_b (M^{-1})	BSA binding, K (M^{-1})	Cytotoxicity (IC_{50}, μM)			Ref
	Aquation			**HCT-116**	**HepG-2**	**A549**	**[63]**
1	$(1.26 \pm 0.13) \times 10^4$	nd	nd	2.6 ± 0.1	9.1 ± 0.4	50.6 ± 0.1	
2	$(60.2 \pm 5.5) \times 10^4$			1.9 ± 0.1	1.6 ± 0.1	0.9 ± 0.1	
	Tu			**HeLa**	**PANC-1**	**MRC-5**	**[65]**
3	1.225 ± 0.004	$(5.3 \pm 0.1) \times 10^4$	$(4.7 \pm 0.1) \times 10^4$	90 ± 10	410 ± 10	78 ± 2	
4	0.935 ± 0.002	$(5.5 \pm 0.1) \times 10^4$	$(4.9 \pm 0.1) \times 10^4$	80 ± 10	> 1000	240 ± 70	
	Tu			**HepG2**			**[66]**
5	$(6.25 \pm 0.05) \times 10^2$	$(1.13 \pm 0.04) \times 10^4$	$(1.93 \pm 0.02) \times 10^5$	15.7 ± 1.6			
6	$(7.95 \pm 0.07) \times 10^2$	$(3.03 \pm 0.08) \times 10^4$	$(2.97 \pm 0.07) \times 10^5$	14.9 ± 1.4			
7	$(9.44 \pm 0.1) \times 10^2$	$(5.77 \pm 0.09) \times 10^4$	$(5.34 \pm 0.10) \times 10^5$	17.9 ± 2.0			
	Tu			**MSC**			**[68, 69]**
8	$(1.56 \pm 0.07) \times 10^4$	nd	nd	250			
9	$(1.30 \pm 0.07) \times 10^4$			4.3			
10	$(8.0 \pm 0.40) \times 10^3$			5.6			

K_b = DNA binding constant; K = BSA association binding constant; IC_{50} = Half maximal inhibitory concentration; nd = not determined.

1.4.2 Palladium(II) complexes

Besides Pt(II)/(IV) complexes, Pd(II) complexes represent another class of compounds that have been widely studied as anti-cancer agents. However, hydrolysis in Pd(II) complexes is too rapid *ca*. 10^5 faster than the corresponding Pt(II) analogues, a factor that makes them readily dissociate in solution, and thus are unable to reach the target, DNA. The considerably high kinetic reactivity can be controlled by varying the ligand around the metal centre [70-72]. Strong donor ligands and bulky carrier ligands generate stable metal-ligand bonds and steric shelter that maintain the structural identity of the compounds long enough *in vivo.* One such example is the reports of Ćoćić and co-workers [65] using

Pd(II) complexes; [Pd(H_2L^{tBu})Cl]Cl (**11**) and [Pd(Me_2L^{tBu})Cl]Cl (**12)** (where H_2L^{tBu} = 2,6-bis(5-(tert-butyl)-1H-pyrazol-3-yl)pyridine and Me_2L^{tBu} is 2,6-bis(5-(tert-butyl)-1-methyl-1H-pyrazol-3-yl)pyridine) as represented in Figure 1.9. The rates of reactivity of complexes **11** and **12** with the biological nucleophiles, **Tu**, **L-Cys**, **L-Met**, and **5'-GMP** decreases in the sequence **11** > **12**. For example, the rate constants for **11** and **12**, with **5'-GMP** as the incoming nucleophile are (2.81 ± 0.06) x 10^4 and (2.28 ± 0.04) x 10^4 M^{-1} s^{-1} (Table 1.2), demonstrating that kinetic reactivity is controlled by steric hindrance. The binding affinities of complexes **11** and **12** to DNA and BSA were also studied and found to follow the order **11** > **12**, which is in good agreement with the kinetic reactivity of the compounds. The cytotoxicity study of complexes **11** and **12** on Hela, PANC-1 and MRC-5 cell lines, show complex **11** to be more active than complex **12** as given in Table 1.2. Thus in this work there is a positive correlation between the kinetic lability of the complexes and their DNA/BSA binding affinities and the resultant cytotoxicity activities. The higher cytotoxicity of **11** is attributable to the reduced over-crowding at the metal centre, which promotes facile and strong interactions with the CT-DNA and BSA. The observed trend in the substitution behaviour, protein and BSA binding, indicate that the metal-sulfur adduct act as a drug reservoir and thus protecting the drug from reacting with other biomolecules. Nonetheless, both complexes **11** and **12** displayed non selectivity, SI < 2, on HeLa and PANC-1 cell lines after 24 h.

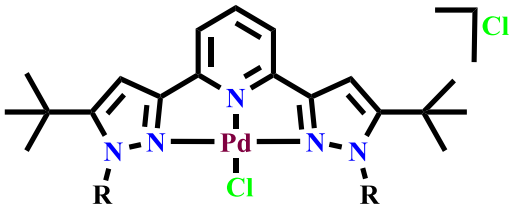

R = H (11)
CH_3 (12)

Figure 1.9: Mononuclear (pyrazolyl)pyridine Pd(II) complexes showing positive correlation on the rates of substitution reactions, DNA/BSA interactions and the resultant cytotoxic effects [65].

In an earlier report, Keter *et. al.* [73] investigated the steric effects of the ancillary substituents on the kinetic reactivity and cytotoxicity of some pyrazolyl Pd(II) of the general formula [$PdCl_2$(3,5-R_2bpza)] (where bpza = bis-pyrazolyl acetic acid, R = H, **13** R =CH_3, **14**), Figure 1.10. The rates of kinetic reactivity for the diaqua species of **13** and **14** with **L-Cys** are 5.98 x 10^2 and 7.01 x 10^2 M^{-1} s^{-1}, respectively (Table 1.2).The observation is unexpected, since **14** (CH_3) should demonstrate a lower reactivity than **13** (H), due to the steric effects of the methyl substituents. The *in vitro* cytotoxicity examinations showed poor activity for complexes **13** and **14**, IC_{50} value of the two compounds being > 1000 μM. Compared to the other Pd(II) complexes in this review, the poor cytotoxic effect of complexes **13** and **14** could be explained by their relatively low ligand-exchange kinetics that hinder facile interactions with the target, DNA. Compounds with very low kinetic reactivity are likely to be excreted easily through the human body before reaching the DNA, for example it is well known that 90% of carboplatin can be recovered from the urine [74, 75].

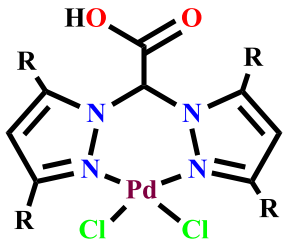

R = H (13)
CH_3 (14)

Figure 1.10: Mononuclear bis(pyrazolyl) Pd(II) complexes examined by Keter *et al*, displaying low kinetic reactivity compared to the other Pd(II) compounds accompanied by low cytotoxic [73].

Recently Jaganyi and co-workers [76] reported the role of 2,6-bis(pyrazol-2- yl)pyridine ligands on the substitution kinetics, DNA interactions, and *in vito* cytotoxic activities of Pd(II) complexes. The studied

complexes were of the type [chloride-(2,2′:6′,2″-terpyridine)Pd(II)]Cl (**15**), [chlorido(2,6-bis(*N*-pyrazol-2-yl)pyridine)Pd(II)]Cl (**16**), [chlorido(2,6-bis(3,5-dimethyl-*N*-pyrazol-2-yl)pyridine)Pd(II)]Cl (**17**) and [chlorido(2,6-bis(3,5-dimethyl-*N*-pyrazol-2-ylmethyl)pyridine)Pd(II)]BF_4 (**18**), (Figure 1.11). The substitution kinetics of the complexes with the thiourea nucleopiles *i.e*. **Tu**, **Dmtu**, **Tmtu** decreases in the form: **15 (**k_2 =118,000 M^{-1} s^{-1}, **Tu)** > **16** (k_2 =12,600 M^{-1} s^{-1}, **Tu**) > **17** (k_2 =10,100 M^{-1} s^{-1}, **Tu**) >> **18 (**k_2 = 1.46 M^{-1} s^{-1}, **Tu**), Table 1.2, ascribed to π-acceptor ability and steric influence of the carrier ligand(s). The binding of the complexes towards CT-DNA followed the same order as kinetic reactivity (Table 1.2), demonstrating a positive correlation between the two parameters. The anti-tumour activities of the complexes on MCF7 cell lines, showed 4 ± 0.5 μM for **15**, 13 ± 1 μM for **16**, and 27 ± 2 μM for **17**, and 22 ± 0.5 μM for **18** μM, for **15**, **16**, **17** (Table 1.2), depicting a rough correlation on substitution kinetics and cytotoxicity. The higher cytotoxic effects of **15** could well be explained by a combination of a more planar and unhindered geometry and a better π-conjugation of the spectator ligand. These factors result to facile DNA interaction, and thus enhancing cytotoxicity.

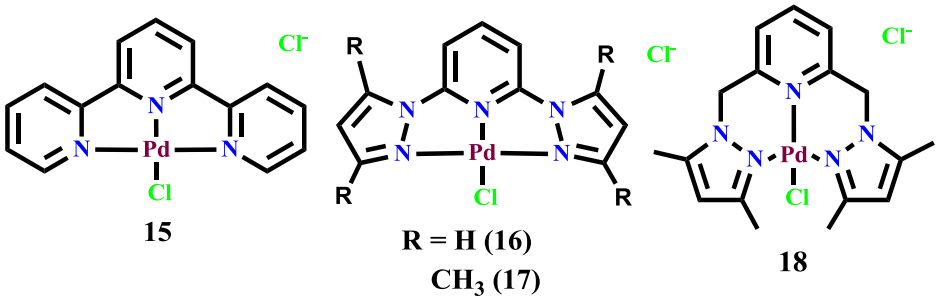

Figure 1.11: Mononuclear [2,6-bis(pyrazol-2-yl)pyridine] Pd(II) complexes, highlighting a positive correlation on kinetic reactivity, DNA binding ability, and a rough direct relationship with the anti-tumour activities [76].

In another study, the influence of pyrazine and bipyridine ligands on the rate of ligand substitution reactions, DNA/BSA interactions and antitumour activity of dinuclear Pd(II) complexes was evaluated

by examining a series of bridged complexes of the formula, [{Pd(2,2′-bipy)Cl}$_2$(μ-pz)](ClO$_4$)$_2$ (**19**), [{Pd(dach)Cl}$_2$(μ-pz)](ClO$_4$)$_2$ (**20**), [{Pd(en)Cl}$_2$(μ-pz)](ClO$_4$)$_2$ (**21**), [{Pd(2,2′-bipy)Cl}$_2$(μ-4,4′-bipy)](ClO$_4$)$_2$ (**22**), [{Pd(dach)Cl}$_2$(μ-4,4′-bipy)](ClO$_4$)$_2$ (**23**) and [{Pd(en)Cl}$_2$(μ-4,4′-bipy)](ClO$_4$)$_2$ (**24**) (where 2,2′-bipy = 2,2′-bipyridyl, pz = pyrazine, dach = trans-(±)-1,2-diaminocyclohexane, en = ethylenediamine, 4,4′-bipy = 4,4′-bipyridyl) were prepared (Figure 1.12), [77]. The kinetic reactivity of the compounds with pyrazine as bridging ligand with the nucleophiles, **Tu**, **L-Met**, **L-Cys**, **L-His**, and **5′-GMP** follows the order **19** > **21** > **20** (Table 1.2). The highest reactivity of complex **19** was assigned to the π-acceptor ability of the 2,2′-bipy ligand that increases the electrophilicity of the Pd(II) centre. The interactions of complexes **19**, **20** and **21** with CT-DNA follows a slightly different sequence of **19** < **21** < **20** (Table 1.2), indicating a negative correlation between the rate of reactivity and DNA binding. With respect to BSA , the order of relative binding affinities of the complexes is in the form **19** > **21** > **20**, showing a positive correlation between the kinetics of ligand substitution reactions and BSA interactions. The cytotoxic effect of the complexes on the HeLa cancer cell lines follows the order **19** (IC_{50} = 6 ± 3 μM) > **20** (IC_{50} = 80 ± 10 μM) > **21** (IC_{50} = 90 ± 30 μM), (Table 1.2). The greater cytotoxicity of complex **19** in comparison to complexes **20** and **21** may be ascribed to the planarity of 2,2′-bipy ligand in **19**, which promotes facile binding to the DNA and BSA. This argument is well supported by the results of DNA/BSA binding studies, in which complex **19** display the greatest affinity. The values of rate constants for the reactions of complexes of 4,4′-bipy as bridging ligand with the investigated nucleophile follow the order **22 > 24 > 23** (Figure 1.12). This trend may be explained using the same concept as complexes **19**, **20** and **21** bearing pyrazine bridging ligand. The interactions of complexes **22-24** with CT-DNA follows the order **23** > **24** > **22** and thus, reflecting a negative correlation between substitution kinetics reactions and CT-DNA binding. On the other hand, compounds **22, 23** and **24** showed good binding affinity towards BSA protein giving the order, **22** > **24** > **23**, in line with the trends reported for rate constants, k_2. The inhibitory effect of **22**, **23** and **24** on HeLa cell lines decrease in the order; **22** (IC_{50} = 15 ± 5 μM) > **23** (IC_{50} =57 ± 9 μM) > **24** (IC_{50} >100 μM), Table 1.2, and the trend is explained as those with pyrazine as bridging ligand (i.e. **19**, **20** and **21**).

Compound **22** demonstrates a better cytotoxicity on HeLa cell line than **23** and **24** and the argument is supported by relatively high kinetic reactivity, and BSA binding constants, demonstrating that the S-bound drug is behaving as a drug-resevoir, acting as an intermediate of the reaction of the metal complex. Generally, the growth inhibition of cancer cells is higher for **19**, **20** and **21** in comparison to **22**, **23**, and **24**. The better cytotoxicity of **19-21** could be attributed to their relatively higher BSA protein constants compared to **22-24**, which facilitate efficient transportation of the compounds to the target, DNA.

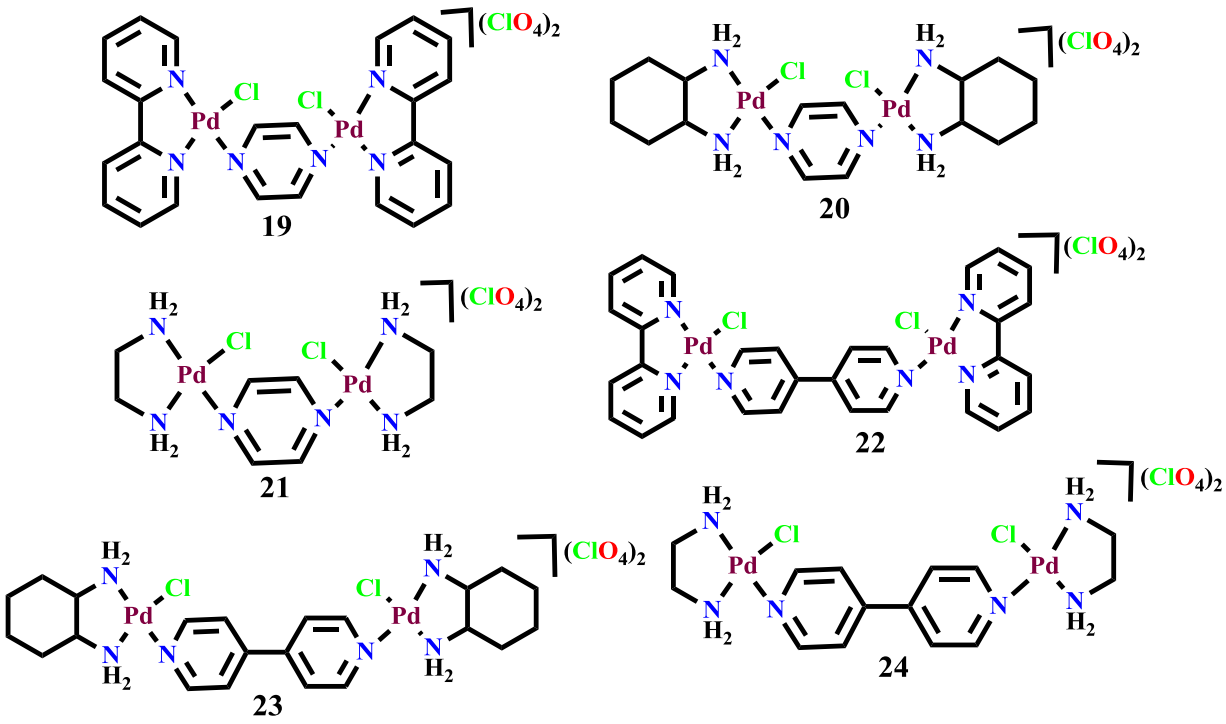

Figure 1.12: Mono-dinuclear bridged-pyrazine and 4,4'-bipyridine Pd(II) complexes, indicating a positive correlation between kinetic reactivity and BSA affinity, but no relationship between the rate of kinetic reactivity and inhibitory effects was observed [77].

In a related study, the competing effects of the π-back-donation and σ-donation of the spectator chelating ligands on substitution kinetics reactions, DNA/BSA binding abilities and cytotoxicity of bimetallic Pd(II) complexes of the type [{PdCl(bipy)}{μ-(pyrazine)}{PtCl(bipy)}]Cl(ClO_4) **25** and

[{PdCl(en)}{μ-(pyrazine)}{PtCl(en)}]Cl(ClO_4) **26**, (where bipy and en are 2,2′-bipyridine and ethylenediamine, respectively) were analysed (Figure 1.13) [78]. The nucleophilic substitution reactions of complex **25** proceeds faster than **26**, with k_2 values of (3.1 ± 0.1) x 10^4 and (6.0 ± 0.2) x 10^3 M^{-1} s^{-1}, respectively (Table 1.2). The higher reactivity of complex **25**, is induced by the π-acceptor capacity of the bipyridine ligand, while the slower reactivity of **26** is due to the σ-donor ability of ethylenediamine ligand. The CT-DNA and BSA binding constants of complex **26** are higher compared to **25** (Table 1.2) and follow the same order seen for the rates of ligand substitution reactions. The cytotoxicity of complexes **25** and **26** on HeLa cell line revealed IC_{50} value of 21 ± 2 μM for **25** and 196 ± 4 μM for **26** (Table 1.2). The enhanced inhibitory effect of complex **25** is assigned to its π-conjugation (aromaticity), which increases hydrophilicity and lipophilicity and thus high cytotoxicity of the complex. Thus in this study, a positive correlation between the rates of ligand substitution reactions and cytotoxicity is reported. In addition, the negative correlation between DNA/BSA bindings and cytotoxicity of complexes **25** and **26**, demonstrates that cytotoxicity is not just a consequence of DNA/BSA binding, but may be controlled by several factors such as secondary intracellular interactions.

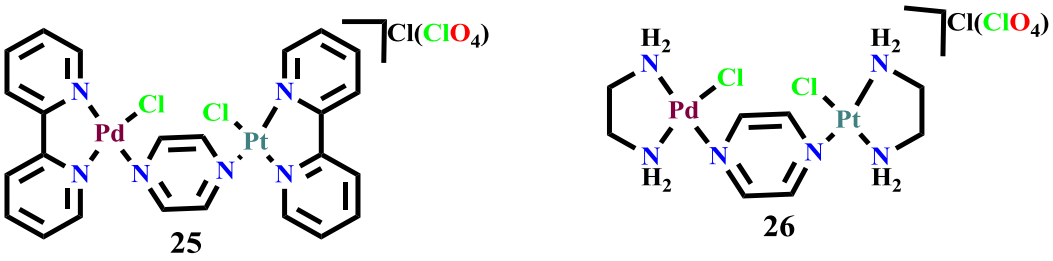

Figure 1.13: Hetero-dinuclear bridged-pyrazine Pd(II)/Pt(II) complexes exhibiting inverse correlation between substitution kinetics and DNA/BSA affinities. A direct correlation between the kinetics of ligand substitution reactions and cytotoxicity is reported [78].

Table 1.2: A summary of the rates of ligand substitution reactions, DNA/BSA bindings and cytotoxic activities of mononuclear and dinuclear Pd(II) complexes

Complex	Kinetics reactions (s^{-1} or $M^{-1} s^{-1}$)	DNA binding, K_b (M^{-1})	BSA binding, K (M^{-1})	Cytotoxicity (IC_{50}, μM)			Ref
	Tu			**HeLa**	**PANC-1**	**MRC-5**	**[65]**
11	$(2.81 \pm 0.06) \times 10^4$	$(1.9 \pm 0.1) \times 10^4$	$(1.9 \pm 0.1) \times 10^4$	60 ± 10	67 ± 7	45 ± 8	
12	$(2.28 \pm 0.04) \times 10^4$	$(2.4 \pm 0.2) \times 10^4$	$(3.2 \pm 0.2) \times 10^4$	240 ± 40	360 ± 10	240 ± 20	
	L-cysteine			**CHO**			**[73]**
13	5.98×10^2	nd	nd	1500 ± 200			
14	7.01×10^2			1100 ± 100			
	Tu		nd	**MCF-7**			[**76**]
15	$(1.18 \pm 0.02) \times 10^5$	$(9.9 \pm 0.2) \times 10^4$		4 ± 0.5			
16	$(1.26 \pm 0.03) \times 10^4$	$(2.7 \pm 0.1) \times 10^4$		13 ± 1			
17	$(1.01 \pm 0.01) \times 10^4$	$(1.0 \pm 0.1) \times 10^4$		27 ± 2			
18	1.46 ± 0.01	$(0.8 \pm 0.1) \times 10^4$		22 ± 2			
	Tu			**HeLa**	**MDA-MB-231**		**[77]**
19	$(5.51 \pm 0.06) \times 10^4$	$(4.8 \pm 0.2) \times 10^4$	$(1.24 \pm 0.05) \times 10^5$	6 ± 3	17 ± 4		
20	$(1.53 \pm 0.05) \times 10^4$	$(1.6 \pm 0.1) \times 10^5$	$(1.03 \pm 0.03) \times 10^5$	80 ± 10	26 ± 3		
21	$(2.05 \pm 0.03) \times 10^4$	$(1.1 \pm 0.1) \times 10^5$	$(1.13 \pm 0.06) \times 10^5$	90 ± 30	25 ± 4		
22	$(3.60 \pm 0.1) \times 10^4$	$(1.9 \pm 0.2) \times 10^5$	$(1.18 \pm 0.01) \times 10^5$	15 ± 5	70 ± 20		
23	$(8.70 \pm 0.04) \times 10^3$	$(2.9 \pm 0.1) \times 10^5$	$(5.26 \pm 0.02) \times 10^4$	57 ± 9	>100		
24	$(1.34 \pm 0.03) \times 10^4$	$(2.6 \pm 0.2) \times 10^5$	$(7.60 \pm 0.40) \times 10^4$	>100	>100		
	Tu			**A375**	**HeLa**		**[78]**
25	$(3.1 \pm 0.1) \times 10^4$	$(2.1 \pm 0.1) \times 10^5$	$(6.1 \pm 0.4) \times 10^4$	49 ± 2	21 ± 2		
26	$(6.0 \pm 0.2) \times 10^3$	$(3.6 \pm 0.1) \times 10^5$	$(1.2 \pm 0.04) \times 10^5$	>200	196 ± 4		

K_b = DNA binding constant; K = BSA association binding constant; IC_{50} = Half maximal inhibitory concentration; nd = not determined.

1.4.3 Ruthenium(II)/(III) complexes

Besides platinum and palladium complexes, ruthenium compounds have also witnessed significant growth with respect to their design and applications as anti-cancer agents [79-81]. The variable oxidation states of ruthenium (+2, +3 and +4), under biological conditions, make them suitable candidates in the anticancer study [82]. Compared to platinum and palladium complexes, ruthenium compounds are known to have relatively slower ligand-exchange kinetics, a property that allows them to remain unchanged as they approach DNA [83]. For example, Keppler and co-workers demonstated that the structure of NAMI-A-type complexes affect the rate of their aquation, protein binding, and antiproliferative activity [35]. The examined complexes; [*trans*-RuCl4(1*H*-imidazole)(dmso-*S*)] (**27**), indazolium [*trans*-RuCl4(1*H*indazole)(dmso-*S*)] (**28**), 1,2,4-triazolium [*trans*-RuCl4(1*H*-1,2,4-triazole)(dmso-*S*)] (**29**), 4-amino-1,2,4-triazolium [*trans*-RuCl4(4-amino-1,2,4-triazole)(dmso-*S*)] (**30**), and 1-methyl-1,2,4-triazolium [*trans*-RuCl4(1-methyl-1,2,4-triazole)(dmso-*S*)] (**31**) are depicted in Figure 1.14. The rate constants for the aquation reactions (k_{aqua}) of the complexes at physiological conditions (pH 7.4 and 37 °C) are ordered as **30** (0.050 ± 0.012 min^{-1}) > **27** (0.031 ± 0.006 min^{-1}) > **29** (0.025 ± 0.004 min^{-1}) > **28** (0.020 ± 0.005 min^{-1}) > **31** (0.012 ± 0.002 min^{-1}), Table 1.3. The rates of binding kinetics (k_{bind}) for the reactions of the complexes **27**, **28**, **29**, and **31** with the transferrin protein are 0.064 ± 0.024, 0.206 ± 0.027, 0.094 ± 0.014, 0.258 ± 0.054, and 0.009 ± 0.003 min^{-1}, respectively (Table 1.3). Comparing the rate constants of the hydrolytic reactions to those of transfferin proteins binding, it is clear that complex **30** demonstrates highest affinity to the transferrin protein, consistent with its rapid rate of aquation. From a clinical perspective, this observation suggests that complex **30** is likely to bind to the DNA easily and strongly. The presence of the primary amine moiety accelerates the complex-protein interactions by allowing the hydrogen bonding towards electron-acceptor protein residues [84]. Ths is in constrast to the methyl group in complex **31**, which inhibits the hydrogen-bonding interactions. With the HT-29 cell line, the cytotoxic effects of the complexes **28** (IC_{50} = 212 ± 22 μM) > **31** (IC_{50} = 315 ± 22 μM) > **29** (IC_{50} = 322 ± 32 μM) > **27** (IC_{50} = 339 ± 68 μM) > **30** (IC_{50} = 621 ± 5 μM), Table 1.3. The IC_{50} values of the complexes indicate that protein binding is not

necessarily a function of anticancer activity (complex **30** with the fastest aquation and protein binding has the least cytotoxic effect in the series).

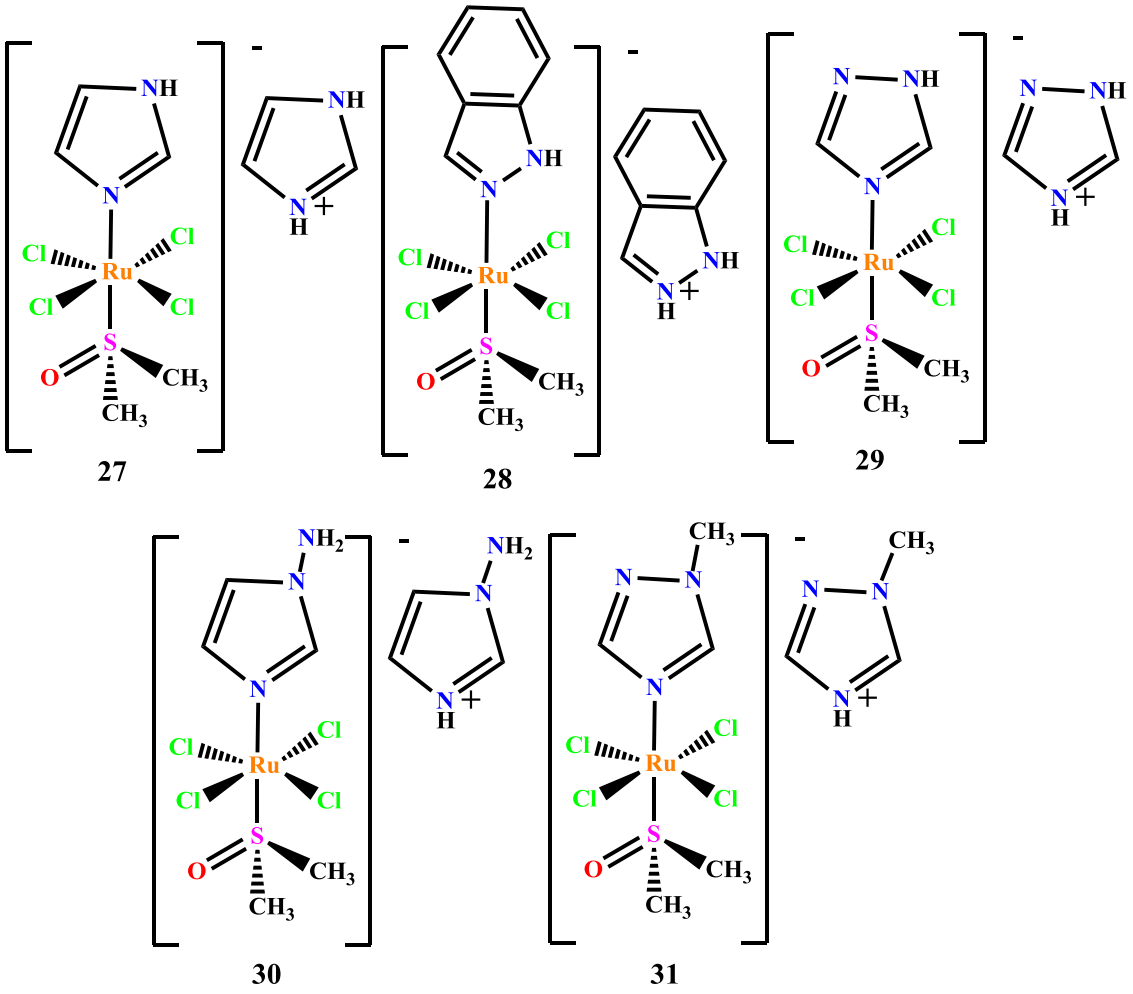

Figure 1.14: NAMI-A-type complexes, showing that the anticancer activity of metallo-drugs does not necessarily depend on their ability to bind on the transferrin protein, which is responsible for the delivery of therapeutic agents to the target, DNA [35].

In another report, Haghdoost *et. al.* studied the link between the rate of hydrolysis, and antiproliferative activity of Ru(II) arene complexes of N ^ O donor Schiff-base ligands [85]. The evaluated complexes of the type [{(E)-1-(((furan-2-ylmethyl)imino)methyl)naphthalen-2-ol} Ru(η^6-benzene)Cl], **32**; [{(E)-1-((pentylimino)methyl)naphthalen-2-ol} Ru(η^6-benzene)Cl], **33**; [{(E)-1-((benzylimino)methyl)

naphthalen-2-ol} Ru(η^6-benzene)Cl], **34**;[{(E)-1-(((cyclohexylmethyl)imino)methyl)naphthalen-2-ol} Ru(η^6-benzene)Cl], **35** are given Figure 1.15. The rate constants observed for the hydrolysis of the complexes was found to be in the form **32** > **35** > **33** > **34** (Table 1.3). The inhibitory activity of the complexes on A2780 cancer cell is displayed as **35** (IC_{50} = 30.4 ± 2.0 μM) > **33** (IC_{50} = 40.1 ± 6.2 μM) > **34** (IC_{50} = 69.0 ± 3.4 μM) > **32** (IC_{50} =134.8 ± 4.0 μM), Table 1.3. The minimal cytotoxicity of **32**, could possibly be attributed to its rapid aquation. Complexes **33** and **35**, with moderate rate of aquations, demonstrate better antiproliferative activity in relation to **32**, suggesting the timescale of hyrolysis is responsible for the distinct antiproliferative activity of the complexes.

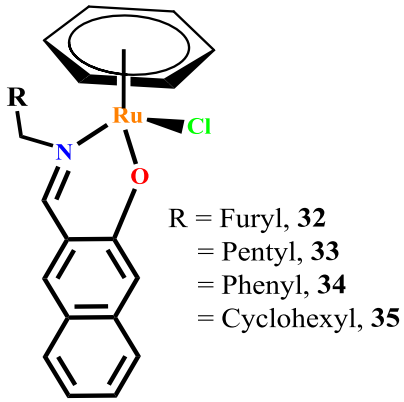

Figure 1.15: Ru(II) arene complexes of N ^ O donor Schiff-base ligands ([Ru(η6-benzene)(N-O)Cl]), showing hydrolysis as a crucial process in the the inhibitory activity of Ru(II) arene complexes. Noteworthy, the stability of the hydrolised species in aqueous media is essential for their pharmaceutical preparedness [85].

Bugarčić and co-workers reported mononuclear Ru(II) complexes of polypyridyl ligands; [Ru(Cl-Ph-tpy)(en)Cl]Cl (**36**), [Ru(Cl-Ph-tpy)(dach)Cl]Cl (**37**) and [Ru(Cl-Ph-tpy)(bpy)Cl]Cl (**38**) (where Cl-Ph-tpy = 4'-(4-chlorophenyl)-2,2':6',2''-terpyridine, en = 1,2-diaminoethane, dach = 1,2-diaminocyclohexane, bpy = 2,2'-bipyridine), Figure 1.16, [86]. The rates of substitution reactions of Ru(II) complexes with CT-DNA at 37 °C follow the order **36** > **37** > **38**, Table 1.3. Complexes **36** and **37**, with an aliphatic diamine chelate, react faster than **38**, bearing the bpy motif. This is attributable to

the steric hindrance caused by the bpy ligand on the Ru(II) metal centre compared to the more compact en and dach ligands. A possible reason for the lower reactivity of complex **37** in comparison to **36**, could be due to the steric and positive inductive effects of the cyclohexane ring in **37**. In another study, Milutinović and colleagues [87] reported the rates of hydrolysis of complexes **36**, **37** and **38** and the study indicated that complexes **36** and **37** hydrolyse at a similar rate; **36** and **37** hydrolyse faster than **38** and *ca*. two order of magnitude higher than cisplatin (6.32×10^{-5} and 2.5×10^{-5} s^{-1}) for the first and second aquation process, respectively). Further, the CT-DNA and BSA binding efficiencies of the complexes follow the order, **36** < **37** < **38**, Table 1.3, indicative of a negative correlation between substitution kinetics reactions and CT-DNA/BSA binding. The *in vitro* cytotoxicity of complex **38** is better than those of complexes **36** and **37**. For example, IC_{50} values of complexes **36**, **37** and **38** on HeLa cell line are 84.81 ± 4.7, 96.28 ± 3.8 and 12.68 ± 1.9 μM, respectively (Table 1.3). Complex **38** is about 5-6 times more cytotoxic than both **36** and **37** on the HeLa cell line, presumably due its favourable stable nature (*i.e*. relatively slower kinetic reactivity) that allows the compound to reach DNA and intercalate with it strongly. The assertion is further justified by the higher DNA/BSA binding constant of **38** compared to complexes **36** and **37**. In addition, the introduction of an aromatic substituent on **38** may result to an increase of its cytotoxic activity, notwithstanding the kinetics properties, as was reported by Sadler and co-workers [88]. The three complexes **36**, **37** and **38** showed positive log *P*o/w values, revealing the hydrophobic/lipophilic nature of the compounds. Compound **38** (0.39) is more hydrophilic than **36** (0.27) and **37** (0.20), which facilitates improved cellular uptake and thus better cytotoxic efficacy compared to **36** and **37**.

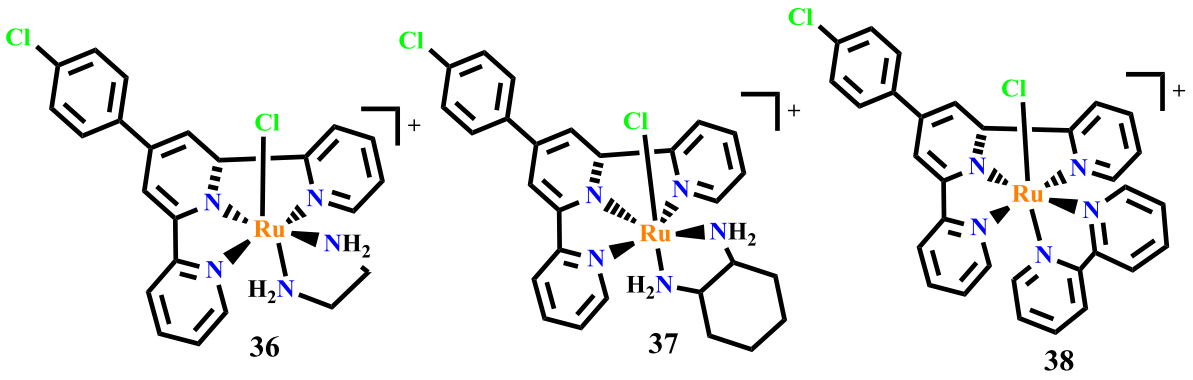

Figure 1.16: Mononuclear Ru(II) chlorophenyl terpyridine complexes displaying inverse correlation between substitution kinetics reactions and DNA/BSA affinities [86, 87].

In another work focusing on the impact of aromaticity on the kinetic reactivity, DNA/BSA interactions and cytotoxic properties, the Ru(II) complexes [Ru(Cl-Ph-tpy)(phen) Cl]Cl, (**39)** and [Ru(Cl-Ph-tpy)(o-bqdi)Cl]Cl, (**40**) (where Cl-Ph-tpy = 4′-(4-chlorophenyl)-2,2′:6′,2″-terpyridine, phen = 1,10-phenanthroline, o-bqdi = o-benzoquinonediimine) were prepared (Figure 1.17), [89]. Complex **39** displays slower rate of ligand substitution reactions with the guanine derivatives *i.e*. **5'-GMP** than complex **40**, with k_2 values of 0.87 ± 0.05 and 1.20 ± 0.06 M^{-1} s^{-1}, respectively (Table 1.3). The slower rate of substitution of **39** is due to the steric hindrance caused by the bulky phen ligand on the Ru(II) metal centre, while the higher reactivity of **40** is due to the of π-acceptor ability of the aromatic rings. In line with the lower rates of substitution reactions, the binding affinities of complexes towards DNA is lower, display values of (2.0 ± 0.2) x 10^4 M^{-1} for **39** and (3.0 ± 0.1) x 10^4 M^{-1} for **40** (Table 3). On the other hand, the BSA binding abilties of complexes **39** and **40** show an opposite trend where complex **35** shows higher binding constant than complex **40** (Table 1.3). The *in vitro* studies on A549 cell line revealed higher cytotoxic activity for compound **39** compared to **40**, with IC_{50} values of 4.6 ± 2.1 and 21.7 ± 4 μM, respectively (Table 1.3), a trend which contrasts the rates of substitution reactions. Nonetheless, complex **39** gave positive log *P*o/w values (1.13), indicating its hydrophobic/lipophilic nature, while complex **40** showed negative log *P*o/w values (-1.14), showing the hydrophilic nature of

the compound. Thus cytotoxic potency of **39** is as a result of increased aromaticity in the ligand framework which increases lipohilicity and hence high cellular uptake [90, 91].

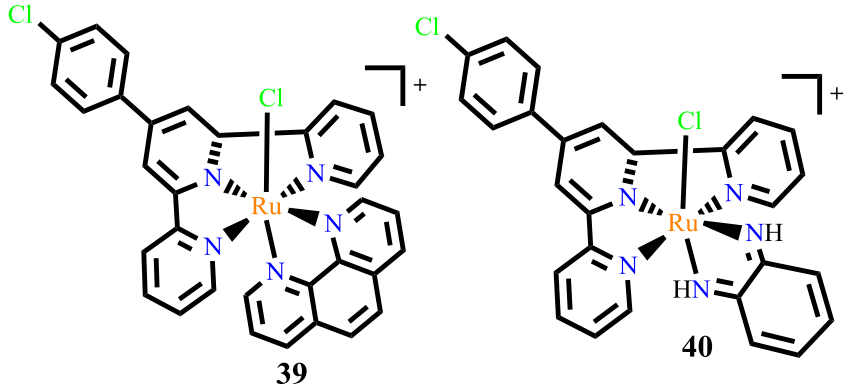

Figure 1.17: Polypyridyl Ru(II) complexes evaluated by Bugarc˘ić, depicting an inverse relationship on kinetic reactivity, BSA binding and the resultant cytotoxic activity [89].

The influence of the identity of the halide leaving group in Ru(II) complexes of the general formula $[RuX_2([9]aneS3)(S\text{-dmso})]$ (X = Cl, **41**, Br, **42**), as depicted in Figure 1.18, on the rates of substitution reactions and cytotoxicity property has been studied by O'Riley *et al* [92]. The rate constant for the hydrolysis of dichloro complex **41**, $(4.5 \pm 0.2) \times 10^{-4}$ s^{-1} is greater than that of the the corresponding dibromide analogue, complex **42**, $(2.6 \pm 0.2) \times 10^{-4}$ s^{-1} (Table 1.3). The trend is unusual, since the bromo ligand is expected to be a better leaving group than the chloro ligand, due to its lower basicity (good leaving groups are weak bases) [93]. The respective anti-cancer activities of the complexes **41** and **42** against MDA-MB-231 breast cancer cell line, follow the same trend observed for their kinetic lability, with IC_{50} value of 5.3 μM for **41** and 6.0 μM for **42**. The superior anti-invasive ability of **41** is consistent with the previous predictions that highly reactive species are likely to have the strongest anti-invasive efficacies [94, 95].

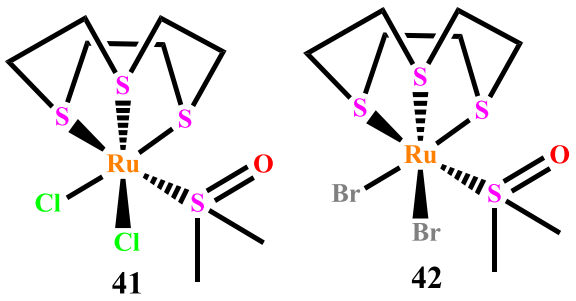

Figure 1.18: Mononuclear Ru(II) complexes anchored on thiaether macrocyclic ligands displaying a direct relationship between kinetic reactivity and anti-invasive activity [92].

Our research group [96] recently investigated the influence of heteroatoms on the substitution kinetic reactivity and cytotoxic activity of Ru(III) complexes of the type[{2-(2-pyridyl) benzimidazole} $RuCl_3$], **43**, [{2-(2-pyridyl) benzoxazole} $RuCl_3$], **44**, [{2-(2-pyridyl)benzothiazole} $RuCl_3$], **45** and [{1-propyl-2- (pyridin-2-yl)-H-benzoimidazole} $RuCl_3$], **46**, (Figure 1.19). The sequence of kinetic reactivity of the complexes with the S-donor nucleophiles *i.e.* **Tu**, **Dmtu**, and **Tmtu** decreases in the form **43** > **44** > **45** > **46**, (Table 1.3). The trend in reactivity is due to the electronegativity of the heteroatoms which was found to decrease in the order NH > O > S > N-propyl. The *in vitro* cytotoxicity study revealed that the complexes have poor cytotoxicity (with IC_{50} values > 200 µM) compared to the standard, doxorubicin (with IC_{50} = 0.8 µM), Table 1.3. Compared to the other ruthenium complexes, the lack of cytotoxic effect of complexes **43-46** could be assigned to their very slow rate of substitution reactions compared to other ruthenium-based complexes in this review. The lower kinetic reactivity and the minimal inhibitory effects of these complexes could be assigned to their low aromaticity as found in previous anticancer studies of ruthenium complexes [90, 91].

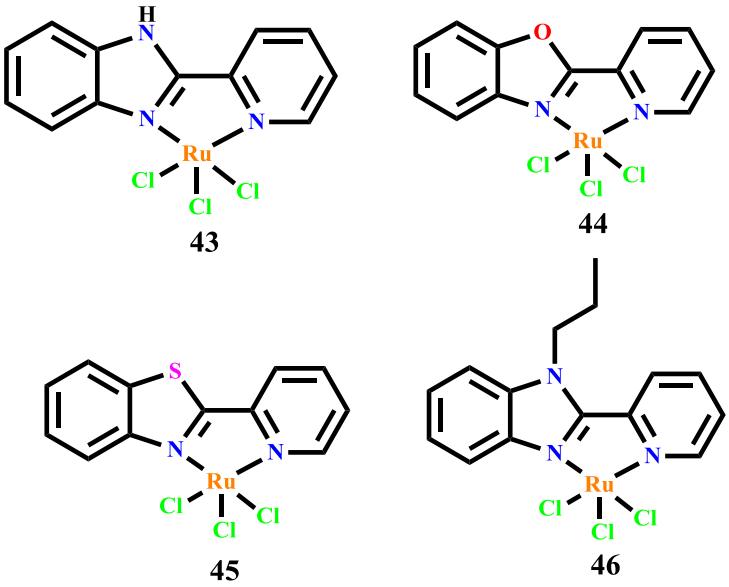

Figure 1.19: (Pyridyl)benzoazole Ru(III) complexes demonstrating very slow kinetic reactivity and no cytotoxic effects [96].

In a follow up study, Ojwach and co-workers studied the impact of the molecular interactions of metal-based drugs with bio-molecules on their inhibitory properties, using Ru(III) complexes [$RuCl_3$(**L1**)], **47**, [$RuCl_3$(**L2**), **48**, and [$RuCl_3$(**L3**)], **49** {where **L1** = 2-bromo-6(3,5-dimethyl-1H-pyrazol-1-yl)pyridine, **L2** = 2,6-di(1H-pyrazol-1-yl)pyridine and **L3** = 2,6-bis(3,5-dimethyl-1H-pyrazol-1-yl)pyridine}, Figure 1.20, [97] . The results of the substitution kinetics reactions with the thiourea nucleophiles follows the sequence, **47** > **48** > **49** (Table 1.3). The observed trend in reactivity is ascribed to the electronic effect of the spectator ligands. The pyridine ring is a π-acceptor, while the pyrazole ring is a better σ-donor and thus supports the higher reactivity of complex **47** in comparison to complexes **48** and **49**. Complexes **47**, **48** and **49** seem to exhibit anti-proliferative activity at higher micromolar concentrations (> 200 µM), values lower than those of the reference, doxorubicin (with IC_{50} = 0.8 µM), Table 1.3.

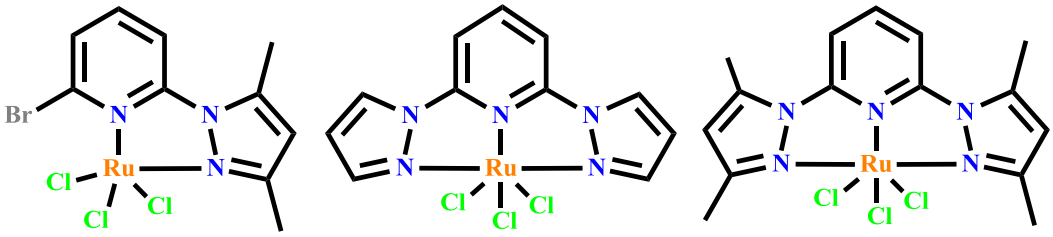

Figure 1.20: (Pyrazolyl)pyridine Ru(III) complexes reported by Ojwach and co-workers, displaying low kinetic reactivity and poor cytotoxicity against Hela cell lines [97].

Jaganyi and co-workers have also investigated the reactivity and interactions of Ru(II)/Ru(III) complexes with biologically relevant biomolecules such as sulfur-donor nucleophiles, DNA and BSA protein [98]. In this study, mono-dinuclear Ru(II) complexes anchored on different π-conjugated ditopic *N,N*-chelate bridging ligands *viz*: 2,2'-bipyrimidine (**50**), 2,3-*bis*(2-pyridyl)-pyrazine (**51**), 2,3-*bis*(2-pyridyl)-quinoxaline (**52**) and 6,7-dimethyl-2,3-*bis*(2-pyridyl)quinoxaline (**53**), Figure 1.21, were investigated. The observed rate constants for the complexes, with thiourea as the entering ligand are $(2.47 \pm 0.02) \times 10^{-2}$ M^{-1} s^{-1} for **50**, $(1.33 \pm 0.04) \times 10^{-2}$ M^{-1} s^{-1} for **51**, $(4.6 \pm 0.02) \times 10^{-3}$ M^{-1} $s^{-1}$for **52**, and $(2.0 \pm 0.01) \times 10^{-3}$ M^{-1} s^{-1} for **53**, Table 1.3. Noteworthy, the reactivity trend of the complexes is in line with stereo-electronic and steric effects of the rigid N,N-aromatic bridging ligand. The higher reactivity of **50** is assigned to the symmetric A-A ditopicity (a ditopic ligand is a ligand that is capable of coordinating at two separate sites) of the bridging ligand that makes the space around the metal centre less restricted compared to the A-B ditopic bridging ligands in **51**, **52** and **53** [99]. As such, the incoming nucleophile experiences less steric hindrance in accessing the metal centre in **50** relative to other complexes. More significantly, the binding propensities of the complexes towards CT-DNA and BSA followed the same order of kinetic reactivity of **50** > **51** > **52** > **53** (Table 1.3), depicting direct dependence of the DNA binding properties on the kinetic reactivity of these complexes. Compound **50** displays the highest binding affinity compared to **51**, **52** and **53**, owing to its smaller and planar bipyrimidine bridging ligand that facilitate facile binding to the CT-DNA and BSA. Unfortunately, no

cytotoxicity studies for these compounds was done, which would have offered some insight on the trends and dependence on their kinetic reactivity and DNA interactions behaviour.

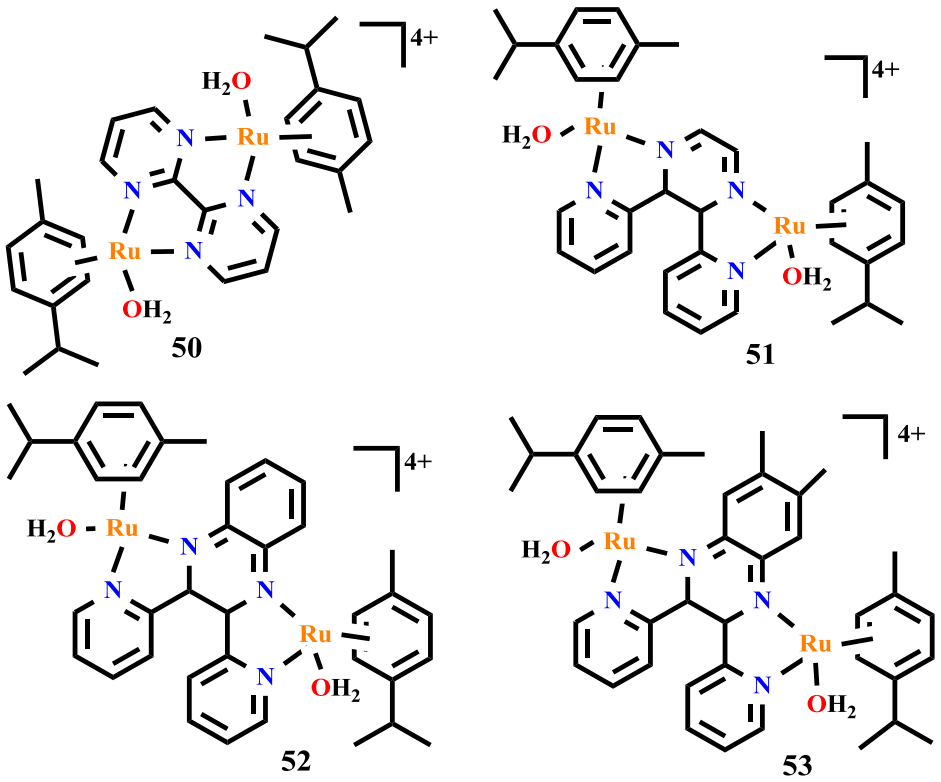

Figure 1.21: Mono-dinuclear (η^6-*p*-cymene)Ru(II) complexes reported by Jaganyi and co-workers, illustrating a positive correlation between kinetic reactivity and DNA/BSA interactions [98].

Recently, Medjedović and the group [91] studied the substitution reactions, DNA/BSA interactions and cytotoxic activities of mono-dinuclear Ru(II) polypyridyl complexes, *i.e.* $[\{RuCl(bpy)_2\}_2(\mu\text{-pzn})][PF_6]_2$ (**54**), and $[\{RuCl(phen)_2\}_2(\mu\text{-pzn})][PF_6]_2$ (**55**) (bpy = 2,2-bipyridine, phen = 1,10-phenanthroline, μ -pzn = pyrazine), Figure 1.22. The substitution kinetics reactions of complexes **54** and **55** with **5'-GMP** at, pH= 7.2, 25°C, are (27 ± 3) x 10^2 and (1.0 ± 0.04) x 10^2 M^{-1} s^{-1}, respectively (Table 1.3). The order of kinetic reactivity is attributed to the influence of the bulky and rigid phenanthroline on the Ru(II) metal centre. The binding strengths of the complexes towards DNA and

BSA follow the same sequence **55** > **55** (Table 1.3), and the higher binding affinity of **50**, is ascribed the minimal steric hindrance that favours strong DNA and BSA interactions. The *in vitro* studies towards MDA-MB-231 HCT-11, showed a lower cytotoxic effect of 71.7 μM for **54** in comparison to 55.2 μM for **55** (Table 1.3), and thus depicting a negative correlation between substitution kinetics reactions and the antitumour properties of the complexes. The better cytotoxic efficacy of **55** could be due to the increased π- conjugation in the ligand motif that enhances solubity and thus cellular uptake [90, 100].

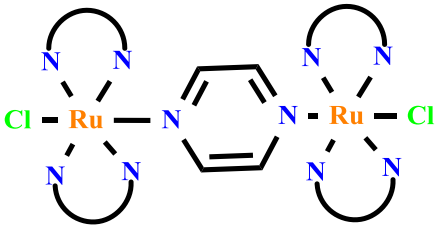

N-N = bby (**54**), phen (**55**)

Figure 1.22: Mono-dinuclear Ru(II) polypyridyl complexes exhibiting a positive correlation between substitution kinetics reactions and DNA/BSA interactions, but negative correlations between kinetic reactivity and cytotoxic effects [91].

Table 1.3: A summary of the correlative studies of substitution kinetics reactions, DNA/BSA bindings and cytotoxic activities of mononuclear and dinuclear Ru(II)/Ru(III) complexes

Complex	Kinetics reactions (min^{-1}, s^{-1} or M^{-1} s^{-1})	DNA binding, K_b (M^{-1})	BSA binding, K (M^{-1})/ k_{bind} (min^{-1})	Cytotoxicity (IC_{50}, μM)			Ref
	Aquation			**HT-29**	**SK-BR-3**		**[35]**
27	0.031 ± 0.006		0.064 ± 0.024	339 ± 68	472 ± 25		
28	0.020 ± 0.005	nd	0.206 ± 0.027	212 ± 22	169 ± 10		
29	0.025 ± 0.004		0.094 ± 0.014	322 ± 32	415 ± 48		
30	0.050 ± 0.012		0.258 ± 0.054	621 ± 5	>1000		
31	0.012 ± 0.002		0.009 ± 0.003	315 ± 22	517 ± 70		
	Aquation			**MCF-7**	**SH-SY5Y**	**A2780**	**[85]**
32	277.83 ± 15.07	nd	nd	>150	>150	134.8 ± 4.0	
33	52.25 ± 3.15			108.2 ± 4.0	91.7 ± 3.4	40.10 ± 6.2	
34	15.22 ± 1.35			132.1 ± 4.9	126.7 ± 14.1	69.00 ± 3.4	
35	124.1 ± 5.80			88.7 ± 5.9	67.1 ± 0.7	30.40 ± 2.0	
	CT-DNA			**HeLa**	**A549**	**MRC-5**	**[87],**
36	(2.1 ± 0.1) x 10^3	(1.0 ± 0.2) x 10^6	2.0 x 10^4	84.81 ± 4.7	>100	>100	**[86]**
37	(1.3 ± 0.2) x 10^3	(2. 8 ± 0.1) x 10^6	3.0 x 10^4	96.28 ± 3.8	>100	>100	
38	22 ± 2	(9.0 ± 0.2) x 10^6	5.0 x 10^4	12.68 ± 1.9	53.80 ± 4.4	97.67 ± 6.9	
	5'-GMP			**A549**	**MCF7**		**[89]**
39	0.87 ± 0.05	(2.0 ± 0.2) x 10^4	4.3 x 10^4	4.6 ± 2.1	13.8 ± 1.8		
40	1.20 ± 0.06	(3.0 ± 0.1) x 10^4	2.7 x 10^4	21.7 ± 4.3	14.6 ± 0.9		
	Aquation			**MDA-MB-231**			**[92]**
41	(4.5 ± 0.2) x 10^{-4}	nd	nd	5.3 ± 0.7			
42	(2.6 ± 0.2) x 10^{-4}			6.0 ± 0.7			
	Tu			**HeLa**			**[96]**
43	(2.47 ± 0.02) x 10^{-2}	nd	nd	>200			
44	(1.33 ± 0.04) x 10^{-2}			>200			
45	(4.60 ± 0.02) x 10^{-3}			>200			
46	(2.00 ± 0.01) x 10^{-3}			>200			
	Tu			**HeLa**			**[97]**
47	(5.00 ± 0.03) x 10^{-2}	nd	nd	>200			
48	(2.25 ± 0.01) x 10^{-2}			>200			
49	(0.24 ± 0.00) x 10^{-2}			>200			
	Tu						**[98]**
50	28.71 ± 0.30	(8.77 ± 0.10) x 10^5	(6.80 ± 0.30) x 10^5	Nd			
51	5.91 ± 0.05	(5.26 ± 0.07) x 10^5	(2.85 ± 0.20) x 10^5				
52	0.17 ± 0.01	(3.99 ± 0.05) x 10^5	(0.81 ± 0.20) x 10^5				
53	0.12 ± 0.12	(1.14 ± 0.02) x 10^5	(0.35 ± 0.10) x 10^5				
	5'-GMP			**MDA-MB-231**	**HCT-11**		**[91]**
54	(27.0 ± 3.00) x 10^2	(1.9 ± 0.1) x 10^5	3.6 x 10^4	71.7			
55	(1.00 ± 0.04) x 10^2	(1.5 ± 0.1) x 10^5	1.9 x 10^4	55.2			

K_b = DNA-binding constant; K = BSA association binding constant; IC_{50} = Half maximal inhibitory concentration; nd = not determined.

1.4.4 Gold(III) complexes

Gold is another metal among the platinum group metals that has not been ignored in the quest to find better metallo-based anti-cancer agents. A plethora of mechanistic studies strongly suggest that the interactions of Au(I)/(II)/(III) compounds with DNA molecule is not as strong as those reported for the Pt(II) and Pd(II) complexes, pointing to possible different biological pathways to cytotoxicity for gold complexes [101-106]. These investigations have prompted attention for the gold-protein interactions aimed at determining the possible biological targets responsible for their cytotoxicity activities. Compared to Pt(II)/Pt(IV), Pd(II) and Ru(II)/Ru(III) complexes, substitution reactions, DNA/BSA interactions and antitumour properties of Au(III) complexes have not been extensively investigated. This feature has largely been attributed to their lower rate of substitution kinetics and the tendency of Au(III) to undergo reduction to Au(I) and disproportionation to colloid Au(0), [107] under reducing intracellular conditions. To the best of our knowledge, at this moment there are only two studies on the kinetics of ligand substitution reactions and cytotoxicity of gold complexes.

The first study involved the kinetics of complex formation and cytotoxicity of Au(III) complexes, $[AuCl_2(en)]$(**56)** and $[AuCl_2(SMC)]$ (**57)** (en = ethylenediamine, SMC = S-methyl-L-cysteine) shown in Figure 1.23, [108]. The study shows that biologically relevant *N*-donor nucleophiles have a high affinity for Au(III) complexes. The reactions of complex **57** with **5'-GMP** are about three order of magnitude faster than those of complex **56** (Table 1.4), a feature attributable to the electronic differences in en and SMC ligands. *In vitro* cytotoxicity screening of complexes **56** and **57** on CLL cell line demonstrates inhibitory effect of 38% and 8% cell deaths for complexes **56** and **57** respectively (Table 1.4), illustrating a negative correlation between substitution kinetics and cytotoxic effects of the complexes. The better cytotoxic effects of **56** is due to its positive charge that promotes efficient cellular uptake across the cell membrane, which is made up of negatively charged lipophilic phospholipids [90].

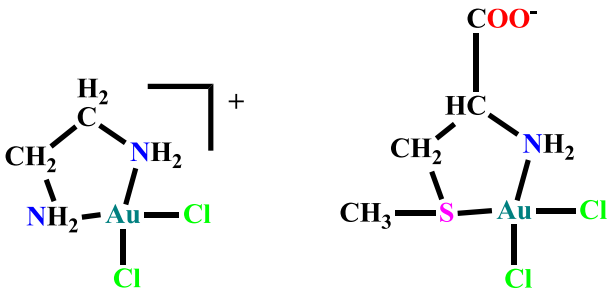

56 57

Figure 1.23: Au(III) complexes probed by Milovanović *et al* displaying a negative correlation between kinetic reactivity and cytotoxic effects [108].

In another study, ligand substitution reactions and *in vitro* cytotoxicity of Au(III) complexes; dichloride(1,2-diaminocyclohexane)aurate(III)-ion (**58)** and dichlorido(2,2'-bipyridyl)aurate(III)-ion (**59)** were found to be controlled largely by electronic effects [109], Figure 1.24. The rate constants for the first and second steps of the substitution reactions of complex **59** with **5'-GMP**, are faster than in the case of complex **58** at pH 7.2, 298 K (Table 1.4). The trend in reactivity is explained by the π-acceptor ability of the 2,2′-bipy ligand in **59** and a positive inductive effect of cyclohexane ring in **58**. The *in vitro* cytotoxic evaluations on A549 shows a considerable cytotoxic activity of compound **59** than **58**, with 61% and 22% cell death, respectively (Table 1.4), thus demonstrating a positive correlation between substitution reactions and cytotoxic effects and this could be due to the increased π-conjugation of the ligand architecture of **59** that increases hydrophilicity and thus better cellular uptake.

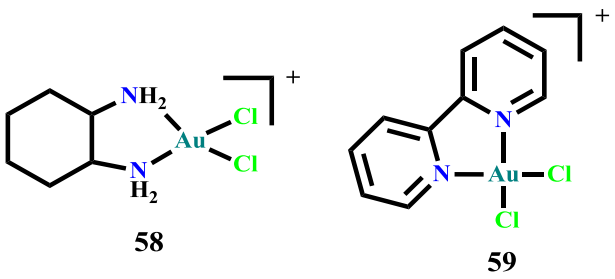

Figure 1.24: Au(III) complexes showing positive correlation between kinetic reactivity and cytotoxicity [109].

In a more recent work, Petrović and the group [110] examined the nucleophilic substitution reactions, DNA/BSA interactions, cytotoxic activity of tetra- and penta-coordinated Au(III) complexes *i.e.* $[Au(DPP)Cl_2]^+$ (**60**) and $[Au(DMP)Cl_3]$ (**61**) complexes (where DPP = 4,7- diphenyl-1,10-phenanthroline and DMP = 2,9-dimethyl-1,10-phenanthroline), Figure 1.25. The substitution reactions of the complexes with the biologically relevant ligands, **Tu**, **5'-GMP**, **GSH** and **L-Met** revealed a trend of **60** > **61**. For instance with **5'-GMP** as the incoming nucleophile, the rate constants for complexes **60** and **61** are $3.8 \pm 0.3) \times 10^4$ and $(2.4 \pm 0.7) \times 10^4$ $M^{-1}s^{-1}$, respectively (Table 1.4). Even though the authors argued that difference in the reactivity is due to the steric effects of the spectator ligand(s) which hinders the incoming ligand from accessing the metal centre, we believe that the kinetic reactivity of the two complexes can be explained in terms of σ-donation and π-back-donation due to the presence of methyl substituents and bipyridine moiety, respectively. The interactions of the complexes with DNA follow the same trend as kinetic reactivity, depicting a positive correlation between the two variables. On the other hand, the binding ability of the complexes towards BSA protein display an opposite trend with K values of $(3.4 \pm 0.5) \times 10^5$ M^{-1} for **60** and $(5.0 \pm 0.3) \times 10^5$ M-1 for **61** (Table 1.4). The cytotoxic effects of complexes **60** and **61** against HCT-116 colorectal cancer demonstrate noticeable activity with $1C_{50}$ values of 3.13 and 14.57 μM, respectively (Table 1.4). The enhanced anti-tumour activities of complex **60** in comparison to **61** is due to the increased pi-conjugation in the carrier ligand, which increases aromaticity and lipophilicity.

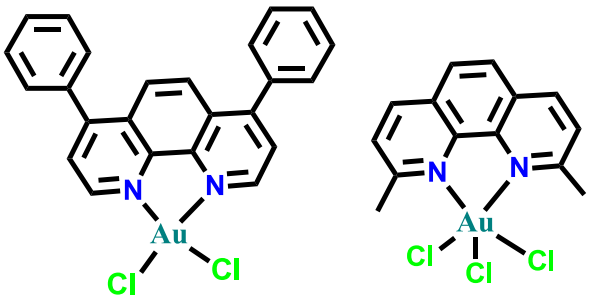

Figure 1.25: Au(III) complexes bearing phenanthroline ligand, showing direct relationship between kinetic reactivity and DNA interactions, as well as inhibitory effects, but a negative relationships between rate constants and BSA binding constants [110].

Table 1.4: A summary of the correlative studies of substitution kinetics reactions, DNA/BSA binding and cytotoxic activities of some Au(III) complexes

Complex	Kinetics reactions with 5'-GMP ($M^{-1} s^{-1}$)	DNA binding, K_b (M^{-1})	BSA binding, K (M^{-1})	Cytotoxicity	Ref
				CLL	
56	$(3.30 \pm 0.20) \times 10^1$	nd	nd	38% cell death	**[108]**
57	$(1.71 \pm 0.07) \times 10^4$			8 % cell death	
				A549	
58	$(6.60 \pm 0.20) \times 10^1$	nd	nd	22 % cell death	**[109]**
59	$(1.49 \pm 0.05) \times 10^2$			61 % cell death	
				HCT-116	**[110]**
60	$(3.8 \pm 0.3) \times 10^4$	$(1.29 \pm 0.02) \times 10^3$	$(3.4 \pm 0.5) \times 10^5$	3.13	
61	$(2.4 \pm 0.7) \times 10^4$	$(4.21 \pm 0.09) \times 10^2$	$(5.0 \pm 0.3) \times 10^5$	14.57	

K_b = DNA-binding constant; K = BSA association binding constant; IC_{50} = Half maximal inhibitory concentration; nd = not determined.

1.5 Statement of problem

Despite the achievements of the current platinum drugs, their theurapeutic efficacy has been limited by toxicity (including ototoxicity, renal tubular injury, neuromuscular complication, and gastrointestinal symptoms), resistance, and poor oral bioavailability [111-115]. There is therefore, a need to design and develop alternative metal complexes with reduced pharmacological profile and theurapeutic efficacy. *In vitro* cytotoxicity of metal complexes is greately influenced by the kinetics of ligand exchange reactions around the metal centre in addition to the relative DNA/BSA binding affinities [110, 116]. While reports on a multitude of substitution kinetics, DNA-/protein-binding ability, and cytotoxicity studies appear independently, very few of such studies attempt to examine the relationships linking these parameters. To the best of our current knowledge, there is no study that has attempted to capture the relationships of these three variables. Therefore, this field of study is still in its infancy stage, and there is still enough space for further research. We strongly believe that proper understanding on the correlations of kinetic substitution rates, DNA/Binding, and anti-neoplastic properties could result to the design of exquisite metal-based anticancer drugs, with impressive biological efficacy and safety.

1.6 Justification and rationale of study

The documented limitations of platinum-based drugs have triggered a growing demand for the search of alternative platinum-based antitumour drugs with improved selectivity, cytoxicity, and reduced resistance profiles [11-15, 34]. Among the non-platinum based agents that are currently being considered, Pd(II) complexes have gained a considerable attention presumably due to their thermodynamic and structural resemblance to Pt(II) complexes and promising antitumour activity towards platinum resistant cells [117-121]. However, the kinetic lability of Pd(II) complexes are $\approx 10^3$-10^5 more reactive than similar Pt(II) analogues [122], a property that does not allow them to maintain their structural identity in the biological fluis long enough to reach the cellular target. To circumvent this challenge, the selection of suitable carrier ligands is critical for their easy transport (by proteins) to

DNA, DNA without much interference from other biological molecules (particularly the sulfur donor nucleophiles). Bulky and strong donor chelating ligands can generate significant steric shelter and stable metal-ligand bonds, slowing down the rates of dissociation of Pd(II) complexes [65, 73, 76, 77]. Steric and electronic properties, and geometry of metal complexes can be controlled by varying the spectator ligand(s) around the metal centre, to enrich the drug to to cancer cells and increase selectivity.

1.7 Aim and objectives

The overall aim of this thesis, is to study the influence of steric and electronic parameters on the structural behaviours, substitution kinetics and biological activities of mixed-donor palladium(II) complexes, improving their selectivity and therapeutic efficacy. The the specifics objectives to realise this aim include:

1. To synthesise and characterise palladium(II) complexes containing mixed-donor (N-; S-, O-, C) tridentate ligands.
2. To carry-out kinetics of ligand substitution reactions of mixed-donor palladium(II) complexes with biological nucleophiles; thiourea (**Tu**), L-methionine (**L-Met**), guanosine-5'-monophosphate (**5'-GMP**).
3. To employ theoretical studies (density functional theory, and molecular docking simulations) to rationalise the experimental results.
4. To study DNA/BSA protein interactions of palladium(II) complexes of mixed-donor tridentate ligands.
5. To examine the *in vitro* cytotoxicity of these tridentate mixed-donor palladium(II)complexes.

The results of these studies are described in Chapters 3-6, while keys findings and overall conclusions are summarised in Chapter 7.

1.8 References

[1] D.K. Sales, L.M. Simplício, C.D. da Silva, C.M. Enju, V.B. Silva, T.d.F. Paulo, I.P. Santos, H.C. Quadros, C.S. Meira, M.B. Soares, Inorg. Chim. Acta. 516 (2021) 120-125.

[2] P. Sukanya, C.V.R. Reddy, J. Biomol. Struct. Dyn. (2021) 1-12.

[3] P.A. Ajibade, F.P. Andrew, A.A. Fatokun, A.E. Oluwalana, J. Mol. Struct. 1230 (2021) 129894.

[4] A.R. Simović, J. Bogojeski, B. Petrović, S. Jovanović-Stevića, Macroheterocycles 13 (2020) 201-209.

[5] Q.-M. Wei, Z.-Z. Wei, J.-J. Zeng, L. Yang, Q.-P. Qin, M.-X. Tan, H. Liang, Polyhedron 196 (2021) 115004.

[6] Z. Liu, Z. Li, T. Du, Y. Chen, Q. Wang, G. Li, M. Liu, N. Zhang, D. Li, J. Han, Dalton Trans. 50 (2021) 362-375.

[7] S. Rottenberg, C. Disler, P. Perego, Nat. Rev. Cancer. 21 (2021) 37-50.

[8] G.-B. Liang, Y.-C. Yu, J.-H. Wei, W.-B. Kuang, Z.-F. Chen, Y. Zhang, Eur. J. Med. Chem. 188 (2020) 112033.

[9] A. Khoury, K.M. Deo, J.R. Aldrich-Wright, J. Inorg. Biochem. 207 (2020) 111070.

[10] L. Nagyal, A. Kumar, R. Sharma, R. Yadav, P. Chaudhary, R. Singh, Curr. Bioact. Compd. 16 (2020) 726-737.

[11] X. Wei, Y. Yang, J. Ge, X. Lin, D. Liu, S. Wang, J. Zhang, G. Zhou, S. Li, J. Inorg. Biochem. 202 (2020) 110857.

[12] Y. Wen, C. Ouyang, Q. Li, T.W. Rees, K. Qiu, L. Ji, H. Chao, Dalton Trans. 49 (2020) 7044-7052.

[13] S. De, R.S. Kumar, A. Gauthaman, S.A. Kumar, P. Paira, A. Moorthy, S. Banerjee, Inorg. Chim. Acta. 515 (2021) 120066.

[14] H. Luo, B. Cao, A.S. Chan, R.W.Y. Sun, T. Zou, Angew. Chem. Int. Ed. 59 (2020) 11046-11052.

[15] M.N. Lone, G.N. Yatoo, J.A. Banday, I.A. Wani, Advances in Metallodrugs: Preparation and Applications in Medicinal Chemistry (2020) 247-271.

[16] T. Storr, M. Merkel, G.X. Song-Zhao, L.E. Scott, D.E. Green, M.L. Bowen, K.H. Thompson, B.O. Patrick, H.J. Schugar, C. Orvig, J. Am. Chem. Soc. 129 (2007) 7453-7463.

[17] S.M. Meier-Menches, C. Gerner, W. Berger, C.G. Hartinger, B.K. Keppler, Chem. Soc. Rev. 47 (2018) 909-928.

[18] S. Gomez-Ruiz, D. Maksimović-Ivanić, S. Mijatović, G.N. Kaluđerović, Bioinorg Chem Appl. 2012 (2012).

[19] G. Gasser, I. Ott, N. Metzler-Nolte, J. Med. Chem. 54 (2011) 3-25.

[20] A.R. Simović, R. Masnikosa, I. Bratsos, E. Alessio, Coord. Chem. Rev. 398 (2019) 113011.

[21] J.P. Coverdale, T. Laroiya-McCarron, I. Romero-Canelón, Inorganics 7 (2019) 31.

[22] V. Brabec, O. Hrabina, J. Kasparkova, Coord. Chem. Rev. 351 (2017) 2-31.

[23] E. Alessio, L. Messori, Molecules 24 (2019) 1995.

[24] A.R. Timerbaev, C.G. Hartinger, S.S. Aleksenko, B.K. Keppler, Chem. Rev.106 (2006) 2224-2248.

[25] X. Zhou, K. Ling, M. Liu, X. Zhang, J. Ding, Y. Dong, Z. Liang, J. Li, J. Zhang, Theranostics 9 (2019) 6568.

[26] S. Ghosh, Bioorg. Chem. 88 (2019) 102925.

[27] S.A. Aldossary, Biomed. Pharmacol. J. 12 (2019) 7-15.

[28] I.A. Riddell, S.J. Lippard, Met. Ions Life Sci. 18 (2018) 1-42.

[29] T. Makovec, Radiology and Oncology 53 (2019) 148-158.

[30] M. Hanif, C.G. Hartinger, Future Med. Chem. 10 (2018) 615-617.

[31] M. Abid, F. Shamsi, A. Azam, Mini-Rev Med Chem. 16 (2016) 772-786.

[32] M. Pal, U. Nandi, D. Mukherjee, Eur. J. Med. Chem. 150 (2018) 419-445.

[33] C.S. Allardyce, P.J. Dyson, Platinum Met. Rev. 45 (2001) 62-69.

[34] R. Kanaoujiya, M. Singh, J. Singh, S. Srivastava, J. Sci. Res. 64 (2020).

[35] M. Groessl, E. Reisner, C.G. Hartinger, R. Eichinger, O. Semenova, A.R. Timerbaev, M.A. Jakupec, V.B. Arion, B.K. Keppler, J. Med. Chem. 50 (2007) 2185-2193.

[36] I. Kostova, Curr. Med. Chem. 13 (2006) 1085-1107.

[37] G. Sava, A. Bergamo, S. Zorzet, B. Gava, C. Casarsa, M. Cocchietto, A. Furlani, V. Scarcia, B. Serli, E. Iengo, Eur. J. Cancer. 38 (2002) 427-435.

[38] P. Schluga, C.G. Hartinger, A. Egger, E. Reisner, M. Galanski, M.A. Jakupec, B.K. Keppler, Dalton Trans. (2006) 1796-1802.

[39] S.E. Miller, D.A. House, Inorg. Chim. Acta. 173 (1990) 53-60.

[40] S.E. Miller, D.A. House, Inorg. Chim. Acta. 166 (1989) 189-197.

[41] S.E. Miller, D.A. House, Inorg. Chim. Acta. 161 (1989) 131-137.

[42] S.E. Miller, D.A. House, Inorg. Chim. Acta. 187 (1991) 125-132.

[43] R.J. Knox, F. Friedlos, D.A. Lydall, J.J. Roberts, Cancer Res. 46 (1986) 1972-1979.

[44] S.P. Fricker, Dalton Trans. (2007) 4903-4917.

[45] L. Canovese, L. Cattalini, G. Chessa, M.L. Tobe, J. Chem. Soc., Dalton Trans. (1988) 2135-2140.

[46] U. Frey, J.D. Ranford, P.J. Sadler, Inorg. Chem. 32 (1993) 1333-1340.

[47] A.J. Di Pasqua, J. Goodisman, D.J. Kerwood, B.B. Toms, R.L. Dubowy, J.C. Dabrowiak, Chem. Res. Toxicol. 19 (2006) 139-149.

[48] P. Carloni, M. Sprik, W. Andreoni, J Phys Chem B. 104 (2000) 823-835.

[49] K.J. Barnham, M.I. Djuran, P.d.S. Murdoch, J.D. Ranford, P.J. Sadler, Inorg. Chem. 35 (1996) 1065-1072.

[50] E. Jerremalm, P. Videhult, G. Alvelius, W.J. Griffiths, T. Bergman, S. Eksborg, H. Ehrsson, J. Pharm. Sci. 91 (2002) 2116-2121.

[51] M.F.A. Lucas, M. Pavelka, M.E. Alberto, N. Russo, J Phys Chem B. 113 (2008) 831-838.

[52] S. Mukherjee, I. Mitra, S. Mahata, W. Linert, S.C. Moi, Chem. Phys. Lett. 663 (2016) 115-122.

[53] N. Farrell, Chem. Soc. Rev. 44 (2015) 8773-8785.

[54] J. Reedijk, Chem. Rev. 99 (1999) 2499-2510.

[55] Y.P. Ho, S.C. Au-Yeung, K.K. To, Med Res Rev. 23 (2003) 633-655.

[56] T. Lazarević, A. Rilak, Ž.D. Bugarčić, Eur. J. Med. Chem. 142 (2017) 8-31.

[57] M. Fanelli, M. Formica, V. Fusi, L. Giorgi, M. Micheloni, P. Paoli, Coord. Chem. Rev. 310 (2016) 41-79.

[58] M. Vojtek, S. Gonçalves-Monteiro, E. Pinto, S. Kalivodová, A. Almeida, M. P. Marques, C. Diniz, Pharmaceuticals, 14 (2021), 173.

[59] M.D. Hall, T.W. Hambley, Coord. Chem. Rev. 232 (2002) 49-67.

[60] Q. Mi, S. Shu, C. Yang, C. Gao, X. Zhang, X. Luo, C. Bao, X. Zhang, J. Niu, J Appl Clin Med Phys. 7 (2018) 231.

[61] B.J. Pages, D.L. Ang, E.P. Wright, J.R. Aldrich-Wright, Dalton Trans. 44 (2015) 3505-3526.

[62] J.C. García-Ramos, R. Galindo-Murillo, F. Cortés-Guzmán, L. Ruiz-Azuara, J Mex Chem Soc. 57 (2013) 245-259.

[63] J. Zhao, Z. Xu, J. Lin, S. Gou, Inorg. Chem. 56 (2017) 9851-9859.

[64] Ž.D. Bugarčić, J. Bogojeski, B. Petrović, S. Hochreuther, R. van Eldik, Dalton Trans. 41 (2012) 12329-12345.

[65] D. Ćoćić, S. Jovanović, S. Radisavljević, J. Korzekwa, A. Scheurer, R. Puchta, D. Baskić, D. Todorović, S. Popović, S. Matić, J. Inorg. Biochem. 189 (2018) 91-102.

[66] R. Bellam, D. Jaganyi, A. Mambanda, R. Robinson, M.D. BalaKumaran, RSC Adv. 9 (2019) 31877-31894.

[67] I. Łakomska, H. Kooijman, A.L. Spek, W.-Z. Shen, J. Reedijk, Dalton Trans. (2009) 10736-10741.

[68] T. Soldatović, S. Jovanović, Ž.D. Bugarčić, R. van Eldik, Dalton Trans. 41 (2012) 876-884.

[69] M. Arsenijević, M. Milovanović, V. Volarević, D. Čanović, N. Arsenijević, T. Soldatović, S. Jovanović, Ž.D. Bugarčić, Transit. Met. Chem. 37 (2012) 481-488.

[70] N.P. Barry, P.J. Sadler, Chem. Commun. 49 (2013) 5106-5131.

[71] B. Lippert, Cisplatin: chemistry and biochemistry of a leading anticancer drug, John Wiley & Sons, 1999.

[72] E. Alessio, Bioinorganic medicinal chemistry, John Wiley & Sons, 2011.

[73] F.K. Keter, S.O. Ojwach, O.A. Oyetunji, I.A. Guzei, J. Darkwa, Inorg. Chim. Acta. 362 (2009) 2595-2602.

[74] R.C. Gaver, G. Deeb, Cancer Chemother. Pharmacol. 16 (1986) 201-206.

[75] R.S. Go, A.A. Adjei, J Clin Oncol. 17 (1999) 409-409.

[76] D.O. Onunga, R. Bellam, G.K. Mutua, M. Sitati, M.D. BalaKumaran, D. Jaganyi, A. Mambanda, J. Inorg. Biochem. 213 (2020) 111261.

[77] D. Ćoćić, S. Jovanović, M. Nišavić, D. Baskić, D. Todorović, S. Popović, Ž.D. Bugarčić, B. Petrović, J. Inorg. Biochem. 175 (2017) 67-79.

[78] S. Jovanović, K. Obrenčević, Ž.D. Bugarčić, I. Popović, J. Žakula, B. Petrović, Dalton Trans. 45 (2016) 12444-12457.

[79] R. Trondl, P. Heffeter, C.R. Kowol, M.A. Jakupec, W. Berger, B.K. Keppler, J Chem Sci. 5 (2014) 2925-2932.

[80] E.S. Antonarakis, A. Emadi, Cancer Chemother. Pharmacol. 66 (2010) 1-9.

[81] W. Han Ang, P.J. Dyson, Eur. J. Inorg. Chem. 2006 (2006) 4003-4018.

[82] W.H. Ang, A. Casini, G. Sava, P.J. Dyson, J. Organomet. Chem. 696 (2011) 989-998.

[83] C.S. Allardyce, P.J. Dyson, Platin. Met. Rev. 45 (2001) 62.

[84] J. Costa Pessoa, I. Tomaz, Curr. Med. Chem. 17 (2010) 3701-3738.

[85] M. Haghdoost, G. Golbaghi, M. Létourneau, S.A. Patten, A. Castonguay, Eur. J. Med. Chem. 132 (2017) 282-293.

[86] M.M. Milutinović, S.K. Elmroth, G. Davidović, A. Rilak, O.R. Klisurić, I. Bratsos, Ž.D. Bugarčić, Dalton Trans. 46 (2017) 2360-2369.

[87] M.M. Milutinović, A. Rilak, I. Bratsos, O. Klisurić, M. Vraneš, N. Gligorijević, S. Radulović, Ž.D. Bugarčić, J. Inorg. Biochem. 169 (2017) 1-12.

[88] R. Aird, J. Cummings, A. Ritchie, M. Muir, R. Morris, H. Chen, P. Sadler, D. Jodrell, Br. J. Cancer. 86 (2002) 1652-1657.

[89] P. Čanović, A.R. Simović, S. Radisavljević, I. Bratsos, N. Demitri, M. Mitrović, I. Zelen, Ž.D. Bugarčić, JBIC J. Biol. Inorg. Chem. 22 (2017) 1007-1028.

[90] L. Zeng, P. Gupta, Y. Chen, E. Wang, L. Ji, H. Chao, Z.-S. Chen, Chem. Soc. Rev. 46 (2017) 5771-5804.

[91] M. Medjedović, A.R. Simović, D. Ćoćić, M. Milutinović, L. Senft, S. Blagojević, N. Milivojević, B. Petrović, Polyhedron 178 (2020) 114334.

[92] H.A. O'Riley, A. Levina, J.B. Aitken, P.A. Lay, Inorg. Chim. Acta. 454 (2017) 128-138.

[93] G. Bartoli, P.E. Todesco, Acc. Chem. Res. 10 (1977) 125-132.

[94] A. Levina, A. Mitra, P.A. Lay, Metallomics 1 (2009) 458-470.

[95] A. Casini, C. Temperini, C. Gabbiani, C.T. Supuran, L. Messori, ChemMedChem. 5 (2010) 1989-1994.

[96] R.O. Omondi, D. Jaganyi, S.O. Ojwach, A.A. Fatokun, Inorg. Chim. Acta. 482 (2018) 213-220.

[97] R.O. Omondi, S.O. Ojwach, D. Jaganyi, A.A. Fatokun, Inorg. Chem. Commun. 94 (2018) 98-103.

[98] G.K. Mutua, R. Bellam, D. Jaganyi, A. Mambanda, J. Coord. Chem. (2019) 1-26.

[99] I.A. Salimova, A.V. Berezina, E.S. Barskaya, M.S. Abramovich, K.A. Lyssenko, N.V. Zyk, E.K. Beloglazkina, Polyhedron 179 (2020) 114403.

[100] A. Zamora, S.A. Pérez, M. Rothemund, V. Rodríguez, R. Schobert, C. Janiak, J. Ruiz, Chem. Eur. J. 23 (2017) 5614-5625.

[101] A. Casini, L. Messori, Curr. Top. Med. Chem. 11 (2011) 2647-2660.

[102] E. Marta Nagy, L. Ronconi, C. Nardon, D. Fregona, Mini-Rev Med Chem 12 (2012) 1216-1229.

[103] S.J. Berners-Price, A. Filipovska, Metallomics 3 (2011) 863-873.

[104] I. Ott, Coord. Chem. Rev. 253 (2009) 1670-1681.

[105] T. Zou, C.T. Lum, C.-N. Lok, J.-J. Zhang, C.-M. Che, Chem. Soc. Rev. 44 (2015) 8786-8801.

[106] C. Nardon, G. Boscutti, D. Fregona, Anticancer Res. 34 (2014) 487-492.

[107] N. Cutillas, G.S. Yellol, C. de Haro, C. Vicente, V. Rodríguez, J. Ruiz, Coord. Chem. Rev. 257 (2013) 2784-2797.

[108] M. Milovanović, A. Djeković, V. Volarević, B. Petrović, N. Arsenijević, Ž.D. Bugarčić, J. Inorg. Biochem. 104 (2010) 944-949.

[109] M. Arsenijevic, M. Milovanovic, V. Volarevic, A. Djekovic, T. Kanjevac, N. Arsenijevic, S. Dukic, Z. D Bugarcic, Med Chem. 8 (2012) 2-8.

[110] S. Radisavljević, A.Đ. Kesić, D. Ćoćić, R. Puchta, L. Senft, M. Milutinović, N. Milivojević, B. Petrović, New J. Chem. 44 (2020) 11172-11187.

[111] S. Dilruba, G.V. Kalayda, Cancer Chemother. Pharmacol. 77 (2016) 1103-1124.

[112] A. Khan, R. Rashid, G. Murtaza, A. Zahra, Trop. J. Pharm. Res. 13 (2014) 1169-1177.

[113] P. Borst, S. Rottenberg, J. Jonkers, Cell cycle 7 (2008) 1353-1359.

[114] K. Barabas, R. Milner, D. Lurie, C. Adin, VET COMP ONCOL 6 (2008) 1-18.

[115] H. Zhao, T. Bi, Z. Qu, J. Jiang, S. Cui, Y. Wang, Oncol. Rep. 32 (2014) 1003-1012.

[116] S. Radisavljević, B. Petrović, Front. Chem. 8 (2020) 379.

[117] T.J. Carneiro, R. Araújo, M. Vojtek, S. Gonçalves-Monteiro, C.D.A.L. Batista de Carvalho, M.P.M. Marques, A.M. Gil, Metabolites 11 (2021) 114.

[118] Y. Liu, J. Li, M. Chen, X. Chen, N. Zheng, Theranostics 10 (2020) 10057.

[119] J. Espino, E. Fernández-Delgado, S. Estirado, F. de la Cruz-Martinez, S. Villa-Carballar, E. Viñuelas-Zahínos, F. Luna-Giles, J.A. Pariente, Sci. Rep. 10 (2020) 1-16.

[120] Q. Peña, G. Sciortino, J.-D. Maréchal, S. Bertaina, A.J. Simaan, J. Lorenzo, M. Capdevila, P. Bayón, O. Iranzo, Ò. Palacios, Inorg. Chem. 60 (2021) 2939-2952.

[121] B. Naureen, G. Miana, K. Shahid, M. Asghar, S. Tanveer, A. Sarwar, J. Mol. Struct. 1231 (2021) 129946.

[122] J.D. Atwood, Inorganic and organometallic reaction mechanisms, VCH Publishers, 1997.

CHAPTER 2

Methodology and instrumentation

2. 1 General background

The chapter presents general materials, methods, instrumentation, synthetic procedures, and analytical data for Pd(II) complexes. The chapter also outlines the procedures for electrochemistry, computational chemistry (density functional theory and molecular docking), and stability behaviours of Pd(II) complexes. The methodologies for ligand substitution reactions, DNA/BSA interactions, and *in vitro* cytotoxicity of the complexes are also herein described.

2.2 General considerations

All synthetic manipulations were performed under dry and oxygen free nitrogen atmosphere using standard Schlenk line techniques, unless otherwise stated. 32% hydrochloric acid (HCl), 25% ammonia solution, polyphosphoric acid, methanol and sodium carbonate were obtained from Merck. The chemicals, pyridine-2,6-dicarboxylic acid (99.0%), *o*-phenylenediamine (99.5%), 2-aminophenol (99.0%), 2-aminothiophenol (99.0%), iminodiacetic acid (≥98.0%), pyrazole (98.0%), sodium hydride (90.0%), bis(2-chloroethyl)amine (99.0%), bis(2-chloroethyl)ether (99.0%), sodium sulfide nonahydrate (98.0%), 2-bromoethanol (95.0%), pyrazine-2-carboxylic acid (99%), pyridine-2-carboxylic acid (99%), 2-picolylamine (99%), quinoline-2-carboxylic acid (98%), 8-aminoquinoline (98%), triphenylphosphite (97%), palladium(II) dichloride (99%), 2,6-dibromopyridine (98.0%), 1,3-dibromobenzene (98.0%), 1-methylimidazole (≥99.0%), silver(I) oxide (≥99.0%), 1-ethylimidazole (≥95.0%), sulfur powder (≥99.0%), silver tetrafluoroborate (98.0%), tetrabutylammonium tetrafluoroborate ($TBABF_4$) for electrochemical analysis (99%), thiourea (≥99.0%), L-methionine (≥98.0%), guanosine 5′-diphosphate disodium salt (≥96.0%), Hepes buffer (N-2-hydroxyethylpiperazine-N′-2-ethanesulfonic acid) (≥99.5%), tris(hydroxymethyl)aminomethane

(99%), 32 wt. % hydrochloric acid (98%), ethidium bromide (EB) (95.0%), and calf thymus DNA (CT-DNA) were purchased from Merck and were used without further purification. Ultrapure water (Modulab Systems) was used for all aqueous reactions. The starting material, $PdCl_2(NCMe)_2$ was synthesised based on the reported procedure [1].

The synthesis of bis(benzazole) ligands, 2,6-bis(benzimidazol-2-yl)pyridine (**L_1**), 2,6-bis(benzoxazol-2-yl)pyridine (**L_2**), 2,6-bis(benzothiazol-2-yl)pyridine (**L_3**), bis[(1H-benzimidazol-2-yl)methyl] amine (**L_4**) was performed following literature procedures [2, 3]. Ligands 2,6-bis[(1H-pyrazol-1-yl)methyl]pyridine (**L_5**), bis[2-(1H-pyrazol-1-yl)ethyl]amine (**L_6**), bis[2-(1H-pyrazol-1-yl)ethyl]ether (**L_7**), bis[2-(1H-prazol-1-yl)ethyl]sulphide (**L_8**) were prepared according to the published methods [4-6]. The carboxamide ligands N-(pyridin-2-ylmethyl)pyrazine-2-carboxamide (**L_9**), N-(quinolin-8-yl)pyrazine-2-carboxamide (**L_{10}**), N-(quinolin-8-yl)picolinamide **(L_{11}**), N-(quinolin-8-yl)quinoline-2-carboxamide (**L_{12}**) were synthesised following the synthetic protocols described in the literature [7]. Ligands 2,6-bis(3-methylimidazolium-1-yl)pyridine dibromide (**L_{13}**), 2,6-bis(3-ethylimidazolium-1-yl)pyridine dibromide (**L_{14}**), 2,6-bis(1-methylimidazole-2-thione)pyridine (**L_{15}**), 2,6-bis(1-ethylimidazole-2-thione)pyridine (**L_{16}**) were prepared according to the same synthetic procedure described in literature [8, 9].

Cell culture reagents including Dulbecco's Modified Eagle Medium (DMEM), phosphate-buffered saline (PBS), trypsin (TrypLE), L-glutamine and antibiotic-antimycotic (anti-anti) solution were obtained from Life Technologies (ThermoFisher Scientific). Foetal Bovine Serum (FBS) was obtained from Sigma. Z-VAD-fmk was obtained from Tocris Bioscience (Bio-Techne) while DMSO (tissue culture grade), 3,4-Dihydro-5-[4-(1-piperidinyl)butoxyl]-1(2H)-isoquinolinone (DPQ), and 3-(4,5-Dimethyl-2-thiazolyl)-2,5-diphenyl-2H-tetrazolium bromide (MTT) were purchased from Sigma-

Aldrich (UK). Cell lines were obtained originally from the European Collection of Authenticated Cell Cultures (ECACC).

Nuclear magnetic resonance spectra were acquired on a Bruker Avance spectrometer in DMSO-d6 solution at room temperature. Chemical shifts were determined relative to internal tetramethylsilane and are given in δ (ppm) and all coupling constants (J) are reported in hertz, (Hz). Elemental analyses were carried out using CHNS-O Flash 2000 thermo scientific analyser. Mass spectral analyses were measured on an LC Premier micro-mass spectrometer. The infrared spectra were recorded on Agilent Technologies Cary 630 in the 3800- 600 cm^{-1} range. X-ray data were recorded on a Bruker Apex Duo diffractometer equipped with an Oxford Instrument. Voltammetric studies were performed using an Autolab Potentiostat coupled with a three-electrode system: a carbon working electrode, a pseudo Ag/AgCl reference electrode, and a Pt counter electrode. A Cary 100 Series UV-vis spectrophotometer with a temperature controller (± 0.05 °C) was used to determine suitable wavelength for kinetic measurements, and CT-DNA titrations. The observed rate constants for the kinetic reactions of were monitored on an Applied Photophysics SX 20 stopped-flow reaction analyser coupled with an online data acquisition system with controlled temperature within ± 0.1 °C. Fluorescence emission spectra were recorded using a Perkin Elmer LS 45 Fluorescence Spectrometer using 1 cm path length cuvettes at room temperature. Jenway 4330 combined pH and conductivity meter with a 4.5 mm diameter microelectrode was used to determine the pH of the solutions.

2.3. Synthesis of Pd(II) complexes

2.3.1 [{2,6-bis(benzimidazol-2-yl)pyridine}PdCl]BF_4 (PdL_1)

To a solution of $PdCl_2(NCMe)_2$ (0.10 g, 0.39 mmol) in CH_2Cl_2 (30 mL) was added 2,6-bis(benzimidazol-2-yl)pyridine (**L_1**) (0.12 g, 0.39 mmol) and $NaBF_4$ (0.04, 0.39 mmol) to give a yellow solution. The resultant mixture was stirred for 12 h and filtered through a short pad of Celite to remove

the precipitate of NaCl. Hexane (10 mL) was added to the filtrate to afford **PdL$_1$** as a yellow solid. Yield: 0.12 g (57%). ^{1}H NMR (400 MHz, DMSO-d$_6$): δ_H (ppm): 7.24-7.33 (m, 4H, bz$_{im}$); 7.57 (d, $^3J_{HH}$ = 8.0, 2H, bz$_{im}$); 7.93 (d, $^3J_{HH}$ = 8.0, 2H, bz$_{im}$); 8.06 (d, $^3J_{HH}$ = 8.0, 2H, py); 8.35 (t, 1H, $^3J_{HH}$ = 8.0, H, py). ^{13}C NMR (DMSO-d$_6$): δC (ppm): 114.62; 116.73; 122.05; 124.91; 140.06; 142.87; 147.54; 152.97. FT-IR (cm^{-1}): υ(N-H) = 2728; υ(C=C) =1571; υ(C=N) = 1476. TOF MS ES$^+$, *m/z* (%) = 451 [M, 100]$^+$. HRMS-ESI [M + 3H]$^+$: *m/z* calc: 449.9738; found: 449.9730. Anal. Calcd (%) for $C_{19}H_{13}BClF_4N_5Pd$: C, 42.26; H, 2.43; N, 12.97. Found (%): C, 41.95; H, 2.70; N, 12.71

Complexes **PdL$_2$-PdL$_3$** were prepared following the protocol described for **PdL$_1$** using appropriate ligands 2,6-bis(benzoxazol-2-yl)pyridine (**L$_2$**), 2,6-bis(benzothiazol-2-yl)pyridine (**L$_3$**), respectively.

2.3.2 [{2,6-bis(benzoxazol-2-yl)pyridine}PdCl]BF$_4$ (PdL$_2$)

Ligand **L$_2$** (0.12 g, 0.39 mmol), $PdCl_2(NCMe)_2$ (0.10 g, 0.39 mmol) and $NaBF_4$ (0.04 g, 0.39 mmol). Off yellow solid. Single crystals were grown by allowing diethyl ether to diffuse into acetonitrile solution. Yield: 0.11 g (52%).^{1}H NMR (400 MHz, DMSO-d$_6$): δ_H (ppm): 7.53-7.55 (m, 2H, H, bz$_{ox}$); 7.57-7.58 (m, 2H, bz$_{ox}$); 7.96 (t, $^3J_{HH}$ = 7.8, 4H, bz$_{ox}$); 8.34 (t, $^3J_{HH}$ = 7.8, 1H, py); 8.57 (d, $^3J_{HH}$ = 7.8, 2H, py). ^{13}C NMR (DMSO-d$_6$): δC (ppm): 111.54; 120.50; 125.31; 125.63; 126.61; 139.40; 141.14; 145.80; 150.61; 160.62. FT-IR (cm^{-1}): υ(C=C) =1544; υ(C=N) = 1408; υ(C-O) = 1036. LC MS/ESI$^+$, *m/z (*%) = 453 [M, 100] $^+$. HRMS-ESI [M + H]$^+$: *m/z* calc: 453.9581; found: 453.9575. Anal. Calcd (%) for $C_{19}H_{11}BClF_4N_3O_2Pd.CH_2Cl_2$: C, 42.10; H, 2.05; N, 7.75. Found (%): C, 41.72; H, 2.19; N, 7.36.

2.3.3 [{2,6-bis(benzothiazol-2-yl)pyridine}PdCl]BF$_4$ (PdL$_3$)

L$_3$ (0.13 g, 0.39 mmol), $PdCl_2(NCMe)_2$ (0.10 g, 0.39 mmol) and $NaBF_4$ (0.04 g, 0.39 mmol). Off yellow solid. Single crystals were grown by allowing diethyl ether to diffuse into acetonitrile solution at room

temperature. Yield: 0.14 g (63%). ^{1}H NMR (400 MHz, DMSO-d_6): δ_H (ppm): 7.57 (t, $^{3}J_{HH}$ = 7.2, 2H, bz_{thio}); 7.62 (t, $^{3}J_{HH}$ = 8.0, 2H, bz_{thio}); 8.17 (d, $^{3}J_{HH}$ = 8.0, 2H, bz_{thio}); 8.27 (m, 3H, py); 8.49 (d, $^{3}J_{HH}$ = 7.2, 2H, bz_{thio}). ^{13}C NMR (DMSO-d_6): δC (ppm): 122.25; 122.74; 123.51; 126.28; 126.83; 135.52; 139.79; 150.54; 153.76; 167.69. FT-IR (cm^{-1}): υ(C=C) =1584; υ(C=N) = 1448; υ(C-S) = 1015. LC MS/ESI^{+}, *m/z (*%) = 485 [M, 100] $^{+}$. HRMS-ESI [M + H]$^{+}$: *m/z* calc: 485.9118; found: 485.9120. Anal. Calcd (%) for $C_{19}H_{11}BClF_4N_3PdS_2$: C, 39.75; H, 1.93; N, 7.32, S, 11.17. Found (%): C, 39.44; H, 1.68; N, 6.94, S, 10.94.

2.3.4 [{bis⟨(1H-benzimidazol-2-yl)methyl⟩ amine}PdCl]Cl (PdL$_4$)

To a solution of compound bis[(1H-benzimidazol-2-yl)methyl] amine, **L$_4$**, (0.11 g, 0.39 mmol) in CH_2Cl_2 (15 mL) was added a solution of $PdCl_2(NCMe)_2$ (0.10 g, 0.39 mmol) in CH_2Cl_2 (15 mL). The resultant yellow solution was stirred for 24 h and the product precipitated by the addition of hexane (10 mL) to give a white-yellowish solid. Single crystals were grown via vapour diffusion of diethyl ether into a saturated solution of **PdL$_4$** in DMSO. Yield: 0.10 g (51 %). ^{1}H NMR (400 MHz, DMSO-d_6): δ_H (ppm): 4.49 (dd, $^{3}J_{HH}$ = 7.4, 2H, CH_2); 4.93 (dd, 2H, $^{3}J_{HH}$ = 7.4, 2H, CH_2); 7.35-7.41 (m, 4H, bz_{im}); 7.64-7.68 (m, 2H, bz_{im}); 8.14 (s, 1H, NH); 8.27-8.31 (m, 2H, bz_{im}); 13.90 (s, 2H, NH).^{13}C NMR (DMSO-d_6): δC (ppm): 51.39; 112.85; 116.90; 123.54; 124.09; 132.12; 138.91; 158.94. FT-IR (cm^{-1}): υ(N-H) = 3619; υ(C=C) =1589; υ(C=N) = 1433. LC MS/ESI^{+}, *m/z (*%) = 417 [M, 100] $^{+}$; 838 [2M, 10%]$^{+}$. HRMS-ESI [M + H]$^{+}$: *m/z* calc: 418.0051; found: 418.0060. Anal. Calcd (%) for $C_{16}H_{15}Cl_2N_5Pd$: C, 42.27; H, 3.33; N, 15.40. Found (%): C, 41.97; H, 3.52; N, 15.09.

Complexes **PdL$_5$-PdL$_8$** were prepared in a similar fashion to complex **PdL$_1$** using relevant ligands 2,6-bis[(1H-pyrazol-1-yl)methyl]pyridine (**L$_5$**), bis[2-(1H-pyrazol-1-yl)ethyl]amine (**L$_6$**), bis[2-(1H-pyrazol-1-yl)ethyl]ether (**L$_7$**), bis[2-(1H-prazol-1-yl)ethyl]sulphide (**L$_8$**), respectively.

2.3.5 {[2,6-bis((1H-pyrazol-1-yl)methyl)pyridine]PdCl}BF_4 (PdL_5)

L_5 (0.10 g, 0.39 mmol), $PdCl_2(NCMe)_2$ (0.10 g, 0.39 mmol) and $NaBF_4$ (0.04 g, 0.39 mmol). Yellow solid. Single crystals were grown by allowing diethyl ether to diffuse into dichloromethane solution. Yield: 1.1 g (60 %).^{1}H NMR (400 MHz, DMSO-d_6): δ_H (ppm): 6.10 (s, 4H, CH_2); 6.63 (t, $^3J_{HH}$ = 3.3, 2H, pz); 7.92 (dd, $^3J_{HH}$ = 3.3, 2H, pz); 7.95 (d, $^3J_{HH}$ = 7.8, 2H, pz); 8.30 (dd, $^3J_{HH}$ = 3.3, 2H, py); 8.37 (t, $^3J_{HH}$ = 7.8, 2H, py). ^{13}C NMR (DMSO-d_6): δC (ppm): 60.13; 107.8; 121.42; 137.21; 139.01; 148.11; 156.85. FT-IR (cm^{-1}): υ(C-H) = 3080; υ(C=C) =1510; υ(C=N) = 1415; υ(C-N) = 1071. TOF MS/ES$^+$, *m/z* (%) 381 (M^+, 100). Anal. Calcd (%) for $C_{13}H_{13}BClF_4N_5Pd$: C, 33.37; H, 2.80; N, 14.97. Found (%): C, 33.63; H, 2.58; N, 15.17.

2.3.6 ⟨{ bis[2-(1H-pyrazol-1-yl)ethyl]amine}PdCl⟩BF_4 (PdL_6)

L_6 (0.16 g, 0.78 mmol), [$PdCl_2(CH_3CN)_2$] (0.20 g, 0.78 mmol) and $NaBF_4$ (0.08 g, 0.78 mmol). Yellow solid. Recrystallisation of **PdL_6** using CH_2Cl_2/Et_2O solvent mixture afforded single crystals suitable for X-ray analysis. Yield: 0.28 g (83%). ^{1}H NMR (400 MHz, DMSO-d_6): δ_H (ppm): 2.97-3.03 (m, 4H, CH_2); 4.54-4.60 (m, 2H, CH_2); 4.82-4.89 (m, 2H, CH_2); 6.54 (t, $^3J_{HH}$ = 2.0, 2H, pz); 7.13 (s, 1H, NH); 8.00 (dd, $^3J_{HH}$ = 2.0, 2H, pz); 8.15 (d, $^3J_{HH}$ = 2.0, 2H, pz). ^{13}C NMR (DMSO-d_6): δC (ppm): 49.50; 49.89; 106.94; 134.99; 143.05. FT-IR (cm^{-1}): υ(C-H) = 3096; υ(C=C) =1520; υ(C=N) = 1408; υ(C-N) = 1035. LC MS/ESI$^+$, *m/z (*%) = 346 [M^+, 100]; 692 [M^+, 10]. Anal. Calcd (%) for $C_{10}H_{15}BClF_4N_5Pd$: C, 27.68; H, 3.48; N, 16.14. Found (%): C, 27.44; H, 3.78; N, 15.80.

2.3.7 ⟨{bis[2-(1H-pyrazol-1-yl)ethyl]ether}PdCl⟩BF_4 (PdL_7)

L_7 (0.16 g, 0.78 mmol), [$PdCl_2(CH_3CN)_2$] (0.20 g, 0.78 mmol) and $NaBF_4$ (0.08 g, 0.78 mmol). Yellow solid. Upon recrystallization from slow liquid diffusion of diethyl ether into dichloromethane solution afforded yellow crystals suitable for single-crystal analysis. Yield: 0.29 g (85%). ^{1}H NMR (400 MHz, DMSO-d_6): δ_H (ppm): 3.51 (d, $^3J_{HH}$ = 10.0, 2H, CH_2); 4.24 (t, $^3J_{HH}$ = 10.0, 2H, CH_2); 4.59 (d, $^3J_{HH}$ =

12.1, 1H, CH); 4.71 (d, $^{3}J_{HH}$ = 10.0, 2H, CH_2); 4.99 (t, $^{3}J_{HH}$ = 12.1, 1H, CH); 6.51 (t, $^{3}J_{HH}$ = 2.4, 1H, pz); 6.58 (t, $^{3}J_{HH}$ = 2.4, 1H, pz); 8.06 (d, $^{3}J_{HH}$ = 2.3, 1H, pz); 8.12 (d, $^{3}J_{HH}$ = 2.3, 1H, pz); 8.20 (d, $^{3}J_{HH}$ = 2.0, 1H, pz); 8.57 (d, $^{3}J_{HH}$ = 2.0, 1H, pz). ^{13}C NMR (DMSO-d_6): δC (ppm): 51.61; 52.30; 69.58; 70.13; 107.07; 107.66; 135.43; 136.66; 141.37; 142.43. FT-IR (cm^{-1}): υ(C-H) = 3107; υ(C=C) =1511; υ(C=N) = 1412; υ(C-O) = 1275; υ(C-N) = 1049. LC MS/ESI$^+$, *m/z (*%) = 347 [M^+, 100]. Anal. Calcd (%) for $C_{10}H_{14}BClF_4N_4OPd$: C, 27.62; H, 3.24; N, 12.88; O, 3.68. Found (%): C, 27.43; H, 3.16; N, 12.49; O, 3.82.

2.3.8 ⟨{bis[2-(1H-pyrazol-1-yl)ethyl]sulphide}PdCl⟩BF_4 (**PdL$_8$**)

L$_8$ (0.17 g, 0.78 mmol), $[PdCl_2(NCMe)]_2$ (0.20 g, 0.78 mmol) and $NaBF_4$ (0.08 g, 0.78 mmol). Yellow solid. Recrystallisation of a solution of the crude product in CH_2Cl_2 solution at room temperature afforded yellow single crystals suitable for X-ray analysis. Yield: 0.3 g (85%). ^{1}H NMR (400 MHz, DMSO-d_6): δ_H (ppm): 3.36 (d, $^{3}J_{HH}$ = 2.8, 2H, CH_2); 3.63 (q, $^{3}J_{HH}$ = 2.8, 2H, CH_2); 5.06 -5.11 (m, 2H, CH_2); 5.24-5.31 (m, 2H, CH_2); 6.58 (t, $^{3}J_{HH}$ = 2.0, 2H, pz); 8.01 (d, $^{3}J_{HH}$ = 2.0, 2H, pz); 8.19 (d, $^{3}J_{HH}$ = 2.0, 2H, pz). ^{13}C NMR (DMSO-d_6): δC (ppm): 36.14 (CH_2); 52.31; 107.63; 135.99; 144.03. FT-IR (cm^{-1}): υ(C-H) = 3142; υ(C=C) =1515; υ(C=N) = 1415; υ(C-N) = 1058; υ(C-S) = 776. LC MS/ESI$^+$, *m/z (*%) = 364 [M^+, 100]. Anal. Calcd (%) for $C_{10}H_{14}BClF_4N_4PdS$: C, 26.63; H, 3.13; N, 12.42; S, 7.11. Found (%): C, 26.94; H, 2.87; N, 12.57; S, 7.39.

Complexes **PdL$_9$**-**PdL$_{12}$** were synthesised using the same synthetic procedure described for **PdL$_4$** using appropriate ligands N-(pyridin-2-ylmethyl)pyrazine-2-carboxamide (**L$_9$**), N-(quinolin-8-yl)pyrazine-2-carboxamide (**L$_{10}$**), N-(quinolin-8-yl)picolinamide (**L$_{11}$**), N-(quinolin-8-yl)quinoline-2-carboxamide (**L$_{12}$**), respectively.

2.3.9 [{N-(pyridin-2-ylmethyl)pyrazine-2-carboxamide}PdCl] (PdL_9)

L_9 (0.08 g, 0.39 mmol) in CH_2Cl_2 (15 mL), and $[PdCl_2(NCMe)]_2$ (0.10 g, 0.39 mmol). Light-yellow solid. Yield: 0.09 g (65%). ^{1}H NMR (400 MHz, DMSO-d_6): δ_H (ppm): 4.98 (s, 2H, CH_2); 7.54 (t, $^3J_{HH}$ = 6.0, 1H, py); 7.67 (d, $^3J_{HH}$ = 7.4, 1H, py); 8.12 (q, $^3J_{HH}$ = 7.8, 1H, py); 8.62-8.64 (m, 2H, py, pyz); 8.88 (d, $^3J_{HH}$ = 1.2, 1H, pyz); 9.00 (d, $^3J_{HH}$ = 2.9, 1H, pyz). ^{13}C NMR (DMSO-d6): δC (ppm): 55.08; 123.13; 123.88; 140.24; 143.25; 145.71; 149.31; 149.61; 150.38; 166.30; 168.67 (C=O). FT-IR (cm^{-1}): υ(C=O) =1641; υ(C=C) = 1524; υ(amidic C-N) = 1471. Anal. Calcd (%) for $C_{11}H_9ClN_4OPd$: C, 37.21; H, 2.55; N, 15.78; O, 4.51. Found (%): C, 36.83; H, 2,81; N, 15.36; O, 4.86.

2.3.10 [{N-(quinolin-8-yl)pyrazine-2-carboxamide}PdCl] (PdL_{10})

L_{10} (0.10 g, 0.39 mmol) and $[PdCl_2(NCMe)]_2$ (0.10 g, 0.39 mmol). Dark brown solid. Recrystallisation of the crude product from a dichloromethane-diethyl ether solvent system afforded single-crystals suitable for X-ray analysis. Yield: 0.09 g (60%).^{1}H NMR (400 MHz, DMSO-d_6): δ_H (ppm): 7.67-7.72 (m, **2**H, quin); 7.74-7.77 (dd, $^3J_{HH}$ = 5.3, 1H, quin); 8.66 (dd, $^3J_{HH}$ = 1.6, 1H, quin); 8.70-8.73 (m, 2H, quin); 8.84 (dd, $^3J_{HH}$ = 1.4, 1H, pyz); 9.04 (d, $^3J_{HH}$ = 1.1, 1H, pyz); 9.06 (d, $^3J_{HH}$ = 2.9, 1H, pyz). ^{13}C NMR (DMSO-d6): δC (ppm): 119.99; 121.87; 122.80; 129.41; 130.27; 140.43; 143.05; 144.15; 146.75; 146.98; 149. 73; 150.64; 150.93; 168.54. FT-IR (cm^{-1}): υ(C=O) =1633; υ(C=C) = 1577; υ(amidic C-N) = 1458. Anal. Calcd (%) for $C_{14}H_9ClN_4OPd$: C, 42.99; H, 2.32; N, 14.32; O, 4.09. Found (%): C, 43.27; H, 2.52; N, 13.91; O, 3.78.

2.3.11 [{N-(quinolin-8-yl)picolinamide}PdCl] (PdL_{11})

L_{11} (0.10 g, 0.39 mmol) and $[PdCl_2(NCMe)]_2$ (0.10 g, 0.39 mmol). Light yellow solid. Single crystals were obtained by allowing Et_2O to diffuse into CH_2Cl_2 solution. Yield = 0.11 g (73%).^{1}H NMR (400 MHz, DMSO-d_6): δ_H (ppm): 7.62-7.66 (t, $^3J_{HH}$ = 6.7, 2H, quin); 7.72 (dd, d, $^3J_{HH}$ = 5.0, 1H, quin); 7.78-7.81 (m, 1H, quin); 7.90 (dd, $^3J_{HH}$ = 1.0, 1H, quin); 8.30 (dt, $^3J_{HH}$ = 1.5, 1H, quin); 8.66-8.68 (m, 2H,

py); 8.71 (dd, $^{3}J_{HH}$ = 1.0, 1H, py); 8.84 (dd, $^{3}J_{HH}$ = 1.5, 1H, py). ^{13}C NMR (DMSO-d6): δC (ppm):119.91; 121.54; 122.67; 126.02; 128.63; 129.33; 130.23; 140.10; 141.62 (quinoline carbons); 144.51; 146.92; 149.82; 150.69; 156.64; 166.18. FT-IR (cm^{-1}): υ(C=O) =1633; υ(C=C) = 1594; υ(amidic C-N) = 1497. Anal. Calcd (%) for $C_{15}H_{10}ClN_3OPd$: C, 46.18; H, 2.58; N, 10.77; O, 4.10. Found (%): C, 45.90; H, 2.91; N, 11.20; O, 3.82.

2.3.12 [{N-(quinolin-8-yl)quinoline-2-carboxamide}PdCl] (PdL_{12})

L_{12} (0.11 g, 0.39 mmol) and $[PdCl_2(NCMe)]_2$ (0.10 g, 0.39 mmol). Yellow solid. Recrystallisation of the crude product from a dichloromethane–diethyl ether solvent system afforded single-crystals suitable for X-ray analysis. Yield: 0.13 g (76%). ^{1}H NMR (400 MHz, DMSO-d_6): δ_H (ppm): 7.65-7.70 (m, 2H, quin); 7.76-7.83 (m, 2H, quin); 7.95 (t, $^{3}J_{HH}$ = 8.0, 1H, quin); 8.09 (d, $^{3}J_{HH}$ = 8.3, 1H, quin); 8.17 (d, $^{3}J_{HH}$ = 7.2, 1H, quin); 8.69 (d, $^{3}J_{HH}$ = 8.3, 1H, quin); 8.79 (dd, $^{3}J_{HH}$ = 6.7, 1H, quin); 8.91 (d, $^{3}J_{HH}$ = 8.3, 1H, quin); 9.18 (dd, $^{3}J_{HH}$ = 5.3, 1H, quin); 9.69 (d, $^{3}J_{HH}$ = 8.8, 1H, quin). ^{13}C NMR (DMSO-d6): δC (ppm): 120.52; 121.83; 121.91; 122.42; 128.73; 128.83; 129.05; 129.31; 130.26; 130.76; 131.99; 136.53; 140.31; 142.75; 144.43; 146.30; 150.09; 158.95; 167.06. FT-IR (cm^{-1}): υ(C=O) =1627; υ(C=C) = 1567; υ(amidic C-N) = 1460. Anal. Calcd (%) for $C_{19}H_{12}ClN_3OPd$: C, 51.84; H, 2.75; N, 9.55; O, 3.63. Found (%): C, 51.45; H, 3.12; N, 9.17; O, 3.86.

2.3.13 [{2,6-bis(3-methylimidazolium-1-yl)pyridine dibromide}PdCl]BF_4 (PdL_{13})

L_{13} (0.50 g, 1.25 mmol) was suspended in acetonitrile (30 mL) and methanol (3 mL) added to effect dissolution. Ag_2O (0.29 g, 1.25 mmol) was added and the resulting black suspension was protected from light and stirred at 50 ºC for 24 h. To the reaction mixture, $AgBF_4$ (0.24 g, 1.26 mmol) was added, followed by $PdCl_2(MeCN)_2$ (0.32 g, 1.25 mmol). The reaction mixture was protected from light and stirred at 50 ºC for 24 h. The mixture was then allowed to cool to room temperature. After filtration, the

solvent was removed in *vacuo* and the yellow residue washed with CH_2Cl_2 and diethyl ether to give a brown-yellow solid. Yield: 0.42 g (72%). ^{1}H NMR (400 MHz, DMSO-d_6): δ_H (ppm): 3.91 (s, 6H, CH_3); 7.61 (s, 2H, imid); 7.92 (d, $^3J_{HH}$ = 8.2, 2H, py); 8.35 (s, 2H, imid); 8.51 (t, $^3J_{HH}$ = 8.2, 1H, py). ^{13}C NMR (DMSO-d_6): δC (ppm): 36.51; 108.69; 117.93; 125.34; 146.47; 150.25; 166.35. FT-IR (cm^{-1}): υ(C-H, aromatic) = 3615; υ(C-H, alkyl) = 3132; υ(C= N, imidazole) = 1619; υ(C=N, pyridine) = 1587; υ(C-N, imidazole) = 1033. LC MS/ESI$^+$, *m/z (*%) = 382 [M^+, -H, 100]. Anal. Calcd (%) for $C_{13}H_{15}BClF_4N_5Pd$: C, 33.22; H, 3.22; N, 14.90 %. Found: C, 33.51; H, 2.98; N, 14.74 %.

2.3.14 [{2,6-bis(3-ethylimidazolium-1-yl)pyridine dibromide}PdCl]BF_4 (**PdL$_{14}$**)

L$_{14}$ (0.53g, 1.25 mmol), Ag_2O (0.29 g, 1.25 mmol), $AgBF_4$ (0.24 g, 1.26 mmol), and $PdCl_2(MeCN)_2$ (0.32 g, 1.25 mmol). Brown-yellow solid. Recrystallisation of the crude product from CH_2Cl_2/Et_2O solution led to the formation of single-crystals suitable for X-ray analysis. Yield: 0.46 g (74%). ^{1}H NMR (400 MHz, DMSO-d6): δ_H (ppm): 1.37 (t, $^3J_{HH}$ = 7.2, 6H, CH_3); 4.41 (dd, $^3J_{HH}$ = 7.2, 4H, CH_2); 7.75 (d, $^3J_{HH}$ = 2.1, 2H, imid); 7.94 (d, $^3J_{HH}$ = 8.2, 2H, imid); 8.38 (d, $^3J_{HH}$ = 2.1, 2H, py); 8.52 (t, $^3J_{HH}$ = 8.2, 1H, py). ^{13}C NMR (DMSO-d_6): δC (ppm): 16.14; 44.43; 108.73; 118.22; 123.67; 146.46; 150.34; 165.88. FT-IR (cm^{-1}): υ(C-H, aromatic) = 3139; υ(C-H, alkyl) = 2989; υ(C= N, imidazole) = 1621; υ(C=N, pyridine) = 1488; υ(C-N, imidazole) = 1035. LC MS/ESI$^+$, *m/z (*%) = 410 [M^+, -H, 100]. Anal. Calcd (%) for $C_{15}H_{19}BClF_4N_5Pd$: C, 36.18, H, 3.85; N, 14.06. Found: C 35.81; H, 3.53, N, 14.34 %.

Complexes **PdL$_{15}$** and **PdL$_{16}$** were prepared in a similar fashion to **PdL$_1$** using ligands 2,6-bis*(1*-methylimidazole-2-thione)pyridine (**L$_{15}$**), 2,6-bis(1-ethylimidazole-2-thione)pyridine (**L$_{16}$**), respectively.

2.3.15 [{2,6-bis(1-methylimidazole-2-thione)pyridine}PdCl]BF_4 (PdL_{15})

L_{15} (0.12 g, 0.39 mmol), $[PdCl_2(NCMe)]_2$ (0.10 g, 0.39 mmol), and $NaBF_4$ (0.04, 0.39 mmol). Yellow solid. Yield: 0.14 g (67%). ^{1}H NMR (400 MHz, DMSO-d_6): δ_H (ppm): 3.80 (s, 6H, CH_3); 7.89 (d, $^3J_{HH}$ = 2.4, 2H, imid); 8.10 (d, $^3J_{HH}$ = 8.2, 2H, imid); 8.21 (d, $^3J_{HH}$ = 2.4, 2H, py); 8.67 (t, $^3J_{HH}$ = 8.2, 1H, py). ^{13}C NMR (DMSO-d_6): δC (ppm): 35.71, 116.80, 117.53, 120.12, 140.17, 162.2, 170.53. FT-IR (cm^{-1}): υ(C-H, aromatic) = 3465; υ(C-H, alkyl) = 3095; υ(C= N, imidazole) = 1594; υ(C=N, pyridine) = 1460; υ(C=S, imidazole) = 1149, υ(C-N, imidazole) = 1017. LC MS/ESI$^+$, *m/z (*%) = 382 [M^+, -H, 100]. Anal. Calcd (%) for $C_{13}H_{13}BClF_4N_5PdS_2$: C, 29.35; H, 2.46; N, 13.16; S, 12.05 %. Found: C, 29.02; H, 2.17; 12.79, S, 12.26 %.

2.3.16 [{2,6-bis(1-ethylimidazole-2-thione)pyridine}PdCl]BF_4 (PdL_{16})

L_{16} (0.13 g, 0.39 mmol), $PdCl_2(NCMe)_2$ (0.10 g, 0.39 mmol), and $NaBF_4$ (0.04 g, 0.39 mmol). Yellow solid. Yield: 0.15 g (69%). ^{1}H NMR (400 MHz, DMSO-d_6): δ_H (ppm): 1.44 (t, $^3J_{HH}$ = 7.3, 6H, CH_3); 4.23 (dd, $^3J_{HH}$ = 7.2, 4H, CH_2); 7.97 (d, $^3J_{HH}$ = 2.4, 2H, imid); 8.13 (d, $^3J_{HH}$ = 8.2, 2H, imid); 8.25 (d, $^3J_{HH}$ = 2.4, 2H, py); 8.69 (t, $^3J_{HH}$ = 8.2, 1H, py). ^{13}C NMR (DMSO-d_6): δC (ppm): 13.80, 44.54, 116.72, 117.55, 120.81, 140.12, 164.66, 170.45. FT-IR (cm^{-1}): υ(C-H, aromatic) = 3546; υ(C-H, alkyl) = 3092; υ(C= N, imidazole) = 1600; υ(C=N, pyridine) = 1458; υ(C=S) = 1153; υ(C-N, imidazole) = 1021. LC MS/ESI$^+$, *m/z (*%) = 474 [M^+, + H, 55]; 518 [M^+,+2Na, 65]. Anal. Calcd (%) for $C_{15}H_{17}BClF_4N_5PdS_2$: C, 32.16; H, 3.06; N, 12.50; S, 11.45 %. Found: C, 32.44; H, 3.23; N, 12.15; S, 11.76 %.

2.4. Single crystal X-ray crystallography

X-ray data were recorded on a Bruker Apex Duo diffractometer equipped with an Oxford Instruments Cryojet operating at 100(2) K and an Incoatec microsource operating at 30 W power. The data were collected with Mo Kα (λ = 0.71073 Å) radiation at a crystal-to-detector distance of 50 mm. The

following conditions were used for the data collection: omega and phi scans with exposures taken at 30 W X-ray power and 0.50º frame widths using APEX2 [10]. The data were reduced with the programme SAINT[11] using outlier rejection, scan speed scaling, as well as standard Lorentz and polarisation correction factors. A SADABS semi-empirical multi-scan absorption correction was applied to the data. Direct methods, SHELXS-2014 andWinGX [12], were used to solve all three structures. All non-hydrogen atoms were located in the difference density map and refined anisotropically with SHELXL-2014. All hydrogen atoms were included as idealised contributors in the least squares process. Their positions were calculated using a standard riding model with C-$H_{aromatic}$ distances of 0.93 Å and Uiso= 1.2 Ueq, C–$H_{methylene}$ distances of 0.99 Å and Uiso = 1.2 Ueq and C–H_{methyl} distances of 0.98 Å and Uiso= 1.5 Ueq.

2.5 Computational modelling

2.5.1 Density functional theoretical calculations

Computational calculations were performed using density functional theory (DFT) method executed by Gaussian 09W suite of programs. The structures were optimized using the hybrid Becke, 3-parameter, Lee-Yang-Parr (B3LYP basis) functional method, at the standard Los Almos National Laboratory 2 Double ζ (LANL2DZ) basis set [13, 14]. DFT utilises physically observable electron density over a wave-function in the determination of the optimised properties of a molecule or a compound. It is applicable in compounds with a large number of electrons because electron densities are always three dimensional irrespective of the number of electrons involved. The influence of the bulk solvent was examined *via* single point calculations using conductor-like polarisable continuum implicit solvent formalism [15]. The complexes were modelled in water media. To study the electronic properties of the complexes, quantum chemical descriptors such as the values of the highest occupied molecular orbital energy (E_{HOMO}), and the lowest unoccupied molecular orbital energy (E_{LUMO}), chemical hardness (η), back donation energy ($\Delta E_{back\text{-}donation}$), chemical softness (σ),

global electrophilicity indices (ω), nucleophilicity (ε) and dipole moments were calculated. Natural bond orbitals (NBO) analysis was adopted to compute the atomic charges of the selected atoms in the complexes at the same theoretical level [16]. These descriptors are crucial electronic features used to describe chemical reactivity, thermodynamic stability, and other related properties of the complexes. Gaussian 09W programme suite was employed to visualise geometry optimised structures, and to calculate the minimum energy of the structure, using PC with processor Core i7 (8 CPU 1.7 GHz). GaussView 5.0 was utilised to prepare the input files [17].

2.5.2 DNA molecular docking

The complexes were docked onto the right-handed helix of normal double-stranded DNA (B-DNA) using HEX8.0 software [18], which uses spherical polar Fourier correlations to accelerate the calculations. The calculations were carried out on an Intel Core i3-4170 CPU using the following parameters; correlation type: (shape + electro); search order: 25; receptor/ligand: 180; step sizes: 7.5; grid dimension: 0.6; number of solutions: 2000. The coordinates of the complexes were optimised by Gaussian 09 programme and converted to Protein Data bank (PDB) using Mercury 3.3 software. The crystal structure of the B–DNA dodecamer $d(CGCGAATTCGCG)_2$ (PDB ID: 1BNA) was retrieved from the protein data bank [19]. The water molecules were removed before docking calculations with the examined compounds. The docked pose of 1BNA and each complex were viewed using UCSF CHIMERA software [20]. The docking protocol was repeated three times and almost similar docking poses were viewed in each of the runs. The $E_{(\text{lowest energy pose})}$ value of each Pd-complex and DNA interactional pose was examined.

2.6 Electrochemical studies of the palladium complexes

Electrochemical studies were performed in oxygen free solutions of Pd-complexes in DMSO consisting 0.1 M equivalents of $TBABF_4$ as a supporting electrolyte. All electrochemical experiments were conducted at 25.0 ± 0.2 °C. The voltammograms were obtained in a potential window of -2.0 to +2.0 V. CV studies of the complexes were performed at different potential scan rates ranging from 25 - 250 mVs^{-1}. On the other hand, SWV was performed at a set potential of 100 mVs^{-1}.

2.7 Stability of the complexes in aqueous and DMSO media

The stability of complexes **PdL_1-PdL_4** in aqueous solutions, Tris-HCl buffer (pH = 7.2) or DMSO were qualitatively explored by ^{1}H NMR and UV-Vis spectroscopies. The resulting solutions were analysed immediately, and the electronic spectral changes were recorded over a period of 24 h (in the case of water exchange kinetics) or 72 h (for complex stability in DMSO media), at room temperature.

2.8 Substitution kinetics with biomolecules

Substitution reactions were monitored at physiological conditions (pH 7.2) in the presence of 50 μM Tris-HCl buffer (pH = 7.2), maintained at an ionic strength of 50 mM NaCl, to prevent any possibility of spontaneous solvolysis of the complexes. The reactions were followed using UV-Vis and stopped-flow spectrophotometers. Freshly prepared stock solutions of the nucleophiles approximately 50-fold excess of the concentration of the complex was serially diluted with the aqua solution to afford 40, 30, 20, and 10-fold excess of the complex concentration to maintain *pseudo*-first order conditions. The ultraviolet-visible spectral changes resulting from the reactions were recorded over the wavelength range 800-200 nm to establish a suitable wavelength at which the kinetic measurements could be conducted. All reactions were initiated by mixing equal volumes of nucleophile and complex solutions

directly in the stopped-flow spectrophotometer and were followed for at least eight half-lives. Concentration dependence studies were performed at a constant temperature of 298 K, while the temperature dependence reactions were carried out within a range of 25 to 45 °C at an interval of 5 °C to determine activation parameters, $\Delta H^{\neq}$ and $\Delta S^{\neq}$. Observed pseudo-first-order rate constants were examined from the kinetic traces by an online Pro Data SX computer programme [21]. Kinetic traces were fitted into a non-linear least square fit to produce *pseudo*-first-order rate constants (k_{obs}) using equation (1) [22].

$$A_t = A_o + (A_o - A_\infty)\exp(-k_{obs}t) \quad (1)$$

where, At = absorbance at time t, Ao = absorbance at the onset of the reaction, A∞ = absorbance at the end of the reaction. The second-order rate constants (k_2) were derived from the dependence of the observed *pseudo*-first-order rate constant, k_{obs} on the concentration of the incoming nucleophile, [Nu] using equation (2) [23].

$$k_{obs} = k_2[Nu] + k_{-2} \quad (2)$$

where, k_{-2} is the first-order rate constant for the reverse reaction. The values of k_2 and k_{-2} are obtained from the slope and y-intercept of the plot, respectively. A plot with a zero y-intercept means that the forward reaction is irreversible, then the relationship between k_{obs} and [Nu] can be illustrated by equation (3), while one with an appreciable y-intercept imply that reaction procees in a reversible manner or through a coordination of a solvent molecule (solvotic pathway).

$$k_{obs} = k_2[Nu] \quad (3)$$

Temperature dependence reactions were systematically observed over a range of 298 to 318 K at an interval of 5 K. Thermodynamic parameters were computed using Eyring equation (4) [23].

$$\ln (k_2/T) = - \Delta H^{\neq}/RT + (23.8 + \Delta S^{\neq}/R) \quad (4)$$

where, $\Delta H^{\neq}$, $\Delta S^{\neq}$, T and R, are activation enthalpy, activation entropy, temperature and gas constant, respectively.

The Gibbs energy of activation ($\Delta G^{\neq}$), which consists of $\Delta S^{\neq}$ and $\Delta H^{\neq}$ was calculated using equation (5) [24, 25].

$$\Delta G^{\neq} = \Delta H^{\neq} - T\Delta S^{\neq} \quad (5)$$

where, T is temperature in kelvin

2.9 CT-DNA and BSA binding studies

2.9.1 UV-Vis absorption spectral studies for CT-DNA

UV-visible absorption titration of CT-DNA binding was performed following our previously reported procedures [26]. A constant concentration of the Pd-complexes was titrated with the increasing amounts of DNA stock solution. The Pd-CT-DNA solution were allowed to incubate for 8 min before recording the UV-vis spectra from the region 230-500 nm. The DNA binding abilities of the compounds were determined by calculating the intrinsic binding constant, K_b, using Wolfe-Shimer equation (6) [27].

$$[DNA]/(\varepsilon_a-\varepsilon_f) = [DNA]/(\varepsilon_b-\varepsilon_f)+1/(K_b(\varepsilon_b-\varepsilon_f)) \quad (6)$$

where, [DNA] is the concentration of CT-DNA in base pairs; ε_a is the apparent extinction coefficient; ε_b corresponds to the molar extinction coefficient of free complex; ε_f is the extinction coefficient for the complex in the completely bound form to DNA. The K_b values were computed from the ratio of the slope to intercept of appropriate plots of $[DNA]/(\varepsilon_a - \varepsilon_f)$ *vs* [DNA]. The standard Gibb's free (ΔG) of Pd-compound bound to DNA was obtained using van't Hoff equation (7) [28].

$$\Delta G = -RT \ln K_b. \quad (7)$$

2.9.2 Fluorescence quenching studies for CT-DNA

The fluorescence quenching experiments with EB-DNA was also carried out based on our previously published procedures [26]. The Pd-CT-DNA solution were allowed to incubate for 8 min before recording the UV-vis spectra from the region 230-500 nm. The equilibrium time for metallo drug - DNA

spectra being less than 30 seconds. The Stern-Volmer binding constant (K_{SV}), bimolecular quenching rate constant (K_q), and were computed from the classical the Stern-Volmer equation (8) [3].

$$I_o/I = 1 + K_{sv}[Q] = 1 + k_q\tau_0[Q] \quad (8)$$

where, I_o and I are the emission intensities of EB-CT-DNA adduct in the absence and presence of the quencher (complex) at concentration [Q]. K_{sv} was obtained from the ratio of the slope to the intercept of the linear plot of I_o/I *vs.* [Q]. τ_0 is the average fluorescence lifetime of the EB-CT-DNA in the absence of the quencher. The apparent association constant, K_{app}, was calculated from the equation (9) [29].

$$K_{EB}[EB] = K_{app}[Q] \quad (9)$$

where, [Q] is the concentration of quencher causing 50% reduction in fluorescence intensity of EB-bound CT-DNA, $K_{EB} = 10^7$ M^{-1}. In addition, binding constant, K_F and the number of binding sites per nucleotide, (n) were determined from Scatchard equation (10) [30].

$$\log(I_o - I) / I = \log K_F + n \log[Q] \quad (10)$$

2.9.3 Fluorescence spectral studies for BSA

The quenching of BSA by the complexes was performed to determine their binding constants on the protein. Stock concentration of BSA (12.0 μM) was prepared in 5 mM Tris-HCl/50 mM NaCl buffer solution at a pH of 7.2. A stock solution of BSA was freshly prepared before use. The concentration of BSA was measured spectrophotometrically by dividing the absorbance at 278 nm by the molar extinction coefficient (4.4×10^4 $M^{-1}cm^{-1}$) [31]. A solution of BSA was titrated with increasing amounts of metallo complexes concentration (0-130 μM). The emission spectra were recorded in the range of 250-400 nm at an excitation wavelength of 278 nm (with 10 min incubation period, at 25 °C). The fluorescence quenching of the complexes is described by the Stern-Volmer and Scatchard equations as discussed above.

2.9.4 Filter effect corrections

Data correction was employed to the spectrophotometric titrations to compensate for the existing primary and/or secondary inner filter effects following described literature procedures [32], using equation (11) [33].

$$F_{corr} = F_{obs}10(A_{ex}+A_{em})/2 \quad (11)$$

where, F_{corr} and F_{obs} are designated as the corrected and observed fluorescence intensities, respectively, caused by quencher/ fluorophore addition in a 1 cm path-length cuvette. Notably, the equation was adopted because it is valid and applicable in the case of typical fluorophores where scattering is negligible, and the extinction is dominated by absorption.

2.10 Cell culture and *in vitro* cytotoxicity

Cytotoxic effects of the complexes were tested in malignant cell lines; human cervix adenocarcinoma (HeLa), human (foetal) lung carcinoma (MRC5-SV2), lung cancer (A549), prostate cancer (PC-3), colon cancer (HT-29), colon cancer (Caco-2), cervical cancer (HeLa) and normal human foetal lung fibroblast cell line (MRC-5), and KMST-6. The combination of cancer cells and normal cells enabled us to assess the differences in the sensitivities of cancer cell lines to the complexes, as well as the differences in the sensitivities of a cancer cell line and its normal (healthy) parental line, to determine the potential cancer cell-selective toxicity of the complexes. The experiments were performed following our previously reported literature procedures [26, 34, 35]. Each treatment was done in triplicate. Treatment viability was assessed using MTT (3-(4,5-Dimethyl-2-thiazolyl)-2,5-diphenyl-2H-tetrazolium bromide) assay, following up to 24 h of treatments. Cells were grown in 75cm^2 tissue culture flasks using DMEM supplemented with 10% Foetal Bovine Serum, 2mM L-glutamine and 1% antibiotic-antimycotic solution (containing penicillin, streptomycin and amphotericin B), and incubated at 37 ^oC in a humidified atmosphere of 5% CO_2. To prepare culture plates, the tissue culture flask was

rinsed with phosphate-buffered saline (PBS), trypsinised, and the cells were suspended in the growth medium. Cell density was determined by the use of a haemocytometer and adjusted to 7.5 x 10^4 cells/ml, and 100 µl of the suspension (7500 cells) was seeded into each well of a micro-clear, flat-bottom 96-well plates. Seeded plates were incubated for 24 h before the cultures were treated for up to 48 h with a range of concentrations of each complex or a positive control (cisplatin) prepared in growth medium (stocks were prepared in DMSO (cisplatin was prepared in distilled water), but the final DMSO concentration that cells were exposed to was not more than 0.1%v/v). Each treatment was done in triplicate. Following treatment, viability was assessed using the MTT assay by adding 10 µl of a 5 mg/ml solution of MTT to each well and incubating the plates for 3 h. The content of each well was then aspirated and 100µl of DMSO was added to dissolve the insoluble formazan. Absorbance at 570 nm was then read on a CLARIOstar plate reader (BMG LABTECH, Germany). The mean of triplicate values for each treatment was determined and expressed relative to the mean of the triplicate negative control wells that was set to 100%. An Olympus CKX41 microscope fitted with an Olympus DP71 U-TVIX-2 camera was used to assess and image treatment-induced changes to the morphology of cells. The images were captured with the Olympus cellSens entry software.

2.10.1 Assessment of intracellular levels of reactive oxygen species (ROS)

Changes to intracellular levels of reactive oxygen species (ROS) induced by cisplatin and the complexes in HeLa cells were assessed using the DCFDA Cellular ROS Detection Assay Kit (Abcam, Cat. No. ab113851). Experiments were conducted according to the manufacturer's protocol. HeLa cells were seeded into black, clear bottom 96-well plates at a density of 2.5 x10^5 cells/ml (25,000 cells per well) and incubated overnight at 37 °C in a humidified atmosphere of 5% CO_2. The medium was then aspirated from each well and cultures were washed with the buffer solution (1x) supplied with the kit (Abcam) before they were stained for 45 min with 25 µM of the dichlorofluorescin diacetate (DFCDA) solution at 100 µl/well, with non-stained and blank controls included. Following the 45 min incubation

the stain was removed and cultures were washed with buffer. They were then treated with the compounds which had been diluted to the desired concentrations using the full growth medium that contained no phenol red. Cells were then incubated and the fluorescence (Ex/Em = 485/535 nm) of the plate was read at 3 h and at 24 h after treatment on a CLARIO star plate reader. Treatments were done in duplicates and each experiment was repeated at least three independent times. Data were analysed by setting the fluorescence of the negative control (no compound, vehicle only) to '1' (unity) and then calculating the fold change in fluorescence of each treatment compared to the negative control.

2.10.2 Assessment of mechanisms of cell death

Pharmacological assessment of the potential apoptotic or necrotic nature of the cell death elicited by the most promising complexes and cisplatin was conducted in HeLa cells using Z-VAD-fmk, a pan-caspase inhibitor (caspases are involved in certain forms of apoptosis), and DPQ, an inhibitor of the nuclear enzyme poly (ADP-ribose) polymerase (PARP), which mediates parthanatos, a form of programmed necrosis. The HeLa cells were prepared as reported earlier for cytotoxicity studies. The cultures were pre-treated with Z-VAD-fmk or DPQ for 1 h, after which they were treated with cisplatin or the investigated complex in the continued presence of each inhibitor. Treatments lasted for 48 h, after which MTT was used to assess viability.

2.10.3 Data presentation and statistical analyses

Values are expressed as Mean ± SEM (standard error of the mean) or as otherwise stated. GraphPad Prism (Version 8.3.0) (GraphPad Software, Inc., CA, USA) was used for statistical analyses and the assessment of significant differences between means was done using analysis of variance (ANOVA) followed by a post-hoc test for multiple comparisons (Tukey test), with a p-value of less than 0.05 considered statistically significant. The IC_{50} value for the complexes was determined using GraphPad Prism by fitting the data to the non-linear regression "log [inhibitor] versus normalised response" or

"log [inhibitor] versus response (three parameters)," as appropriate. The selectivity index (SI) of the complexes was calculated by dividing their IC_{50} values in the normal cell, by their respective IC_{50} values in cancer cell line.

The results and key findings of these studies are described in Chapters 3-6, while the overall conclusions are summarised in Chapter 7.

2.11 References

[1] R.E. Rulke, J.M. Ernsting, A.L. Spek, C.J. Elsevier, P.W. van Leeuwen, K. Vrieze, Inorg. Chem. 32 (1993) 5769-5778.

[2] A.W. Addison, P.J. Burke, J. Heterocycl. Chem. 18 (1981) 803-805.

[3] P. Kopel, D. Wawrzak, V. Langer, K. Cihalova, D. Chudobova, R. Vesely, V. Adam, R. Kizek, Molecules 20 (2015) 10360-10376.

[4] T.N. Sorrell, M.R. Malachowski, Inorg. Chem. 22 (1983) 1883-1887.

[5] J. García-Antón, J. Pons, X. Solans, M. Font-Bardia, J. Ros, Eur. J. Inorg. Chem. 2003 (2003) 3952-3957.

[6] S.O. Ojwach, I.A. Guzei, J. Darkwa, S.F. Mapolie, Polyhedron 26 (2007) 851-861.

[7] D. Barnes, R. Chapman, R. Vagg, E. Watton, J. Chem. Eng. Data 23 (1978) 349-350.

[8] J.C. Chen, I.J. Lin, J. Chem. Soc., Dalton Trans. (2000) 839-840.

[9] W.-G. Jia, Y.-C. Dai, H.-N. Zhang, X. Lu, E.-H. Sheng, RSC Adv. 5 (2015) 29491-29496.

[10] B. APeX, Bruker AXS Inc., Madison, Wisconsin, USA (2010).

[11] G.M. Sheldrick, Acta Cryst. C 71 (2015) 3-8.

[12] L.J. Farrugia, J. Appl. Crystallogr. 45 (2012) 849-854.

[13] M. Frisc, G. Trucks, H. Schlegel, G. Scuseria, M. Robb, J. Cheeseman, G. Scalmani, V. Barone, B. Mennucci, G. Petersson, Gaussian Inc, Wallingford (2010).

[14] J. Li, L.-C. Xu, J.-C. Chen, K.-C. Zheng, L.-N. Ji, J. Phys. Chem. A 110 (2006) 8174-8180.

[15] M. Cossi, N. Rega, G. Scalmani, V. Barone, J. Comput. Chem. 24 (2003) 669-681.

[16] M. Frisch, G. Trucks, H. Schlegel, G. Scuseria, M. Robb, J. Cheeseman, G. Scalmani, V. Barone, B. Mennucci, G. Petersson, Inc., Wallingford, CT (2010).

[17] R.A. Gaussian09, Inc., Wallingford CT 121 (2009) 150-166.

[18] S. Saito, G. Silva, R. X. Santos, G. Gosmann, C. Pungartnik, M. Brendel, (2012). Int. J. Mol. Sci. 13 (2012) 2846-2862.

[19] H.R. Drew, R.M. Wing, T. Takano, C. Broka, S. Tanaka, K. Itakura, R.E. Dickerson, Proc Natl Acad Sci U S A. 78 (1981) 2179-2183.

[20] E. Pettersen, T. Goddard, C. Huang, G. Couch, D. Greenblatt, E. Meng, T. Ferrin, J. Comput. Chem 25 (2004) 1605-1612.

[21] R. Bellam, D. Jaganyi, A. Mambanda, R. Robinson, New J. Chem. 42 (2018) 12557-12569.

[22] M.L. Tobe, J. Burgess, Inorganic reaction mechanisms, Longman, 1999.

[23] J.D. Atwood, Inorganic and organometallic reaction mechanisms, VCH Publishers, 1997.

[24] H. Eyring, J Chem Phys. 3 (1935) 107-115.

[25] H.B. Gray, R.J. Olcott, Inorg. Chem. 1 (1962) 481-485.

[26] R.O. Omondi, R. Bellam, S.O. Ojwach, D. Jaganyi, A.A. Fatokun, J. Inorg. Biochem. 210 (2020) 111156.

[27] A. Zianna, G.D. Geromichalos, A.G. Hatzidimitriou, E. Coutouli-Argyropoulou, M. Lalia-Kantouri, G. Psomas, J. Inorg. Biochem. 194 (2019) 85-96.

[28] M. Hosseini-Kharat, K. Karami, M. Saeidifar, C. Rizzoli, R. Zahedi-Nasab, Z. Sohrabijam, T. Sharifi, New J. Chem. 41 (2017) 9897-9907.

[29] R.O. Omondi, R. Bellam, S.O. Ojwach, D. Jaganyi, A.A. Fatokun, J. Inorg. Biochem. (2020) 111156.

[30] C. Ravi, R.K. Vuradi, S. Avudoddi, P.K. Yata, V.R. Putta, G. Srinivas, R. Merugu, S. Satyanarayana, Nucleosides, Nucleotides and Nucleic Acids 38 (2019) 788-806.

[31] E. Alarcon, A. Aspée, M. Gonzalez-Bejar, A. Edwards, E. Lissi, J. Scaiano, Photochem. Photobiol. Sci. 9 (2010) 861-869.

[32] C. Parker, W. Rees, Analyst 87 (1962) 83-111.

[33] M. Puchalski, M. Morra, R. Von Wandruszka, Fresen J Anal Chem. 340 (1991) 341-344.

[34] R.O. Omondi, D. Jaganyi, S.O. Ojwach, A.A. Fatokun, Inorg. Chim. Acta. 482 (2018) 213-220.

[35] R.O. Omondi, S.O. Ojwach, D. Jaganyi, A.A. Fatokun, Inorg. Chem. Commun. 94 (2018) 98-103.

CHAPTER 3

The remote effects of heteroatoms on the structural behaviour, substitution kinetics patterns, DNA interactions, and cytotoxicity of tridentate 2,6-bis(benzazole)pyridines palladium(II) complexes

3.1 Introduction

Despite the success of cisplatin in chemotherapy, its application is limited due to severe side effects, development of drug resistance and limited solubility [1-4]. The interaction of platinum complexes with sulfur containing biomolecules, such as glutathione, L-methionine and L-cysteine has been associated with negative effects such as gastrointestinal toxicity, nephrotoxicity, neurotoxicity, cardiotoxicity, and ototoxicity. These drawbacks have triggered the search for new metallo-drugs with improved specificity and efficacy in tumour treatment. With the rise of an exciting number of antineoplastic properties of other transition metals, the attention is gradually shifting beyond the use of platinum [5-17]. It is well documented that among the non-platinum based compounds, Pd(II) complexes are among the most studied compounds due to their structural similarity to Pt(II) complexes [18-25]. In addition, Pd(II) compounds display higher cytotoxicity, selectivity and better solubility than those of the conventional platinum drugs. However, the rates of ligand-exchange kinetics of Pd(II) complexes are *ca*. 10^3-10^5 times faster than the corresponding Pt(II) compounds [26]. These high reactivities do not allow Pd(II) complexes to maintain their structural identity in the cytoplasm long enough to reach the target, DNA, and thus reducing their cytotoxic efficacy. To overcome this drawback, a judicious choice of the inert chelating ligands is crucial to reduce the kinetic lability of the Pd(II) complexes, and hence maximise their cytotoxic activity [7, 27-29].

Reports by Bugarčić [30] confirm that steric crowding improves interaction with the DNA and antitumour activity of metal complexes. The phenomenon, is explained by the slower kinetic reactivity of the complexes that enables them to reach the DNA, without much interference from other biological molecules in the cytoplasm. Contrarily, steric hindrance of the spectator ligands can also have a negative

influence on the substitution kinetics, DNA-/protein-binding ability and cytotoxic activity [31, 32]. In a previous study, our research group [33] examined the role of bidentate benzazole ligands on the substitution kinetics and cytotoxicity of Ru(III) complexes anchored on (pyridyl)benzazole ligands. The *in vitro* study demonstrated that the complexes exhibited minimal cytotoxicity, which was attributed to their slow rate of substitution reactions. In this current work, our intention was to improve the cytotoxicity by regulating the rate of kinetic substitution using Pd(II) as a metal centre. Our hypothesis is that a combination of the slower spectator ligands and a more labile Pd metal would fine-tune the reactivity of the resultant complexes and give desirable cytotoxicity properties. In this contribution, we thus report the synthesis, structural characterisation of Pd(II) complexes of tridentate N^N^N 2,6-bis(benzazole) ligands and their substitutions reactions with biological donor nucleophiles; thiourea, **Tu**, L-methionine, **L-Met** (and guanosine-5'-monophosphate, **5'-GMP**. The choice of the nucleophiles was based on their aqueous solubility, varied nucleophilicity, binding properties and steric influences. For example, **Tu** and **L-Met** were chosen as model nucleophiles for sulfur-containing biomolecules, which are abundant in the plasma (particularly proteins); while **5'-GMP** was used as a model for binding to the nucleobases that are the main targets for metal-based antitumour drugs. The interactions of the complexes with calf-thymus DNA (CT-DNA) and intercalative agent ethidium bromide (EB) were investigated. Cytotoxic activities of the complexes on the cancer cell lines, human cervix adenocarcinoma (HeLa), human (foetal) lung carcinoma (MRC5-SV2) and normal human foetal lung fibroblast) cell line, (MRC-5), were also studied and are herein reported.

3.2. Results and discussion

3.2.1. Syntheses and characterisation of the compounds

Ligands **L_1-L_3** were synthesised in good yields by the condensation reactions of pyridine-2,6-dicarboxylic acid with the corresponding aniline derivatives following literature procedures [34]. On the other hand, **L_4** was synthesised in good yields (79%) by reactions of *o*-phenylenediamine with

iminodiacetic acid according to the synthetic procedure reported by Kopel *et al* [35], (Scheme 3.1). Complexes **PdL$_1$-PdL$_3$** were afforded by the treatment of equimolar amounts of ligands **L$_1$-L$_4$** with $PdCl_2(NCMe)_2$ in the presence of $NaBF_4$ in CH_2Cl_2 at room temperature. On the other hand, **PdL$_4$** was obtained by the reaction of **L$_4$** with $PdCl_2(NCMe)_2$ in a 1:1 mole ratio in dichloromethane at room temperature, section 2.3 (Scheme 3.1).

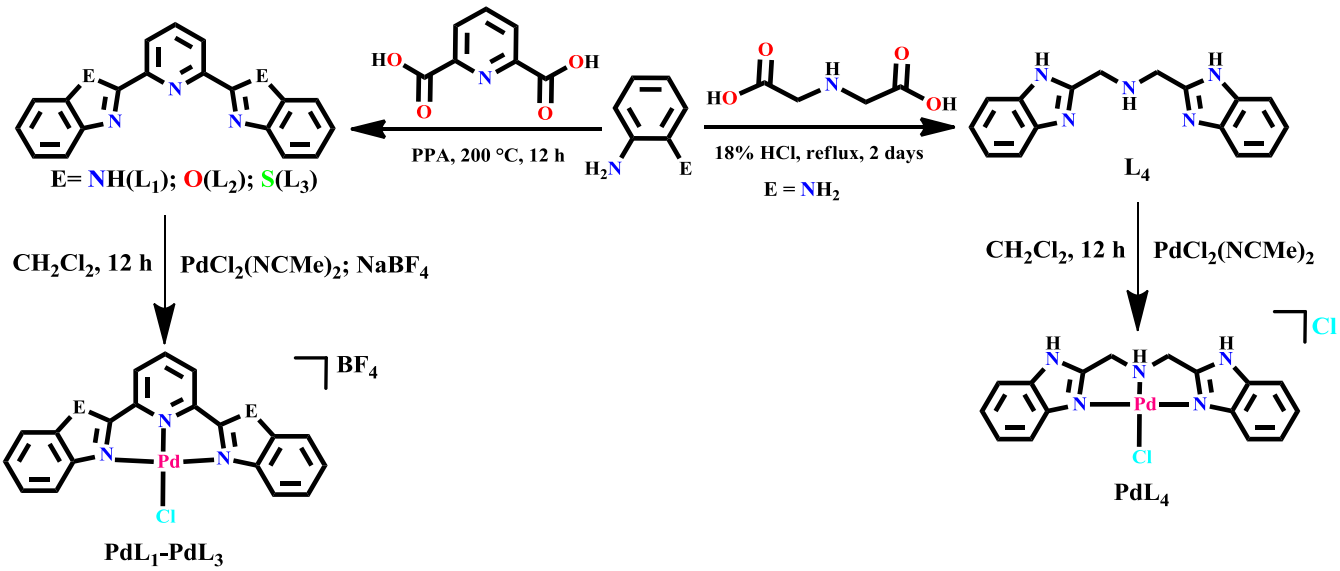

Scheme 3.1: Synthesis of 2,6-bis(benzazole) ligands **L$_1$-L$_4$** and corresponding Pd(II) complexes **PdL$_1$-PdL$_4$**.

The identities of **PdL$_1$-PdL$_4$** were established by a combination of ^{1}H and ^{13}C NMR, FT-IR spectroscopies, mass spectrometry, elemental analyses and single crystal X-ray analyses. Comparison of ^{1}H and ^{13}C NMR spectra and FT-IR spectra of ligands **L$_1$-L$_4$** to the spectra of their corresponding Pd(II) complexes **PdL$_1$-PdL$_4$** established their formation. For example, ^{1}H NMR spectra of **PdL$_4$** showed two doublets for the two CH_2 linker protons at 4.46 ppm and 4.96 ppm compared to the singlet peak, 4.03 ppm, in the respective ligand **L$_4$** (Figure 3.1). The appearance of two doublets of the CH_2 signals in **PdL$_4$** has been reported and is associated with increased rigidity (resulting in the existence of chair and boat conformations) in the complex relative to a more fluxional behaviour in the free ligand

[36]. In the ^{13}C NMR spectral data, the signature carbon peak of the CH_2 group of **PdL$_4$** was observed at 51.39 ppm compared to the peak at 46.48 ppm in the respective ligand (Figure 3.2).

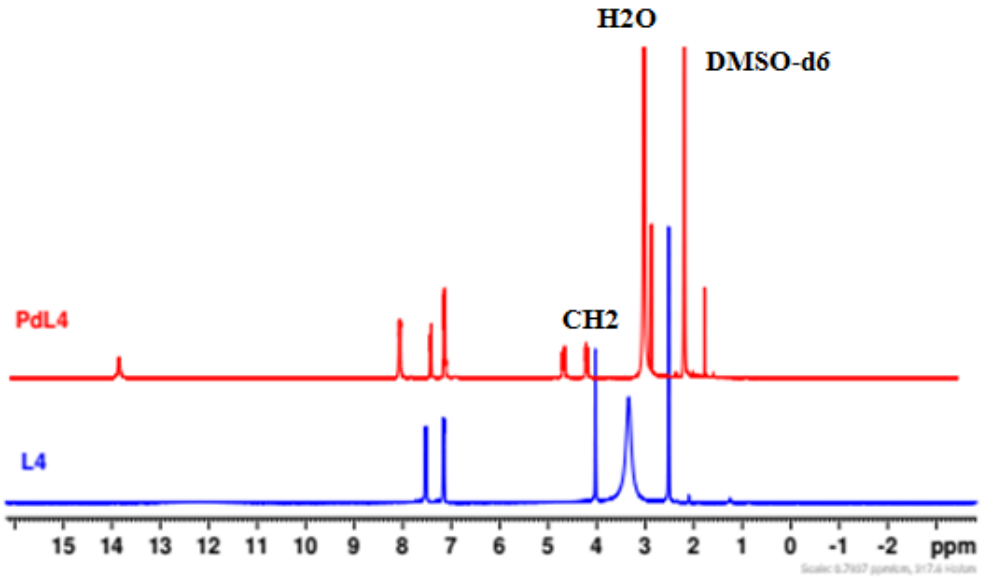

Figure 3.1: Overlays of ^{1}H NMR spectra of **L$_4$** and **PdL$_4$** in DMSO-d6, showing one signal for CH_2 protons at 4.03 ppm (**L$_4$**), and two signals at 4.46 ppm and 4.96 pm (**PdL$_4$**).

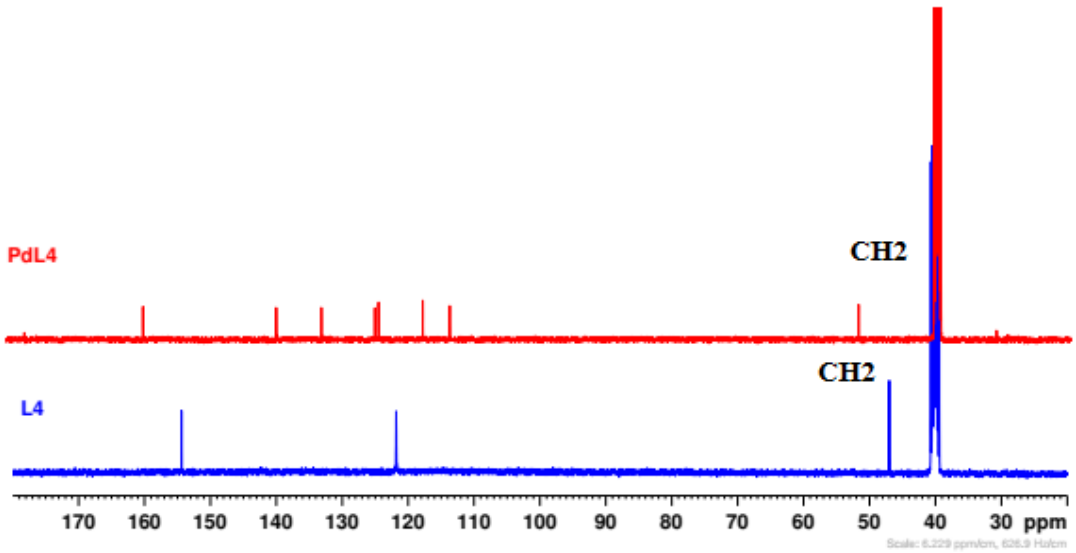

Figure 3.2: Overlays of ^{13}C NMR spectra of **L$_4$** and **PdL$_4$** in DMSO-d6, showing a shift of the signature carbon peak of CH_2 at 46.48 ppm (**L$_4$**) to 51.39 ppm upon complexation (**PdL$_4$**).

In the FT-IR spectral data, a shift of the absorption band of υ(N-H) at 2877 cm^{-1} in **L_4** to 3104 cm^{-1} in **PdL_4** (Figure 3.3) was observed and confirmed the formation of the complex [37]. Mass spectrometry also proved useful in the elucidation of the molecular formulae of the complexes. For example, the mass spectrum of **PdL_4** showed peaks at *m/z (%)* = 417 $[M, 100]^+$, which corresponds to its molecular ion (Figure 3.4).

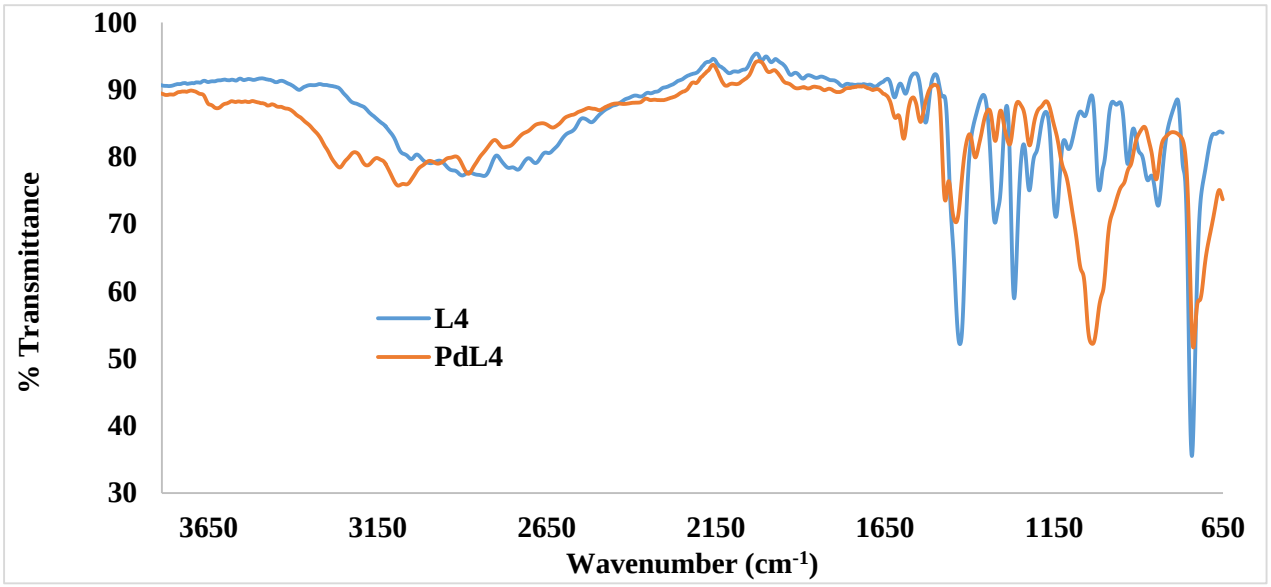

Figure 3.3: Overlays of FT-IR spectra of ligand **L_4** and respective complex **PdL_4,** depicting a shift of the absorption band of υ(N-H) at 2877 cm^{-1} (**L_4**) to 3104 cm^{-1} (**PdL_4**).

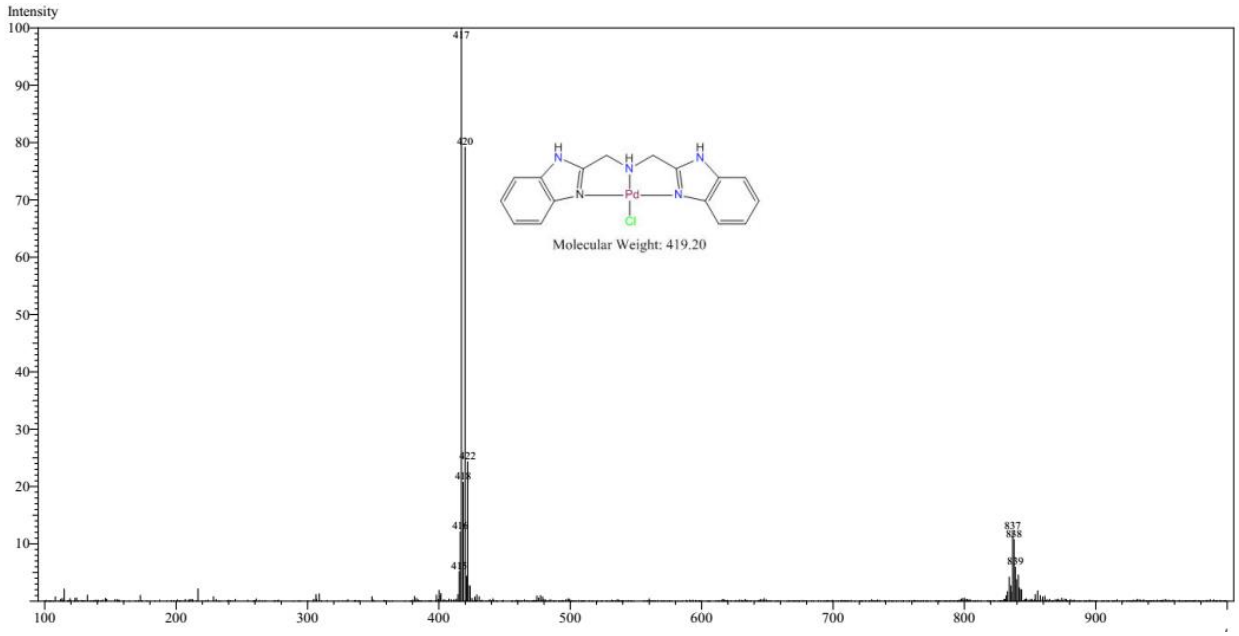

Figure 3.4: Mass spectrum of complex **PdL$_4$** with *m/z* at 417 (100%) corresponding to its molecular weight of 419.

3.2.2. X-ray molecular structure of complex PdL$_2$ -PdL$_4$

Single crystal suitable for X-ray analyses of **PdL$_2$** and **PdL$_3$**, were obtained by slow diffusion of diethyl ether into concentrated solutions of the complexes in CH_3CN, while crystals of **PdL$_4$** were grown by slow diffusion of diethyl ether into DMSO at room temperature. Table 3.1 contains crystallographic data and structural refinement parameters, while Figures 3.5, 3.6 and 3.7 show the molecular structures and selected bond parameters of complexes **PdL$_2$**, **PdL$_3$**, and **PdL$_4$**, respectively.

Figure 3.5: Molecular structure of **PdL$_2$**, with atom numbering Scheme. The displacement ellipsoids of atoms are shown at the 50% probability level. The BF^-_4 counter-anion has been omitted for clarity. Selected bond lengths [Å]: Pd(1)-N(3), 2.024(19); Pd(1)-N(1), 2.017(18); Pd(1)-N(2), 1.968(17); Pd(1)-Cl(1), 2.284(5). Selected bond angles (˚): N(3)-Pd(1)-N(1), 160.04(7); N(3)-Pd(1)-N(2), 80.09(7); N(1)-Pd(1)-N(2), 79.94(7); N(3)-Pd(1)-Cl(1), 99.80(5); N(1)-Pd(1)-Cl(1), 100.16(5); N(2)-Pd(1)-Cl(1), 179.15(5).

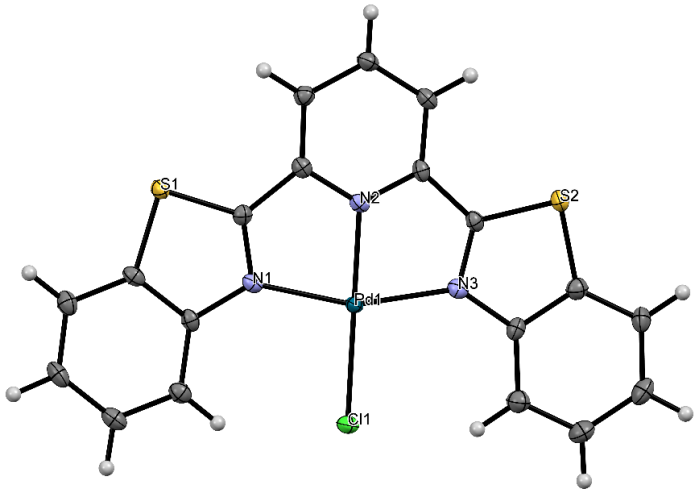

Figure 3.6: Molecular structure of **PdL$_3$**, with atom numbering Scheme. The displacement ellipsoids of atoms are shown at the 50% probability level. The BF^-_4 counter-anion has been omitted for clarity. Selected bond lengths [Å]: Pd(1)-N(3), 2.060(2); Pd(1)-N(1), 2.058(2); Pd(1)-N(2), 1.956(2); Pd(1)-Cl(1), 2.2998(6). Selected bond angles (˚): N(1)-Pd(1)-N(3), 159.84(8); N(3)-Pd(1)-N(2), 79.91(8); N(1)-Pd(1)-N(2), 79.93(8); N(3)-Pd(1)-Cl(1), 100.49(6); N(1)-Pd(1)-Cl(1), 99.66(6); N(2)-Pd(1)-Cl(1), 178.40(7).

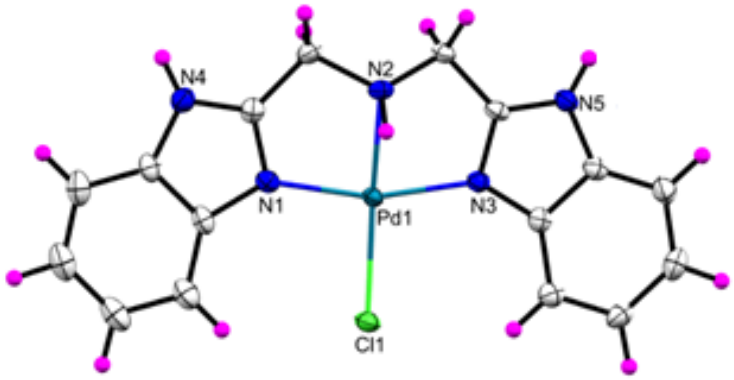

Figure 3.7: Molecular structure of **PdL4**, with atom numbering Scheme. The displacement ellipsoids of atoms are shown at the 50% probability level. Selected bond lengths [Å]: Pd(1)-N(3), 2.011(3) ; Pd(1)-N(1), 2.019(3); Pd(1)-N(2), 2.037(3); Pd(1)-Cl(1), 2.308(8). Selected bond angles [°]: N(3)-Pd(1)-N(1), 163.79(10); N(3)-Pd(1)-N(2), 82.59(10); N(1)-Pd(1)-N(2), 81.97(11); N(3)-Pd(1)-Cl(1), 98.05(7); N(1)-Pd(1)-Cl(1), 97.87(7); N(2)-Pd(1)-Cl(1), 173.20(9).

Table 3.1: Summary of the crystallographic data and structure refinement for complexes **PdL_2-PdL_4**

Parameter	**PdL_2**	**PdL_3**	**PdL_4**
Empirical formula	$C_{21}H_{14}BClF_4N_4O_2Pd$	$C_{40}H_{25}C_{l6}N_7Pd_3S_4$	$C_{18}H_{21}Cl_2N_5OPdS$
Formula weight	583.02	1263.81	532.76
Temperature	100 (2) K	100(2) K	101(2) K
Wavelength	0.71073 Å	1.54178 Å	0.71073 Å
Crystal system	Monoclinic	Monoclinic	Orthorhombic
Space group	P 21/c	C 2/c	P b c a
Unit cell dimensions			
a (Å)	6.6715(4)	18.5006(4) Å	19.527(3)
b (Å)	12.8094(7)	19.7935(4) Å	19.008(3)
c (Å)	24.5913(14)	22.4429(5) Å	11.4356(19)
α (°)	90	90°	90
β (°)	91.713(2)	98.6140(10)°	90.000(7)
γ (°)	90	90°	90
Volume	2100.6(2) $Å^3$	8125.7(3) $Å^3$	4244.5(12) $Å^3$
Z	4	8	8
Density (calculated)	1.844 Mg/m^3	2.066 Mg/m^3	1.667 Mg/m^3
Absorption coefficient	1. 075 mm^{-1}	16.515 mm^{-1}	1.244 mm^{-1}
F(000)	1152.0	4944	2144
Crystal size	0.220 x 0.180 x 0.150 mm^3	0.070 x 0.060 x 0.040 mm3	0.800 x 0.240 x 0.160 mm^3
Theta range for data collection	1.657 to 28.985°.	3.290 to 68.167°	2.086 to 28.377°.

In both structures, the coordination around the Pd metal centre consists of one tridentate ligand and one chloride ligand to give four-coordination environments. The *cis* angles, for instance N1-Pd1-N2 of 79.94(7)° (**PdL$_2$**), 79.93(8)° (**PdL$_3$**), and 81.97(11)° (**PdL$_4$**) deviate from the ideal 90°. This is also reflected in the *trans* angles, of N2–Pd1–Cl1 of 179.15(5)^o for **PdL$_2$**, 178.40(7)^o for **PdL$_3$** and 173.20(9)^o for **PdL$_4$** which deviate somewhat from the linearity. Thus, **PdL$_2$-PdL$_4$** adopt slightly distorted square planar geometries, consistent for d^8 Pd(II) complexes [38]. The five membered chelate ring, N(1)-Pd(1)-N(2) of 79.94(7)° (**PdL$_2$**) and 79.93(8)° (**PdL$_3$**) are smaller than the angle N(1)-Pd(1)-N(2) of 81.97(11)° (**PdL$_4$**). This can be assigned to the the rigid pyridine ring (**PdL$_2$** and **PdL$_3$**), when compared to the more flexible CH_2 linker (**PdL$_4$**).

The bond distances Pd(1)-N(3) of 2.024(19), 2.060(2), 2.011(3) Å in **PdL$_2$**, **PdL$_3$**, and **PdL$_4$**, respectively, are statistically similar, presumably due to the remote proximity of the heteroatoms to the Pd(II) metal centre. A similar trend is observed in the bond lengths for Pd(1)-N(1) of 2.017(18) Å, 2.058(2), and 2.019(3) Å for **PdL$_2$**, **PdL$_3$** and **PdL$_4$** respectively. The shorter bond length for Pd(1)-Cl(1) of 2.284(5) Å (**PdL$_2$)** and 2.2998(6) Å (**PdL$_3$**) compared to the Pd(1)-Cl(1) bond distance of 2.308(8) Å (**PdL$_4$**) may be ascribed to the aromatic pyridine ring in **L$_2$** and **L$_3$** which are pi-acceptor (less *trans*-influence) in comparsion to the sigma-donor N-H group in **L$_4$**. The Pd-Cl bond lengths of 2.284 (5) Å for **PdL$_2$** and 2.2998(6) Å for **PdL$_3$** are within the average bond distance of 2.289 Å ± 0.023 obtained for 20 related Pd complexes. Similarly, the Pd-Cl bond length of 2.308(8) Å in **PdL$_4$** falls within the average bond distance of 2.327 ± 0.017 Å reported for 19 similar structures [39]. The Pd(1)-N_{py} bond distance for **PdL$_2$** and **PdL$_3$** of 1.968(17) Å and 1.956(2) Å agrees well with the averaged bond lengths of 1.950 ± 0.039 Å reported in 15 structures. Likewise, the bond distance of Pd-Nim of 2.037 (3) is comparable to the bond distance of Å 2.048 ± 0.025 Å (**PdL$_4$**), averaged for 16 related structures [40]. The mean bond distances of Pd–N (1&3) of 2.021 Å (**PdL$_2$**) and 2.059 Å (**PdL$_3$**) compare well with the averages of 2.025 ± 0.038Å (16 structures). Also, 2.015 Å **PdL$_4$** is within the mean bond length of 1.980 ± 0.053 (15 structures) obtained for similar complexes respectively [40].

3.2.3 DFT-computational optimisation, calculations and analysis

DFT simulations were performed to gain an insight on the electronic and structural properties of Pd-ccomplexes. The optimised geometry structures, frontier orbital density distributions (HOMOs and LUMOs), and planarity of the complexes are depicted in Figure 3.8, while key geometrical data are summarised in Table 3.2. The DFT optimised structures reveal that the electron densities of the HOMO orbitals are predominately contributed by the *4d*-orbitals of Pd(II) metal centre and the π-system of the entire inert ligand architecture, and in the case of **PdL$_4$** the electrons are also contributed by the 3p-orbitals of the chlorine atoms. On the other hand, the LUMO electron clouds are mainly localised on the pyridyl ligand moiety and Pd(II) ion, and in the case of **PdL$_4$**, the electrons are also distributed on the chloride atom. The slight increase in the HOMO energy level across the series of Pd(II) complexes, indicates that electron donation density around Pd(II) metal increases, while the increase on the LUMO energy in a similar fashion demonstrates a reduction in π-acceptability of the ligand system in the complexes. The computed energy gap, $\Delta E_{LUMO–HOMO}$ gradually increases from **PdL$_1$** to **PdL$_4$**. It is noticed that the LUMO energies of **PdL$_1$-PdL$_3$** are raised in the increasing order of the electronegativity of the heteroatom on the spectator ligand. This indicates that the HOMOs are stabilised and LUMOs are destabilised, as a result smaller $\Delta E_{LUMO–HOMO}$ causing an observed decrease in reactivity. It is clear that **PdL$_4$** shows relatively high $\Delta E_{LUMO–HOMO}$ when compared to **PdL$_1$**.This can be attributed to the absence of pyridine ring on the head of the ligand system on **PdL$_4$**, which indicates the absence of π-back bonding. The planarity around the Pd(II) metal centre, as made possible through the in-plane pyridine/benzoazole ligand system, seems to offer little or no steric hindrance to the incoming nucleophile in **PdL$_1$**, **PdL$_2$**, and **PdL$_3$**. Conversely, the auxiliary ligand in **PdL$_4$** lies out of the plane due to the slight flexibility of **L$_4$**.

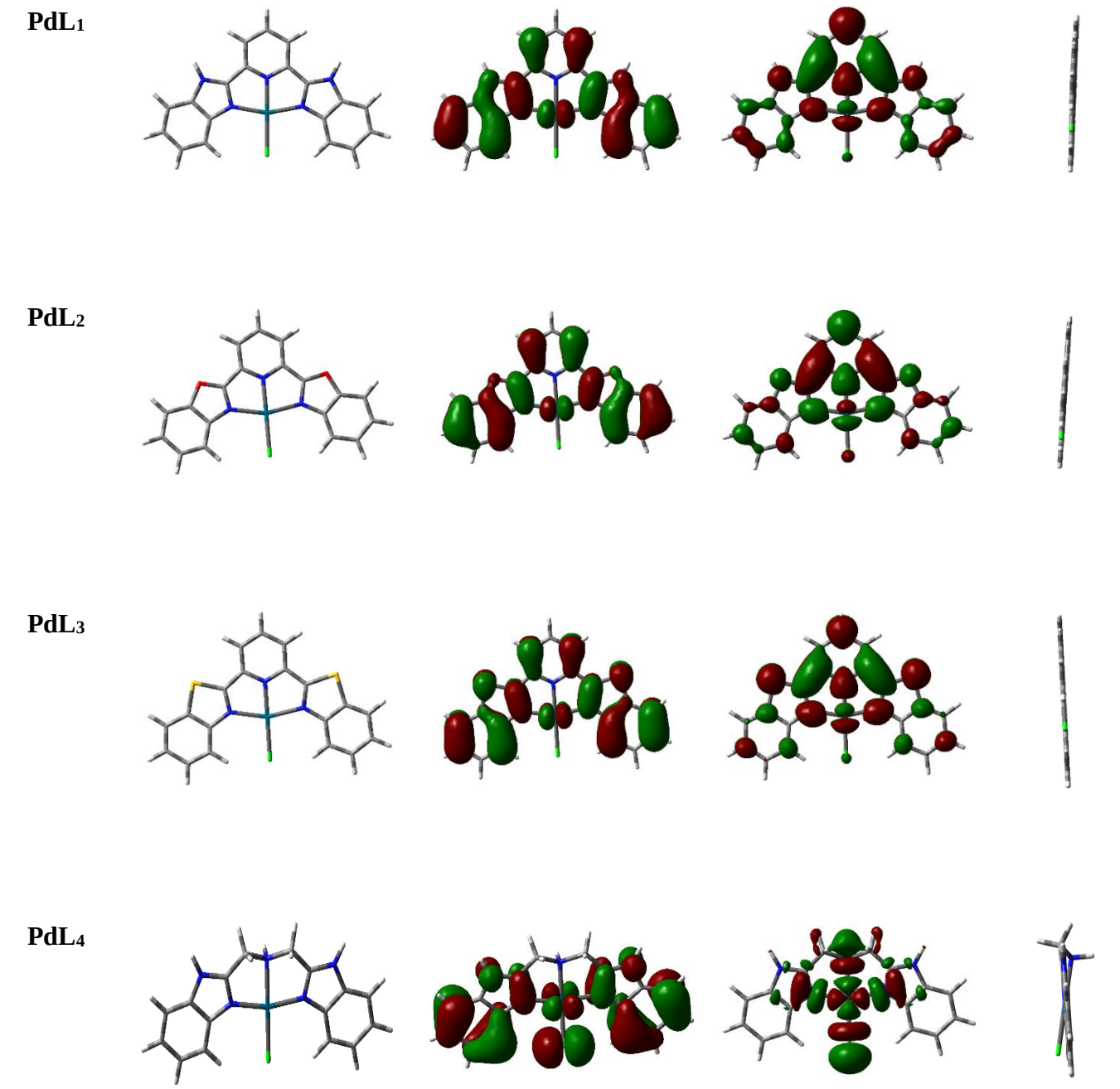

Figure 3.8: DFT optimised HOMO, LUMO frontier molecular orbitals, with respective planarity structures of Pd(II) complexes.

Table 3.2: Summary of selected DFT-calculated data for complexes **PdL_1-PdL_4**

Complexes	**PdL_1**	**PdL_2**	**PdL_3**	**PdL_4**
NBO Charge				
Pd^{2+}	0.675	0.619	0.549	0.482
Cl^-	-0.508	-0.485	-0.496	-0.505
N_{trans} to Cl	-0.427	-0.427	-0.427	-0.636
N_{cis} to Cl	-0.513	-0.497	-0.478	-0.540
X = Heteroatom	-0.548	-0.499	0.416	-0.557
Bond angle (°)				
TransN-Pd-Cl	179.98	179.99	178.00	171.49
HOMO-LUMO energy / eV				
LUMO/eV	-3.693	-3.514	-3.233	-2.754
HOMO/eV	-7.190	-7.084	-6.848	-6.750
ΔE/eV	3.497	3.570	3.615	3.996
Chemical hardness (η)	1.749	1.785	1.807	1.9982
Chemical softness (σ)	0.572	0.560	0.553	0.501
Electronic chemical potential (μ)	-5.442	-5.299	-5.040	-4.752
Electrophilicity index (ω)	8.468	7.864	7.028	5.651
Dipole moment (Debye)	15.552	13.733	12.946	11.086

3.2.4 Kinetic and mechanistic measurements with biomolecules

The rate of the displacement of the coordinated chloro ligand from the four complexes was studied with three biologically-relevant nucleophiles: **Tu**, **L-Met** and **5'-GMP**, under *pseudo*-first order conditions. Representative plots of k_{obs} versus the concentration of the entering ligand, [Nu], for **PdL$_1$** is given in Figure 3.9. The plots gave straight lines with zero-intercept, signifying the absence of reverse or non-solvotic pathways. The relationship between k_{obs} and the concentration of the entering ligand can be best described by equation (3). The second order rate constants (k_2) were derived from the slopes of the graphs and the values are given in Table 3.3.

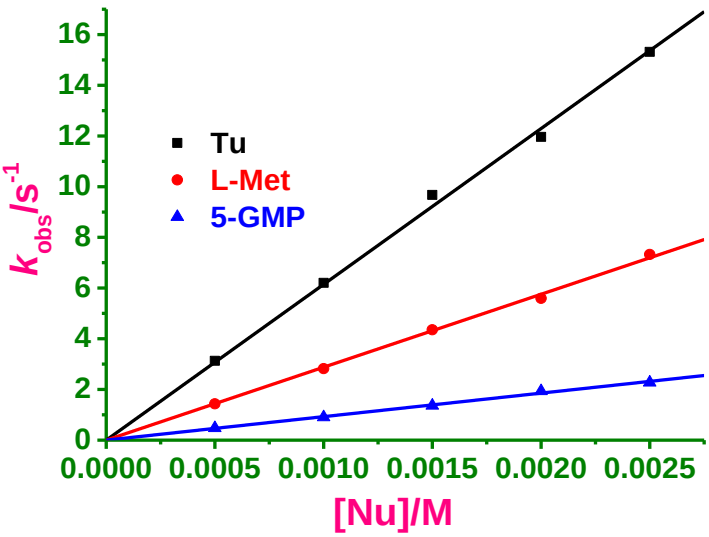

Figure 3.9: Dependence of k_{obs} on the nucleophile concentration for chloride substitution from **PdL$_1$** at T = 298 K in aqua media, 50 μM Tris-HCl buffer (pH = 7.2), and 50 mM NaCl

Table 3.3: Summary of the second order rate constants, k_2 and activation parameters, $\Delta H^{\neq}$ and $\Delta S^{\neq}$ for the substitution reactions of complexes **PdL₁-PdL₄** by **Tu**, **L-Met** and **5-GMP**.[a]

Complex	Nu	k_2/M^{-1} s^{-1}	$\Delta H^{\neq}$/ kJ mol^{-1}	$\Delta S^{\neq}$/J mol^{-1}K^{-1}
	Tu	6146 ± 78	27 ± 1.0	-83 ± 3.0
PdL₁	**L-Met**	2877 ± 28	30 ± 1.0	-79 ± 3.0
	5'-GMP	927 ± 13	30 ± 1.4	-86 ± 4.4
	Tu	5433 ± 41	33 ± 2.5	-62 ± 8.0
PdL₂	**L-Met**	2072 ± 18	35 ± 1.0	-62 ± 3.0
	5'-GMP	830 ± 3	33 ± 2.2	-78 ± 7.0
	Tu	3908 ± 30	32 ± 0.3	-69 ± 1.0
PdL₃	**L-Met**	1363 ± 17	34 ± 0.3	-72 ± 1.0
	5'-GMP	599 ± 4	37 ± 1.0	-68 ± 3.3
	Tu	1072 ± 9	34 ± 1.3	-73 ± 4.2
PdL₄	**L-Met**	486 ± 3	33 ± 1.0	-85 ± 3.3
	5'-GMP	178 ± 3	34 ± 1.0	-90 ± 3.1

[a]Reactions performed in aqua media, 50 μM Tris-HCl buffer (pH = 7.2), and 50 mM NaCl

Comparing the rates of the substitution of the chloride ligands from the complexes by **Tu**, decreases in the order **PdL₁** > **PdL₂** > **PdL₃** > **PdL₄** (Table 3.3). The observed trend in the rate for te reaction with **Tu** applies for the other two nucleophiles. The marked differences in the observed reactivity can be rationalised in terms of the presence of electronic interactions between inert tridentate ligands and Pd(II) metal centre. A comparison of the reactivity of complexes **PdL₁** and **PdL₄** shows that **PdL₁** is ≈ 45 more reactive than **PdL₄** (Table 3.3), attributed to the effective π back-bonding of the in-plane-coordinated pyridine moiety (in **PdL₁**) with non-bonding *d*-electrons that increase electrophilicity of the metal ion [32, 41]. The enhanced π-acceptor ability of **PdL₁**, compared to **PdL₄**, is further evidenced

by the high electrophilicity index of **PdL$_1$** than **PdL$_4$** (Table 3.2). Further, the non-planar geometry of **PdL$_4$** in comparison to **PdL$_1$**- **PdL$_3$** (Figure 3.8) offers a slight steric hindrance between the ipso-hydrogen and the incoming nucleophile, thus lowering its reactivity. In addition, DFT computations support the role of the π-back donation of the pyridyl moiety from the dipole moments of 15.5524 and 11.0864 for **PdL$_1$** and **PdL$_4$**, respectively (Table 3.2). Likewise, the diminution of the HOMO-LUMO energy separation of complexes at ground state [42], illustrates an upward trend as one moves from **PdL$_1$** to **PdL$_4$**, thus confirming the more stable nature of **PdL$_4$** than the other complexes. Overall, DFT calculated data shows higher ionisation potential, high chemical hardness, and smaller $\Delta E_{LUMO–HOMO}$ values for complex **PdL$_4$** compared to the other complexes.

The trend of reactivity of **PdL$_1$-PdL$_3$** is controlled by the basicity of the nature of the benzazole ligands, i.e benzimidazole (conjugate acid, pK_a = 5.56) **PdL$_1$** , benzoxazole (conjugate acid, pK_a = 6.70) **PdL$_2$**, and benzothiazole (conjugate acid, pK_a = 7.30) **PdL$_3$** [43]. Therefore, the pi-acceptor ability of the moieties decreases in the form, benzimidazole > benzoxazole > benzothiazole, signifying that the Pd(II) ion of **PdL$_1$** is the most electron-deficient, while that for **PdL$_3$** is the least electron-attracting. The observed kinetic trend is supported by the DFT data (Table 3.2), indicating the decrease in the negative NBO charges of the heteroatoms from **PdL$_1$** to **PdL$_3$**, leading to a decrease in the removal of electron density from the Pd(II) ion. This is also supported by the electrophilicity indices (Table 3.2) of the complexes which corroborates with the reactivity. In addition, the chemical hardness and electrochemical potentials are also in line with the experimental reactivity trend of the complexes. With respect to the solid-state structures, one would expect a higher rate of substitution of the Cl ligand in **PdL$_4$** due its longer Pd - Cl bond (2.308 (8) Å) in comparison to complexes **PdL$_2$** (Pd - Cl = 2.284 (5) Å) and **PdL$_3$** (Pd-Cl = 2.2998(6) Å). In contrast, the higher reactivity of complexes **PdL$_2$** and **PdL$_3$**, thus implicates nucleophilic attack to the Pd atom as the rate determining step, rather than Pd-Cl breakage, consistent with an associated mode of substitution reactions.

With respect to the incoming biological nucleophile, the reactivity of the three nucleophiles follows the order; **Tu** > **L-Met** > **5'-GMP** (Table 3.3). **Tu** is relatively less sterically demanding in comparisons to **L-Met** > **5'-GMP** nucleophiles (Figure 3.10). The higher reactivity of **L-Met** than **5'-GMP**, can be explained by the presence of sulfur donor atom, which is known to have a higher affinity for soft Pd(II) cation than the nitrogen atom [43]. Notably, lower reactivity exhibited by **5′-GMP** nucleophile, may be ascribed to the presence of the N-donor atom and the steric bulk of the **5′-GMP**.

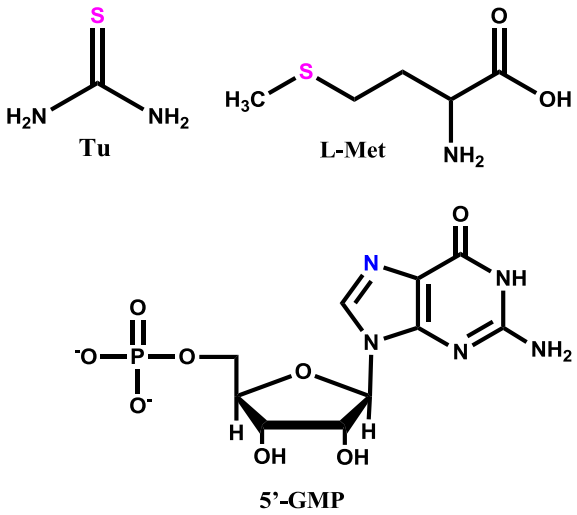

Figure 3.10: Molecuar structures of the nucleophiles.

To determine the activation properties of the substitution process, the reaction temperature was varied from 298 to 328 K at an interval of 10 K. Activation parameters ($\Delta H^{\neq}$ and $\Delta S^{\neq}$) were calculated using the Eyring equation [26]. Typical Eyring plots obtained for complex **PdL_1** are shown in Figure 3.11 and the values of $\Delta H^{\neq}$ and $\Delta S^{\neq}$ are given in Table 3.3. For all the investigated complexes, the activation enthalpies ($\Delta H^{\neq}$) and entropies ($\Delta S^{\neq}$) were positive and negative, respectively. The large sensitivity of the rate constants for the σ-donor properties of the nucleophiles is in tandem with an associative mode of substitution. Furthermore, the activation parameters, ($\Delta H^{\neq} > 0$, $\Delta S^{\neq} < 0$) support an associative mechanism, in agreement with square-planar d^8 metal complexes [44, 45].

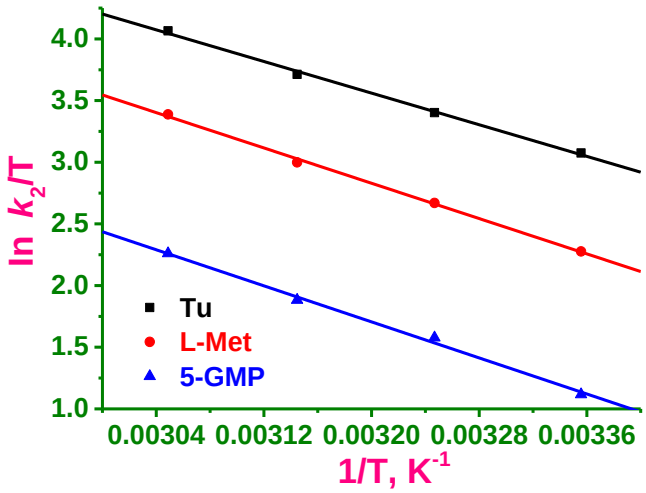

Figure 3.11: Eyring plots for the reaction of **PdL_1** with the nucleophile in aqueous solution, 50 μM Tris-HCl buffer (pH = 7.2), and 50 mM NaCl

3.2.5 CT-DNA interactions

For most metal-based antitumour agents, DNA is a potential pharmacological target, and distortion of the DNA structures are always associated with their antitumour properties [46]. Thus, the study of the interaction of these complexes with DNA can give simulative information which is essential in understanding the mode of tumour inhibition and relate it to the variation in their chemotherapeutic potential. The major tools that are employed to study the binding of the drug molecules with the DNA include UV-visible, fluorescence spectroscopies, circular dichroism, mass spectrometry, electrophoresis, thermal denaturation, viscosity measurements, differential pulse voltammetry, square wave and cyclic voltammetry studies [46]. In this thesis, we have focused on UV–Visible and fluorescence spectroscopies since they are the simplest and most commonly used techniques for investigating the interactions of DNA with other molecules. The interactions of transition metal complexes with DNA double helix occurs *via* both and/or covalent and noncovalent modes [47]. In the the case of covalent bonding, a labile ligand of the complex is replaced by a nitrogen atom of DNA bases such as guanine N7. Conversely, the noncovalent DNA interactions include electrostatic, groove,

and intercalative binding/intercalation of metal complexes outside of DNA helix, along major or minor groove [48, 49].

3.2.5.1 UV-visible absorption measurement

The interactions between metal complexes and duplex CT-DNA were monitored by following the changes in the absorbance upon addition of CT-DNA to a fixed concentration of the Pd(II) complex. A typical graph is given in Figure 3.12 (**PdL$_1$**) for the spectral charges due to the Pd – CT-DNA interactions. The equilibration time for the Pd-CT-DNA spectra was observed to be less than 30 s. The spectral titration curves showed a common hypochromic shift with an increase in CT-DNA concentration. The observed hypochromism may be attributed to π–π stacking interaction between the aromatic chromophore of the complexes and DNA base pairs, consistent with intercalative binding mode, while the red-shift was indicative of the stabilisation of the DNA duplex [50]. The intrinsic binding constants K_b, of complexes were obtained using Wolfe-Shimer equation (6). The K_b values of (0.53-5.53) x 10^6 M^{-1}, Table 3.4, are comparable to those obtained for other metal complexes [50-55], and demonstrate strong intercalative binding mode. The higher K_b values of **PdL$_1$**, **PdL$_2$** and **PdL$_3$** may be assigned to the planarity of the complexes, consistent with the DFT calculations.

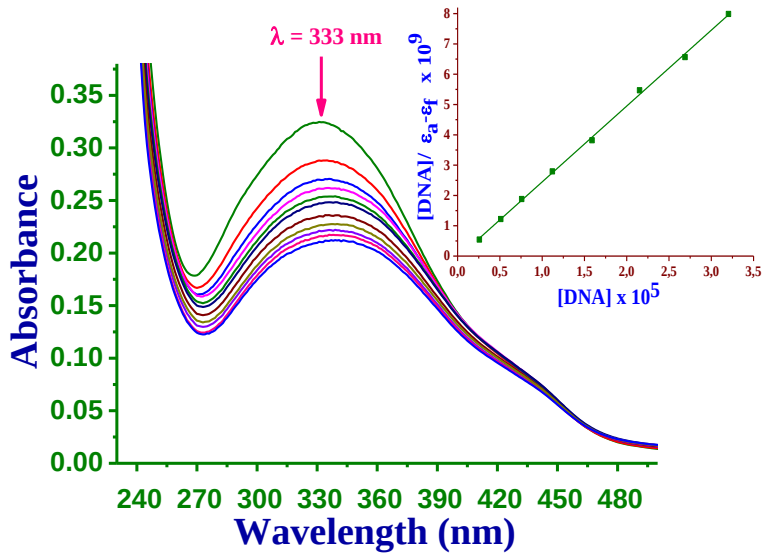

Figure 3.12: Absorption spectra of **PdL₁** complex (20 μM) in Tris-HCl/50 mM buffer at pH 7.2 upon addition of CT-DNA (0 - 40 μM). The arrow shows the change in absorbance upon increasing the CT-DNA concentration. Inset: plot of [CT-DNA] versus [DNA]/(ε_a- ε_f).

Table 3.4: The binding constants and quenching constants for **PdL₁-PdL₄** complexes with CT-DNA

Complex	UV titration	EB fluorescence exchange titration				
	K_b x 10^6, M^{-1}	K_{sv} x 10^4, M^{-1}	K_{app} x 10^6, M^{-1}	k_q x 10^{12}, M^{-1} s^{-1}	K_F x 10^5, M^{-1}	*n*
PdL₁	5.53	5.43 ± 0.21	2.96 ± 0.19	2.36 ± 0.27	16.59 ± 0.13	1.34
PdL₂	2.20	2.84 ± 0.17	1.07 ± 0.15	1.24 ± 0.21	6.88 ± 0.10	1.39
PdL₃	1.01	1.92 ± 0.13	0.80 ± 0.09	0.84 ± 0.14	0.44 ± 0.08	1.00
PdL₄	0.53	0.54 ± 0.08	0.16 ± 0.03	0.23 ± 0.10	0.09 ± 0.19	1.17

Intrinsic binding constant, K_b is given in M^{-1}; stern-volmer quenching constant, K_{sv} expressed in M^{-1}; apparent binding constant, K_{app} given in M^{-1}; bimolecular quenching rate constant, k_q provided in $M^{-1}s^{-1}$ binding constant, K_F presented in M^{-1}; and number of DNA binding sites, n.

3.2.5.2 Competitive CT-DNA-EB binding studies

To further support the interaction mode of the complexes with DNA, competitive binding studies were performed by following the quenching of the fluorescence emission intensity of CT-DNA-EB complex after each addition of the Pd(II) complex. A typical fluorescence emission graph of EB-DNA in the absence and presence of complex **PdL$_1$** is presented in Figure 3.13a. In all cases, the intensity of emission was quenched with a notable red shift of λ_{max}, pointing to the existence of strong intercalative binding to CT-DNA. The Stern-Volmer quenching constant, K_{sv} and bimolecular quenching rate constant k_q were calculated from the Stern-Volmer equation (8). Representatives plots for complex **PdL$_1$** are shown in Figure 3.13b, and the values of the binding constants for the complexes are provided in Table 3.4. The K_{sv} values of (0.54-5.43) x 10^4 M^{-1}, suggest that EB are efficiently replaced by the complexes through intercalative binding [22, 50], and the values are comparable to those of similar Pd-complexes. The apparent binding affinity constant, K_{app}, was computed from equation (9) and the values are provided in Table 3.4. The values of K_{app}, (10^5-10^6 M^{-1}), are lower than those of classical intercalators (10^7 M^{-1}) [56], implying intercalative binding mode. The k_q values (10^{11}-10^{12} M^{-1} s^{-1}), are higher than those of strong biopolymer fluorescence quenchers (10^{10} M^{-1} s^{-1}), indicating that the complexes quench EB fluorescence statically rather than dynamically [57]. DNA binding constant, K_F and the number of binding sites per nucleotide, *n* were computed from the Scatchard equation (10). Representatives straight-line plots of **PdL$_1$** are presented in Figure 3.13c, and the results are given in Table 3.4. The computed K_F values (1.00-16.59) x 10^5 M^{-1}, illustrate strong intercalative mode of binding. The *n* values obtained for all the complexes were approximately equal to 1, demonstrating that the complexes bind to CT-DNA in a 1:1 mole ratio. EB, which shows a K_F of ~ 10^5 M^{-1}, was assumed to occupy more than one DNA binding site [58]. The magnitude of the binding constants and quenching rate constants decrease according to the ability of the complexes to displace EB of the base pairs and followed the trend **PdL$_1$** > **PdL$_2$** > **PdL$_3$** > **PdL$_4$**. Complex **PdL$_4$** displayed the lowest binding affinity, consistent with the DNA binding data described *vide supra*.

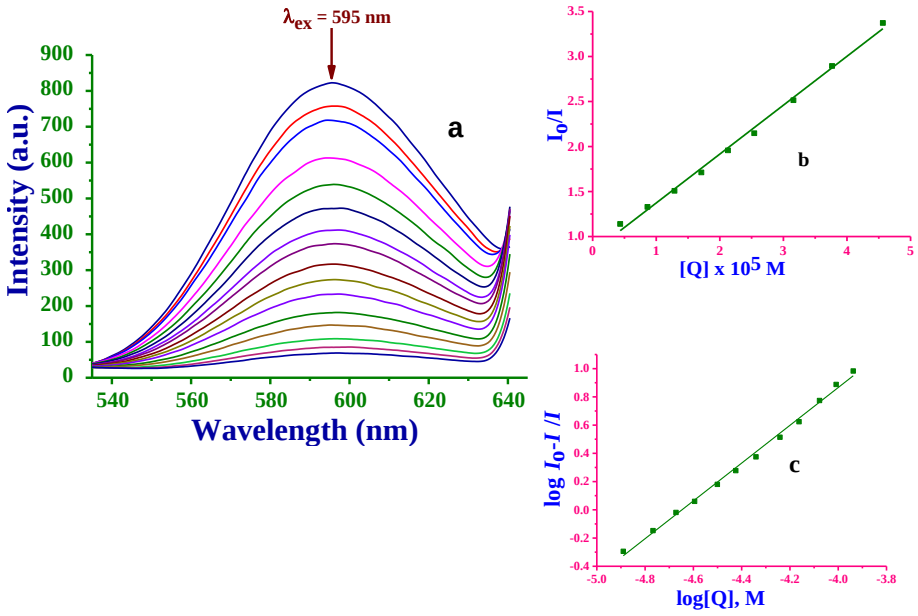

Figure 3.13: (**a**); Fluorescence emission spectra of EB bounded to CT-DNA in the presence of **PdL₁**: [EB] = 6.5 µM, [CTDNA] = 6.5 µM and [**PdL₁**] = 0-200 µM. The arrow shows the intensity changes upon increasing the **PdL₁** complex concentration. **(b)**; Stern-Volmer plot of I_o/I versus [Q]. **(c)**; Scatchard plot of log[(I_o–I)/I] versus log[Q].

3.2.6 Molecular docking with B-DNA

To further elucidate the observed spectroscopic binding trends of **PdL₁-PdL₄**, molecular docking simulations were performed to determine the minimum energy of DNA-complex structure and the preferred binding site and best orientation of the complexes (Figure 3.14). The complexes were docked onto B-DNA and the minimum energy of the docked poses for **PdL₁-PdL₄** revealed that the complexes fitted into the curved contours of the B-DNA located in the G–C (~13.4 Å) bases sequence. The best orientation for the complexes is within the minor DNA groove, and thus depicting minor groove binding. The observation contradicts the experimental results that suggest an intercalative mode of DNA binding, proving the challenge with the docking method in the prediction of ligands (i.e. metal complexes) proper orientation inside a binding site. The minimised free energies of the docked structures of complexes **PdL₁**, **PdL₂**, **PdL₃**, and **PdL₄** were found to be -270.07, -268.81, -266.11 and

-263.96 kJ mol^{-1}, respectively (Figure 3.14). The observation is consistent with the DNA binding propensity of the complexes (Table 3.5).

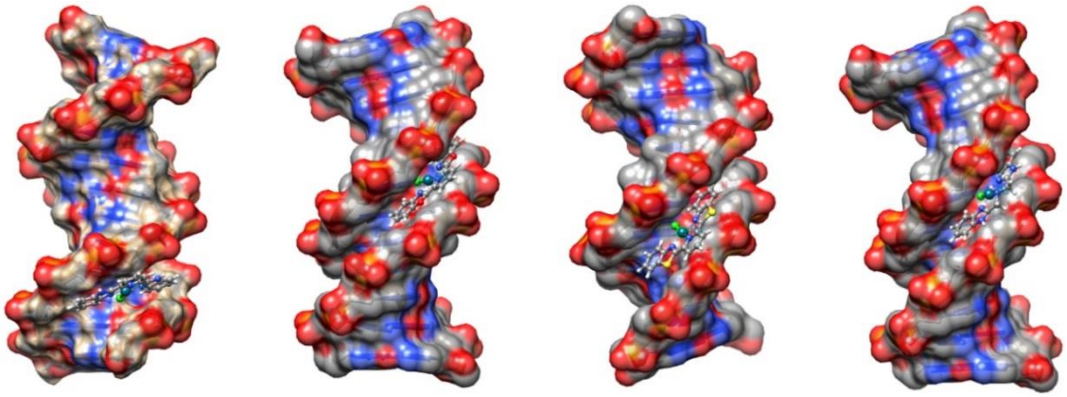

PdL_1 **PdL_2** **PdL_3** **PdL_4**

Figure 3.14: Computational docking models illustrating the interactions of **PdL_1**, **PdL_2**, **PdL_3**, and **PdL_4** with B-DNA duplex, with docking score of -270.07, -268.81, -266.11, and -263.96 Kcal/Mol, respectively and thus indicating a positive correlation between the simulated and experimental results.

3.2.7 Anti-tumour properties of complexes PdL_1-PdL_4

3.2.7.1 Cytotoxic activities of cisplatin and the complexes PdL_1-PdL_4 against HeLa, MRC5-SV2 and MRC5 cells

The cytotoxicities of Pd(II) complexes and cisplatin (used as a reference drug) were investigated in two malignant cell lines (HeLa, MRC5-SV2) and in a healthy cell line (MRC5) using the MTT assay, following up to 48 h of treatment (Figures 3.15-3.16, and Table 3.5). Notewothy, the complexes were found to be very stable in the DMSO media, evidence by the solid-state structure of complex **PdL_4** (obtained by slow diffusion of diethyl ether into concentrated solution of the complex in DMSO). Figure 3.15 shows the effects of complexes **PdL_1-PdL_4** and cisplatin on the viability of HeLa, MRC5-SV2 and MRC5 cells, while Figure 3.16 depicts morphological damage to each of the cell lines, using cisplatin as the standard drug control. Cisplatin and the complexes (6.25–100 µM) each reduced the

viability of each of the three cell lines in a concentration-dependent manner (Figure 3.15). In addition, we confirmed that the effects of both cisplatin and **PdL$_1$** were also time-dependent, as the reductions in viability at 48 h were significantly higher than at 24 h (Figure 3.15a and 3.15c). In fact, at 25, 50 and 100 μM concentrations, both cisplatin and **PdL$_1$** revealed profound differences between their toxic effects at 24 h and at 48 h, with toxic effects (indicated by reduction in viability) at 48 h almost double or triple those at 24 h. The three cell lines exhibited differential sensitivities to cisplatin and the Pd(II) complexes. Based on the calculated IC_{50} values (Table 3.5), cisplatin was equipotent (IC_{50} of 11.4 μM) in its toxicity against the cancer cells lines HeLa and MRC5-SV2, while it was less cytotoxic against the normal cell line MRC5. The IC_{50} of **PdL$_1$** for the HeLa cells (16.3 ± 4.9) was not statistically significantly different from that of cisplatin, demonstrating the equipotency of **PdL$_1$** and cisplatin against the HeLa cell. However, all the four complexes were less potent than cisplatin against the MRC5-SV2 cell, with **PdL$_1$** being twice less potent than cisplatin. **PdL$_2$**, **PdL$_3$** and **PdL$_4$** were each much less potent than **PdL$_1$** or cisplatin against the HeLa cell (four-, five- and nearly 5-fold less potent, respectively, compared to **PdL$_1$**), whereas **PdL$_2$** and **PdL$_3$** were almost equipotent with **PdL$_1$** against the MRC5-SV2 cell, and **PdL$_4$** was only one-and-a-half times less potent than **PdL$_1$** against the MRC5-SV2 cell. The orders of potencies against HeLa and MRC5-SV2 cells, respectively, are **PdL$_1$** > **PdL$_2$** > **PdL$_4$** > **PdL$_3$** and **PdL$_3$** > **PdL$_2$** > **PdL$_1$** > **PdL$_4$**.

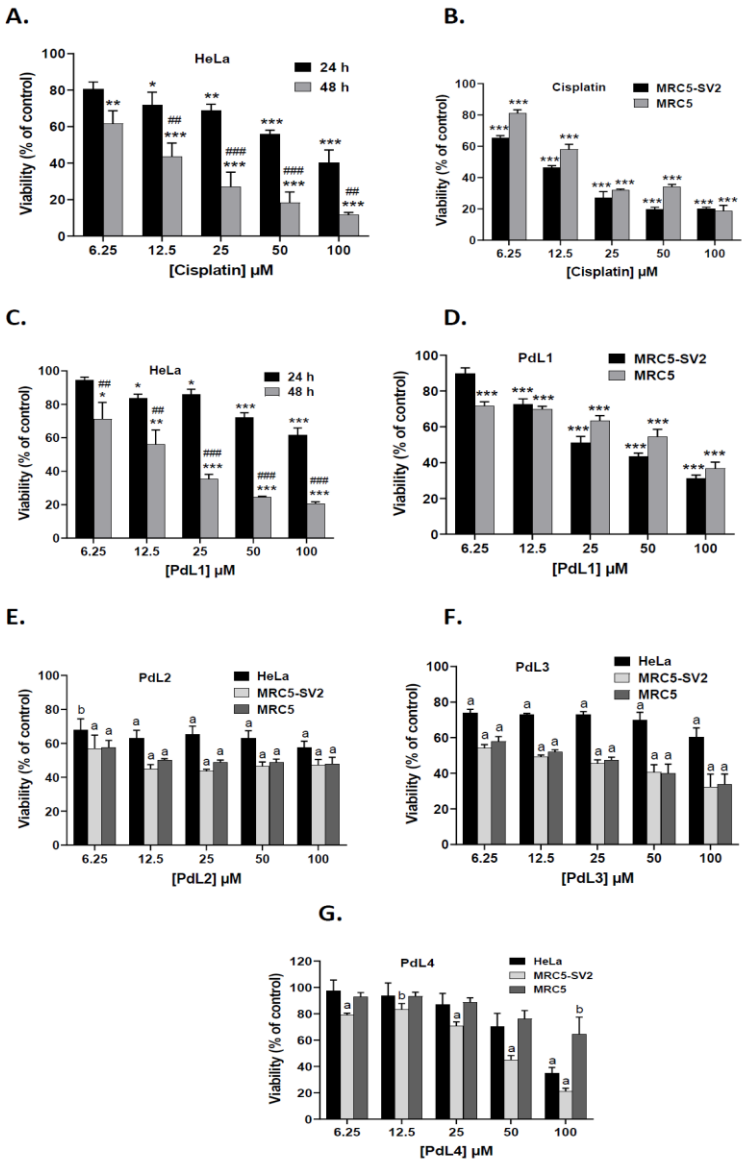

Figure 3.15: Effects of complexes **PdL₁-PdL₄** and cisplatin on the viability of HeLa, MRC5-SV2 and MRC5 cells. (a) Concentration-dependent effects of cisplatin on HeLa cell viability. (b) Effects of 48 h treatment with cisplatin on the viability of MRC5-SV2 and MRC5 cells. (c) Concentration-dependent effects of **PdL₁** on HeLa cell viability. (d) Effects of 48 h treatment with **PdL₁** on the viability of MRC5-SV2 and MRC5 cells. (e) Effects of 48 h treatment with **PdL₂** on the viability of HeLa, MRC5-SV2 and MRC5 cells. (f) Effects of 48 h treatment with **PdL₃** on the viability of HeLa, MRC5-SV2 and MRC5 cells. (g) Effects of 48 h treatment with **PdL₄** on the viability of HeLa, MRC5-SV2 and MRC5 cells. Each value is expressed as Mean ± SEM of 3 or 4 independent experiments. *P<0.05, **P<0.01 (or ^{b}P<0.01) and ***P<0.001 (or ^{a}P<0.001) compared to the negative control; ##P<0.01 and ###P<0.001 for the comparison of the effects at 24 h and 48 h.

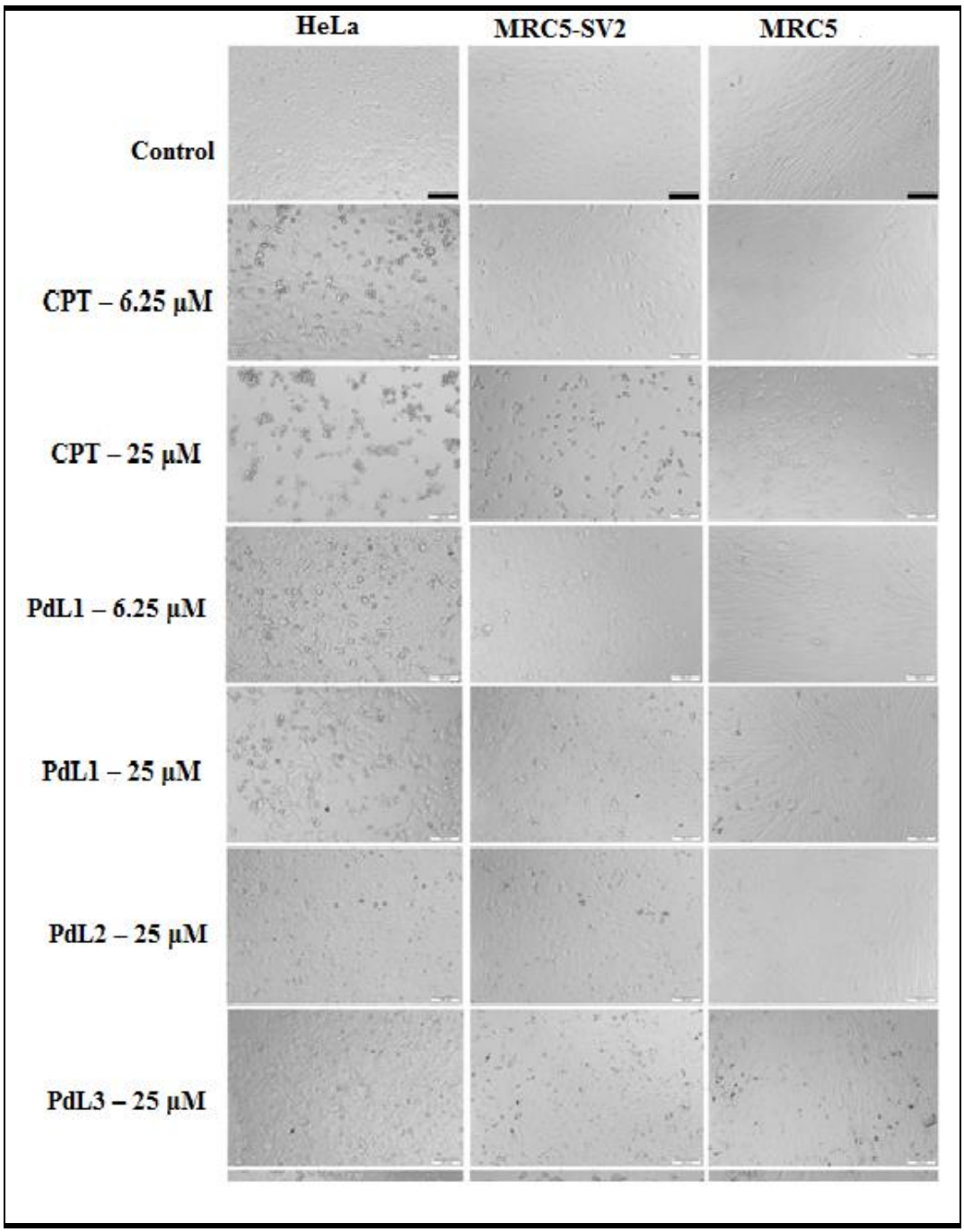

Figure 3.16: Morphological damages for each of the cell lines

Overall, **PdL_4** exhibited the least cytotoxic effects on the tumour cell lines (not much different to **PdL_2** or **PdL_3** in its effect against HeLa, but about twice less potent than **PdL_1-PdL_3** against MRC5-SV2). The presence of the pyridyl rings in **PdL_1-PdL_3** is thought to increase the hydrophobicity of the **PdL_1-PdL_3** complexes and could have eased their passage through the cell membrane to allow more

complexes into the cells [59]. However, the reduced toxicity of **PdL$_4$** suggests that the removal of a pyridine ring (reduced number of conjugation) on the inert ligand architecture leads to a decrease in cytotoxic (anti-tumour) activity [60]. The lower cytotoxic activity of **PdL$_4$** could also be due to the steric hindrance caused by methylene moiety, as illustrated by the planarity diagram in DFT (Figure 3.8) and lower DNA binding constants (Table 3.4). The minimal cytotoxicity of **PdL$_4$** could also be attributed to its slower ligand exchange kinetic behaviour, since the complex was the least reactive as per the kinetics data in Table 3.3 [33].

Table 3.5: Cytotoxic potencies and cancer-cell selectivities of cisplatin and **PdL$_1$-PdL$_4$**

	IC_{50} (μM)			
	HeLa	**MRC5-SV2**	**MRC5**	**Selectivity Index (SI)**
Cisplatin	11.4 ± 3.5	11.4 ± 0.5	18.7 ± 1.3	1.6
PdL$_1$	16.3 ± 4.9	25.0 ± 0.3	37.3 ± 0.2	1.5
PdL$_2$	70.3 ± 16.6	21.1 ± 4.0	26.1 ± 3.3	1.2
PdL$_3$	88.4 ± 21.5	18.5 ± 2.6	20.5 ± 1.9	1.1
PdL$_4$	73.6 ± 7.0	39.8 ± 3.4	96.8 ± 0.7	2.4

IC_{50} values, rank orders of cytotoxic potencies and selectivity indices (SI) for cisplatin (as the standard) and **PdL$_1$-PdL$_4$** against two cancer cell lines (HeLa and MRC5-SV2 cells) and a normal (healthy) cell line (MRC5) that is parental to the MRC5-SV2 cell. SI is calculated as a ratio of the IC_{50} for the compound against the normal cell line (MRC5) and its IC_{50} against the cancer cell line (MRC5-SV2). Each IC_{50} value is expressed as Mean ± SEM.

As a major goal in chemotherapy is to selectively target cancer cells while relatively sparing normal cells, we assessed the cancer-cell selectivity of cisplatin and the complexes, based on the Selectivity Index (SI) parameter. As shown in Table 3.5, both cisplatin and **PdL$_1$** had similar SI values of 1.6 and 1.5, respectively, which depicts that they are almost twice as potent in killing cancer cells as they are in killing normal cells. Of all compounds tested, **PdL$_4$** had the highest SI (2.4), which could be attributed to its low potency in general. On the other hand, both **PdL$_2$** and **PdL$_3$** yielded very low SI values (1.2

and 1.1, respectively), suggesting that they had little selectivity for cancer cells over normal cells and are thus, in drug discovery context, not optimal in their current forms for therapeutic applications. In general, among the Pd(II) complexes investigated, the effects of the complexes on cell viability and their cancer-cell selectivities reveal **PdL$_1$** as the most promising compound.

3.2.7.2 ROS generation as potential mechanism for the cytotoxicity of complexes

Cytotoxic and chemotherapeutic compounds could engage a variety of mechanisms to induce their cytotoxicity in cancer and normal cells, including the generation of significant levels of reactive oxygen species (ROS) within the cell [61]. The ROS could trigger a host of downstream toxic responses culminating in cell death, including damage to lipids, proteins and DNA [62]. For example, cisplatin chemotherapy generates oxidative stress in normal cells, which is responsible for its non-specific toxicity. We, therefore, explored, using HeLa cells, whether the complexes could induce significant ROS levels intracellularly. Interestingly, contrary to previous reports [63], we did not find any evidence within our experimental system that the reduction in cell viability (toxicity) induced by cisplatin was dependent on its generation of a significant level of ROS (Table 3.6), as the ROS levels at 3 h and 24 h following treatment with cisplatin up to 100 µM were not different from the basal ROS level (Table 3.6). This suggests that cisplatin's toxicity could depend on contributions from ROS-dependent and independent processes, a phenomenon which could depend on other factors including the cellular environment. Similarly, **PdL$_1$** did not initially have any effect on basal ROS level (3 h) but decreased (at 25 µM and 100 µM) basal ROS level at 24 h (Table 3.6), a time point at which it had begun to elicit moderate but significant toxic effects, thus presenting a conundrum. We opine that, for **PdL$_1$**, cytotoxic mechanisms other than raised levels of ROS might operate in a much greater proportion that overwhelms any beneficial and, perhaps, transient anti-ROS effect induced by **PdL$_1$**, thus resulting in a net toxic effect.

Complexes **PdL$_2$** and **PdL$_4$** did not have any significant effect on intracellular ROS levels. While **PdL$_3$** was five times less potent than **PdL$_1$** in its toxicity against the HeLa cell, it was the only complex that induced a significant increase in intracellular ROS. At 100 µM, **PdL$_3$** increased ROS level significantly and relatively quite early on in the treatment (3 h), nearly doubling ROS level compared to the basal (control) level, an effect that was sustained up to the much later 24 h time point. This clearly indicates that the generation of ROS contributes to the cytotoxicity of **PdL$_3$**, unlike was the case for the other complexes. We, therefore, on the basis of ROS, identified the four complexes as belonging to two mechanistic groups: one which induces cytotoxicity through ROS, and the other whose cytotoxicity is rather ROS-independent.

Table 3.6: Changes to intracellular ROS levels induced by cisplatin and **PdL$_1$-PdL$_4$**

	Intracellular Reactive Oxygen Species (ROS) levels (fold change vs. control)					
	3 h			**24 h**		
	6.25µM	**25µM**	**100µM**	**6.25µM**	**25µM**	**100µM**
Cisplatin	1.1 ± 0.1	1.1 ± 0.1	1.1 ± 0.1	0.8 ± 0.1	0.7 ± 0.1	0.7 ± 0.1
PdL$_1$	1.1 ± 0.0	1.0 ± 0.0	1.1 ± 0.1	0.9 ± 0.0	0.7 ± 0.0*****	0.6 ± 0.0*******
PdL$_2$	1.1 ± 0.1	1.2 ± 0.0	1.2 ± 0.1	1.0 ± 0.0	0.9 ± 0.0	1.1 ± 0.1
PdL$_3$	1.1 ± 0.1	1.4 ± 0.1	1.8 ± 0.2*****	1.0 ± 0.0	1.1 ± 0.0	1.7 ± 0.2*****
PdL$_4$	1.0 ± 0.0	1.1 ± 0.1	1.3 ± 0.1	0.8 ± 0.1	0.9 ± 0.1	1.1 ± 0.2

Effects of cisplatin and complexes **PdL1-PdL4** on the intracellular levels of reactive oxygen species (ROS) as measured by DCFDA. Following treatment of HeLa cells with the indicated compounds, the fluorescence of DCFDA was read at 3 h and 24 h at an excitation wavelength of 485 nm and an emission wavelength of 535 nm (fluorescein). Values represent Mean ± SEM (n=3 or 4 independent experiments) of fold change in ROS levels (compared to the negative control that was set to unity). Values are rounded up to 1 decimal place. *P<0.05, ***P<0.001 compared to the control.

3.2.7.3 Nature of cell death induced by cisplatin and PdL$_1$

Cytotoxic or chemotherapeutic agents induce cellular damage, which could result in one or, more usually, a combination of some of the various forms of cell death, including but not limited to apoptosis and necrosis [64]. We, therefore, investigated the potential proportions of apoptosis or necrosis in the cell death induced by **PdL$_1$**, the most promising of the complexes, and cisplatin. The cultured HeLa cells were treated with either cisplatin or **PdL$_1$** in the absence or presence of a chemical inhibitor of apoptosis or necrosis. The inhibitor of apoptosis used, Z-VAD-fmk, blocks caspases, which mediate apoptosis, while DPQ, an inhibitor of the enzyme poly (ADP-ribose) polymerase (PARP), blocks parthanatos (PARP-1-dependent cell death) [65], now considered a type of programmed necrosis [66]. The results are as presented in Figure 3.17.

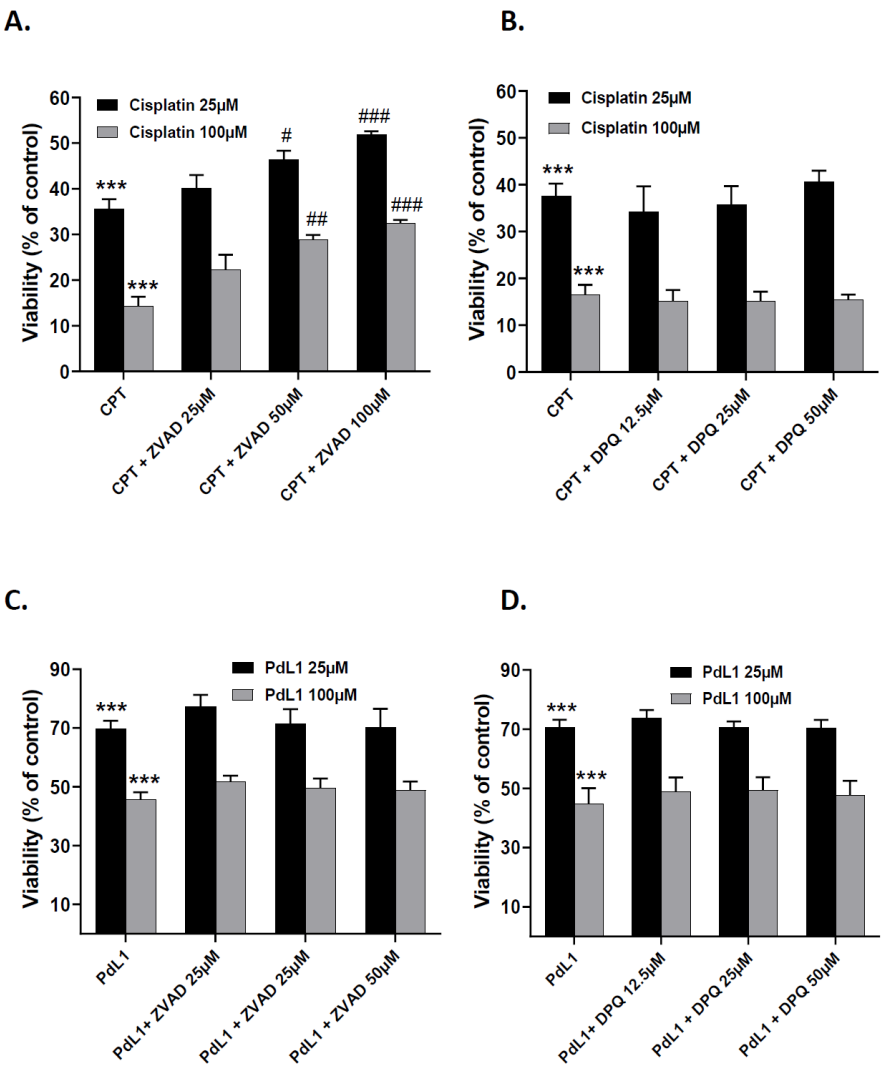

Figure 3.17: Induction of apoptotic or necrotic cell death by cisplatin (CPT) and **PdL$_1$** (48 h treatment). (A) Concentration-dependent protective effects of the pan-caspase inhibitor, Z-VAD-fmk (25 -100 μM), against the cytotoxic effect of low (25 μM) and high (100 μM) concentration of cisplatin. (B) Lack of effect of the PARP inhibitor, DPQ (12.5 – 50 μM), against the cytotoxic effect of low (25μM) and high (100 μM) concentration of cisplatin. (C) Lack of effect of the pan-caspase inhibitor, Z-VAD-fmk (25 - 100 μM), against the cytotoxic effect of low (25 μM) and high (100 μM) concentration of **PdL$_1$**. (D) Lack of effect of the PARP inhibitor, DPQ (12.5 – 50 μM), against the cytotoxic effect of low (25μM) and high (100 μM) concentration of **PdL$_1$**. Each value is expressed as Mean ± SEM of 3 independent experiments. ***P<0.001 compared to the negative control; #P<0.05, ##P<0.01 and ###P<0.001 compared to CPT alone or **PdL$_1$** alone.

The cytotoxic effects of cisplatin, whether at a low or a high concentration, were significantly ameliorated by the pan-caspase inhibitor, Z-VAD-fmk, but not affected by the PARP inhibitor DPQ, suggesting that, at least, the cell death induced by cisplatin was significantly apoptotic in nature, with little evidence of necrosis, consistent with earlier reports [67]. On the other hand, the cytotoxic effects of **PdL$_1$** were not affected by the inhibitors, implying that caspase-dependent apoptosis and PARP-dependent programmed necrosis of parthanatos might not play a significant role in **PdL$_1$**-induced cell death, at least within the context of our experimental system. The differences both in the cell death mechanisms predominantly engaged by cisplatin and **PdL$_1$** and in the manner of their inducing changes to, or not affecting, intracellular ROS levels, support the establishment of the fact that cisplatin and **PdL$_1$** do not share exactly the same mechanisms of action. This could be advantageous in the development of novel metallodrugs that are endowed with toxic mechanisms dissimilar to those of cisplatin.

3.3. Conclusions

Palladium(II) complexes of tridentate bis(benzazole) ligands have been synthesised and structurally characterised. The solid-state structure of the complexes **PdL$_1$**-**PdL$_4$** established a tridentate coordination mode of the ligands to give square planar complexes. The rates of substitution kinetics of the Pd(II) complexes were mainly controlled by the electronic properties of the auxiliary ligands and incoming nucleophile, with **PdL$_1$** demonstrating the highest reactivity, while **PdL$_4$** showing the lowest kinetic reactivity. DFT calculations supported the reactivity trends. The calculated values of activation parameters of the complexes, ($\Delta H^{\neq} > 0$, $\Delta S^{\neq} < 0$) suggest an associative mode of activation. The results of DNA experiments indicate intercalative binding mode, in contrary to the molecular docking which depicts groove binding. The experimental binding strength which is in the form **PdL$_1$** > **PdL$_2$** > **PdL$_3$** > **PdL$_4$**, is consistent with the simulated binding energies. Complex **PdL$_1$** displayed cytotoxic potency and selectivity comparable to those of cisplatin. Only **PdL$_3$** significantly increased ROS levels while

PdL$_4$ was the most cancer cell-selective but the least potent. There was no evidence that **PdL$_1$** induces significant apoptotic cell death, unlike cisplatin. Complexes **PdL$_1$** and **PdL$_2$** showed good correlations on the rates of substitution kinetics, DNA binding affinities and cytotoxicity activities, thus providing evidence on the use of substitution kinetics and DNA binding studies to probe the cytotoxicity of these types of Pd(II) complexes.

3.4 References

[1] S. Dilruba, G.V. Kalayda, Cancer Chemother. Pharmacol. 77 (2016) 1103-1124.

[2] A. Khan, R. Rashid, G. Murtaza, A. Zahra, Trop. J. Pharm. Res. 13 (2014) 1169-1177.

[3] H. Zhao, T. Bi, Z. Qu, J. Jiang, S. Cui, Y. Wang, Oncol. Rep. 32 (2014) 1003-1012.

[4] C.J. Jones, J.R. Thornback, Medicinal applications of coordination chemistry, Royal Society of Chemistry, 2007.

[5] E. Tiekink, Inflammopharmacology 16 (2008) 138-142.

[6] G. Gasser, N. Metzler-Nolte, Curr. Opin. Chem. Biol. 16 (2012) 84-91.

[7] E. Alessio, Bioinorganic medicinal chemistry, John Wiley & Sons 2011.

[8] J. Yellol, S.A. Pérez, A. Buceta, G. Yellol, A. Donaire, P. Szumlas, P.J. Bednarski, G. Makhloufi, C. Janiak, A. Espinosa, J. Med. Chem. 58 (2015) 7310-7327.

[9] A. Zamora, C.A. Denning, D.K. Heidary, E. Wachter, L.A. Nease, J. Ruiz, E.C. Glazer, Dalton Trans. 46 (2017) 2165-2173.

[10] T. Zou, C.-N. Lok, P.-K. Wan, Z.-F. Zhang, S.-K. Fung, C.-M. Che, Curr. Opin. Chem. Biol. 43 (2018) 30-36.

[11] A.A. Fathy, I.S. Butler, M.A. Elrahman, B.J. Jean-Claude, S.I. Mostafa, Inorg. Chim. Acta. 473 (2018) 44-50.

[12] R. Kanaoujiya, M. Singh, J. Singh, S. Srivastava, J. Sci. Res. 64 (2020) 264-268

[13] V. Vidimar, C. Licona, R. Cerón-Camacho, E. Guerin, P. Coliat, A. Venkatasamy, M. Ali, D. Guenot, R. Le Lagadec, A.C. Jung, Cancer letters 440 (2019) 145-155.

[14] N. Mirzadeh, T.S. Reddy, S.K. Bhargava, Coord. Chem. Rev. 388 (2019) 343-359.

[15] C.K. Adokoh, RSC Adv. 10 (2020) 2975-2988.

[16] H. Zhang, F. Xie, M. Cheng, F. Peng, J. Med. Chem. 62 (2019) 6985-6991.

[17] L. Noriega, M.E. Castro, J.M. Perez-Aguilar, N.A. Caballero, B.L. Sanchez-Gaytan, E. González-Vergara, F.J. Melendez, J. Inorg. Biochem. 203 (2020) 110862.

[18] H. Mansouri-Torshizi, S. Shahraki, Z.S. Nezami, A. Ghahghaei, S. Najmedini, A. Divsalar, H. Ghaemi, A.-A. Saboury, Complex Metals, 1 (2014) 23-31.

[19] C. Icsel, V.T. Yilmaz, Y. Kaya, H. Samli, W.T. Harrison, O. Buyukgungor, Dalton Trans. 44 (2015) 6880-6895.

[20] K.A. Abu-Safieh, A.S. Abu-Surrah, H.D. Tabba, H.A. AlMasri, R.M. Bawadi, F.M. Boudjelal, L.H. Tahtamouni, J. Chem. (2016).

[21] J. Haribabu, C. Balachandran, M.M. Tamizh, Y. Arun, N.S. Bhuvanesh, S. Aoki, R. Karvembu, J. Inorg. Biochem. (2020) 110988.

[22] X. Wei, Y. Yang, J. Ge, X. Lin, D. Liu, S. Wang, J. Zhang, G. Zhou, S. Li, J. Inorg. Biochem. 202 (2020) 110857.

[23] L. Fuentes, A.G. Quiroga, J.A. Organero, A.I. Matesanz, J. Inorg. Biochem. 203 (2020) 110875.

[24] M.N. Zafar, S. Masood, T.S.T. Muhammad, A.F. Dalebrook, M.F. Nazar, F.P. Malik, E.U. Mughal, L.J. Wright, Dalton Trans. 48 (2019) 15408-15418.

[25] T.T.H. Fong, C.N. Lok, C.Y.S. Chung, Y.M.E. Fung, P.K. Chow, P.K. Wan, C.M. Che, Angew. Chem. Int. Ed. 55 (2016) 11935-11939.

[26] J.D. Atwood, Inorganic and organometallic reaction mechanisms, VCH Publishers, 1997.

[27] N.P. Barry, P.J. Sadler, Chem. Commun. 49 (2013) 5106-5131.

[28] B. Lippert, Cisplatin: chemistry and biochemistry of a leading anticancer drug, John Wiley & Sons, 1999.

[29] Y. Li, Z. Gu, C. Zhang, S. Li, L. Zhang, G. Zhou, S. Wang, J. Zhang, Eur. J. Med. Chem. 144 (2018) 662-671.

[30] M.M. Milutinović, A. Rilak, I. Bratsos, O. Klisurić, M. Vraneš, N. Gligorijević, S. Radulović, Ž.D. Bugarčić, J. Inorg. Biochem. 169 (2017) 1-12.

[31] P. Čanović, A.R. Simović, S. Radisavljević, I. Bratsos, N. Demitri, M. Mitrović, I. Zelen, Ž.D. Bugarčić, JBIC J. Biol. Inorg. Chem. 22 (2017) 1007-1028.

[32] D. Ćoćić, S. Jovanović, S. Radisavljević, J. Korzekwa, A. Scheurer, R. Puchta, D. Baskić, D. Todorović, S. Popović, S. Matić, J. Inorg. Biochem. 189 (2018) 91-102.

[33] R.O. Omondi, D. Jaganyi, S.O. Ojwach, A.A. Fatokun, Inorg. Chim. Acta. 482 (2018) 213-220.

[34] A.W. Addison, P.J. Burke, J. Heterocycl. Chem. 18 (1981) 803-805.

[35] P. Kopel, D. Wawrzak, V. Langer, K. Cihalova, D. Chudobova, R. Vesely, V. Adam, R. Kizek, Molecules 20 (2015) 10360-10376.

[36] S.O. Ojwach, I.A. Guzei, J. Darkwa, S.F. Mapolie, Polyhedron 26 (2007) 851-861.

[37] W.M. Motswainyana, M.O. Onani, S.O. Ojwach, B. Omondi, Inorg. Chim. Acta. 391 (2012) 93-97.

[38] L. Yang, D.R. Powell, R.P. Houser, Dalton Trans. (2007) 955-964.

[39] I.J. Bruno, J.C. Cole, M. Kessler, J. Luo, W.S. Motherwell, L.H. Purkis, B.R. Smith, R. Taylor, R.I. Cooper, S.E. Harris, J Chem Inform Comput Sci. 44 (2004) 2133-2144.

[40] F.H. Allen, Crystallogr. B 58 (2002) 380-388.

[41] M. Kosović, S. Jovanović, G.A. Bogdanović, G. Giester, Ž. Jaćimović, Ž.D. Bugarčić, B. Petrović, J Coord Chem. 69 (2016) 2819-2831.

[42] A. Mambanda, D. Jaganyi, Adv Inorg Chem 70 (2017) 243-276.

[43] R. Notario, M., Herreros, E. Ballesteros, M. H. Essefar, J. L. M., Abboud, I. D . Sadekov, J. Elguero, J. Chem. Soc. Perkin Trans. 11 (1994) 2341-2344.

[44] R. Van Eldik, T. Asano, W. Le Noble, Chem. Rev. 89 (1989) 549-688.

[45] M. Tobe, J. Burgess, Inorganic reaction mechanisms, Essex, Addison Wiley, 1999

[46] M. Sirajuddin, S. Ali, A. Badshah, J. Photochem. Photobiol. B. 124 (2013) 1-19.

[47] S.U. Rehman, T. Sarwar, M.A. Husain, H.M. Ishqi, M. Tabish, Arch. Biochem. Biophys. 576 (2015) 49-60.

[48] S. Mondal, M. Chakraborty, A. Mondal, B. Pakhira, A.J. Blake, E. Sinn, S.K. Chattopadhyay, New J. Chem. 42 (2018) 9588-9597.

[49] R. Palchaudhuri, P.J. Hergenrother, Curr. Opin. Biotechnol. 18 (2007) 497-503.

[50] R. Bellam, D. Jaganyi, A. Mambanda, R. Robinson, M.D. BalaKumaran, RSC Adv. 9 (2019) 31877-31894.

[51] R.K. Vuradi, K. Dandu, P.K. Yata, R.R. Mallepally, N. Chintakuntla, R. Ch, S.S. Thakur, C.M. Rao, S. Satyanarayana, New J. Chem. 42 (2018) 846-859.

[52] S. De, S.R. Chaudhuri, A. Panda, G.R. Jadhav, R.S. Kumar, P. Manohar, N. Ramesh, A. Mondal, A. Moorthy, S. Banerjee, New J. Chem. 43 (2019) 3291-3302.

[53] M. Howe-Grant, K.C. Wu, W.R. Bauer, S.J. Lippard, Biochemistry 15 (1976) 4339-4346.

[54] G.K. Mutua, R. Bellam, D. Jaganyi, A. Mambanda. J Coord Chem. 72 (2019) 2931-2956.

[55] E. Sindhuja, R. Ramesh, N. Dharmaraj, Y. Liu, Inorg. Chim. Acta. 416 (2014) 1-12.

[56] M. Cory, D.D. McKee, J. Kagan, D. Henry, J.A. Miller, J. Am. Chem. Soc. 107 (1985) 2528-2536.

[57] I. Mitra, S. Mukherjee, B. Misini, P. Das, S. Dasgupta, W. Linert, S.C. Moi, New J. Chem. 42 (2018) 2574-2589.

[58] R.R. Monaco, J. Biomol. Struct. Dyn. 25 (2007) 119-125.

[59] Z. Liu, A. Habtemariam, A.M. Pizarro, S.A. Fletcher, A. Kisova, O. Vrana, L. Salassa, P.C. Bruijnincx, G.J. Clarkson, V. Brabec, J. Med. Chem. 54 (2011) 3011-3026.

[60] M. Tian, J. Li, S. Zhang, L. Guo, X. He, D. Kong, H. Zhang, Z. Liu, Chem. Commun., 53 (2017) 12810-12813.

[61] S. Mukherjee, I. Mitra, P. Das, B. Misini, W. Linert, S.C. Moi, ChemistrySelect, 3 (2018) 3871-3885.

[62] A.A. Fatokun, T.W. Stone, R.A. Smith, Front. Biosci. 13 (2008) 3288-3311.

[63] W. Yu, Y. Chen, J. Dubrulle, F. Stossi, V. Putluri, A. Sreekumar, N. Putluri, D. Baluya, S.Y. Lai, V.C. Sandulache, Sci. Rep. 8 (2018) 1-12.

[64] A. Tkachenko, A. Onishchenko, V. Gopkalov, T. Gorbach, E. Kharchenko, D. Sklyaruk, JMBS 4 (2019) 32–37

[65] A.A. Fatokun, V.L. Dawson, T.M. Dawson, Br. J. Pharmacol. 171 (2014) 2000-2016.

[66] L. Galluzzi, I. Vitale, S.A. Aaronson, J.M. Abrams, D. Adam, P. Agostinis, E.S. Alnemri, L. Altucci, I. Amelio, D.W. Andrews, Cell Death Differ. 25 (2018) 486-541.

[67] Y. Xu, C. Wang, Z. Li, Mol Clin Oncol. 2 (2014) 3-7.

CHAPTER 4

Exploring the influence of *trans*-heteroatoms on the coordination chemistry, substitution kinetics, DNA/BSA interactions, and cytotoxicity activities of palladium(II) complexes of pincer ligands

4.1 Introduction

The main challenge for the development of antitumour Pd(II) complexes is their high hydrolysis and reactivities, particularly toward sulfur-containing molecules under the biological environment [1-4]. Consequently, the selection of a suitable carrier ligand to control the reactivity and stability of Pd(II) complexes is one of the foremost challenges in the design and development of Pd(II)-based antitumour drugs. Pincer carrier ligands have become increasingly popular in the development of physiologically stable Pd(II)-based anticancer drugs [5-7], owing to their ability to stabilise the metal centres more effectively than their related mono and bidentate variants.

Pincer ligand backbones can easily be fine-tuned, both structurally and electronically, to ensure desirable kinetic reactivity. For example, Bugarčić [8-11] and Jaganyi [12, 13] laboratories have examined the nucleophilic substitution reactions of Pd(II) complexes containing pincer ligands with nitrogen donor atoms. The findings of these studies depict that π-acceptor and π/σ-donor effects play an essential role in controlling the reactivity of the complexes. In another study, Ćoćić and the group [14] used pincer-type ligands to control the kinetic reactivity of Pd(II) complexes and thus improving their resultant antitumour properties. The work revealed that steric crowding reduces the lability of the leaving groups, DNA/BSA interactions and cytotoxic effects of Pd(II) complexes. In chapter three of the thesis (work recently [15]), we were able to electronically fine-tune the kinetic reactivity of Pd(II) complexes using heteroatoms positioned remotely on the spectator ligand(s) backbone, and thereby enhancing DNA binding propensity and cytotoxic effects. Overall, Pd(II) complexes with high kinetic lability in the study, demonstrated strong binding affinities, and improved cytotoxic activities on the

studied tumour cell lines. It is against this backdrop, that the present chapter aims to evaluate the competing roles of *trans*-heteroatoms on carrier ligands typified by N^E^N donor atom (where E = N, O, S) on coordination behaviour, kinetic reactivity and biological activities of Pd(II) complexes. We report in detail the synthesis and structural characterisation of Pd(II) complexes supported by pincer ligands. The ligand substitution reactions were studied using biological nicleophiles; thiourea (**Tu**), L-methionine (**L-Met**) and guanosine-5'-monophosphate (**5'-GMP**). We also investigated DNA and BSA interactions of the complexes and ther resultant cytotoxic properties.

4. 2. Results and discussion

4.2.1. Syntheses and characterisation of the compounds

The tridentate nitrogen, oxygen, and sulfur-bridged bis-(pyrazolyl) ligands used in the study were synthesised in good yields *via* phase transfer catalysed alkylation of pyrazole using 2,6-bis(chloromethyl)pyridine (**L_5**), bis(2-chloroethyl)amine (**L_6**), bis(2-chlroethyl)ether (**L_7**), and (2-chloroethyl)-1H-pyrazole (**L_8**) following previously reported literature procedures [16-18] (Scheme 4.1). Subsequent treatment of equimolar amounts of **L_5-L_8** with $[PdCl_2(NCMe)_2]$ in the presence of $NaBF_4$ in CH_2Cl_2 at room temperature afforded the corresponding Pd(II) complexes **PdL_5-PdL_8**, respectively, section 2.3 (Scheme 4.1). The complexes were isolated as yellow solids in moderate to good yields (60-85%). The complexes, **PdL_5-PdL_8** are air stable and can be stored at room temperature for a long period of time.

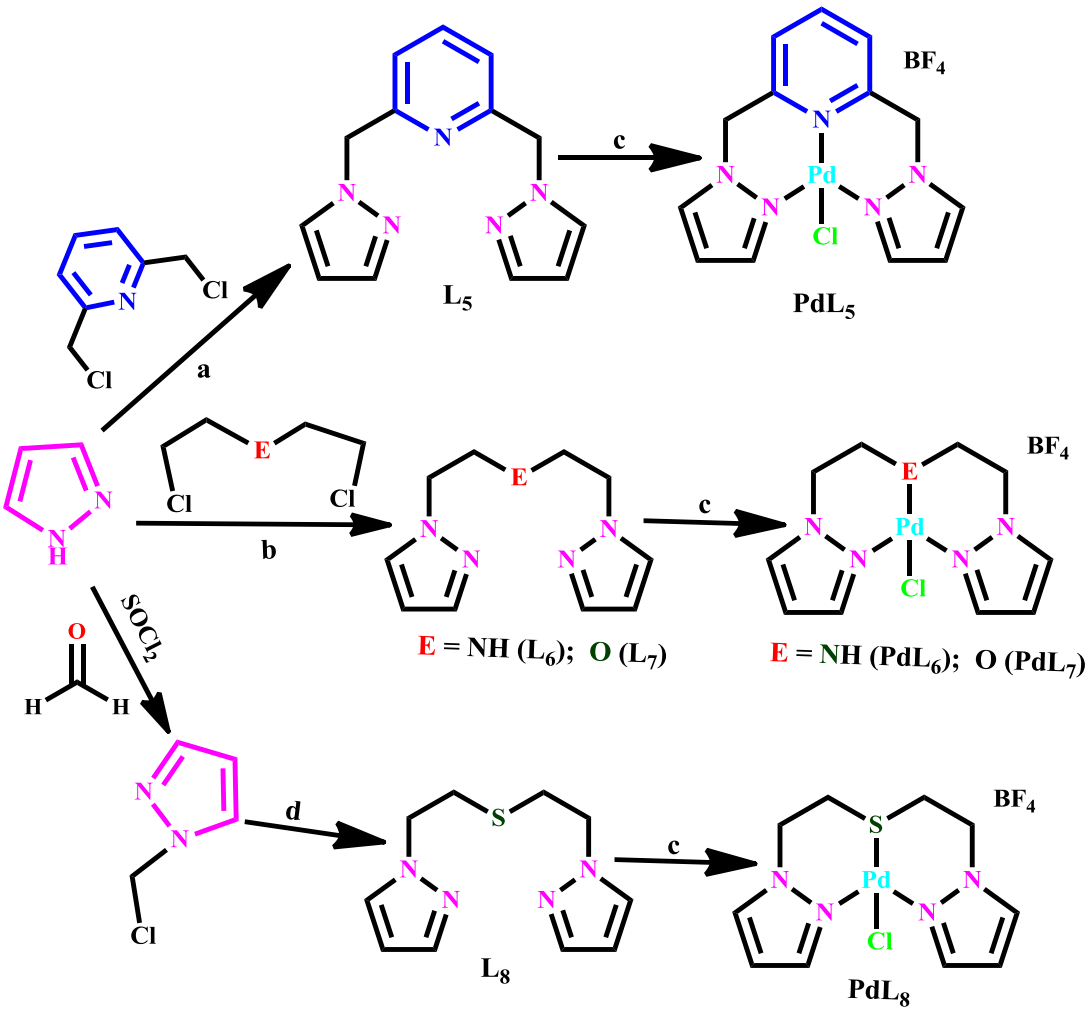

Scheme 4.1: Synthetic protocol for ligands and their respective Pd(II) complexes. *Reagents and conditions*; (**a**) 40% NaOH, 40% TBAB, Toluene, 18 h; (**b**) NaH, Dry DMF, 60°C, 30 h; (**c**) $PdCl_2(NCCH_3)_2$, CH_2Cl_2, $NaBF_4$, 12 h; (**d**) $Na_2S.9H_2O$, NaOH, H_2O/Et_2OH.

The purity and structures of **PdL$_5$-PdL$_8$** were established using ^{1}H and ^{13}C NMR spectroscopy, mass spectrometry, elemental analysis, and single-crystal X-ray analyses. For example, ^{1}H NMR spectrum of ligand **L$_8$** showed two well-defined triplets for the methylene protons compared to the four sets of signals for the CH_2 linker protons in the respective **PdL$_8$** (Figure 4.1). The appearance of the four sets of CH_2 signals in **PdL$_8$** is attributed to the increased restricted rotations (structural rigidity) arising from the occurrence of chair and boat conformations in the complex in relation to the more fluxional behaviour in the free ligand [18]. Also from the ^{13}C NMR, the downfield shifts of the resonance of

methylene carbon at 31.18 and 51.05 ppm (**L_8**) to 36.14 and 52.31 ppm (**PdL_8**) is in tandem with formation of the complex (Figure 4.2).

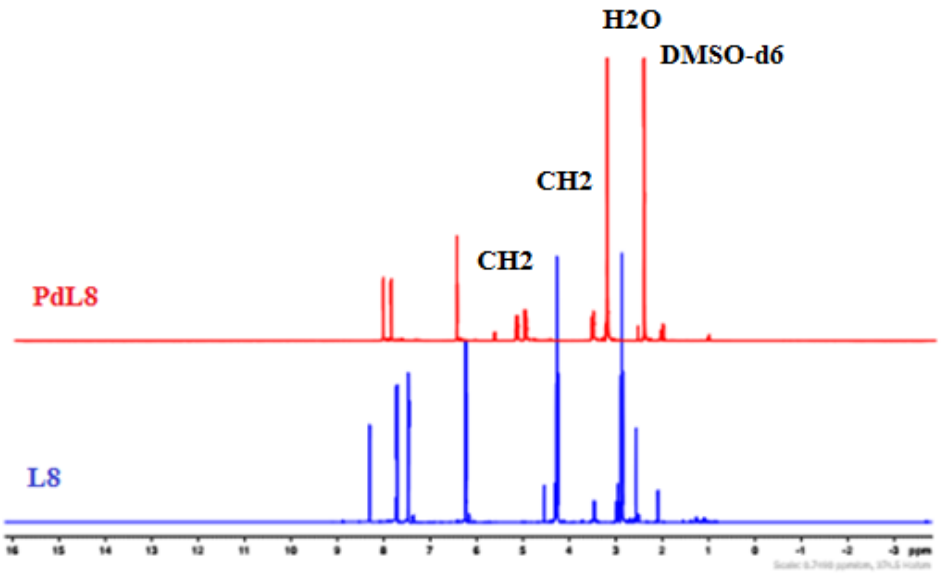

Figure 4.1: Overlays of ^{1}H NMR spectra of ligand **L_8** and the respective complex **PdL_8** in DMSO-d6, showing two signals for CH_2 (**L_8**) and four signals for the CH_2 (**PdL_8**).

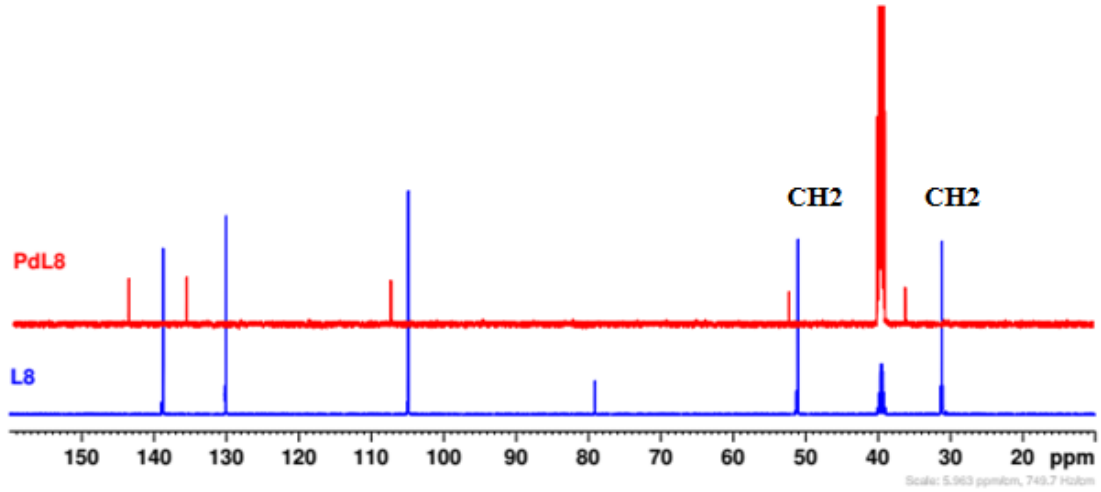

Figure 4.2: Overlays of ^{13}C NMR spectra of ligand **L_8** and the respective complex **PdL_8** in DMSO-d6, showing shifts of the carbon peak of CH_2 at 31.18 and 52.31 ppm (**L_8**) to 36.14 and 52.31 ppm (**PdL_8**) upon complexation.

FT-IR spectroscopy was also employed in the elucidation of the identity of the complexes. For example, a shift of the absorption bands of υ (C=N) from 1395 cm^{-1} (**L_8**) to higher frequency of 1415 cm^{-1} (**PdL_8**), confirmed the coordination of the Pd(II) ion to the nitrogen atoms of the pyrazolyl units (Figure 4.3). Similarly, an up field shift of the υ (C-S) signal from 748 cm^{-1} (**L_8**) to 776 cm^{-1} (**PdL_8**) is also consistent with the formation of the complexes. A shift of the absorption bands to higher frequencies upon coordination, indicate the sigma donor ability of the spectator ligand [18]. The identities of the compounds were also confirmed by mass spectrometry, and all complexes gave the expected molecular ion. For instance, the experimental LC-MS spectrum of **PdL_8** compare well with the calculated isotopic mass distributions (Figure 4.4). Also, the experimental values of elemental analyses of complexes **PdL_5**-**PdL_8** are in tandem with the proposed structures in Scheme 4.1, the values also confirm the purity of the bulk materials.

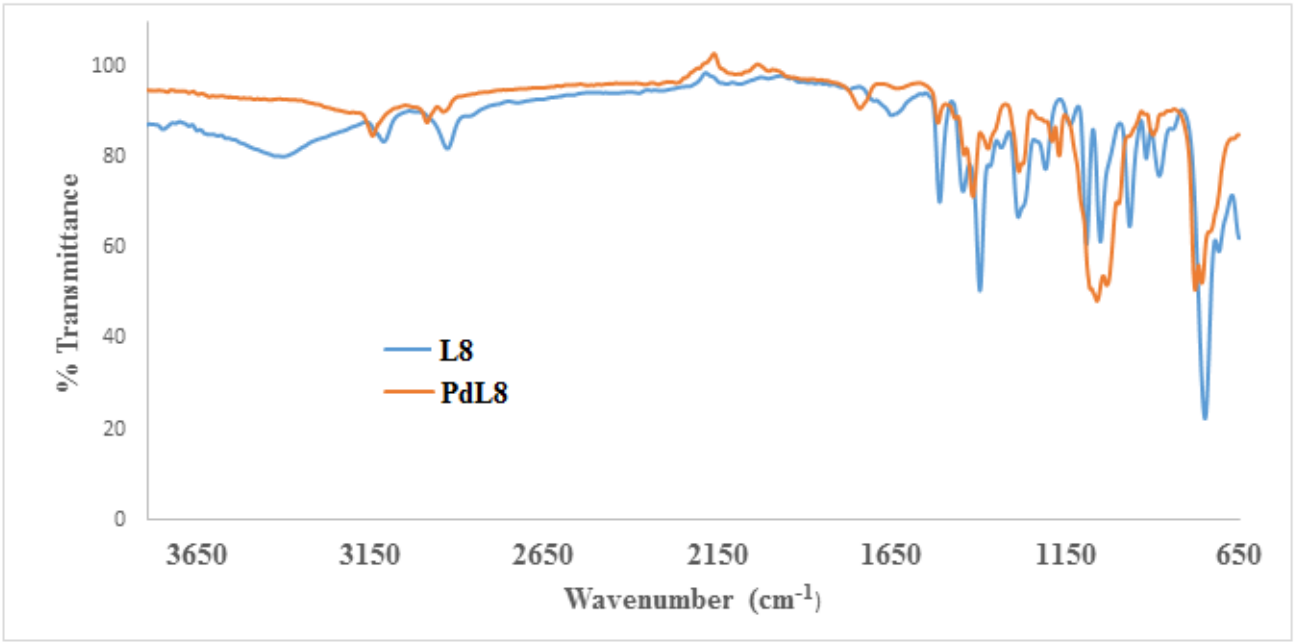

Figure 4.3: Overlays of FT-IR spectra of ligand **L_8** and respective complex **PdL_8**, illustrating a shift of absorption bands of υ (C=N) at 1395 cm^{-1} (**L_8**) to 1415 cm^{-1} (**PdL_8**). Also υ (C-S) signal shifts from 748 cm^{-1} (**L_8**) to 776 cm^{-1} (**PdL_8**), depicting the formation of the complex.

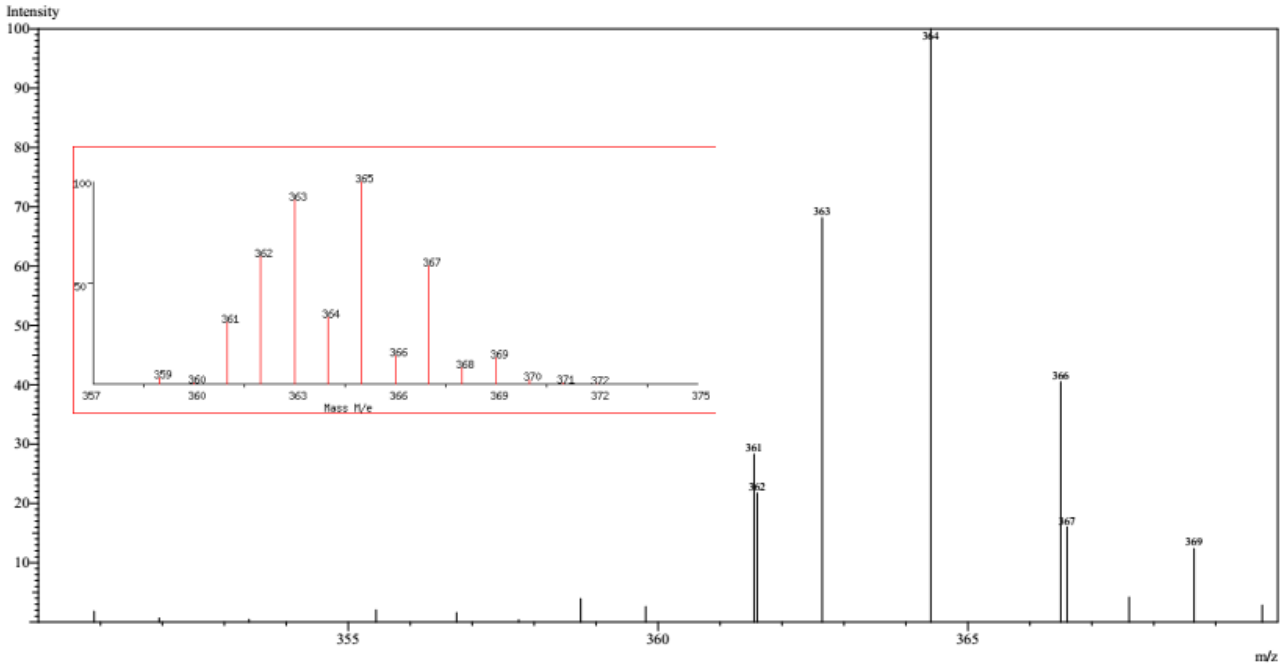

Figure 4.4: **Figure 4.4:** The expanded ESI mass spectrum of complex **PdL$_8$** with *m/z* at 362 (64%) corresponding to the exact mass of 362.97. The spectrum is consistent with the calculated isotopic mass distributions (insert shows the mass spectrum of the calculated isotopic distribution).

4.2.2. X-ray molecular structure of complexes PdL$_5$-PdL$_8$

The single crystals of complexes **PdL$_5$-PdL$_8$** suitable for X-ray diffraction were obtained by slow evaporations of CH_2Cl_2/diethyl ether solutions at room temperature. ORTEP representations of the molecular structures of **PdL$_5$**, **PdL$_6$**, **PdL$_7$**, and **PdL$_8$** are shown with selected bond distances and angles in Figures 4.5, 4.6, 4.7 and 4.8, respectively. Table 4.1 shows crystallographic data and structural refinement parameters for the complexes.

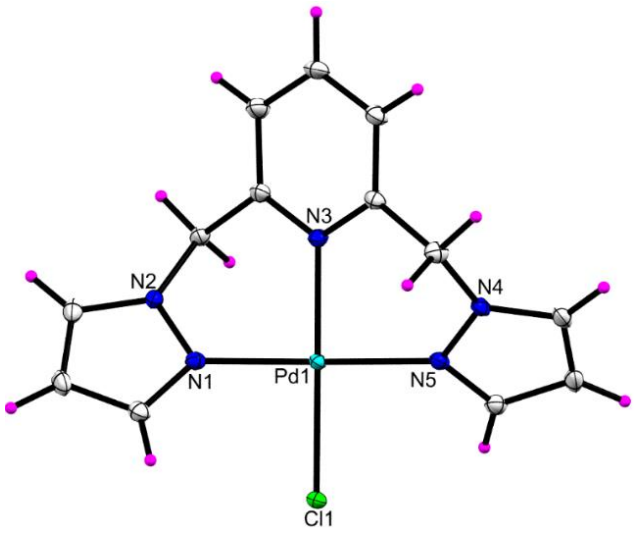

Figure 4.5: ORTEP diagram (50% thermal ellipsoids) of **PdL$_5$**, hydrogen atoms are depicted as spheres of common arbitrary radius. The BF^-_4 counter-anion has been omitted for clarity. The selected bond lengths (Å) and angles (°): Pd(1)-N(1), Pd(1)-N(5), 1.994(2); Pd(1)-N(3), 2.035(2); Pd(1)-Cl(1), 2.2793(6); N(1)-Pd(1)-N(3), 89.81(8); N(5)-Pd(1)-N(3), 89.34(8); N(5)-Pd(1)-N(1),178.80(9); N(1)-Pd(1)-Cl(1), 90.01(6); N(5)-Pd(1)-Cl(1) 90.86(6); N(3)-Pd(1)-Cl(1)178.88(6).

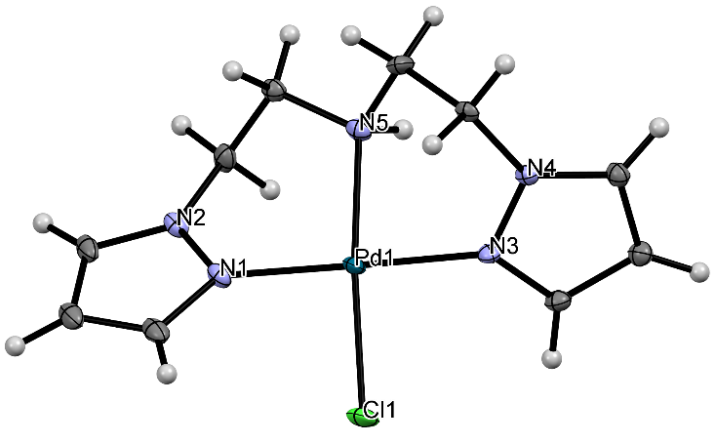

Figure 4.6: ORTEP diagram (50% thermal ellipsoids) of **PdL$_6$**, hydrogen atoms are depicted as spheres of common arbitrary radius. The 2[PdLCl][$PdCl_4$] counter ion has been omitted for clarity. The selected bond lengths (Å) and angles (°): Pd(1)-N(1), 1.999(4); Pd(1)-N(3), 1.985(4); Pd(1)-N(5), 2.065(7); Pd(1)-Cl(1), 2.293(2); N(1)- Pd(1)- N(5), 93.5(3); N(3)- Pd(1)- N(5), 94.6(3); N(3)- Pd(1)- N(1), 176.1(2); N(1)- Pd(1)- Cl(1), 91.02(17); N(3)- Pd(1)- Cl(1), 90.71(17); N(5)- Pd(1)- Cl(1), 174.8(2).

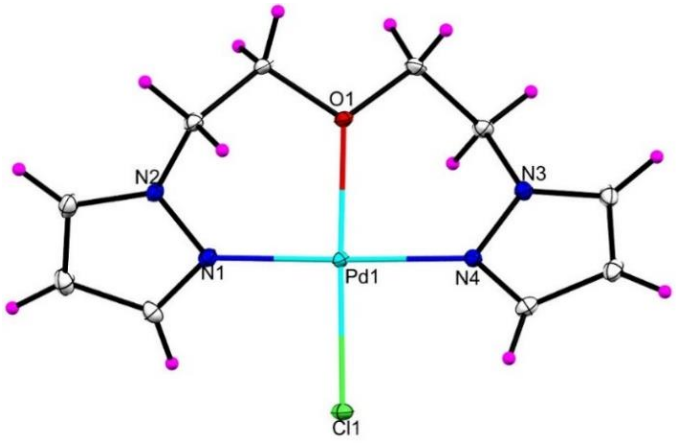

Figure 4.7: ORTEP diagram (50% thermal ellipsoids) of **PdL$_7$**, hydrogen atoms are depicted as spheres of common arbitrary radius. The BF^-_4 counter-anion has been omitted for clarity. The selected bond lengths (Å) and angles (°): Pd(1)-N(1), 1.9988(15); Pd(1)-N(4), 1.9953(14); Pd(1)-O(1), 2.0849(12); Pd(1)-Cl(1), 2.2574(4); N(1)-Pd(1)-O(1), 90.98(5); N(4)-Pd(1)-O(1), 87.52(5); N(4)-Pd(1)-N(1), 178.44(6); N(1)-Pd(1)-Cl(1), 91.10(4); N(4)-Pd(1)-Cl(1), 90.39(4); O(1)-Pd(1)-Cl(1), 177.79(4).

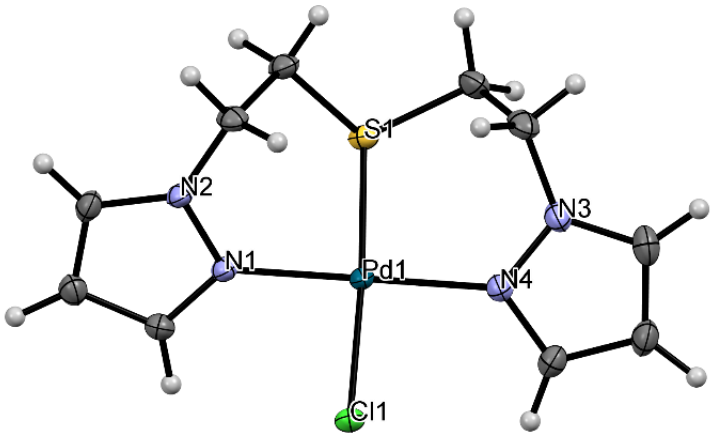

Figure 4.8: ORTEP diagram (50% thermal ellipsoids) of **PdL$_8$**, hydrogen atoms are depicted as spheres of common arbitrary radius. The BF^-_4 counter-anion has been omitted for clarity. The selected bond lengths (Å) and angles (°): Pd(1)-N(1), 2.004(2); Pd(1)-N(4), 2.012(2); Pd(1)-S(1); 2.2885(6); Pd(1)-Cl(1), 2.3149(6); N(1)-Pd(1)-S(1), 86.98(6), N(4)-Pd(1)-S(1), 92.94(6); N(1)-Pd(1)-N(4), 179.50(9); N(1)-Pd(1)-Cl(1), 89.45(6); N(4)-Pd(1)-Cl(1), 90.64(6); S(1)-Pd(1)-Cl(1), 176.42(2).

Table 4.1: Crystal data and structure refinement details for complexes **PdL_5–PdL_8**

Parameter	**PdL_5**	**PdL_6**	**PdL_7**	**PdL_8**
Empirical formula	$C_{13}H_{13}BClF_4N_5Pd$	$C_{20}H_{30}Cl_6N_{10}Pd_3$	$C_{10}H_{14}BClF_4N_4OPd$	$C_{20}H_{28}B_2Cl_2F_8N_8Pd_2S_2$
Formula weight	467.94	942.44	434.91	901.94
Temperature (K)	100(2)	99.99 K	100	100(2) K
Wavelength (Å)	0.71073	0.71073	0.71073	1.54178 Å
Crystal system	Monoclinic	Monoclinic	Monoclinic	Monoclinic
Space group	P 21/n	P 21/c	P 21/ c	P 21/n
Unit cell dimension				
a (Å)	8.8899(6)	16.8800(11)	7.7670(6)	7.5712(2)
b (Å)	10.3653(6)	23.0986(14)	13.7211(11)	13.8322(4)
c (Å)	18.0293(11)	7.7857(5)	13.6736(11)	31.7133(9)
α (°)	90	90	90	90°
β (°)	102.323(3)	100.412(3)	92.843(4)	93.9930(10)°.
γ (°)	90	90	90	90°
Volume ($Å^3$)	1623.06(18)	2985.7(3)	1455.4(2)	3313.16(16)
Z	4	4	4	4
Density (Mg/m^3)	1.915	2.097	1.985	1.808
F(000)	920	1840.0	856.0	1776

As shown in Figures 4.5-4.8, the solid-state structures of complexes **PdL$_5$-PdL$_8$**, contain one Pd metal centre, one tridentate ligand and a chloride ligand, completing a four-coordination sphere. The *cis* angles for instance N(1)-Pd(1)-N(3) of 89.81(8) ˚ (**PdL$_5$**); N(1)- Pd(1)- N(5), 93.5(3) ˚ (**PdL$_6$**); N(1)-Pd(1)-O(1), 90.98(5) ˚ (**PdL$_7$**); N(1)-Pd(1)-S(1), 86.98(6) ˚ (**PdL$_8$**) deviate from the expected 90° for a perfect square planar geometry. Furthermore, the chelate *trans* angles N(3)-Pd(1)-Cl(1)178.88(6) ° **(PdL$_5$)**; N(5)- Pd(1)- Cl(1), 174.8(2) ° (**PdL$_6$**); O(1)-Pd(1)-Cl(1), 177.79(4) ° (**PdL$_7$**) and S(1)-Pd(1)-Cl(1), 176.42(2) ° (**PdL$_8$**) depart from linearity (180°), consistent with the distorted square planar geometries [19]. The six-membered chelate ring, N(1)-Pd(1)-$N_{pyridine}$, of 89.81(8) ° (**PdL$_5$**) is smaller than N(1)-Pd(1)- NH of 93.5(3) ° (**PdL$_6$**), N(1)-Pd(1)-O of 90.98(5)° (**PdL$_7$**) a characteristic of the greater constraint imposed by the rigid pyridine ring (**PdL$_5$**) than the more flexible CH_2 linkers (**PdL$_6$** and **PdL$_7$**). Unexpectedly, N(1)-Pd(1)-N_{py}, of 89.81(8) ° (**PdL$_5$**) is larger than N(1)-Pd(1)-S(1), 86.98(6) (**PdL$_8$**).

The longer bond length Pd(1)-Cl(1) of 2.3149(6) (**PdL$_8$**) in comparison to Pd(1)-Cl(1), 2.293(2) (**PdL$_6$**) and Pd(1)-Cl(1), 2.2574(4) (**PdL$_7$**) is due to the strong *trans*-influence of S-atom (soft ligating atom) than N_{im} and O-atom (which are hard bases). Also, the observed longer Pd(1)-Cl(1) of **PdL$_6$** in relation to **PdL$_7$** is ascribed the higher polarizability of N_{im} than O-atom, resulting to a stronger σ-bonding to Pd-metal centre (increasing *trans*-labilization effect). The shorter bond distances of Pd(1)-Cl(1) of 2.2793(6) Å (**PdL$_5$**) than Pd(1)-Cl(1) of 2.293(2) Å **(PdL$_6$)** is attributable to better *trans*-influence of NH specie (σ-donor) than the pyridine moiety (π-acceptor). The Pd(1)-Cl(1) bond distance of 2.2793(6) (**PdL$_5$**) compare well with the average of 2.289 ± 0.013 Å reported for 20 similar structures [20]. With the exception of Pd(1)-Cl(1) bond distances 2.2574(4) Å for **PdL$_7$** (lower than the minimum value 2.281 Å), Pd(1)-Cl(1) bond distances of 2.293(2) and 2.3149(6) for **PdL$_6$** and **PdL$_8$**, respectively correlate well with the mean of 2.308 ± 0.020 Å obtained for 25 related structures [21]. The Pd(1)-$N_{pyridine}$ bond length of 2.035(2) Å for **PdL$_5$** is within the average mean of 2.041 ± 0.023 Å reported for 29 related Pd-compounds [20]. Except for bond distance Pd(1)-S(1) of 2.2885(6) for **PdL$_8$** (longer than the

maximum values 2.257 Å), the bond lengths Pd(1)-NH of 2.065(7) for **PdL$_6$** and Pd(1)-O of 2.0849(12) Å for **PdL$_7$** are consistent with the mean of 2.199 ± 0.047 Å reported for similar structure (11 structures) [22].

4.2.3 Stability of PdL$_5$-PdL$_8$ in DMSO solutions

The stability tests of complexes **PdL$_5$-PdL$_8$** in DMSO medium were conducted by UV-Vis spectroscopy. Often metal-complexes undergo ligand dissociation upon dissolution in DMSO stock solutions used in biological assays, and thus we studied the effects of DMSO on **PdL$_5$-PdL$_8$**, before reporting their *in vitro* biological activity. No significant change in the electronic absorption spectral traces were observed within 72 h (Figure 4.9), indicative of their stability.

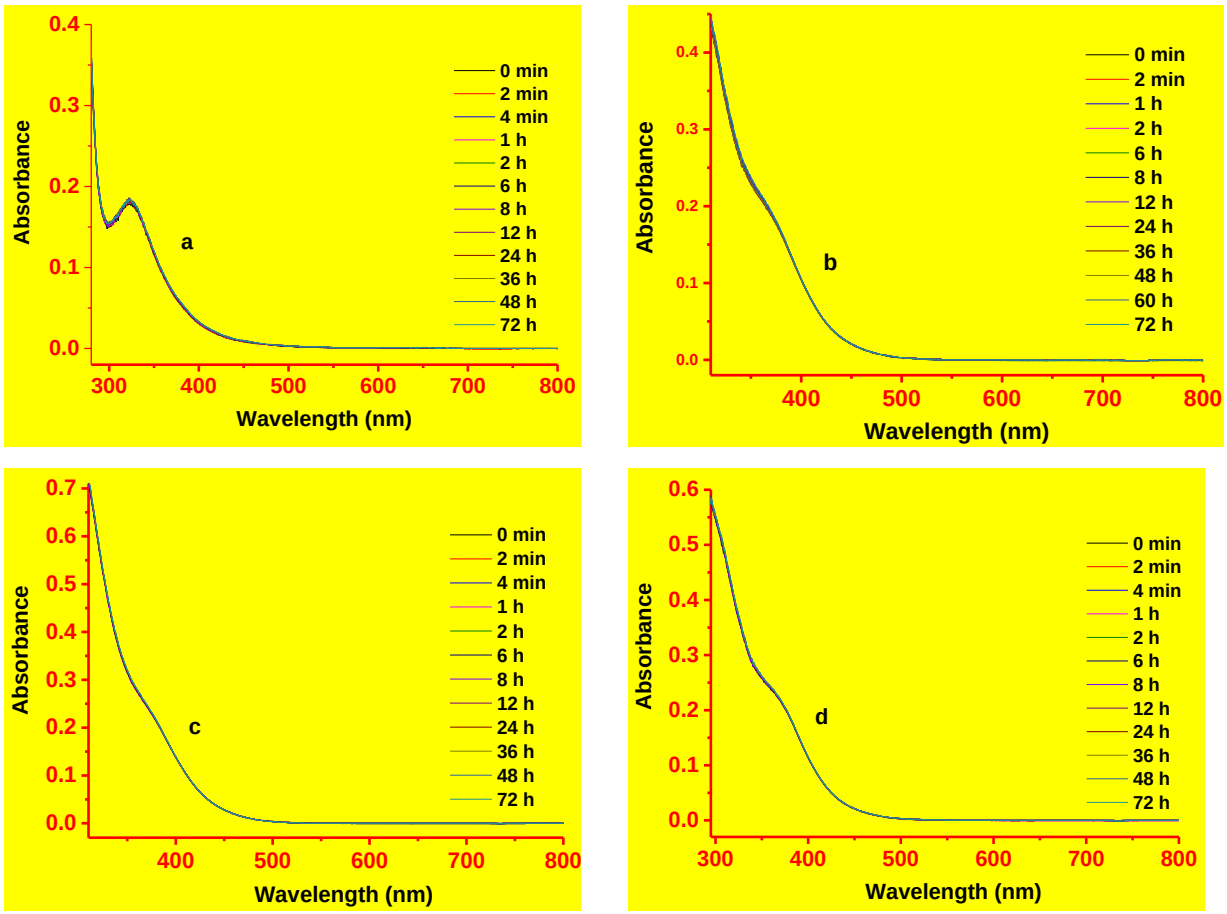

Figure 4.9: Time-dependent UV–Vis spectra of **PdL$_5$** (a), **PdL$_6$** (b), **PdL$_7$** (c), and **PdL$_8$** (d) in DMSO solution at 25 °C recorded within different time spans (over 72 h period).

4.2.4 DFT-computational optimisation, calculations, and analysis

Simulations of the complexes at the DFT level was performed to obtain a detailed understanding of the structural and electronic properties of the complexes. The DFT optimised structures and frontier orbital energy maps for the HOMO and LUMO of the complexes are shown in Figure 4.10, while the geometrical data are summarised in Table 4.2. In general, the nature of the HOMO and LUMO orbitals provide information on the electron donor-acceptor ability of the inert chelating ligand. A closer look at the frontier orbital mappings reveal that the electron densities of HOMO orbitals are mainly localised on the *4d*-orbitals of the 3p-orbitals of the chlorine atoms. While the LUMO electron clouds are not only distributed on the Pd metal centre, and chloride ligand but are also significantly concentrated on the heteroatoms, and the N-atoms of the pyridine and pyrazoles. The considerable localisation of the LUMO on the Pd character, suggest the potential σ-donor ability of the spectator ligands, making it difficult for π-back donation.

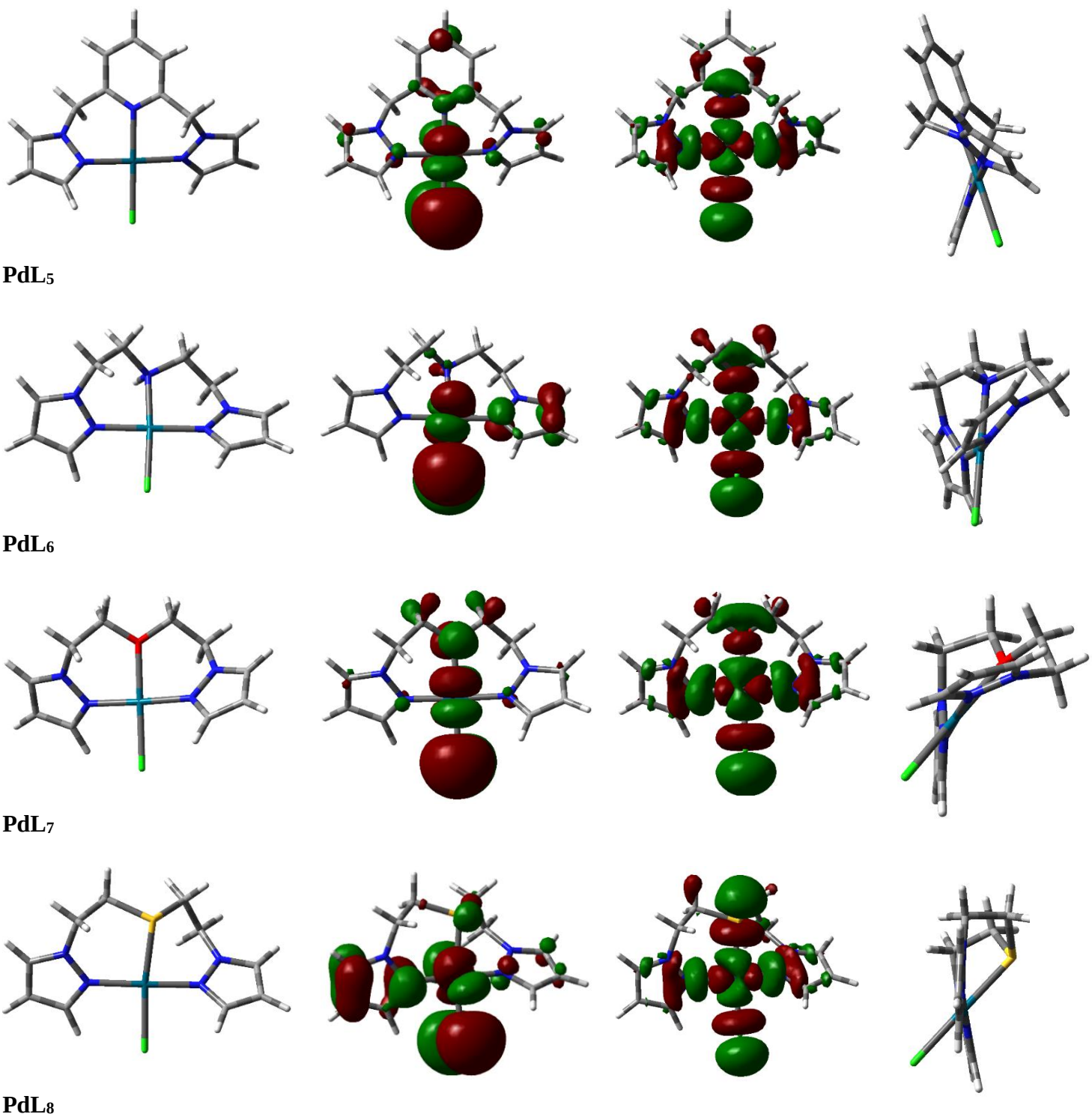

Figure 4.10: DFT-optimised frontier orbital density distributions, and planarity for complexes **PdL$_5$**-**PdL$_8$** determined by the B3LYP/LANL2DZ method.

Table 4.2: Summary of selected DFT-calculated data for complexes **PdL_5-PdL_8**

Properties	**PdL_5**	**PdL_6**	**PdL_7**	**PdL_8**
NBO charge				
Pd^{2+}	0.443	0.423	0.463	0.233
X = Heteroatom	-0.280	-0.439	-0.412	0.324
Bond lengths (Å)				
Computed Pd-Cl	2.304	2.397	2.390	2.427
X-ray Pd(1)-Cl(1)	2.279(6)	2.293(2)	2.257(4)	2.315(6);
Computed Pd-N_{trans}/O/S	2.088	2.139	2.147	2.027
X-ray Pd-N_{trans}/O/S	2.035(2)	2.065(7)	2.085(12)	2.289(6);
HOMO-LUMO energy / eV				
$-E_{HOMO}$	7.329	7.423	7.244	7.106
$-E_{LUMO}$	3.305	3.295	2.772	2.801
$\Delta E_{LUMO–HOMO}$	4.024	4.128	4.472	4.305
Chemical hardness (η)	2.012	2.064	2.236	2.152
$-\Delta E_{back\text{-}donation}$	0.503	0.516	0.559	0.538
Chemical softness (σ)	0.497	0.484	0.447	0.465
Electronegativity ($\chi = -\mu$)	5.317	5.359	5.008	5.054
Electrophilicity index (ω)	7.025	6.957	5.608	5.669
Dipole moment (*Debye*)	15.093	15.538	14.226	14.822

4.2.5 Kinetic and mechanistic study

4.2.5.1 Concentration effect

The kinetics of displacing the chloro ligands with the nucleophiles was studied spectrophotometrically by monitoring the changes in the absorbance of the spectra with time. Typical stopped-flow kinetic trace recorded for the reactions of **PdL$_8$** with **Tu** at 298 K is presented in Figure 4.11a. Kinetic traces from the stopped flow were of excellent fit to a single-exponential decay function, to produce the observed pseudo-first-order rate constants (k_{obs}) using equation (1), indicating that the reactions were first-order. The k_{obs} values obtained were plotted against nucleophile concentrations [Nu]. Representative plots of k_{obs} against [Nu] obtained for **PdL$_8$** at 298 K is given in Figure 4.11b. A linear dependence of k_{obs} on [Nu] with zero intercept was exhibited in all complexes, suggesting irreversible or non-solvotic pathways. By reducing the positive inductive effect, the reactions can best be described by equation (3). The second order rate constants (k_2) were derived from the gradient of a linear regression of a plot of k_{obs} versus [Nu], and the acquired values are presented in Table 4.3.

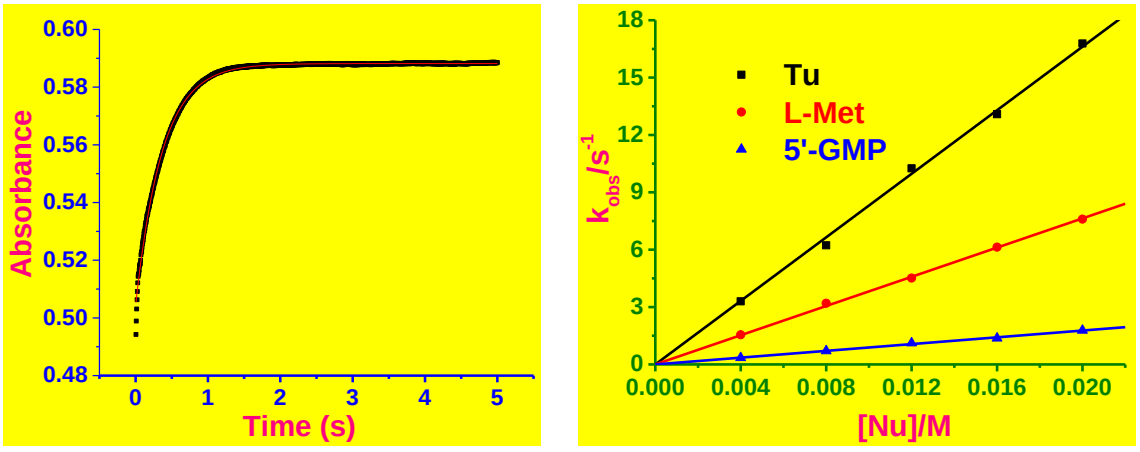

(**a**) (**b**)

Figure 4.11: (**a**); Stopped-flow kinetic trace at 385 nm of **PdL$_8$**, at T = 298 K in aqua media, 50 μM Tris-HCl buffer (pH = 7.2), and 50 mM NaCl. (**b**); Concentration dependence of k_{obs} for the displacement of Cl ligand from **PdL$_8$**.

Table 4.3: Summary of the second order rate constants, k_2, at 298 K, and activation parameters, $\Delta H^{\neq}$, $\Delta S^{\neq}$ and $\Delta G^{\neq}_{25°C}$ for the substitution reactions of Pd(II) complexes with Nu.[a]

Complex	Nu	k_2/M^{-1} s^{-1}	$\Delta H^{\neq}$/ kJ mol^{-1}	$-\Delta S^{\neq}$/J mol^{-1}K^{-1}	$\Delta G^{\neq}_{25°C}$/kJ mol^{-1}
	Tu	595 ± 10	14 ± 1	147 ± 3	58 ± 2
PdL$_5$	**L-Met**	218 ± 4	20 ± 1	134 ± 3	60 ± 2
	5'-GMP	54 ± 2	25 ± 1	129 ± 3	63 ± 2
	Tu	432 ± 4	15 ± 1	144 ± 3	57 ± 1
PdL$_6$	**L-Met**	186 ± 4	20 ± 1	135 ± 4	60 ± 3
	5'-GMP	30 ± 1	25 ± 1	134 ± 4	65 ± 3
	Tu	237 ± 3	24 ± 1	120 ± 3	60 ± 2
PdL$_7$	**L-Met**	105 ± 2	31 ± 1	103 ± 4	62 ± 3
	5'-GMP	13 ± 0.1	34 ± 1	110 ± 3	67 ± 2
	Tu	830 ± 10	14 ± 1	141 ± 3	56 ± 2
PdL$_8$	**L-Met**	381 ± 3	22 ± 1	122 ± 3	58 ± 2
	5'-GMP	88 ± 1	22 ± 1	134 ± 3	62 ± 2

[a]Reactions performed in aqua media, 50 μM Tris-HCl buffer (pH = 7.2), and 50 mM NaCl

The k_2 values of complexes **PdL$_6$-PdL$_8$** with all the nucleophiles are ordered as; **PdL$_8$** > **PdL$_6$** > **PdL$_7$** (Table 4.3) The observed reactivity is fundamentally related to the electronic properties of the auxiliary ligand(s). The higher reactivity of **PdL$_8$** (S) in comparison to both **PdL$_6$** (NH) and **PdL$_7$** (O) is due to the preference of Pd atom (soft acid) to coordinate with the soft donor S-atom as opposed to NH and O-atom (hard bases), resulting to the accumulation of electron cloud in the bonding area and thus a stronger σ-bonding to the metal centre [23]. This leads to the shortening of the Pd(II)-heteroatom bond length. The consequence of this is the weak and elongated bond *trans* to the leaving group, which accelerate the rate of reactivity [24, 25]. The DFT bond distances of Pd-S (2.027) < Pd-NH (2.139) < Pd-O (2.147)

affirm the argument (Table 4.2). This is also reflected in the DFT calculated Pd-Cl bond distance presented in Table 4.2, **PdL$_6$** (2.397 Å), **PdL$_7$** (2.390 Å), and **PdL$_8$** (2.427 Å). The Pd(1)-Cl(1) bond distances of solid-state structures of 2.293(2), 2.2574(4), and 2.315(6) Å, for **PdL$_6$**, **PdL$_7$** and **PdL$_8$** also support the argument.

The higher intrinsic reactivity of **PdL$_6$** (NH) than **PdL$_7$** (O), is due to the better polarizability of NH (with larger and more diffuse electron cloud) compared to O-atom. On the rows of the periodic table, polarizability decreases from left to right [26]. Polarizability allows for easy movement of electrons between the heteroatom and Pd(II) ion (causing a stronger sigma-bond), leading to the elongation of Pd-Cl bond distance. The claims are supported by the shorter X-ray bond distances of Pd(1)-NH of 2.065(7) (**PdL$_6$**) in comparison to Pd(1)-O of 2.0849(12) Å (**PdL$_7$**). The solid-state structure Pd(1)-Cl(1) bond length of 2.293(2) Å for **PdL$_6$**, and 2.2574(4) Å for **PdL$_8$** are consistent with the assertion that the NH specie causes more *trans*-influence than the O-atom. Likewise, the computed bond lengths of Pd-heteroatoms and Pd-Cl for **PdL$_6$** and **PdL$_7$** (Table 4.2), are in tandem with the observed kinetic trend. Moreover, the higher polarizability of the heteroatoms in the complexes induce greater dipole moments [27]. The observation agrees well with the computed dipole moments of 15.538 (**PdL$_6$**) and 14.226 (**PdL$_7$**), Table 4.2.

The observed high reactivity of **PdL$_5$** in relation to **PdL$_6$** can be accounted both by the steric and electronic effects of the spectator ligand(s). The out-of-square conformations of **PdL$_6$** compared to the rigid planar structure of **PdL$_5$** introduces sterics, minimising facile nucleophilic attack. The assertion is evidenced by the X-ray dihedral angle of N(1)-Pd(1)-N(3), 89.81(8) ˚ (**PdL$_5$**) which is smaller than N(1)- Pd(1)- N(5), 93.5(3) ˚ (**PdL$_6$**). With regards to the electronic effects, the π-acceptor ability of the pyridine moiety (**PdL$_5$**) reduces electron density on the Pd(II) ion, while NH moiety (**PdL$_6$**) a good sigma donor donates electrons to the metal centre [28-30]. The argument is well supported by the high positive NBO charge of Pd atom in **PdL$_5$** (0.443) in comparison to **PdL$_6$** (0.423), Table 4.2. This is

further evidenced by the lower $\Delta E_{LUMO–HOMO}$ for **PdL$_5$** (4.024 eV) than **PdL$_6$** (4.128 eV). The ΔE back-donation of 0.503, and 0.516 eV for **PdL$_5$** and **PdL$_6$**, respectively agree with the observed reactivity trend. Likewise, the chemical hardness (η), and electrophilicity index (ω) support the observed kinetic trend.

Biological nucleophiles, **Tu**, **L-Met** and **5'-GMP** were studied as entering ligands because of their different electronic and steric demands, binding properties, and bio-relevance. The reactivities for the incoming ligands follow the order **Tu** > **L-Met** > **5'-GMP** for all complexes. Sulfur-donor ligands (**Tu** and **L-Met**) display higher reactivity to **5'-GMP** (a nitrogen-donor ligand), owing to the fact that soft acids such as Pd(II) ions exhibit a high affinity for soft bases such as sulfur-donor molecules [31]. Also, **Tu** demonstrates the highest reactivity since it is the least sterically demanding ligand. The slightly higher reactivity of **L-Met** can be explained by the positive inductive effect of the methyl substituents that enhance its nucleophilicity. The least reactivity of **5'-GMP** can also be accounted by its steric bulkiness in comparison to the other two nucleophiles.

4.2.5.2 Temperature effect and iso-kinetic relationship

To determine the activation parameters, enthalpy of activation ($\Delta H^{\neq}$), entropy of activation ($\Delta S^{\neq}$) and Gibbs free energy of activation ($\Delta G^{\neq}_{25°C}$), the temperature dependence of k_2 were investigated within the temperature range of 25 to 45 °C at intervals of 5 °C. The activation parameters were determined from linear plots of $\ln(k_2/T)$ versus T^{-1}/K^{-1} according to the Eyring equation (4). Representative plots for **PdL$_8$** with the nucleophiles are shown in Figure 4.12a. The slopes and intercepts of the plots gave $\Delta H^{\neq}$, and $\Delta S^{\neq}$, respectively. The values of the activation parameters are reported in Table 4.3. The apparent negative values of $\Delta S^{\neq}$ in the complexes can be attributed to an increase in solvent electrostriction in the transition state due to partial charge separation that characterises the elongation of the Pd–Cl bond in the transition state, increasing the dipole moment of the complexes. Consequently, as shown in Table 4.2, the dipole characters of **PdL$_8$** in the transition state is larger than **PdL$_6$** and **PdL$_7$**.

The negative $\Delta S^{\neq}$ values indicate an associative mechanism of substitution reaction [32], dominated by bond-making with the incoming nucleophile, forming transition states which are more ordered compared to the starting reactants and the final product [33]. The preposition is also supported by the sensitivity of the k_2 values to the concentration and steric bulkiness of the entering ligand [33]. The rates of the reactions increase with the increase in the concentration of the nucleophile up to a limiting rate, which is probably due to the completion of the outer sphere association complex formation.

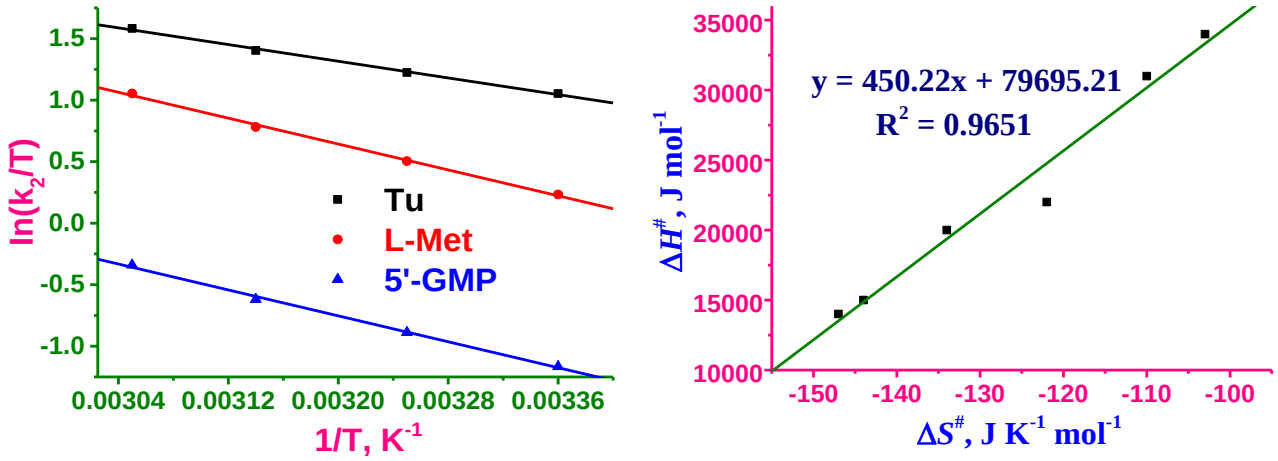

(a) **(b)**

Figure 4.12: **(a)**; Eyring plots for the reaction of **PdL$_8$** with the entering ligand in aqua, in 50 µM Tris-HCl buffer (pH = 7.2), and 50 mM NaCl and temperature range of 298-318 K. **(b)**; *Iso*-kinetic plots for ligand substitution reactions of complexes **PdL$_5$-PdL$_8$** with the biological nucleophiles.

A linear free energy relationship (LFER) of thermal activation was determined from the plots of $\Delta H^{\neq}$ versus $\Delta S^{\neq}$ using equation (5). The straight line of the plots indicated the existence of a linear *iso*-kinetic free energy relationship between the activation variables of the studied complexes and the incoming nucleophiles. The slopes of the plots provided the *iso*-kinetic temperature, a theoretical temperature at which all the reactions of the complexes and the entering ligands would proceed at equal rates of substitution, while the intercept gave Gibbs free energies, $\Delta G^{\#}$ for the substitution processes. The *iso*-kinetic temperature for the reactions of the complexes, **PdL$_5$-PdL$_8$** was predicted at 450.22 K, while

$\Delta G^{\neq}$ was determined at 79695.21 kJ mol^{-1} (Figure 4.12b). The magnitude of $\Delta G^{\#}_{25°C}$ values (Table 4.3), for the reactions of the four Pd complexes with the nucleophiles are all comparable, suggesting that the reactions follow the same mechanism which is associative [34, 35]. Moreover, the graph shows a near linear fit with R^2 value of 0.9651, indicating a correlation between $\Delta H^{\neq}$ and $\Delta S^{\neq}$.

4.2.6 CT-DNA interactions studies

4.2.6.1 UV-Vis absorption spectral studies

The CT-DNA binding ability of complexes **PdL_5-PdL_8** was investigated by the electronic absorption titration method. The electronic absorption spectral curve for **PdL_8** is shown in Figure 4.13. The observed equilibration time for Pd-CT-DNA complexes, being less than 30 s. From the titration curves, it was clear that upon increasing the concentration of CT-DNA, the bands of the metal complexes showed hypochromism shift, indicative of the existence of intercalative mode of binding, involving strong stacking interaction between complexes and the DNA base pairs [36]. The intrinsic binding constant, K_b, obtained from Wolfe-Shimer equation (6), and free energy (ΔG) of the complex-induced DNA, computed from van't Hoff equation (7), are presented in Table 4.4. The computed K_b values (ranging from 1.38 x 10^5 M^{-1} to 5.54 x 10^5 M^{-1}) correspond well with those of the previously reported for similar Pd(II) complexes [37-39], and indicate moderate to strong binding to DNA helix *via* intercalative binding mode. The negative values of ΔG show that the binding between the Pd-complexes and CT-DNA occurs spontaneous [40, 41].

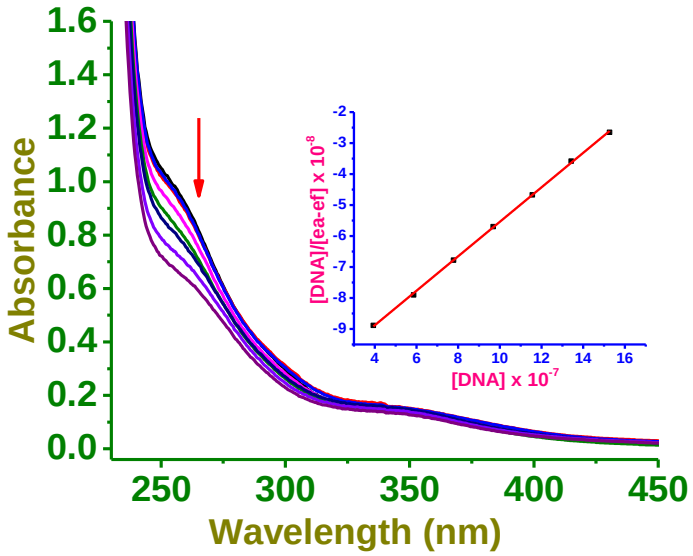

Figure 4.13: Electronic spectra of **PdL$_8$** 50 μM Tris buffer consisting of 50 mM NaCl at pH = 7.2 upon addition of CT-DNA (0-40 μM). The arrow shows the change in absorbance upon increasing the CT-DNA concentration. Inset: plot of [CT-DNA] versus [DNA]/(ε_a- ε_f) for the titration of the complex with CT-DNA.

4.2.6.2 Competitive fluorescence measurements for CT-DNA

Fluorescence-quenching experiments using EB-bound CT-DNA was performed to further confirm the mode of interactions between the metal complexes and CT-DNA. The fluorescence quenching curves of EB-DNA in the absence and presence of complex **PdL$_8$** are shown in Figure 4.14a. Significant decrease in the intensity of the emission bands at 597 nm was observed with the increase in the concentration of individual metal complexes, indicating that the complexes can compete with EB for binding to CT-DNA and thus affirming the intercalation of the complexes to base pairs of CT-DNA [38, 39]. From the spectral data, the Stern-Volmer binding constant (K_{SV}), and bimolecular quenching rate constant, k_q, were determined from the Stern-Volmer equation (8), (Figure 4.14b for **PdL$_8$**, and the values of the binding constants are given in Table 4.4. The K_{sv} values of (1.10-26.40) x 10^3 M^{-1} indicate that the complexes can displace EB from DNA base pairs through intercalative binding [2]. The apparent binding ability constant, K_{app}, was calculated from the equation (9). The 10^5-10^6 M^{-1} magnitudes of K_{app}

of **PdL$_5$-PdL$_8$** are lower than the classical intercalators binding constant (10^7 M^{-1}) [42], affirming moderate intercalative binding to DNA. The k_q values of 9.17 x 10^{11} $M^{-1}s^{-1}$ for **PdL$_5$**, 6.92 x 10^{11} $M^{-1}s^{-1}$ for **PdL$_6$**, 4.80 x 10^{10} $M^{-1}s^{-1}$ for **PdL$_7$**, and 11.49 x 10^{11} $M^{-1}s^{-1}$ for **PdL$_8$** (Table 2), are greater than the maximal limit of collisional (dynamic) quenching rate constant (2.0 x 10^{10} M^{-1} s^{-1}), suggesting the presence of static quenching mechanism [43]. The values of DNA binding constant, K_F and the number of binding sites per nucleotide, *n* were computed from the Scatchard equation (10). Scatchard plots are shown in Figure 4.14c (**PdL$_8$**), and the values are provided in Table 4.4. The values of K_F (magnitude 10^2 or 10^3 M^{-1}) are comparable with those reported for similar Pd(II) complexes [38]. The values of n are approximately equal to 1 (Table 4.4), suggesting the existence of a single binding site in CT-DNA for all the complexes. The calculated competitive binding constants are consistent with the outcome of absorption titration experiment (K_b) and substitution kinetics trend.

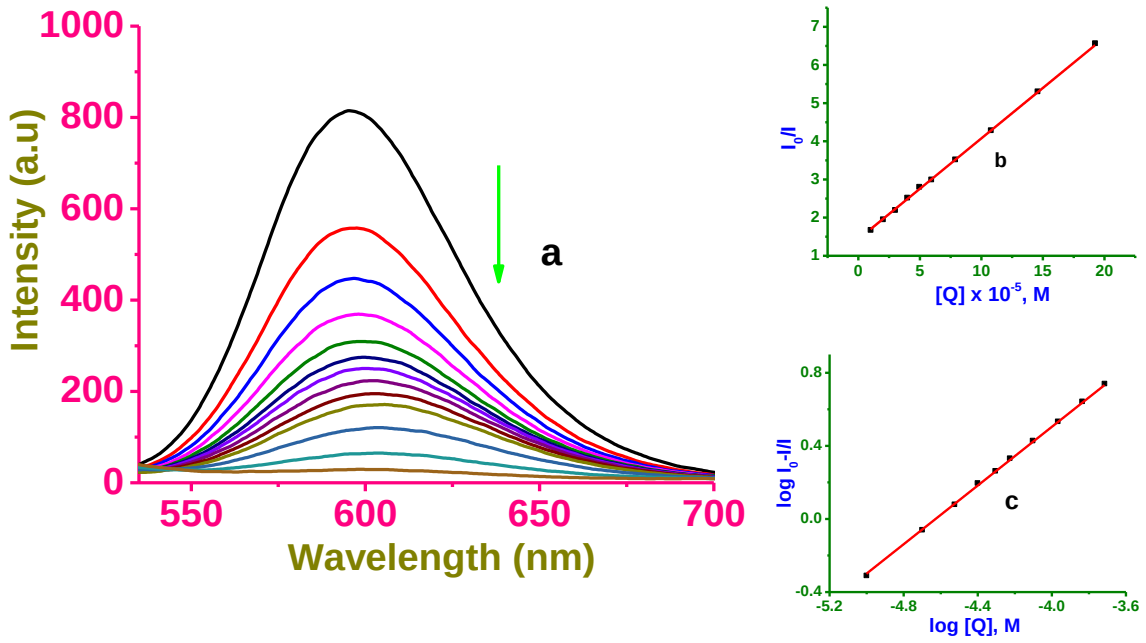

Figure. 4.14: (**a**); The emission spectra of the CT-DNA-EB system in the presence of **PdL$_8$**: [EB] = 50 μM, [CTDNA] = 50 μM and [**PdL$_8$**] = 0-200 μM. The arrow shows the intensity changes upon increasing the concentration of complex **PdL$_8$**. **(b)**; Stern-Volmer plot of I_o/I versus [Q]. **(c)**; Scatchard plot of log[(I_o–I)/I] *vs* log[Q] for the titration of the compound to DNA-EB system.

Table 4.4: Binding constants and thermodynamic parameters for complex-CT-DNA systems

	UV-Vis titration		**EB fluorescence quenching titration**				
Complex	K_b (10^5 M^{-1})	ΔG/k $Jmol^{-1}$	K_{sv} (10^4 M^{-1})	K_{app} (10^6 M^{-1})	k_q (10^{11} M^{-1} s^{-1})	K_F (10^3 M^{-1})	*n*
PdL$_5$	4.99 ± 0.50	-32.51	2.11 ± 0.13	10.76 ± 0.77	9.17 ± 0.32	2.17 ± 0.36	0.74
PdL$_6$	3.66 ± 0.41	-31.74	0.59 ± 0.02	8.43 ± 0.43	6.92 ± 0.11	1.81 ± 0.01	1.09
PdL$_7$	1.38 ± 0.32	-29.32	0.11 ± 0.01	0.80 ± 0.15	0.48 ± 0.02	0.21 ± 0.01	0.79
PdL$_8$	5.54 ± 0.51	-32.77	2.64 ± 0.22	14.71 ± 0.91	11.49 ± 0.81	6.00 ± 0.12	0.82

4.2.7 BSA interactions

4.2.7.1 Fluorescence quenching measurements

In the current study, BSA was chosen as the model protein because of its structural homology with human serum albumin, remarkable ligand binding properties, and availability. The fluorescence quenching effect was examined over the emission wavelength range of 240-320 nm. As shown in Figures 4.15a (**PdL$_8$**), the addition of these complexes to BSA solution, resulted to a considerable decrease in the fluorescence intensity of BSA at 281 nm, proving the interaction of the complexes with BSA. The binding constants, K_{sv}, and k_q were obtained from Stern–Volmer equation (Figure 4.15b for **PdL$_8$**). Conversely, K_F and n values were computed from the Scatchard equations, Figure 4.15c for **PdL$_8$**. The values of K_{SV}, k_q, K_F, and n are shown in Table 4.4. The K_{SV} values (10^5 M^{-1}) for complexes **PdL$_5$-PdL$_8$** indicate that the interaction process is not fully controlled by diffusion [44]. The obtained k_q values (> 10^{13} M^{-1} s^{-1}) which are greater than diverse kinds of dynamic quenchers (2.0 x 10^{10} M^{-1} s^{-1}), suggest the existence of static quenching mechanism [45]. The K_F values (≈ 10^6 or 10^7 M^{-1}) for **PdL$_5$-PdL$_8$** are within the optimal range, they are high enough to ensure that considerable amounts of the complexes are comfortably bound and transported to the desired target cells and can be released reversibly when arriving at the diseased cells affinity [46]. The values of n which are close to 1, demonstrate that only one binding site of BSA is accessible for interaction with the Pd-complexes. The magnitude of the BSA binding follow the order, **PdL$_8$** > **PdL$_6$** > **PdL$_7$**, and **PdL$_5$ > PdL$_6$**, and thus matching the kinetic reactivity trend of the complexes.

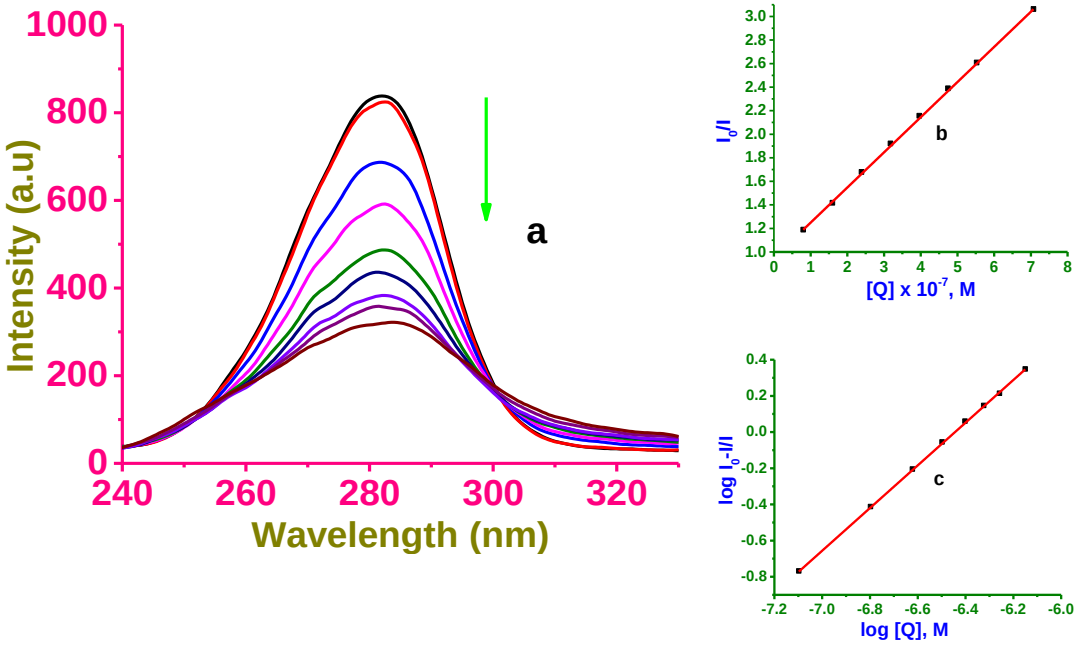

Figure 4.15: (a); Fluorescence emission spectra of BSA in the absence and presence of **PdL$_8$**: [BSA] = 12.0 μM and [**PdL$_8$**] = 0-200 μM. The arrow shows the intensity changes upon increasing the **PdL$_8$** concentration. (b): Stern-Volmer plot of I_o/I versus [Q] and (c): Scatchard plot of log[(I_o–I)/I] *vs* log[Q].

Table 4.5: The binding constant, quenching constants and number of binding sites for the Pd(II) complexes with BSA

Complex	**K_{sv} x 10^6, M^{-1}**	**k_q x 10^{13}, M^{-1} s^{-1}**	**K_F x 10^6, M^{-1}**	**n**
PdL$_5$	2.12 ± 0.13	9.22 ± 0.51	6.70 ± 0.11	1.08
PdL$_6$	2.08 ± 0.24	9.07 ± 0.34	3.24 ± 0.22	1.03
PdL$_7$	1.35 ± 0.21	5.85 ± 0.33	1.00 ± 0.12	1.17
PdL$_8$	2.99 ± 0.14	12.98 ± 0.53	40.16 ± 0.66	1.17

4.2.8 Biomolecular simulations

Molecular docking was carried out to examine the interactions between the synthesised compounds **PdL_5-PdL_8** and DNA. The Compounds **PdL_5-PdL_8** were docked into the binding site of DNA as depicted in Figure 4.16. The properties of binding within specific distance and binding energies of each complexes are shown in Table 4.6. Hydrogen and pi-cation interactions were involved between **PdL_5-PdL_8** and DNA. Complexes **PdL_5-PdL_8** interacted with the thymine base of the B strand of the DNA by hydrogen bonding with the amino groups of their ring structures. **PdL_6** also interacted with adenine bases at positions 6 and 9 with pi-cation interaction. **PdL_5** and **PdL_7** interacted with the thymine of the DNA at position 7 with two hydrogen bonds of different amino groups. Although, no hydrogen interaction was involved in the binding of **PdL_8** to DNA, **PdL_8** interacted with the two strands of the DNA with pi-cation bonds. Interestingly, **PdL_8** bonded with adenine at the 6th position of different strands of the DNA with the same amino group of its ring. The docked energies between these complexes were relatively the same (-12 ± 0.7 Kcal/mol), with very favourable best docked conformation. Complexes **PdL_5-PdL_8** exhibited good binding affinities towards DNA. The energy calculation results ranked **PdL_8** as the most energetically favoured interaction with DNA with a ΔG bind of -50.59 Kcal/mol, while **PdL_5** is least favoured with ΔG bind of 41.94 Kcal/mol. (Table 4.6). Though **PdL_5-PdL_8** are not planar (as depicted Figure 4.10), the docked images in Figure 4.17 demonstrate intercalation binding mode (proper intercalating gap) in tandem with the experimental data.

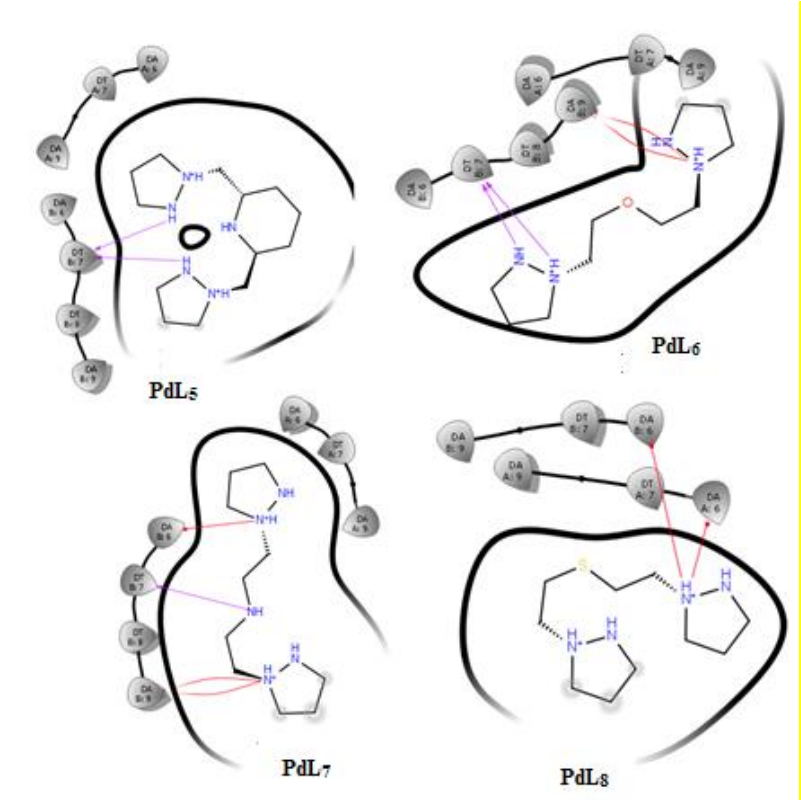

Figure 4.16: 2D interaction of **PdL5-PdL8** with DNA. Red arrows indicate pi-stacking, pink arrows indicate hdrogen bond interaction, and red lines depict pi-cation interactions.

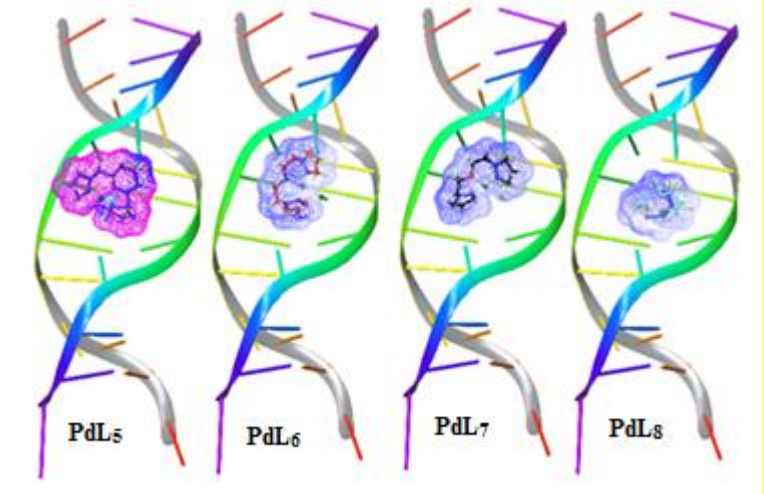

Figure 4.17: Docked images of DNA-**PdL5-PdL8** interactions, indicating intercalative mode of action corroborating the experimental results.

Table 4.6: Interaction properties of complexes DNA-Pd(II) complexes analysed by XP visualizer and MM-GBSA module.

Complex	Dock score	MM-GBSA	H-bond (Å)	Pi-cation (Å)
DNA-PdL$_5$	-12.5	-41.94	Thymine^{7b} (2.24, 2.76)	-
DNA-PdL$_6$	-12.7	-43.42	Thymine^{7b} (2.14)	Adenine^{6b,9b} (4.27, 4.37, 4.60)
DNA-PdL$_7$	-12.3	-49.33	Thymine^{7b} (2.20,2.22)	Adenine^{9b} (3.72, 3.83)
DNA-PdL$_8$	-12.6	-50.95	-	Adenine^{6a,6b} (3.29, 4.57)

Note: Superscript numbers indicate the position of the base while letters shows the type of strand. Numbers indicated within brackets represent the distance of interecting atoms in Amstrong (Å). The more negative the relative binding energy, the stronger the binding between DNA and **PdL$_5$-PdL$_8$**. Generally, the lower relative binding energies of the complexes could be ascribed to their lack of planarity and non-symmetrical nature (as shown in DFT studies, Figure 4.10).

4.2.9 *In vitro* cytotoxicity assay

The cytotoxic effects were examined by MTT assay against cultured tumour cell line HeLa, with cisplatin as the reference (**PdL$_5$-PdL$_8$** being stable in the DMSO media). The cells were exposed at different concentrations (6.25-100 µM) for a period of 48 h (Figure 4.18), and the values are reported in Table 4.6. The percentage of cell viability gradually decreased with the increasing concentration of the complexes (Figure 4.18), indicative of the dose-response sensitive of the complexes on the cell lines. Despite having stronger and reasonable DNA/BSA interactive capabilities (Tables 4.4 and 4.5), the complexes demonstrate significantly lower antiproliferative cellular activities than cisplatin (Table 4.7). Minimal inhibitory effects of the examined complexes as indicated by their high IC_{50} values is ascribed to their limited solubility in DMSO, π-conjugation, lipophilicity, and lower cell membrane permeability [47-49]. The lower activity of the complexes could also be attributable to the resistant nature of HeLa cell compared to other cancer cell type [50]. Also, the relatively low kinetic reactivity of the complexes could account for their lower cytotoxic effects, indicating that high kinetic reactivity favours the formation of metal-sulfur adduct which protect the complexes from reacting with the other biomolecules, allowing the drug to reach DNA in sufficient concentration and in a timely manner [51].

Overall, the results show that cytotoxic effects of the compounds is not just a consequence of DNA/BSA binding, but may also be controlled by other factors.

Table 4.7: Cytotoxic effects (% of negative control) of **PdL_5-PdL_8** on the HeLa cell line[a]

µM	6.25	12.5	25	50	100	IC_{50}
PdL_5	130.9 ± 8.3	132.6 ± 2.3	123.2 ± 5.5	114.0 ± 14.4	93.9 ± 27.2	148.6 ± 13.5
PdL_6	133.7 ± 8.7	127.0 ± 13.7	131.5 ± 29.6	101.2 ± 4.5	83.9 ± 10.5	220.7 ± 18.9
PdL_7	129.2 ± 1.5	107.4 ± 29.9	114.3 ± 9.3	101.9 ± 10.7	90.3 ± 6.8	384.6 ± 33.5
PdL_8	109.3 ± 31.7	115.3 ± 32.2	122.7 ± 9.1	109.3 ± 5.0	88.9 ± 2.5	248.3 ± 31.6
Cisplatin						11.4 ± 3.5

[a]The values (as % of negative control) were obtained using the MTT assay after 48 h drug exposure at different concentrations. The results are expressed as mean ± SD of at least two independent experiments. The SI values were not computed due to the inactivity of the complexes.

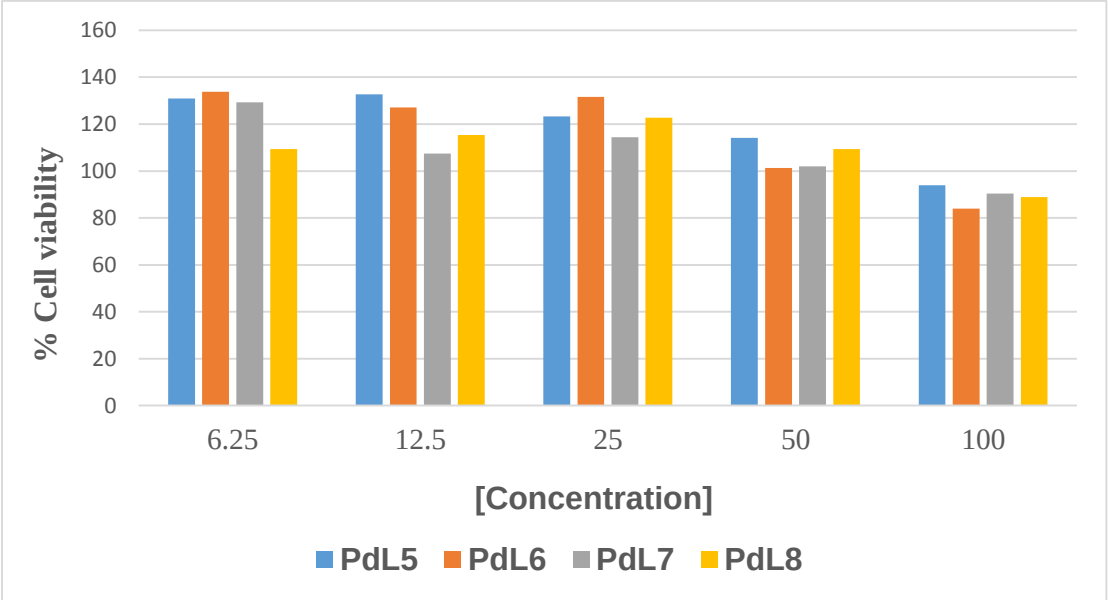

Figure 4.18: Percentage cell viability of complexes **PdL_5-PdL_8** on HeLa cells after 48 h of treatment assessed by MTT assay. Each bar represents the mean ± SEM of triplicate viability values obtained as cellular (cytotoxic) response to treatment with the indicated.

4.3 Conclusions

A series of Pd(II) complexes of NEN pincer ligands have been successfully synthesised and structurally characterised by various spectroscopic techniques. The solid-state structure of the complexes show coordination of tridentate ligand in NEN (where E = N, O, and S) fashion. In these complexes, the Pd(II) ion display a slightly distorted square planar coordination geometry, with one tridentate and chloro ligand. The current work demonstrates that the versatile kinetic behaviours of Pd(II) complexes is dependent on the strength of the σ- donor and π-acceptor character of the *trans* atom on the carrier ligand. The values of activation parameters signify associative mechanism for the substitution process. Based on the kinetic observations and evaluated activation parameters a plausible associative mechanism is proposed for the ligand substitution process. The trend of substitution kinetics was substantiated by DFT results. The *iso*-kinetic linear relationships between $\Delta H^{\neq}$ and $\Delta S^{\neq}$ support a single reaction pathway of the studied Pd(II) complexes with the three entering ligands. The calculated CT-DNA/BSA binding constants indicate strong and favourable binding affinity of the complexes. The mode of binding between the complexes and CT-DNA/BSA was identified as intercalative. The order of DNA/BSA binding is consistent with the substitution kinetics. The *in* vitro cytotoxicity of the complexes reveals minimal activity in comparison to cisplatin.

4.4 References

[1] N. Joksimović, N. Janković, J. Petronijević, D. Baskić, S. Popovic, D. Todorović, M. Zarić, O. Klisurić, M. Vraneš, A. Tot, Med Chem. 16 (2020) 78-92.

[2] X. Wei, Y. Yang, J. Ge, X. Lin, D. Liu, S. Wang, J. Zhang, G. Zhou, S. Li, J. Inorg. Biochem. 202 (2020) 110857.

[3] A.A. Franich, M.D. Živković, D. Ćoćić, B. Petrović, M. Milovanović, A. Arsenijević, J. Milovanović, D. Arsenijević, B. Stojanović, M.I. Djuran, J. Biol. Inorg. Chem. 24 (2019) 1009-1022.

[4] M.A. Lima, V.A. Costa, M.A. Franco, G.P. de Oliveira, V.M. Deflon, F.V. Rocha, Inorg. Chem. Commun. 112 (2020) 107708.

[5] S.G. Churusova, D.V. Aleksanyan, E.Y. Rybalkina, O.Y. Susova, V.V. Brunova, R.R. Aysin, Y.V. Nelyubina, A.S. Peregudov, E.I. Gutsul, Z.S. Klemenkova, Inorg. Chem. 56 (2017) 9834-9850.

[6] M. Muralisankar, S.M. Basheer, J. Haribabu, N.S. Bhuvanesh, R. Karvembu, A. Sreekanth, Inorg. Chim. Acta. 466 (2017) 61-70.

[7] T.T.H. Fong, C.N. Lok, C.Y.S. Chung, Y.M.E. Fung, P.K. Chow, P.K. Wan, C.M. Che, Angew. Chem. Int. Ed. 55 (2016) 11935-11939.

[8] Ž.D. Bugarčić, G. Liehr, R. van Eldik, Journal of the Chemical Society, Dalton Trans. (2002) 951-956.

[9] J. Bogojeski, R. Jelić, D. Petrović, E. Herdtweck, P.G. Jones, M. Tamm, Ž.D. Bugarčić, Dalton Trans. 40 (2011) 6515-6523.

[10] Ž.D. Bugarčić, B. Petrović, E. Zangrando, Inorg. Chim. Acta. 357 (2004) 2650-2656.

[11] T. Soldatović, M. Shoukry, R. Puchta, Ž.D. Bugarčić, R. van Eldik, Eur. J. Inorg. Chem. 2009 (2009) 2261-2270.

[12] D. Jaganyi, F. Tiba, O.Q. Munro, B. Petrović, Ž.D. Bugarčić, Dalton Trans. (2006) 2943-2949.

[13] D.O. Onunga, D. Jaganyi, A. Mambanda, J Coord Chem. (2019) 1-17.

[14] D. Ćoćić, S. Jovanović, S. Radisavljević, J. Korzekwa, A. Scheurer, R. Puchta, D. Baskić, D. Todorović, S. Popović, S. Matić, J. Inorg. Biochem. 189 (2018) 91-102.

[15] R.O. Omondi, R. Bellam, S.O. Ojwach, D. Jaganyi, A.A. Fatokun, J. Inorg. Biochem. (2020) 111156.

[16] T.N. Sorrell, M.R. Malachowski, Inorg. Chem. 22 (1983) 1883-1887.

[17] J. García-Antón, J. Pons, X. Solans, M. Font-Bardia, J. Ros, Eur. J. Inorg. Chem. 2003 (2003) 3952-3957.

[18] A. S. Potapov, E. A. Nudnova, G. A. Domina, L. N. Kirpotina, M. T.Quinn, A. I. Khlebnikov, I. A. Schepetkin, *Dalton Trans*. 23 (2009) 4488-4498.

[19] L. Yang, D.R. Powell, R.P. Houser, Dalton Trans. (2007) 955-964.

[20] S.R.I. Cooper, CrystEngComm. 22 (2020) 7186.

[21] F.H. Allen, Crystallogr. B 58 ((2002)) 380-388.

[22] C.R. Groom, I.J. Bruno, M.P. Lightfoot, S.C. Ward, Acta Crystallogr., Sect. B: Struct. Sci., Cryst. 72 (2016) 171-179.

[23] T. Brinck, A.N. Borrfors, J. Mol. Model. 25 (2019) 1-9

[24] S.V. Nkabinde, G. Kinunda, D. Jaganyi, Inorg. Chim. Acta. 466 (2017) 298-307.

[25] B. Pitteri, M. Bortoluzzi, G. Marangoni, Transition Met. Chem. 30 (2005) 1008-1013.

[26] T.M. Miller, B. Bederson, Adv. At. Mol. Opt. Phys 13 (1978), 1-55.

[27] M.M. Ghahremanpour, P.J. van Maaren, C. Caleman, G.R. Hutchison, D. Van der Spoel, J. Chem. Theory Comput. 14(2018) 5553-5566.

[28] M. Kosović, S. Jovanović, G.A. Bogdanović, G. Giester, Ž. Jaćimović, Ž.D. Bugarčić, B. Petrović, J Coord Chem. 69 (2016) 2819-2831.

[29] M. Kosović, Ž. Jaćimović, Ž.D. Bugarčić, B. Petrović, J Coord Chem. 68 (2015) 3003-3012.

[30] D. Jaganyi, A. Hofmann, R. van Eldik, Angew Chem Int Ed. 40 (2001) 1680-1683.

[31] S. Jovanović, K. Obrenčević, Ž.D. Bugarčić, I. Popović, J. Žakula, B. Petrović, Dalton Trans. 45 (2016) 12444-12457.

[32] J.D. Atwood, Inorganic and organometallic reaction mechanisms, VCH Publishers, 1997.

[33] M. Tobe, J. Burgess, Inorganic reaction mechanisms, Addison Wiley, 1999.

[34] R. Bellam, D. Jaganyi, A. Mambanda, R. Robinson, New J. Chem. 42 (2018) 12557-12569.

[35] R. Bellam, D. Jaganyi, A. Mambanda, R. Robinson, M.D. BalaKumaran, RSC Adv. 9 (2019) 31877-31894.

[36] X.-Q. Zhou, Q. Sun, L. Jiang, S.-T. Li, W. Gu, J.-L. Tian, X. Liu, S.-P. Yan, Dalton Trans. 44 (2015) 9516-9527.

[37] R.K. Vuradi, K. Dandu, P.K. Yata, R.R. Mallepally, N. Chintakuntla, R. Ch, S.S. Thakur, C.M. Rao, S. Satyanarayana, New J. Chem. 42 (2018) 846-859.

[38] R.O. Omondi, R. Bellam, S.O. Ojwach, D. Jaganyi, A.A. Fatokun, J. Inorg. Biochem. 210 (2020) 111156.

[39] D.O. Onunga, R. Bellam, G.K. Mutua, M. Sitati, M.D. BalaKumaran, D. Jaganyi, A. Mambanda, J. Inorg. Biochem. 213 (2020) 111261.

[40] S. Mukherjee, I. Mitra, C. Fouzder, S. Mukherjee, S. Ghosh, U. Chatterji, S.C. Moi, J. Mol. Liq. 247 (2017) 126-140.

[41] K. Karami, M. Alinaghi, Z. Amirghofran, J. Lipkowski, Inorg. Chim. Acta. 471 (2018) 797-807.

[42] M. Cory, D.D. McKee, J. Kagan, D. Henry, J.A. Miller, J. Am. Chem. Soc. 107 (1985) 2528-2536.

[43] I. Mitra, S. Mukherjee, B. Misini, P. Das, S. Dasgupta, W. Linert, S.C. Moi, New J. Chem. 42 (2018) 2574-2589.

[44] M.M. Milutinović, A. Rilak, I. Bratsos, O. Klisurić, M. Vraneš, N. Gligorijević, S. Radulović, Ž.D. Bugarčić, J. Inorg. Biochem. 169 (2017) 1-12.

[45] D.M. Poloni, O. Dangles, J.A. Vinson, J. Agric. Food. Chem. 67 (2019) 9139-9147.

[46] L. Fetzer, B. Boff, M. Ali, M. Xiangjun, J.-P. Collin, C. Sirlin, C. Gaiddon, M. Pfeffer, Dalton Trans. 40 (2011) 8869-8878.

[47] X.-Q. Zhou, Y. Li, D.-Y. Zhang, Y. Nie, Z.-J. Li, W. Gu, X. Liu, J.-L. Tian, S.-P. Yan, Eur. J. Med. Chem. 114 (2016) 244-256.

[48] G. Ayyannan, M. Mohanraj, M. Gopiraman, R. Uthayamalar, G. Raja, N. Bhuvanesh, R. Nandhakumar, C. Jayabalakrishnan, Inorg. Chim. Acta. (2020) 119868.

[49] K. Karami, M. Hosseini-Kharat, H. Sadeghi-Aliabadi, J. Lipkowski, M. Mirian, Eur. J. Med. Chem. 73 (2014) 8-17.

[50] G. Matlashewski, L. Banks, D. Pim, L. Crawford, Eur. J. Biochem. 154 (1986) 665-672.

[51] R.O. Omondi, S.O. Ojwach, D. Jaganyi, Inorg. Chim. Acta. (2020) 119883.

CHAPTER 5

Role of π-conjugation on the coordination behaviour, substitution kinetics, DNA/BSA interactions, and *in vitro* cytotoxicity of carboxamide palladium(II) complexes

5.1. Introduction

The control of the kinetic reactivity of metal complexes can be achieved *via* careful manipulation of the steric and electronic properties of the spectator ligands [1-6]. Pi- conjugated ligands coordinated to metal complexes influence their reactivity through electronic and steric effects as well as their interactions with the DNA nucleobases [7-9]. Pd(II) complexes bearing pi-conjugated ligands are known to be highly reactive, ascribed to the ability of the ligands to accept electrons from the metal centre resulting to the stabilisation of the five coordinate intermediate compared to ground state [10]. To circumvent the problem of high kinetic lability of these conjugated systems, Petrović and co-workers have coupled various sterically bulk ligands to tune rate of substitution kinetics of conjugated systems and their resultant anti-tumour activities of Pd(II) complexes [11]. In their previous work, the group examine the competing effects of π-back-donation and σ-donating ligands on the reactivity, DNA/BSA interactions and anticancer properties of cojugated dinuclear Pd(II) complexes [12]. Complexes with π-acceptor ligands demonstrated enhanced reactivity and biological efficacy compared to those with σ-donor ligands. In another development, Jaganyi and co-workers [13] used pi-conjugated ligands to control the reactivity, DNA interactions and *in vitro* cytotoxic effects of Pd(II) complexes. The results of their investigations showed that stronger π-back donation enhances substition kinetics, DNA binding strength and cytotoxicity. In the recent past, Jaganyi and the group have established that the effect of π-conjugation on reactivity of metal based complexes depend entirely on their position relative to the leaving group [7,8, 14].

In chapter four of the thesis, we largely attributed the mininimal inhibitory effects of the examined complexes to low π-conjugation, lipophilicity and cell membrane permeability. Noteworthy, pi-

conjugated ligands increase the lipophilic character (which consist of negatively charged lipophilic phospholipids) of the metal complexes, improving their cellular uptake and thus better cytotoxic effects [15]. Also, pi-conjugated systems are able to intercalate with DNA easily (causing lengthening, stiffening, and unwinding of DNA double helix) [16], giving rise to compounds that possess better anti-tumour profiles. Thus in this chapter, we aim to to investigate the influence of π-conjugation on the substitution kinetics, DNA/BSA interactions and antiproliferative activities of Pd(II) complexes. The study reports the synthesis, structural characterisation of Pd(II) complexes anchored on some carboxamide ligands, with their substitution kinetics using S-/N-donor biologically relevant nucleophiles; thiourea (**Tu**), L-methionine (**L-Met**), and guanosine-5'-monophosphate (**5'-GMP**). DNA/BSA interactions and their cytotoxicity against a wide range of cell lines have also been investigated and are herein discussed.

5.2. Results and discussion

5.2.1. Syntheses and characterisation of the compounds

Ligands **L_9-L_{12}** were obtained in good yields (72-76%) from condensation reactions between corresponding carboxylic acid derivatives and the appropriate amines following modified literature procedures [17] (Scheme 5.1). Reactions of **L_9-L_{12}** with $PdCl_2(NCMe)]_2$ in a 1:1 mole ratio in CH_2Cl_2 produced the respective Pd(II) complexes (**PdL_9-PdL_{12})** in moderate to good yields (60-76%) as depicted in Scheme 5.1 (section 2.3). The ligands **L_9-L_{12}** and their corresponding Pd(II) complexes were characterised using ^1H and ^{13}C NMR, and FT-IR spectroscopies, mass spectrometry, elemental analyses and in some cases (**PdL_{10}-PdL_{12}**), using single crystal X-ray analyses.

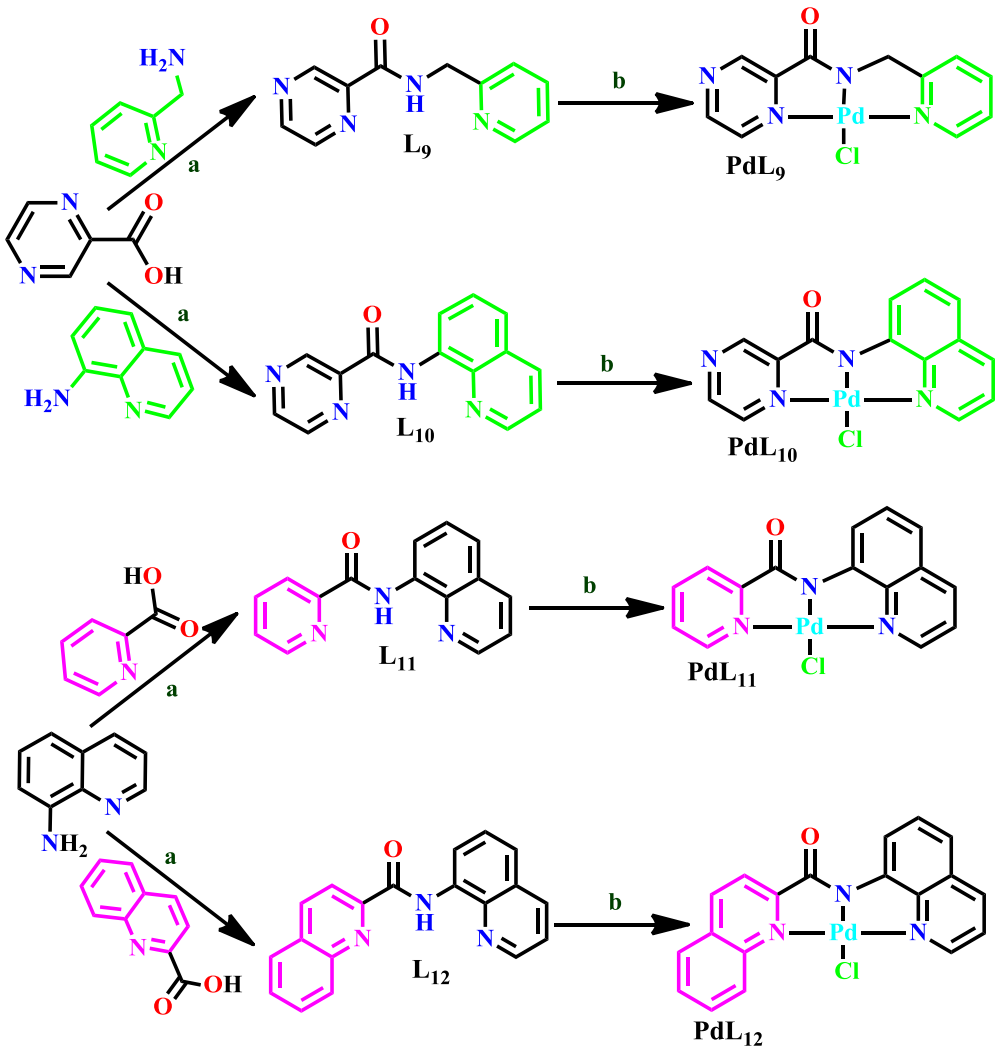

Scheme 5.1: Synthetic pathways for ligands **L9-L12** and their respective Pd(II) complexes (**PdL9-PdL12**). *Reagents and conditions*; (**a**) TPhP, pyridine, 100 °C, 12 h; (**b**) $PdCl_2(NCCH_3)_2$, CH_2Cl_2, 12 h.

In a typical ^{1}H NMR spectrum, the amidic NH proton in the ligands was useful in determination of the formation of their corresponding Pd(II) metal complexes. As an illustration, in the ^{1}H NMR spectrum of **L11**, the amide N-H protons appeared as a singlet at δ 12.17 ppm, and upon complexation (**PdL11**), the N-H peak was not observed, confirming the N-H deprotonation (Figure 5.1). The formation of the Pd(II) complexes was also derived from their ^{13}C NMR spectra. For instance, the carbonyl signal in the spectra of ligand **L11** and complex **PdL11** were observed at nearly the same regions of 161.84 ppm 166.18 ppm (Figure 5.2). This was indicative of the carbonyl O-atom not coordinating to the Pd-atom.

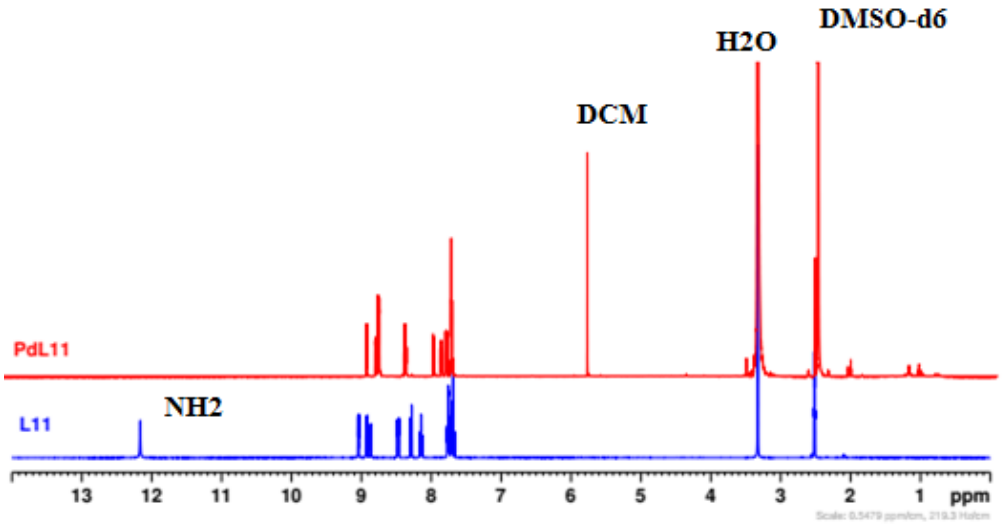

Figure 5.1: Overlays of ^{1}H NMR spectra of ligand **L$_{11}$** and respective complex **PdL$_{11}$** in DMSO-d6, the amidic N-H proton at 12.17 ppm (**L$_{11}$**) disappearing upon complexation (**PdL$_{4}$**).

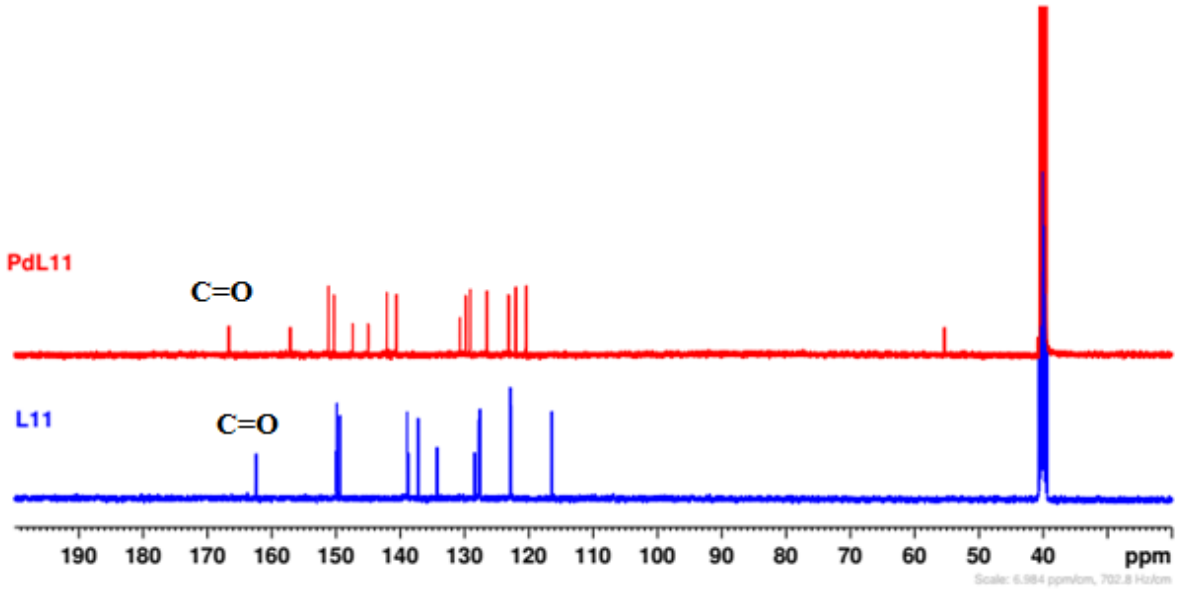

Figure 5.2: Overlays of ^{13}C NMR spectra of ligand **L$_{11}$** and complex **PdL$_{11}$** in DMSO-d6, displaying the C=O signals at 161.84 (**L$_{11}$**) and 166.18 ppm (**PdL$_{11}$**) almost at the same regions. Suggesting that the carbonyl O atom does not coordinate to the Pd(II) ion.

The identities of complexes **PdL$_{9}$-PdL$_{12}$** were further confirmed by comparing their FT-IR spectra to their corresponding ligands (Figure 5.3). For example, the amidic N-H band of **L$_{11}$** was recorded around

3290 cm^{-1}, and is absent in the spectrum of the respective **PdL$_{11}$**, and the observation is in good agreement with the ^{1}H NMR data [18]. In contrast to the NMR trends, the sharp C=O stretching band at 1671 cm^{-1} in **L$_{11}$** is shifted to lower frequencies at 1633 cm^{-1} in **PdL$_{11}$**. This could be ascribed to the resonance enhancement of the deprotonated amide, resulting in the weakening of the C=O bond [19]. Our attempts to analyse the mass spectra (both LC-MS and TOF-MS) of complexes **PdL$_{9}$-PdL$_{12}$** were unsatisfactory. Elemental analyses data of all complexes **PdL$_{9}$-PdL$_{12}$** were consistent with the empirical formulae of the proposed structures in Scheme 5.1 and proved their purity in bulk state.

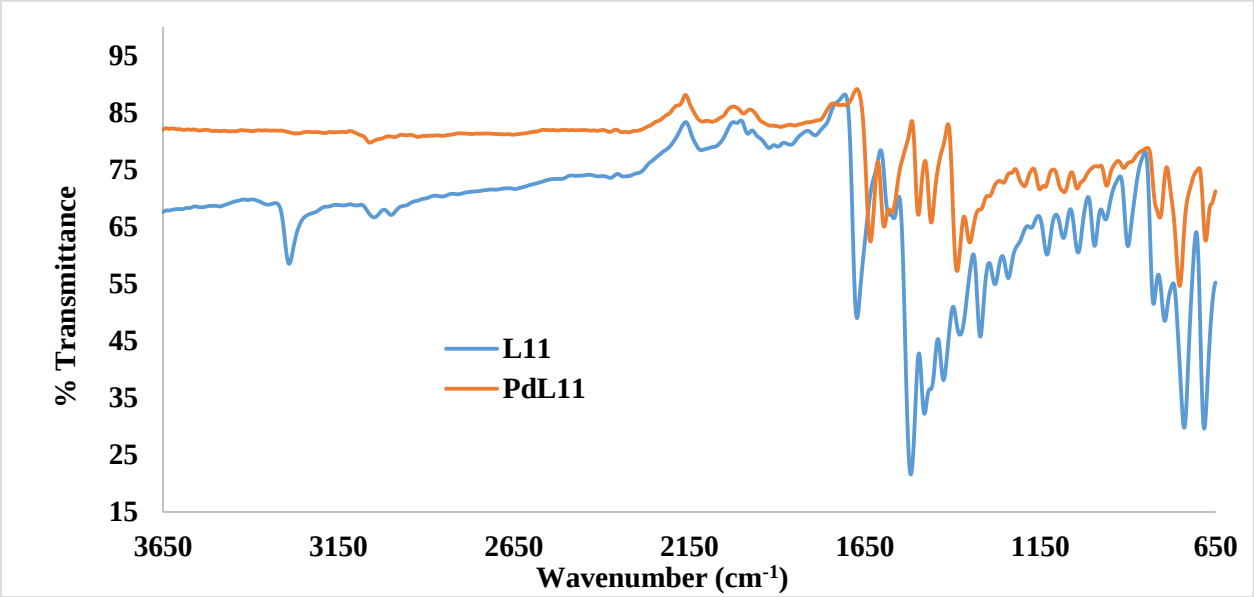

Figure 5.3: Overlays of FT-IR spectra of ligand **L$_{11}$** and respective complex **PdL$_{11}$**; the υ (N-H) at 3290 cm^{-1} disappears upon complexation (**PdL$_{11}$**). The absorption band υ (C=O) at 1671 cm^{-1} (**L$_{11}$)** is also shifted to 1633 cm^{-1} (**PdL$_{11}$**)

5.2.2. Solid-state structures of complexes PdL$_{10}$-PdL$_{12}$

Single crystals of complexes **PdL$_{10}$-PdL$_{12}$** suitable for X-ray analyses were grown from their CH_2Cl_2/Et_2O solutions at room temperature. The molecular structures of **PdL$_{10}$**, **PdL$_{11}$**, and **PdL$_{12}$** are

shown in Figures 5.4, 5.5, and 5.6, respectively, while their crystallographic data and structural refinement parameters are presented in Table 5.1.

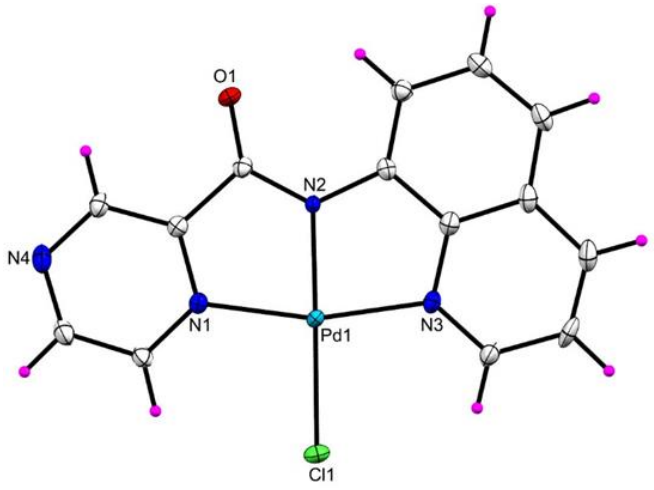

Figure 5.4: Molecular structure of **PdL_{10}**, with atom numbering Scheme. The displacement ellipsoids of atoms are shown at the 50% probability level. Selected bond lengths [Å]: Pd(1)-N(3), 1.961(2); Pd(1)-N(1), 2.014(2); Pd(1)-N(2), 1.961(2); Pd(1)-Cl(1), 2.3191(6). Selected bond angles (°): N(3)-Pd(1)-N(1), 164.30(9); N(3)-Pd(1)-N(2), 82.89(8); N(1)-Pd(1)-N(2), 81.41(8); N(3)-Pd(1)-Cl(1), 97.88(7); N(1)-Pd(1)-Cl(1), 97.81(6); N(2)-Pd(1)-Cl(1), 179.22(6).

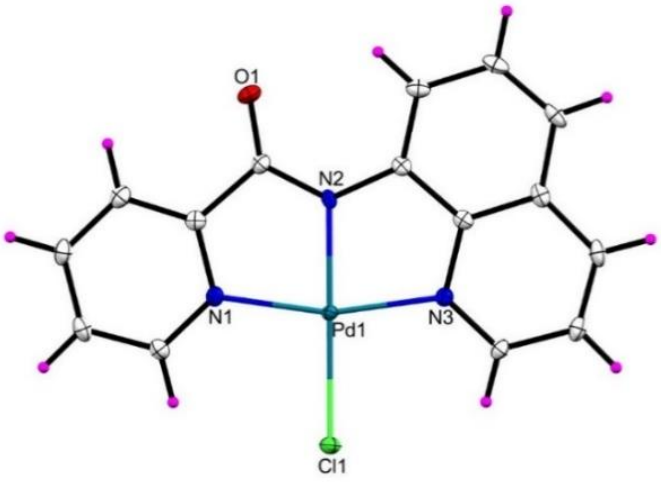

Figure 5.5: Molecular structure of **PdL_{11}**, with atom numbering Scheme. The displacement ellipsoids of atoms are shown at the 50% probability level. Selected bond lengths [Å]: Pd(1)-N(3), 2.017(16); Pd(1)-N(1), 2.022(16); Pd(1)-N(2), 1.980(15); Pd(1)-Cl(1), 2.315(5). Selected bond angles (˚): N(3)-Pd(1)-N(1), 164.12(7); N(3)-Pd(1)-N(2), 82.47(6); N(1)-Pd(1)-N(2), 81.65(6); N(3)-Pd(1)-Cl(1), 97.69(5); N(1)-Pd(1)-Cl(1), 98.69(5); N(2)-Pd(1)-Cl(1), 179.74(5).

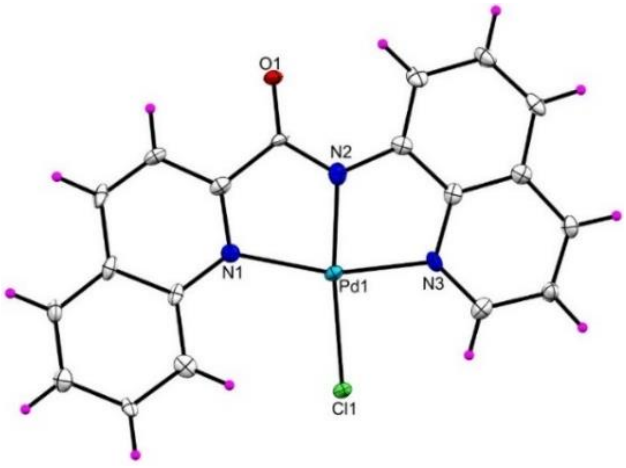

Figure 5.6: Molecular structure of **PdL_{12}**, with atom numbering Scheme. The displacement ellipsoids of atoms are shown at the 50% probability level. Selected bond lengths [Å]: Pd(1)-N(3), 2.024(8); Pd(1)-N(1), 2.113(7); Pd(1)-N(2), 1.959(9); Pd(1)-Cl(1), 2.328(2). Selected bond angles (˚): N(3)-Pd(1)-N(1); 162.5(3); N(3)-Pd(1)-N(2), 81.5(3); N(1)-Pd(1)-N(2), 81.1(3); N(3)-Pd(1)-Cl(1), 91.6(2); N(1)-Pd(1)-Cl(1), 105.9(2); N(2)-Pd(1)-Cl(1), 172.1(3).

Table 5.1: Summary of crystallographic data and structure refinement details for complexes **PdL$_{10}$-PdL$_{12}$**

Parameter	**PdL$_{10}$**	**PdL$_{11}$**	**PdL$_{12}$**
Empirical formula	$C_{14}H_9ClN_4OPd$	$C_{15}H_{10}ClN_3OPd$	$C_{19}H_{12}ClN_3OPd$
Formula weight	391.10	390.11	440.17
Temperature (K)	100(2)	100(2)	101(2)
Wavelength (Å)	0.71073	0.71073	0.71073
Crystal system	Triclinic	Monoclinic	Monoclinic
Space group	P -1	P 21/ c	P n
Unit cell dimension			
a (Å)	8.8485(6)	17.9471(14)	4.5553(3)
b (Å)	10.7306(8)	4.5613(4)	18.3946(3)
c (Å)	15.2015(11)	17.8033(14)	9.1957(4)
α (°)	88.126(3)	90	90
β (°)	74.988(3)	114.681(4)	94.978(2)
γ (°)	69.294(3)	90	90
Volume (Å^3)	1301.30(16)	1324.28(19)	767.63(12)
Z	4	4	2
Density (Mg/m^3)	1.996	1.957	1.904
Absorption coefficient (mm^{-1})	1.634	1.603	1.395
F(000)	768	768	436
Theta range for data collection (°).	1.390 to 28.306°.	2.30 to 28.93°	1.107 to 28.116°.

The Pd centres in **PdL$_{10}$**, **PdL$_{11}$** and **PdL$_{12}$**, are ligated by N^N^N pincer and chloride motifs, forming two five-membered metal chelate rings. The dihedral angles, for examples N(1)-Pd(1)-N(2) of 81.41(8)˚, 81.65(6)˚, and 81.1(3)˚ for **PdL$_{10}$**, **PdL$_{11}$**, and **PdL$_{12}$**, respectively deviate from the expected 90˚. Also the bite angles N(3)–Pd(1)–N(1) of 164.30(9)˚ (**PdL$_{10}$**), 164.12(7)˚ (**PdL$_{11}$**), 162.5(3)˚ (**PdL$_{12}$**)

depart significantly from the regular linearity (180º). Thus, the geometry around the Pd(II) atom in compounds **PdL$_{10}$-PdL$_{12}$**, can best be described as distorted square-planar [20]. Noticeably, the dihedral angle N(1)-Pd(1)-N(2) for the five-membered ring, N(1)-Pd(1)-N(2) (**PdL$_{10}$-PdL$_{12}$**) are statistically similar. However, the angles N(3)-Pd(1)-N(2) of 82.89(8)˚, 82.47(6)˚ for **PdL$_{10}$** and **PdL$_{11}$**, respectively are appreciably larger than the N(3)-Pd(1)-N(2) of, 81.5(3)˚ for **PdL$_{12}$**, possibly due to the steric constraint imposed by the quinoline moiety in **PdL$_{12}$**. The equatorial bond lengths of Pd(1)-N(3), 2.043(14), 2.024(8) and 2.017(16) Å for **PdL$_{10}$**, **PdL$_{11}$**, and **PdL$_{12}$**, respectively are statistically similar. The average bond length of Pd(1)-N(3) for compounds **PdL$_{10}$-PdL$_{12}$** is within the average bond distances of 2.024 ± 0.020 Å averaged for 33 structures [21]. The Pd(1)-Cl(1) bond lengths of 2.3191(6) (**PdL$_{10}$**), 2.315(5) (**PdL$_{11}$**), and 2.328(2) Å (**PdL$_{12}$**) compare well with the mean of 2.327 ± 0.016 Å reported for 35 similar structures [22].

5.2.3 Computational optimisation and calculations

Computational optimisation and calculations were performed to gain a proper understanding of the electronic and structural properties of Pd(II) complexes. DFT-optimised geometry, mappings of the frontier orbitals and planarity of the complexes are shown in Figure 5.7, while selected geometrical data are summarised in Table 5.2. The optimised geometries show that the HOMO electron density are mainly localised on the *4d*-orbitals of Pd(II) metal, carboxamide, quinoline moiety, and the chloride ligand. The HOMOs on the Pd(II) metal indicates possible transfer of electrons from the metal centre to the spectator ligand(s). On the other hand, the LUMOs are predominately distributed on the pyrazine, pyridine, and quinoline units. This distribution of LUMO electrons on the pyrazine, pyridine, and quinoline units, indicates their potential π-acceptor ability of chelated ligand(s). The strength of the pi-acceptor ability of the ligand systems in the complexes is influenced by the more negative value of ε_{LUMO}, which decreases from **PdL$_{9}$-PdL$_{12}$**, Table 5.2. Noticeably, $\Delta E_{LUMO-HOMO}$ decreases with the increasing π-acceptor ability of the inert chelating ligand.

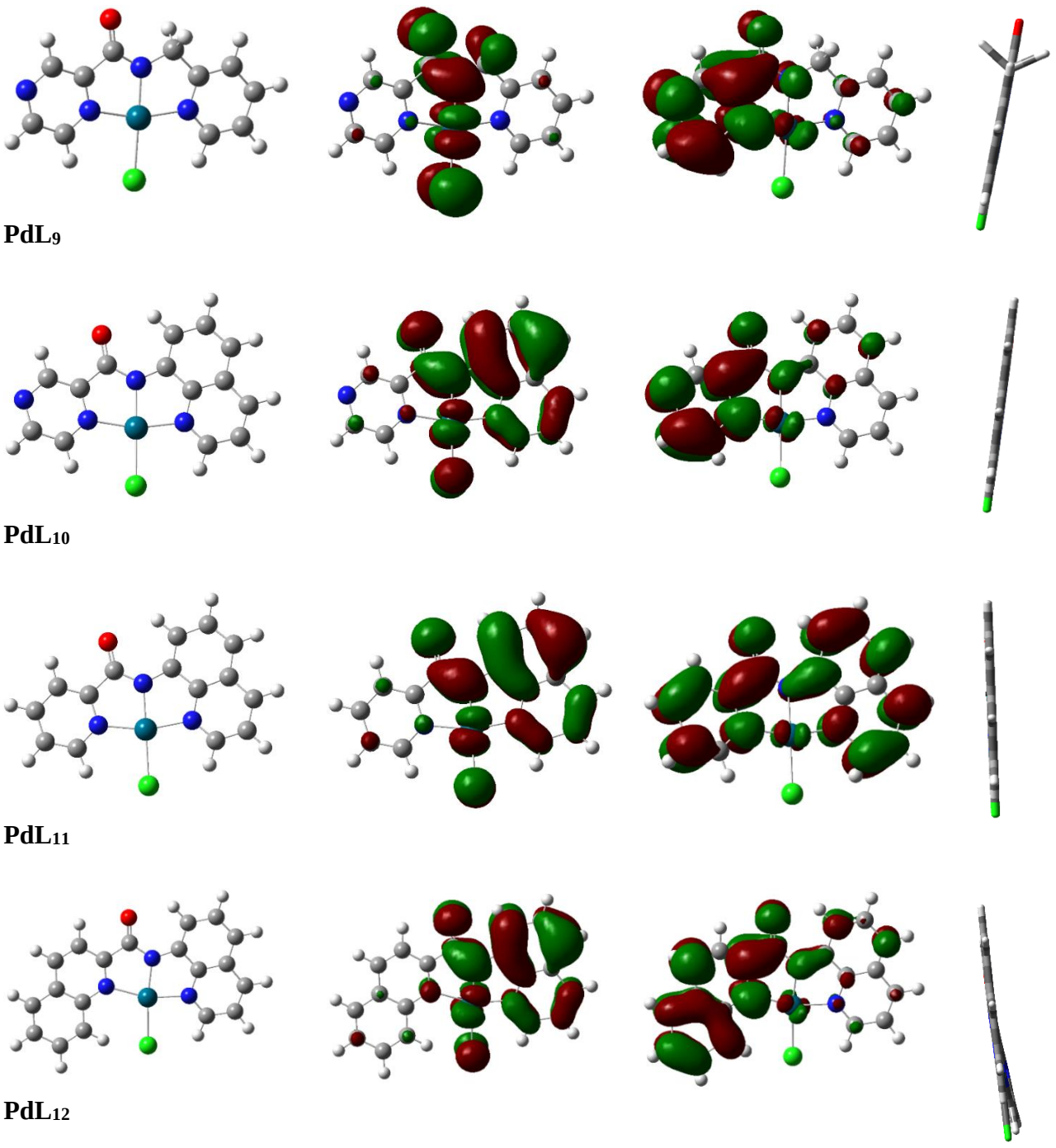

Figure 5.7: DFT-optimised HOMO, LUMO frontier molecular orbitals, with respective planarity structures of **PdL$_9$-PdL$_{12}$**.

Table 5.2: Summary of selected computational data for complexes **PdL_9-PdL_{12}**

Properties	**PdL_9**	**PdL_{10}**	**PdL_{11}**	**PdL_{12}**
NBO charge				
Pd^{2+}	0.348	0.365	0.340	0.359
O^-	0.392	0.348	0.355	0.357
Bond lengths (Å)				
Computed Pd-Cl	2.444	2.433	2.439	2.466
X-ray Pd(1)-Cl(1)	-	2.3191(6)	2.315(5)	2.328(2)
HOMO-LUMO energy / eV				
- LUMO	3.178	2.979	2.517	2.312
- HOMO	6.246	6.125	6.030	5.826
$\Delta E_{LUMO–HOMO}$	3.068	3.146	3.513	3.514
Chemical hardness (η)	1.534	1.573	1.757	1.757
Electronic chemical potential (-μ)	4.711	4.553	4.274	4.069
Electrophilicity index (ω)	7.233	6.589	5.199	4.711
Dipole moment (Debye)	7.249	5.956	2.529	1.816

5.2.4. Electrochemical behaviour of the palladium(II) complexes

To further elucidate the electronic properties of complexes **PdL$_9$-PdL$_{12}$**, their electrochemical property was determined using cyclic voltammetry (CV), and square wave voltammetry (SWV). The values of the redox potentials will be more particularly beneficial in explaining the kinetic trend of the complexes.

A representative voltammogram of **PdL$_{10}$** is shown in Figure 5.8. The observed cyclic voltamograms of **PdL$_9$-PdL$_{12}$**, can be described as irreversible one-electron oxidation reactions. Complexes **PdL$_9$** and **PdL$_{12}$** show similar CV behaviours (two redox processes), with one – electron anodic wave at 0.53, and 0.48 V, respectively, presumably due to metal-based oxidations [Pd(II)] → [Pd(III)]. Thus, **PdL$_9$** is oxidised at slightly higher potential than complex **PdL$_{12}$**. The poor π-acceptor ability of quinoline ligand in **PdL$_{12}$** stabilises the lower oxidation state, to give a less positive potentials for Pd(II) → formation Pd(III) oxidation [23]. The cathodic waves for **PdL$_9$** and **PdL$_{12}$** appear at – 0.94 and – 0.97 V, respectively, tentatively assigned to the ligand-based reduction. Conversely, **PdL$_{10}$**, does not exhibit anodic signal hump, but a cathodic wave at -1.1 V. However, the oxidation peak of the complex **PdL$_{10}$**, was detected at *ca*. 0.50 V by the SWV (showing two redox processes). This higher reduction value (above -1.0 V) can be rationalised in terms of high electron density on the Pd-ion [24], as a consequence of the electron richness of the quinoline moiety. In the case of **PdL$_{11}$**, the CV displays one explicit anodic wave at 0.64 V, and two cathodic signals at - 0.09 and - 0.64 V, indicative of a ligand-based reduction. The two cathode processes correspond to the reduction of [Pd(II)] → [Pd(I)] → [Pd(0)]. The higher oxidation potentials of **PdL$_{11}$**, in comparison to **PdL$_{10}$**, is unusual since the pyrazine unit in **PdL$_{10}$** is a better pi-acceptor (lowers the energy of the dπ-Pd- orbital) than the pyridine moiety in **PdL$_{11}$** (increases the energy of the dπ-Pd- orbital).

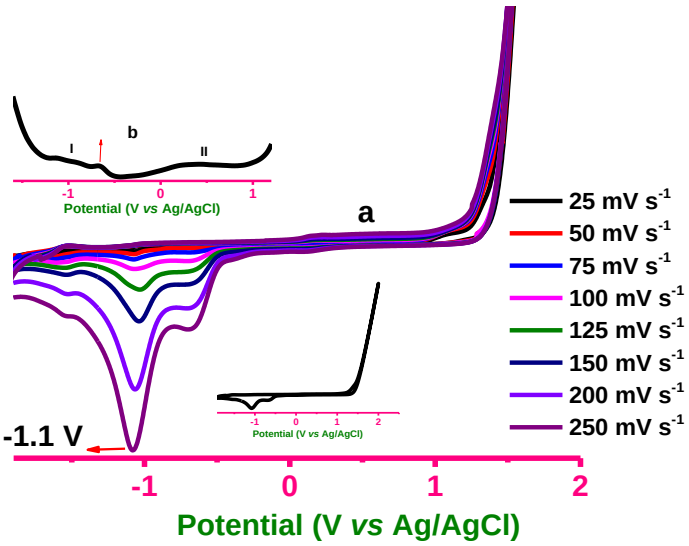

Figure 5.8: (**a**); Overlays of CV; (**b**) SWV of **PdL$_{10}$** in DMSO (2 mM) solution containing 0.1 M TBATFB at 25 °C. Scan rate: incrementing scan rates (25-250 mVs^{-1}) for CV; 100 mVs^{-1} for SWV. The SWV arrow denote aggregate peaks.

5.2.5 Stability of complexes PdL$_9$-PdL$_{12}$ in aqueous and dimethyl sulfoxide (DMSO) solutions

The stability of complexes **PdL$_9$-PdL$_{12}$** in aqueous buffer solutions (50 μM Tris buffer consisting of 50 mM NaCl, pH = 7.2) was performed to determine the absence of any solvotic pathways using UV-Vis spectrophotometer under ambient conditions over 12 h (Figure 5.9). In general, the electronic absorption spectra of the complexes remained invariant for the 12 h period, indicating their stability in aqua media. Similar UV-Vis spectra of other metal complexes have been recorded by Simović [25], and Petrovic´ groups [1]. The stability of metal complexes under physiological conditions is essential in maintaining drug integrity and efficacy [26].

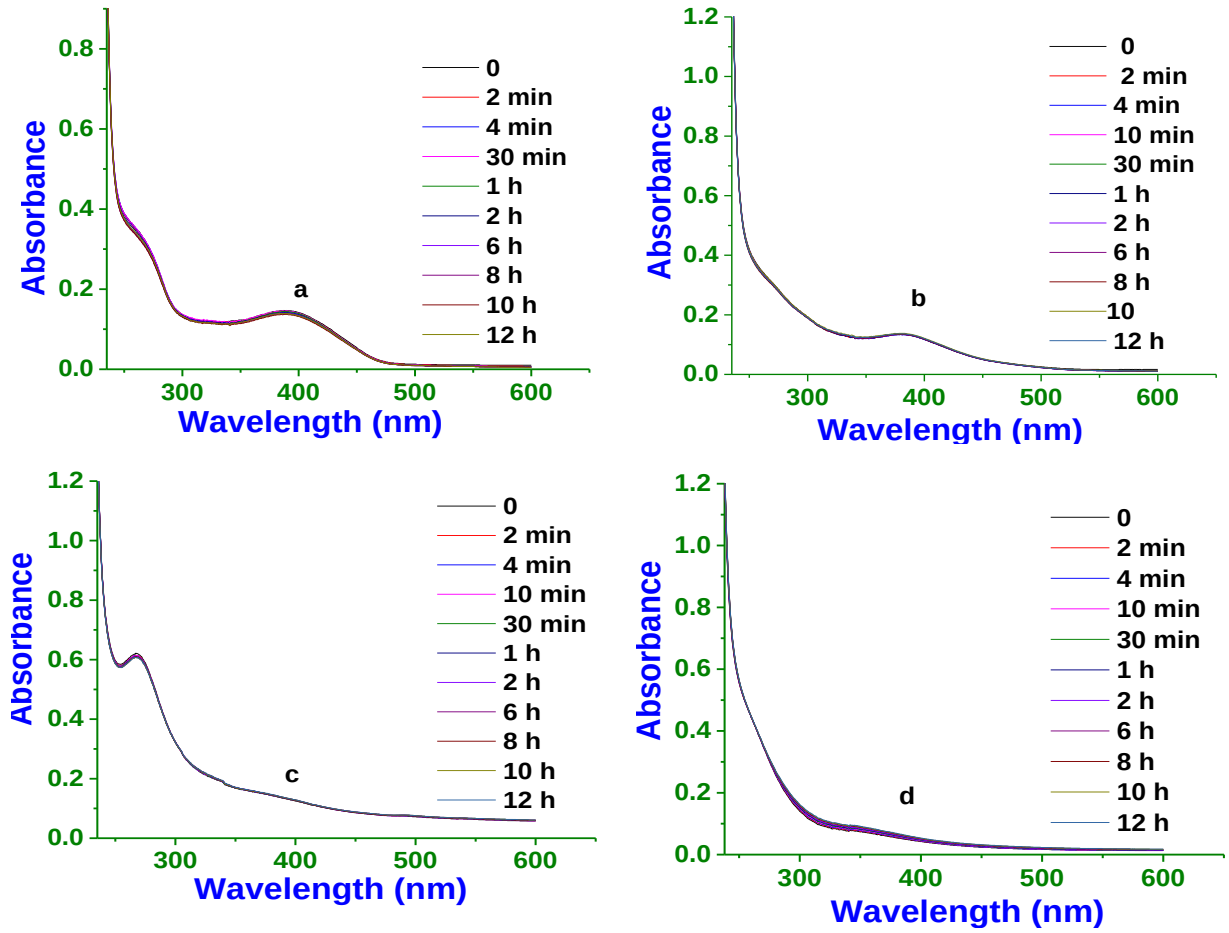

Figure 5.9: UV–Vis spectra of **PdL$_9$** (a), **PdL$_{10}$** (b), **PdL$_{11}$** (c), and **PdL$_{12}$** (d) in buffer (pH = 7.4) over a 12 h period, showing the stability of the complexes in the aqua media.

Since the biological media (used for cytotoxicity studies) usually contains small amounts of DMSO, we also investigated the stability of the complexes in DMSO solutions. This was done by monitoring ^{1}H NMR and UV-Vis spectral changes of the complex solutions in DMSO-d_6 over 72 h. A typical ^{1}H NMR spectra of **PdL$_{10}$** and **PdL$_{11}$** are shown in Figure 5.10. From the spectra, there were no observable changes in the proton chemical shifts, pointing to their stability in DMSO. Also, the UV-Vis spectra of the complexes in DMSO recorded for a period of 72 h did not show any significant changes (Figure 5.11 for **PdL$_{10}$** and **PdL$_{11}$**).

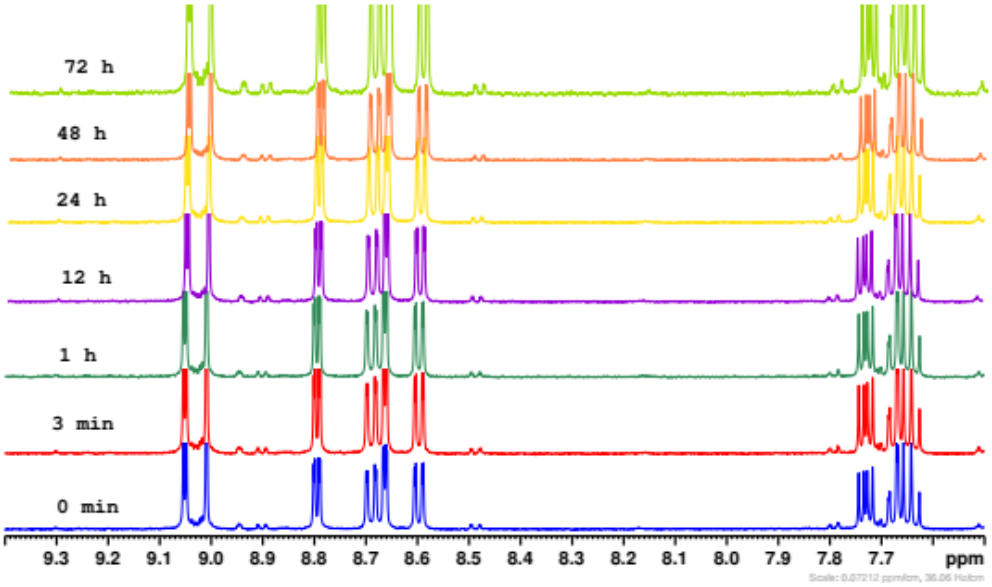

Figure 5.10: ^{1}H NMR spectral data of complex **PdL$_{10}$** in DMSO-d^{6} over 72 h, depicting the stability of the complex in DMSO. The electronic absorption spectral traces were recorded immediately after dissolving the compound in DMSO-d$_6$ at ambient temperature.

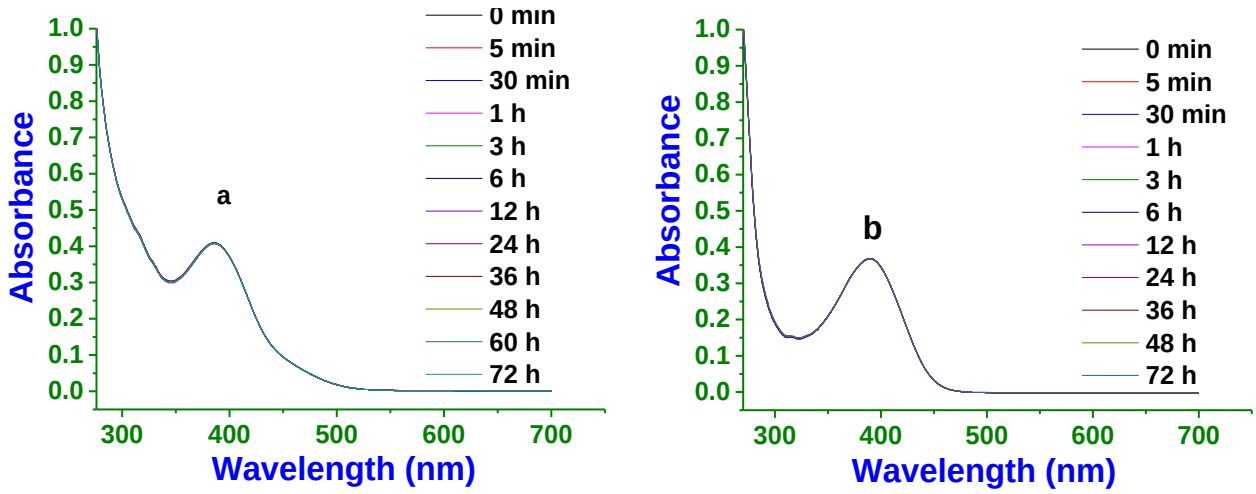

Figure 5.11: UV-Vis absorption spectra of **PdL$_{10}$** (a), **PdL$_{11}$** (b) in DMSO over a 72 h period, indicating the stability of the complexes in DMSO.

5.2.6 Kinetic and mechanistic measurements with biological relevant nucleophiles

5.2.6.1 Concentration effect with the biomolecules

To gain a more understanding of the solution behaviour of **PdL$_9$-PdL$_{12}$**, we monitored the spectral changes caused by the addition of the nucleophiles (stopped-flow kinetic trace for **PdL$_9$** is shown in Figure 5.12a). All kinetic traces from stopped flow were of excellent fit to a single-exponential decay function, to generate the observed pseudo-first-order rate constants (k_{obs}) using equation (1), demonstrating that the reactions were first-order. Plots of k_{obs} versus [Nu] are provided in Figure 5.12b for **PdL$_9$**.The plots gave straight lines with zero-intercept, indicating the absence of reverse or solvotic pathways, consistent with the stability of **PdL$_9$-PdL$_{12}$** in aqua media (Figure 5.9). Therefore, the relationship between k_{obs} and [Nu] can best be described by equation (3). The gradient of the graph of k_{obs} against [Nu] gave the second order rate constant, k_2, and the values obtained are given in Table 5.3.

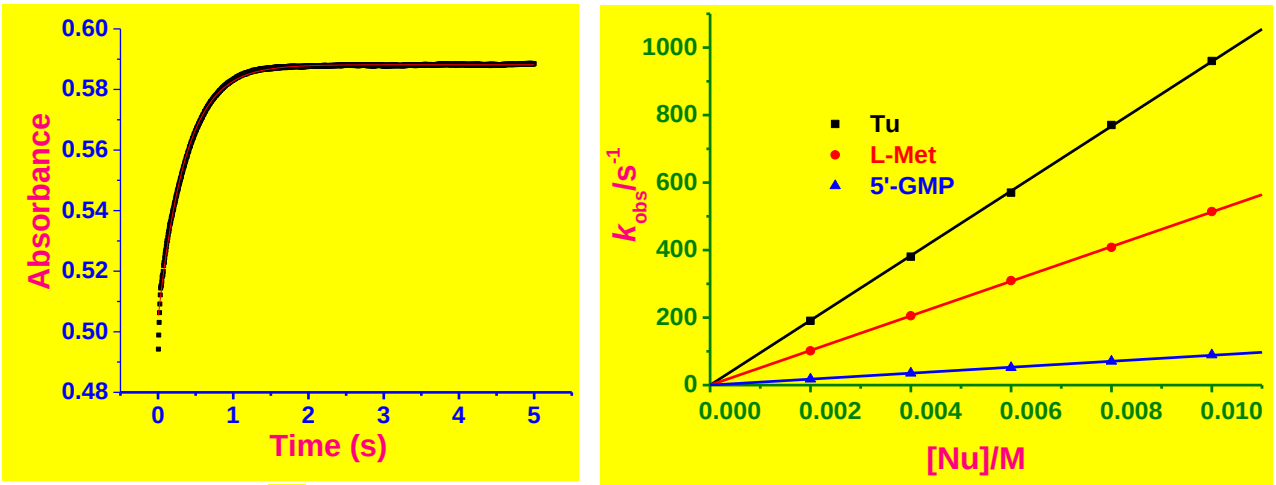

Figure 5.12: (**a**); Stopped-flow kinetic trace at 350 nm of **PdL$_9$** with **Tu**, at T = 298 K in aqua media, 50 μM Tris-HCl buffer (pH = 7.2), and 50 mM NaCl. (**b**); Concentration dependence of k_{obs} for the displacement of Cl ligand from **PdL$_9$** with **Tu**, **L-Met and 5'-GMP** nucleophiles.

Table 5.3: Second order rate constants (k_2) at 298 K, and thermodynamic parameters, $\Delta H^{\neq}$, $\Delta S^{\neq}$ and $\Delta G^{\neq}_{25°C}$ for the displacement of chloro ligands by the nucleophiles.[a]

Complex	Nu	k_2/M^{-1} s^{-1}	$\Delta H^{\neq}$/ kJ mol^{-1}	$-\Delta S^{\neq}$/J mol^{-1}K^{-1}	$\Delta G^{\neq}_{25°C}$/kJ mol^{-1}
	Tu	95866 ± 243	30 ± 1	51 ± 2	45 ± 2.1
	L-Met	51296 ± 114	31 ± 1	55 ± 3	46 ± 1.0
PdL$_9$	**5'-GMP**	8833 ± 54	28 ± 1	80 ± 4	52 ± 3.0
	Tu	34068 ± 180	32 ± 1	51 ± 4	47 ± 1.3
	L-Met	18317 ± 100	28 ± 1	60 ± 3	49 ± 2.4
PdL$_{10}$	**5'-GMP**	3039 ± 20	32 ± 1	70 ± 3	53 ± 1.8
	Tu	25113 ± 116	32 ± 2	51 ± 6	48 ± 3.1
	L-Met	12867 ± 68	32 ± 1	61 ± 3	50 ± 2.0
PdL$_{11}$	**5'-GMP**	2176 ± 15	31 ± 1	77 ± 2	54 ± 1.8
	Tu	10119 ± 65	36 ± 1	47 ± 2	50 ± 2.7
	L-Met	5181 ± 27	34 ± 2	60 ± 5	52 ± 1.2
PdL$_{12}$	**5'-GMP**	867 ± 8	34 ± 1	74 ± 1	56 ± 3.1

[a]Reactions performed in aqua media, 50 μM Tris-HCl buffer (pH = 7.2), and 50 mM NaCl.

In general, the rate of substitution of Pd(II) complexes with the entering ligands followed the order: **PdL$_9$** > **PdL$_{10}$** > **PdL$_{11}$** > **PdL$_{12}$** (Table 5.3). The observed difference in the reactivity trend can be explained in terms of the concerted electronic effects of the spectator ligand motif. With **Tu** as the incoming nucleophile, **PdL$_9$** is ≈ 3 times more reactive than **PdL$_{10}$**. The higher reactivity of **PdL$_9$** is ascribed to the presence of the pyridine ring, a strong π-acceptor [27], withdrawing electrons clouds from the Pd(II) ion *via* π-back donation, making the metal centre more electrophilic for facile nucleophilic attack [27]. Replacing the pyridyl moiety in **PdL$_9$** (k_2 = 95866 M^{-1} s^{-1}, **Tu**) with a good σ-donor quinoline unit [27, 28], in **PdL$_{10}$** (k_2 =34068 M^{-1} s^{-1}, **Tu**) reduces the π-acceptor ability of the

ligand through σ-inductive effects, consistent with the lower reactivity of **PdL$_{10}$**. An increase in the σ-donicity in the ligand system of **PdL$_{10}$** results into the buildup of electron clouds around the Pd(II) centre, retarding the lability of **PdL$_{10}$**. The deduction is in tandem with the the decline of the negative NBO charges of the carboxamide O atom as one moves from **PdL$_9$** (-0.392) to **PdL$_{10}$** (-0.348). The $\Delta E_{LUMO-HOMO}$ of 3.068 and 3.146 eV for **PdL$_9$** and **PdL$_{10}$**, respectively, suggest a larger metal-to-ligand charge-transfer (MLCT) for **PdL$_1$** in relation to **PdL$_{10}$**. The electron build-up around the Pd(II) ion from **PdL$_9$** to **PdL$_{10}$** is consistent with the computed electrophilicity indices, which is a function of the HOMO-LUMO gap. This is further supported by the differences in the dipole moments of 7.249 (**PdL$_9$**) and 5.956 (**PdL$_{10}$**) as given in Table 5.2. The higher reactivity of **PdL$_9$** in relation to **PdL$_{10}$** also correlates with the increased thermodynamic redox potential of **PdL$_1$ (**E_{pc} **= -** 0.94 V**)** than **PdL$_2$** (Epc = -1.1 V), which is concomitant by more electron density being drawn away from Pd- metal centre in **PdL$_9$** than **PdL$_{10}$**.

A comparison of the reactivity of complexes **PdL$_{10}$** and **PdL$_{11}$** reveals that **PdL$_{10}$** is nearly 1.4 times more reactive than **PdL$_{11}$** (Table 5.3). This trend can be assigned to the higher acidity of the pyrazine unit (conjugate acid, pK_a = 0.4) ligand in **PdL$_{10}$** compared to the pyridine motif (conjugate acid, pK_a = 5.2) in **PdL$_{11}$** [29]. Thus, electronically, pyrazine is a better electrophile than pyridine, a property that makes pyrazine to readily accept electrons from the metal centre compared to pyridine. The argument is well supported by the higher dipole moments for **PdL$_{10}$** (5.956) than **PdL$_{11}$** (2.529). The better π-acceptor ability of the spectator ligand system in **PdL$_{10}$** in relation to **PdL$_{11}$**, is further derived from the decrease of the positive NBO charges on the Pd(II) from **PdL$_{10}$** to **PdL$_{11}$** and higher electrophilicity index of **PdL$_{10}$** compared to **PdL$_{11}$**. Moreover, the high electrophilicity index of **PdL$_{10}$** compared to **PdL$_{11}$** supports the observed reactivity trends.

The rate of reactivity decreases with the replacement of the pyridine unit of **PdL$_{11}$** (k_2 = 25113 M^{-1} s^{-1}, **Tu**) with the isoquinolinyl moiety in **PdL$_{12}$** (k_2 = 10119 M^{-1} s^{-1}, **Tu**). This can be largely attributed to the increased *cis*- σ-inductive effects [30], thereby reducing the pi-acceptor abilities of the spectator ligand systems from **PdL$_{11}$** to **PdL$_{12}$**. The trend tallies with the higher redox peak potentials for **PdL$_{11}$** (E_{pc} = 0.64 V) in comparison to **PdL$_{12}$** (E_{pc} = 0.97 V) and the lower electrophilicity of 4.711 eV in **PdL$_{12}$** compared to 5.199 eV for **PdL$_{11}$**. Consequently, the LUMO energy of **PdL$_{12}$** is raised and thus broadening the $\Delta E_{LUMO–HOMO}$ in relation to **PdL$_{11}$** (Table 5.2). The argument is also consistent with the slightly lower NBO charge on the Pd-metal centre in **PdL$_{12}$**. The diminution of the dipole moments of the complexes as one moves from **PdL$_{11}$** to **PdL$_{12}$**, also affirms the stable nature of **PdL$_{12}$** in relation to **PdL$_{11}$**. With reference to the solid-state structure of **PdL$_{11}$**, and **PdL$_{12}$**, one would expect a higher rate of substitution of the Cl ligand in **PdL$_{12}$** due its slightly longer Pd-Cl bond distance (2.328 (2) Å) in relation to **PdL$_{11}$** (Pd - Cl = 2.315 (5) Å). On the contrary, the higher reactivity of **PdL$_{11}$** thus points to nucleophilic attack to the Pd-metal centre as the rate determining step, rather than the Pd-Cl breakage. This argument is consistent with an associated mode of substitution reactions [31].

The DFT calculated data (Table 5.2), shows chemical hardness (η) of 1.534 eV for **PdL$_{9}$**, 1.573 eV for **PdL$_{10}$**, 1.757 eV for **PdL$_{11}$** and 1.757 eV for **PdL$_{12}$**, which correlates with the order of reactivity [32]. Noteworthy, the higher the chemical hardness, the less reactive is the complex [32]. Moreover, the electronic chemical potential (μ), which decreases from **PdL$_{9}$** to **PdL$_{12}$** is consistent with the observed reactivity trends; the higher the value of electronic chemical potential, the higher the reactivity of the compounds. Examination of the role of the incoming biological nucleophiles (Figure 5.13) reveals both steric and electronic contributions [33]. As the steric encumbrance of the nucleophiles increase from **Tu** to **5'-GMP**, the approach towards the metal centre is reduced resulting to transition state destabilisation, and thus decelerating the rate of reactivity (Table 5.3). With regards to the electronic effects, the higher reactivity of the S-donor nucleophiles (**Tu**) compared to the N-bonding nucleophile

(**5'-GMP**) is due to the fact that Pd(II) ion has a high affinity for sulfur-donor nucleophiles than the nitrogen-donor analogues [12].

5.2.6.2 Activation parameters of the iso-kinetic substitution reactions

The activation parameters were examined over the temperature range of 298-318 K at intervals of 5 K. The enthalpy of activation ($\Delta H^{\neq}$), entropy of activation ($\Delta S^{\neq}$) and Gibbs free energy of activation ($\Delta G^{\neq}_{25°C}$) were calculated using the Eyring equation (4) [34]. Archetypical Eyring plots of **PdL$_9$** are presented in Figure 5.13a, and the values of activation parameter are reported in Table 5.3. The activation parameters, $\Delta H^{\neq}$ are positive, while $\Delta S^{\neq}$ are negative (Table 5.3), suggesting an associative mechanism of substitution reaction, where the breakage of Pd-Cl bonds and the formation of Pd-nucleophile bonds are concerted [31]. The observed activation parameters suggest that the transition states are favoured energetically for the formation of new bonds with the entering ligand, generating transition states which are more ordered and compact relative the reactants. Generally, the lower values of enthalpy for **PdL$_9$-PdL$_{12}$** denote the π-accepting ability of the carrier ligands which creates a greater electrophilic character Pd(II), and thus a higher tendency towards the entering ligand [35, 36].

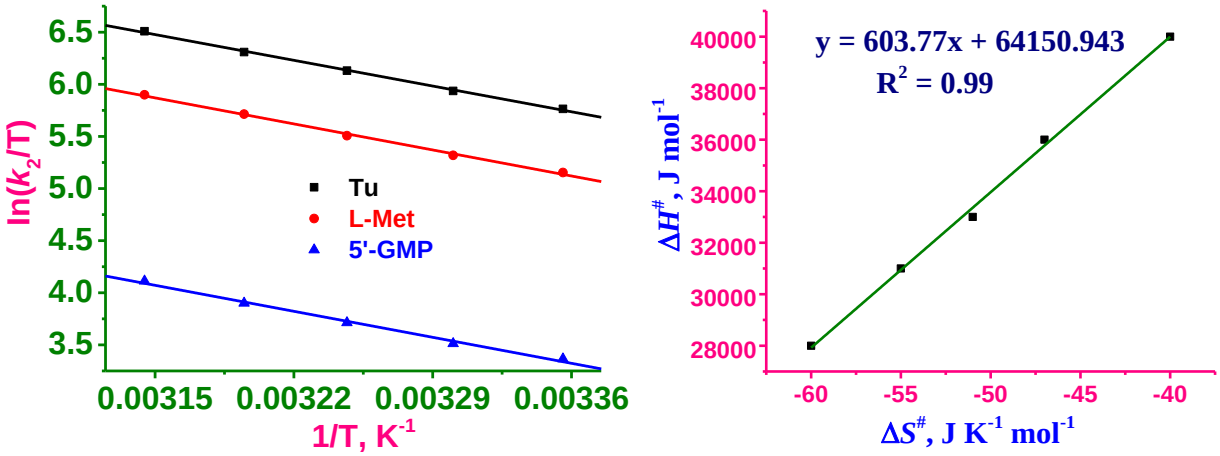

(**a**) (**b**)

Figure 5.13: **(a)**; Eyring plots for the reaction of **PdL$_9$** with the entering ligand in aqua, in 50 µM Tris-HCl buffer (pH = 7.2), and 50 mM NaCl and temperature range of 298-318 K. **(b)**; *Iso*-kinetic plots for ligand substitution reactions of complexes **PdL$_9$-PdL$_{12}$** with the entering ligands.

A linear free energy relationship (LFER) of thermal activation was evaluated by plotting $\Delta H^{\neq}$ against $\Delta S^{\neq}$. The plots demonstrated the existent of a linear *iso*-kinetic free energy relationship between the two activation parameters (Figure 5.13b). The values of *iso*-kinetic temperature and $\Delta G^{\neq}$ were obtained from the slope and intercepts of the graph, respectively. *Iso*-kinetic temperature for the substitution reactions of **PdL$_9$-PdL$_{12}$** was predicted at 603.77 K, while $\Delta G^{\neq}$ was determined at 64.15 kJ mol^{-1}. The values of $\Delta G^{\#}_{25°C}$ (Table 5.3), for **PdL$_9$-PdL$_{12}$** with the entering ligands are similar, indicating that the reactions follow the same associative mechanism [37, 38].

5.2.7 CT-DNA interactions studies

5.2.7.1 UV-Vis absorption spectral studies

The potential interaction between the complexes and CT-DNA can be revealed by the changes in the absorption spectra of complexes on the addition of CT-DNA. Noteworthy, the changes in the UV-Vis spectral patterns seen upon the titration of the complex solutions with CT-DNA solution may indicate

the possible binding mode. It should, however, be noted that the exact binding mode cannot be reliably suggested on the basis of the patterns of the electronic UV/Vis absorption bands alone [39]. The increasing concentration of CT-DNA resulted in absorbency (hypochromism), with bathochromic shift in the spectra of **PdL$_9$-PdL$_{12}$**. A typical graph is shown in Figure 5.14 for the electronic absorption spectrum of **PdL$_9$** in the presence and absence of CT-DNA at different concentration (with the equilibration time for Pd-CT-DNA of less than 30 s). In the presence of increasing concentrations of CT-DNA, a considerable hypochromic shift in the $\pi \rightarrow \pi^*$ transition was observed, indicative of the existence of intercalative mode of binding [39]. The intrinsic binding constants K_b, of complexes **PdL$_9$-PdL$_{12}$** was ascertained by utilising the Wolfe-Shimer equation (6). The K_b values of **PdL$_9$-PdL$_{12}$** which are in the range of 0.35-11.01 x 10^4 M^{-1} (Table 5.4), are comparable to similar complexes reported in the literature [14, 40, 41]. It is noteworthy to mention that the planarity of complexes **PdL$_9$-PdL$_{12}$** as depicted in the DFT-optimised structures (Figure 5.7), facilitates facile CT-DNA binding [11]. Gibb's free energy (ΔG) of the Pd-DNA complex was determined using the Van't Hoff equation (7). The calculated ΔG values of **PdL$_9$-PdL$_{12}$** were negative (Table 5.3), showing the spontaneity of the Pd complex-DNA interaction [42, 43]. The negative ΔG values suggest that the interactions of **PdL$_9$-PdL$_{12}$** with CT-DNA are thermodynamically favourable, with a strong binding to CT-DNA.

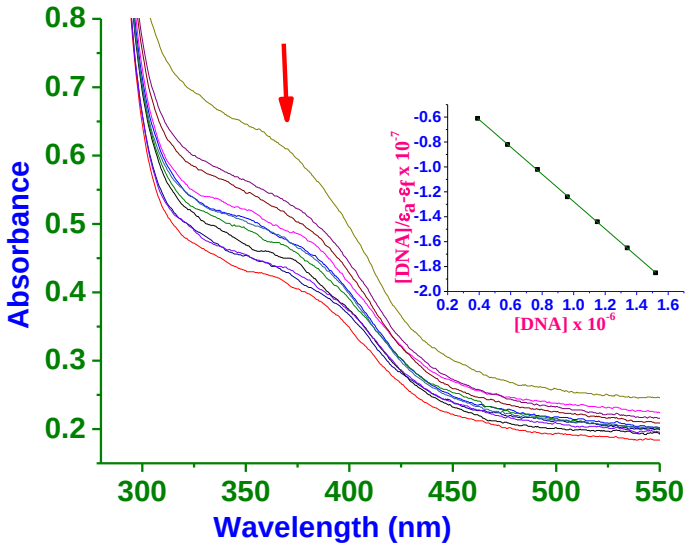

Figure 5.14: Electronic absorption spectrum of complex **PdL$_9$** (50 μM) in the presence of an increasing concentration of CT-DNA (0 - 60 μM) in 50 μM Tris buffer consisting of 50 mM NaCl at pH = 7.2. Inset: plot of [CT-DNA] versus [DNA]/(ε_a- ε_f). The arrow depicts hypochromic and bathochromic shift on the addition of increasing amounts of DNA.

5.2.7.2 Fluorescence quenching studies for CT-DNA

To further confirm the mode of interaction between the metal complexes and CT-DNA, fluorescence studies of the **PdL$_9$-PdL$_{12}$** with EB-CT-DNA was examined. Typical emission spectrum of EB-CT-DNA in the absence and presence of the complex are presented in Figure 5.15a for **PdL$_9$**. The addition of increasing concentration of **PdL$_9$-PdL$_{12}$** to EB-CT-DNA caused a significant decrease in emission intensity at 597 nm, indicative of intercalative mode of interaction between the complexes and CT-DNA [44, 45]. The Stern-Volmer quenching constant, K_{sv} and bimolecular quenching rate constant k_q computed from the Stern-Volmer equation (8) (Figure 5.15b shows typical straight-line plots of **PdL$_9$**) and the data are provided in Table 5.4. The values of K_{sv} (0.05-3.02) x 10^4 M^{-1}, Table 5.4, suggest possible intercalative binding mode of interaction, between the complexes and CT-DNA [8]. The apparent binding affinity constant, K_{app}, was acquired from equation (9) and the values are given in Table 5.4. The values of K_{app} (0.13-6.00 x 10^6 M^{-1}), which are lower than the classical intercalators and

metallointercalators binding constant (10^7 M^{-1}) [46], signify intercalative binding mode. The k_q values which are in the range 0.21-13.16 x 10^{11} $M^{-1}s^{-1}$ (Table 5.4), demonstrate static quenching mechanism. Notably, k_q values of magnitude lower than 10^{10} M^{-1} s^{-1} (for most known biopolymeric fluorescence quenchers), depict dynamic quenching mechanism [14]. Linear plots obtained from Scatchard equation (10) was used to calculate the number of binding sites, *n* and binding constant, K_F (Scatchard plots for **PdL$_9$** are shown in Figure 5.15c) and the results are presented in Table 5.4. The values of n for the Pd(II) complexes were near to unity, suggesting one binding site available on the CT-DNA [47]. Also, the K_F values decrease based to the ability of the complexes to intercalatively exchange EB from CT-DNA, and followed the order; **PdL$_9$** > **PdL$_{10}$** > **PdL$_{11}$** > **PdL$_{12}$**, and the order can be explained by the planarity of the chelated ligands which increase the accessibility of the complexes to the active site in DNA. The quenching rate constants are in agreement with the K_b values, establishing that compounds **PdL$_9$**-**PdL$_{12}$** bind non-covalently to CT-DNA.

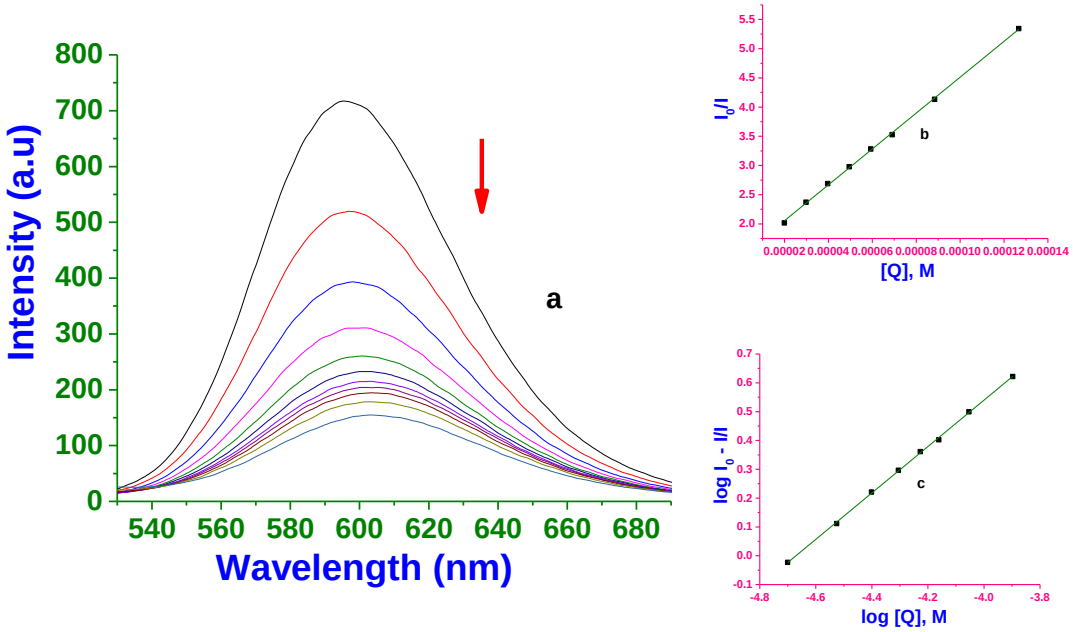

Figure 5.15: (**a**); Fluorescence quenching curve of EB-CT-DNA in the presence of increasing concentration of **PdL₉** in 50 μM Tris buffer consisting of 50 mM NaCl at pH = 7.2: [EB] = 50 μM, [CT-DNA] = 50 μM and [**PdL₉**] = 0-400 μM. **(b)**; Stern-Volmer plot of I_o/I versus [Q]. **(c)**; Scatchard plot of log[(I_o–I)/I] versus log[Q]. The arrow indicates spectral changes on the addition of increasing amounts of metal complex.

Table 5.4: CT-DNA binding parameters of complexes **PdL₉-PdL₁₂**

	UV-Vis titration		**EB fluorescence quenching titration**				
Complex	K_b (10^4 M^{-1})	ΔG/k $Jmol^{-1}$	K_{sv} (10^4 M^{-1})	K_{app} (10^6 M^{-1})	k_q (10^{11} M^{-1} s^{-1})	K_F (10^5 M^{-1})	*n*
PdL₉	11.01 ± 0.52	-28.76	3.02 ± 0.15	6.00 ± 0.17	13.16 ± 0.33	1.83 ± 0.12	0.92
PdL₁₀	1.67 ± 0.44	-24.09	2.09 ± 0.14	3.03 ± 0.15	9.10 ± 0.16	0.89 ± 0.05	1.16
PdL₁₁	0.71 ± 0.01	-21.97	0.18 ± 0.001	0. 21 ± 0.03	0.38 ± 0.03	0.07 ± 0.001	0.76
PdL₁₂	0.35 ± 0.02	-20.22	0.05 ± 0.001	0.13 ± 0.04	0.21 ± 0.06	0.02 ± 0.008	0.89

5.2.8 BSA interactions

The transportation and delivery of pharmaceuticals in the blood-plasma can be determined by calculating drug-BSA binding constant [48]. The value of the binding constant should be sufficiently enough for the drug to bind to the BSA for its distribution (lower than 10^{15} L mol^{-1}). Noteworthy, complex-protein interaction is crucial in the study of drug design dosage. Addition of **PdL_9-PdL_{12}** to BSA resulted to a considerable reduction of emission intensity at 281 nm, typical emission spectra of **PdL_9** are depicted in Figure 5.16a. As described in the CT-DNA-EB studies, k_q, and K_{SV} constants were determined using Stern–Volmer equation (8) (Figure 5.16b shows Stern-Volmer plots for **PdL_9**). On the other hand, the K_F and n values were calculated from the Scatchard equations (10) (Figure 5.16c for **PdL_9**). The examined values of K_{SV}, k_q, K_F, and n are presented in Table 5.5. The magnitude of K_{SV} (10^4-10^5 M^{-1}), Table 5.5, indicates that the interaction process is not fully controlled by diffusion, and thus making k_q larger [48]. The computed k_q values (1.76-15.19 x 10^{12}, M^{-1} s^{-1}), which are about two to three orders of magnitude higher than the most known quenchers (10^{10} M^{-1} s^{-1}), indicate static quenching mechanism [49]. The K_F values (~10^4-10^6 M^{-1}) are comparable to similar Pd(II) complexes reported in the literature, and are within the optimal range [8, 12]. The K_F values of the examined complexes could be considered sufficiently enough to accord effective binding of the complexes to BSA. The K_F values of **PdL_9-PdL_{412}** of magnitude ~10^4- 10^6 M^{-1} are below the value of the association constant (K_F = 10^{15} M^{-1}) of the highest protein-ligand binding affinity [50]. Thus, the complexes can easily be released from BSA upon arrival at the diseased cells. The calculated n values for **PdL_9-PdL_{12}** are close to unity, illustrating that the compounds are bound to BSA in a single active binding site. The data in Table 5.5, reveals that the relative binding affinities of the complexes follow the order; **PdL_9** > **PdL_{10}** > **PdL_{11}** > **PdL_{12}**, consistent with the kinetics trend discussed previously (Table 5.3).

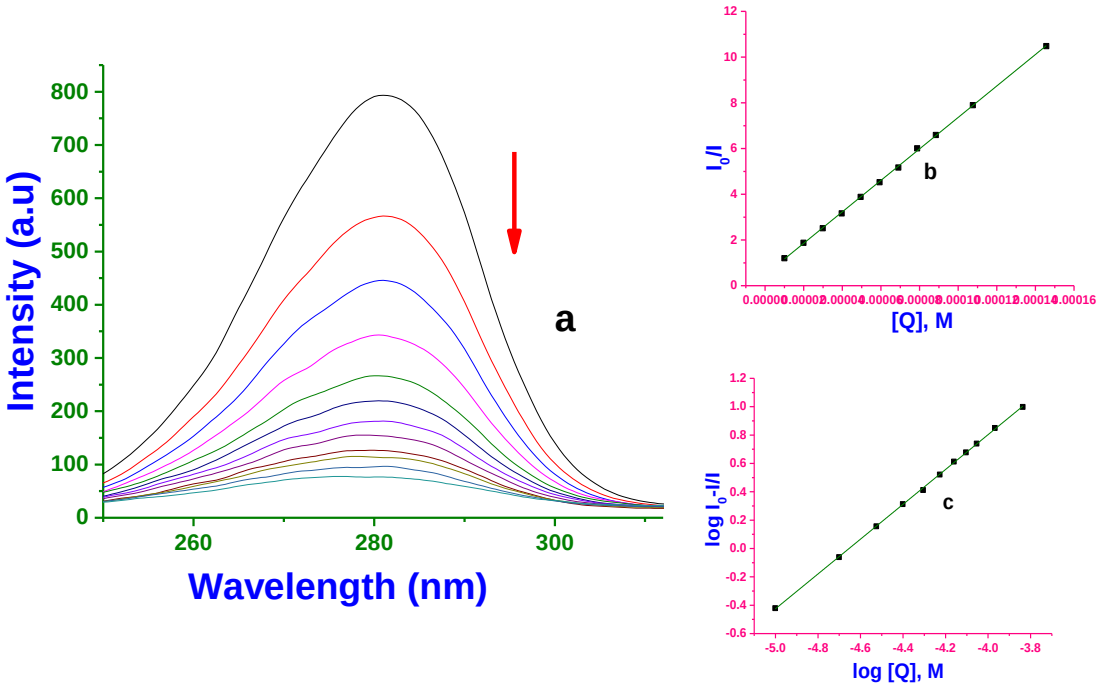

Figure 5.16: (a); Changes in fluorescence spectra of BSA with the increasing concentration of **PdL$_9$** in 50 μM Tris buffer consisting of 50 mM NaCl at pH = 7.2: [BSA] = 12 μM and [**PdL$_9$**] = 0-10 μM. **(b)**; Stern-Volmer plot of I_o/I *vs* [Q]. **(c)**; Scatchard plot of log[(I_o–I)/*I*] versus log[Q]. The arrow indicates emission intensity changes on the addition of increasing amounts of metal complex.

Table 5.5. BSA binding parameters, and the number of binding sites of complexes **PdL$_9$-PdL$_{12}$**

Complex	**K_{sv} x 10^4, M^{-1}**	**k_q x 10^{12}, M^{-1} s^{-1}**	**K_F x 10^5, M^{-1}**	**n**
PdL$_9$	15.19 ± 0.19	15. 19 ± 0.12	12.25 ± 0.14	1.16
PdL$_{10}$	6.85 ± 0.23	6.85 ± 0.24	9.14 ± 0.21	1.22
PdL$_{11}$	4.19 ± 0.13	4.19 ± 0.37	0.422 ± 0.03	0.99
PdL$_{12}$	1.76 ± 0.23	1.76 ± 0.27	0.13 ± 0.01	0.99

5.2.9 *In vitro* cytotoxicity studies Pd(II) complexes

The cytotoxic effects of **PdL$_9$**-**PdL$_{12}$** were examined in five malignant cell lines (A549, PC-3, HT-29, Caco-2, and HeLa) and a normal cell (KMST-6) using the MTT assay (Figure 5.17 and Table 5.6). Complexes **PdL$_9$**, and **PdL$_{10}$** significantly reduced the viabilities of A549, PC-3, HT-29, Caco-2, and HeLa in a concentration dependent manner. Based on the determined IC_{50} values shown in Table 5.5, compound **PdL$_9$** is potent against A549 (IC_{50} of 3.9 µM), PC-3 (IC_{50} of 9.8 µM), HT-29 (IC_{50} of 0.1 µM) and Caco-2 (IC_{50} of 0.04 µM). Complex **PdL$_{11}$** also demonstrated potency on PC-3 and HT-29, with IC_{50} values of 5.4 and 1.9 µM, respectively. Thus, complex **PdL$_9$** showed higher cytotoxic activities towards A549, HT-29 and Caco-2 than cisplatin. Similarly, complex **PdL$_{11}$** demonstrated greater toxicity than cisplatin against HT-29, and in general showed comparable cytotoxicity levels to cisplatin. For example, the IC_{50} values of **PdL$_{11}$** for PC-3 (5.4 µM) and Caco-2 (15.7 µM) were not statistically different from those of cisplatin in the respective cells *i.e.* 6.3 ± 0.9 µM in PC-3 [51] and 16.7 ± 2.3 µM in Caco-2 [52], depicting the equipotency of cisplatin and **PdL$_{11}$** on both PC-3 and Caco-2. However, **PdL$_{10}$** and **PdL$_{12}$** showed minimal cytotoxic effects on the five cell lines. Overall, **PdL$_{12}$** exhibited the least cytotoxic effects with IC_{50} values >100 µM on all the evaluated tumour cell lines. Thus, the order of potencies against the investigated malignant cell lines is **PdL$_9$** > **PdL$_{11}$** > **PdL$_{10}$** > **PdL$_{12}$**.

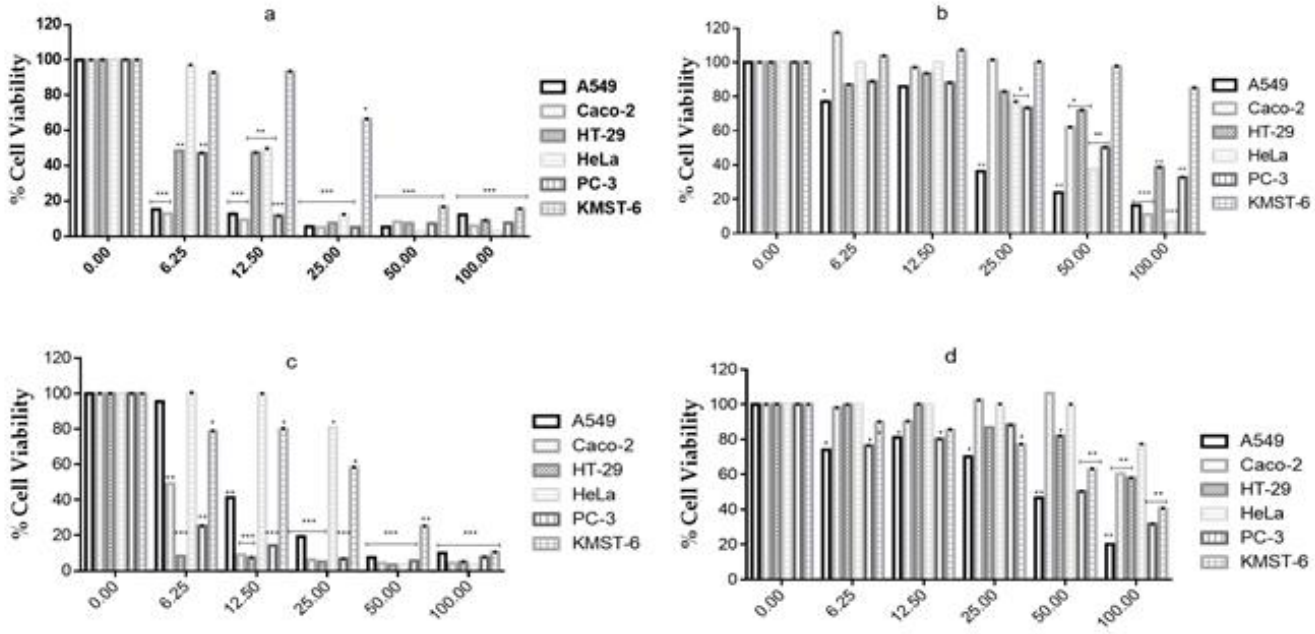

Figure 5.17: Effects of complexes **PdL_9-PdL_{12}** on the viability of A549, PC-3, HT-29, Caco-2, and HeLa and KMST-6. (a), (b), (c), and (d). The cells were exposed to 100 µg/mL of compounds for 24 h. * represent significant difference compared to the control at $p < 0.05$, ** ≤ 0.01, *** ≤ 0.001.

Table 5.6: Cytotoxic activities and selectivity indexes of complexes **PdL_9-PdL_{12}**

	IC_{50} (μM)						Selectivity Index (SI)				
	KMST-6	**A549**	**PC-3**	**HT-29**	**Caco-2**	**HeLa**	**A549**	**PC-3**	**HT-29**	**Caco-2**	**HeLa**
PdL_9	87.8 ± 7.1	3.9 ± 2.1	9.8 ± 1.2	0.1 ± 0.01	0.04 ± 0.01	35.2 ± 2.2	> 2	> 2	> 2	> 2	> 2
PdL_{10}	>100	57.7 ± 3.3	> 100	>100	>100	>100					
PdL_{11}	69.6 ± 3.2	30.8 ± 4.2	5.4 ± 1.1	1.9 ± 1.1	15.7 ± 3.1	86.5 ±4.6	> 2	> 2	> 2	> 2	0.8
PdL_{12}	>100	90.8 ± 8.8	>100	>100	>100	>100					
Cisplatin	44.0 ± 2.1[a]	7.3 ± 0.6[b]	6.3 ± 0.8[c]	2.7 ± 0.1[d]	16.7[e]	26[f]	> 2	> 2	> 2	> 2	1.7

SI values > 2 means that the complex is more than twice more cytotoxic to the maligant cell line than the healthy cell line. SI value less than 1 suggests that the complex is more toxic to a normal cell than a cancer cell (undesirable) [a]Extracted from reference; [53] [b] from [54]; [c] from; [51] [d] from; [55] [e] from; [52] and [f] from [11].

The varying cytotoxicity of the Pd(II) complexes, suggests that the nature of the inert spectator ligand play a crucial role in determining the biological activities of the corresponding complexes. The higher cytotoxic effects of **PdL_9** can be ascribed to its smaller inert chelating ligand that promotes facile and strong binding to the molecular target DNA [11] and this is further justified by its higher kinetic reactivity with **5'-GMP** (a model for binding to the nucleobases**)** in comparison to the other complexes, (Table 5.2), and DNA/BSA binding affinity (Table 5.6). The increased kinetic lability of **PdL_9** with sulfur donor nucleophiles (**Tu** and **L-Met**) relative to the other Pd-complexes is expected to lower its antitumoural activity, due to the deactivation by the non-target biomoelcues cytoplasm [56]. This is believed to result to high toxicity to the healthy cells in addtion to the acquired drug resistance. Thus

higher kinetic lability and growth inhibition of **PdL_9** in comparison to compounds **PdL_{10} -PdL_{12}**, indicate that the Pd-S adduct serves as a drug-reservoir, rather than cause toxicity. Similar trends and observation have recently appeared literature [11, 13, 57].

One would expect compound, **PdL_{12}** to display enhanced inhibitory effects, due to its π-conjugation (aromaticity) in relation to compounds **PdL_9-PdL_{11}** [1, 13]. However, in the current work, **PdL_{12}** is the least active compound. This reverse trend could be ascribed to the slight steric hindrance, caused by the bulky isoquinoline motif (as depicted by the DFT planarity, Figure 5.7), and thus hindering effective interaction of the complex with the DNA target (Table 5.7). The argument is also supported by the slower kinetic reactivity of **PdL_{12}** with the entering bio- nucleophiles and smaller DNA/BSA binding constants (Table 5.7). Significantly, the toxicity of **PdL_9** and **PdL_{11}** (the most potent compounds in the study), against the healthy KMST-6 cell line (IC_{50} values of 87.8 µM for **PdL_1** and 69.6 µM for **PdL_{11}**) were found to be minimal compared to cisplatin (IC_{50} value of 44.0 ± 2.0 µM) [53]. This is further supported by SI values of greater than 2 for compounds **PdL_9** and **PdL_{11}** (Table 5.6), demonstrating that the complexes are specifically toxic to the diseased cells. However, **PdL_{11}** exhibited an SI value of 0.8 on HeLa cell line, implying that it is non-selective to the normal cell line KMST-6.

Table 5.7: A summary of the second order rate constants (k_2), DNA/BSA binding constant (K_{sv}), and cytotoxic effects (IC_{50}) of Pd(II) complexes

Complexes	Tu, k_2, Tu, (10^4 M^{-1} s^{-1})	DNA, *Ksv* (10^4 M^{-1})	BSA, *Ksv* (10^4 M^{-1})	A549, IC_{50} (μM)
PdL_9	9.59	3.02	15.19	3.9
PdL_{10}	3.41	2.09	6.85	57.7
PdL_{11}	2.51	0.18	4.19	30.8
PdL_{12}	1.01	0.05	1.76	90.8

5.3. Conclusions

In conclusion, we have synthesised and structurally characterised carboxamide Pd(II) complexes. Molecular structures of complexes **PdL_{10}**, **PdL_{11}** and **PdL_{12}** reveal tridentate coordination of the anionic ligands to form distorted square planar compounds. Cyclic and square wave voltammograms of complexes **PdL_9-PdL_{12}** in DMSO solution suggest that the compounds are redox active and are characterised by an irreversible one-electron oxidation wave. The kinetic reactivity of the complexes **PdL_9-PdL_{12}** towards the biological molecules is controlled by the electronic properties of the spectator ligand(s) as depicted by the DFT calculated parameters. The order of reactivity of **Tu**, **L-Met**, and **5'-GMP** depends on both the electronic and steric properties of the incoming biological nucleophiles. The activation parameters ($\Delta H^{\neq} > 0$, $\Delta S^{\neq} < 0$) indicate an associative mechanism of activation. The isokinetic linear relationships between $\Delta H^{\neq}$ and $\Delta S^{\neq}$ indicate a single reaction pathway for the Pd-complexes. The DNA/BSA experiments depict intercalative binding mode and the order of binding is consistent with kinetic reactivity. Cytotoxic evaluation of complexes **PdL_9** and **PdL_{11}** reveal potent cytotoxic effects

on A549, PC-3 HT-29 and Caco-2, with IC_{50} values that in some cases are superior compared to the well-known cisplatin drug, while compounds **PdL_{10}** and **PdL_{11}** were inactive. In general, the relative cytotoxicity of compounds **PdL_9-PdL_{12}** correlates with the reduction potentials, ligand exchange rate, and DNA/BSA binding. These relationships may be crucial in the rational design of metal-based anti-cancer drugs.

5.4 References

[1] M. Haghdoost, G. Golbaghi, M. Létourneau, S.A. Patten, A. Castonguay, Eur. J. Med. Chem. 132 (2017) 282-293.

[2] M.M. Milutinović, S.K. Elmroth, G. Davidović, A. Rilak, O.R. Klisurić, I. Bratsos, Ž.D. Bugarčić, Dalton Trans. 46 (2017) 2360-2369.

[4] M.M. Milutinović, A. Rilak, I. Bratsos, O. Klisurić, M. Vraneš, N. Gligorijević, S. Radulović, Ž.D. Bugarčić, J. Inorg. Biochem. 169 (2017) 1-12.

[5] M. Milovanović, A. Djeković, V. Volarević, B. Petrović, N. Arsenijević, Ž.D. Bugarčić, J. Inorg. Biochem. 104 (2010) 944-949.

[6] M. Arsenijevic, M. Milovanovic, V. Volarevic, A. Djekovic, T. Kanjevac, N. Arsenijevic, S. Dukic, Z. D Bugarcic, Med Chem. 8 (2012) 2-8.

[7] T. Papo, D. Jaganyi, A . Mambanda, Inorganica Chim. Acta. 499 (2020) 119180.

[8] G. Kinunda, D. Jaganyi, Transit. Met. Chem. 39 (2014) 451-459.

[9] B.J. Pages, K.B. Garbutcheon-Singh, J.R. Aldrich-Wright, Eur. J. Inorg. Chem. 2017 (2017) 1613-1624.

[10] S. Jovanović, K. Obrenčević, Ž.D. Bugarčić, I. Popović, J. Žakula, B. Petrović, Dalton Trans. 45 (2016) 12444-12457.

[11] D. Ćoćić, S. Jovanović, S. Radisavljević, J. Korzekwa, A. Scheurer, R. Puchta, D. Baskić, D. Todorović, S. Popović, S. Matić, J. Inorg. Biochem. 189 (2018) 91-102.

[12] D. Ćoćić, S. Jovanović, M. Nišavić, D. Baskić, D. Todorović, S. Popović, Ž.D. Bugarčić, B. Petrović, J. Inorg. Biochem. 175 (2017) 67-79.

[13] D.O. Onunga, R. Bellam, G.K. Mutua, M. Sitati, M.D. BalaKumaran, D. Jaganyi, A. Mambanda, J. Inorg. Biochem. 213 (2020) 111261.

[14] D.O. Onunga, D. Jaganyi, A. Mambanda, J Coord Chem. 72 (2019) 499-515.

[15] I. Cassells, T. Stringer, A.T. Hutton, S. Prince, G.S. Smith, J. Biol. Inorg. Chem. 23 (2018) 763-774.

[16] B.J. Pages, K.B. Garbutcheon-Singh, J.R. Aldrich-Wright, Eur. J. Inorg. Chem. 2017 (2017) 1613-1624

[17] D. Barnes, R. Chapman, R. Vagg, E. Watton, J. Chem. Eng. Data. 23 (1978) 349-350.

[18] S. Meghdadi, M. Amirnasr, A. Amiri, Z.M. Mobarakeh, Z. Azarkamanzad, C R Chim. 17 (2014) 477-483.

[19] S. Meghdadi, M. Amirnasr, M. Kiani, F. Fadaei Tirani, M. Bagheri, K.J. Schenk, J. Coord. Chem. 70 (2017) 2409-2424.

[20] L. Yang, D.R. Powell, R.P. Houser, Dalton Trans. (2007) 955-964.

[21] C.R. Groom, I.J. Bruno, M.P. Lightfoot, S.C. Ward, Acta Crystallogr., Sect. B: Struct. Sci., Cryst. 72 (2016) 171-179.

[22] S.R.I. Cooper, CrystEngComm. 22 (2020) 7186.

[23] R.P.-L. Tang, K.M.-C. Wong, N. Zhu, V.W.-W. Yam, Dalton Trans. (2009) 3911-3922.

[24] M. Shabbir, Z. Akhter, I. Ahmad, S. Ahmed, M. Shafiq, B. Mirza, V. McKee, K.S. Munawar, A.R. Ashraf, J. Mol. Struct. 1118 (2016) 250-258.

[25] S. Radisavljević, I. Bratsos, A. Scheurer, J. Korzekwa, R. Masnikosa, A. Tot, N. Gligorijević, S. Radulović, A.R. Simović, Dalton Trans. 47 (2018) 13696-13712.

[26] N.D. Eljack, H.-Y.M. Ma, J. Drucker, C. Shen, T.W. Hambley, E.J. New, T. Friedrich, R.J. Clarke, Metallomics 6 (2014) 2126-2133.

[27] B.B. Khusi, A. Mambanda, D. Jaganyi, J. Coord. Chem. 69 (2016) 2121-2135.

[28] D.A. Vezzu, D. Ravindranathan, A.W. Garner, L. Bartolotti, M.E. Smith, P.D. Boyle, S. Huo, Inorg. Chem. 50 (2011) 8261-8273.

[29] A. Katritzky, C. Ramsden, J. Joule, V. Zhdankin, Handbook of heterocyclic chemistry, Elsevier, 2010.

[30] A. Shaira, D. Reddy, D. Jaganyi, Dalton Trans. 42 (2013) 8426-8436.

[31] J.D. Atwood, Inorganic and organometallic reaction mechanisms, VCH Publishers, 1997.

[32] C. Obuah, M.K. Ainooson, J. Darkwa, RSC Adv. 8 (2018) 5362-5371.

[33] B. Petrović, Z.i.D. Bugarčić, A. Dees, I. Ivanović-Burmazović, F.W. Heinemann, R. Puchta, S.N. Steinmann, C. Corminboeuf, R. Van Eldik, Inorg. Chem. 51 (2012) 1516-1529.

[34] H. Eyring, J Chem Phys. 3 (1935) 107-115.

[35] S. Mukherjee, I. Mitra, R. Saha, S.R. Dodda, W. Linert, S.C. Moi, RSC Adv. 5 (2015) 76987-76999.

[36] I. Mitra, S. Mukherjee, S.C. Moi, Polyhedron, 128 (2017) 46-56.

[37] R. Bellam, D. Jaganyi, A. Mambanda, R. Robinson, New J. Chem. 42 (2018) 12557-12569.

[38] R. Bellam, D. Jaganyi, A. Mambanda, R. Robinson, M.D. BalaKumaran, RSC Adv. 9 (2019) 31877-31894.

[39] A. Tarushi, E. Polatoglou, J. Kljun, I. Turel, G. Psomas, D.P. Kessissoglou, Dalton Trans. 40 (2011) 9461-9473.

[40] A.A. Franich, M.D. Živković, D. Ćoćić, B. Petrović, M. Milovanović, A. Arsenijević, J. Milovanović, D. Arsenijević, B. Stojanović, M.I. Djuran, J. Biol. Inorg. Chem. 24 (2019) 1009-1022.

[41] K. Karami, N. Jamshidian, M. Zakariazadeh, Appl. Organomet. Chem. 33 (2019) e4728.

[42] S. Mukherjee, I. Mitra, C. Fouzder, S. Mukherjee, S. Ghosh, U. Chatterji, S.C. Moi, J. Mol. Liq. 247 (2017) 126-140.

[43] K. Karami, M. Alinaghi, Z. Amirghofran, J. Lipkowski, Inorg. Chim. Acta. 471 (2018) 797-807.

[44] A. Tarushi, K. Lafazanis, J. Kljun, I. Turel, A.A. Pantazaki, G. Psomas, D.P. Kessissoglou, J. Inorg. Biochem. 121 (2013) 53-65.

[45] E.S. Koumousi, M. Zampakou, C.P. Raptopoulou, V. Psycharis, C.M. Beavers, S.J. Teat, G. Psomas, T.C. Stamatatos, Inorg. Chem. 51 (2012) 7699-7710.

[46] M. Cory, D.D. McKee, J. Kagan, D. Henry, J.A. Miller, J. Am. Chem. Soc. 107 (1985) 2528-2536.

[47] R.R. Monaco, J. Biomol. Struct. Dyn. 25 (2007) 119-125.

[48] M.M. Milutinović, A. Rilak, I. Bratsos, O. Klisurić, M. Vraneš, N. Gligorijević, S. Radulović, Ž.D. Bugarčić, J. Inorg. Biochem. 169 (2017) 1-12.

[49] R.O. Omondi, R. Bellam, S.O. Ojwach, D. Jaganyi, A.A. Fatokun, J. Inorg. Biochem. 210 (2020) 111156.

[50] L. Fetzer, B. Boff, M. Ali, M. Xiangjun, J.-P. Collin, C. Sirlin, C. Gaiddon, M. Pfeffer, Dalton Trans. 40 (2011) 8869-8878.

[51] M.P. Heng, S.K. Sinniah, W.Y. Teoh, K.S. Sim, S.W. Ng, Y.K. Cheah, K.W. Tan, Spectrochim. Acta A Mol. Biomol. Spectrosc. 150 (2015) 360-372.

[52] N. Kitada, K. Takara, T. Minegaki, C. Itoh, M. Tsujimoto, T. Sakaeda, T. Yokoyama, Cancer Chemother. Pharmacol. 62 (2008) 577-584.

[53] A.R. Burgoyne, B.C. Makhubela, M. Meyer, G.S. Smith, Eur. J. Inorg. Chem. 2015 (2015) 1433-1444.

[54] J. Zhao, Z. Xu, J. Lin, S. Gou, Inorg. Chem. 56 (2017) 9851-9859.

[55] V. Poindessous, F. Koeppel, E. Raymond, E. Cvitkovic, S.J. Waters, A.K. Larsen, Int. J. Oncol. 23 (2003) 1347-1355.

[56] D. Wang, S. Lippard, (2005). Nat. Rev. Drug Discov. 4(2005) 307-320.

[57] H.A. O'Riley, A. Levina, J.B. Aitken, P.A. Lay, Inorg. Chim. Acta. 454 (2017) 128-138.

CHAPTER 6

Electronic and ring size effects of N-heterocyclic carbenes and derivatives on kinetics of ligand substitution reactions, DNA/protein interactions and cytotoxicity of palladium(II) complexes

6.1 Introduction

N-heterocyclic carbenes (NHCs) and their derivatives (NHC = E, E = S, Se and Te) are versatile ligands used in the coordination chemistry [1-8]. The attractive features of NHCs and NHC = E transition metal complexes have resulted to their wide range of applications across the chemical sciences perspectives i.e. in material science [9, 10], catalysis [11, 12], and therapeutics as anticancer agents [9, 13-15]. Structural modification of these class of ligands allows chemists to fine-tune the electronic and steric properties and solubility of the metal complexes. N-heterocyclic carbenes ligands are often used to stabilise organometallic stabilise metal centres, owing to their strong sigma-donating and poor (weak or even negligible) pi-accepting abilities, forming complexes that are resistant to thermal decomposition [3, 12, 16, 17]. The possibility of NHCs and NHC = E as a ligand for both hard and soft metals is ascribed to their better σ-donor capabilities and donation ability into σ-acceptor orbital of the metal. Noteworthy, the stronger σ-donor properties of NHC =E compared to both NHC and phosphine is attributable to the presence of a larger contribution (66%) of the zwitterionic form (NHC^{+}–E^{-}) [18].

Metal-NHCs have demonstrated promising acceptable biological results, and among these Pd- NHC complexes have been a hot topic over the last decade as a result of their application as potential metal-based anticancer drugs [19-22]. The stability of the spectator ligand(s) is a crucial factor in the design of potential Pd(II)-based drugs, due their rapid rates of ligand-exchange (which does not allow them to maintain their structural identity long enough to reach DNA) [23]. Apart from the delivery method, the bioactivity of Pd(II)-NHC complexes depends on solubility, as most of these complexes have good solubility in the aqueous media [21]. Che and the group [24] have reported the antitumour activity of a class of palladacyclic complexes supported by NHCs ligands. The results of the study revealed that the complexes are more active than palladacyclic derivatives with no NHCs ligands (i.e. with weaker sigma-

donors). The complexes also demonstrated high stability in the presence of physiological thiols. In addition, Pd(II)-NHCs were also found to have better *in vitro* cytotoxicity than cisplatin in all tested cancer lines. In a previous study Gosh and co-workers [25] have examined the antiproliferative properties of Pd(II)-NHC. The compounds were found to have remarkable activity on MCF-7, HCT-116 and HeLa with better IC_{50} values than those of cisplatin. Noteworthy, most investigations have demonstrated that that the main target of Pd-NHCs in cancer cells is DNA similar to cisplatin [25, 26], however their mechanism of action is still elusive. Thus in this chapter, we present the synthesis and structural characterisation of Pd(II) complexes with functionalised NHC and NHC = E ligands. The substitution kinetics of the complexes with biological nucleophiles; thiourea (**Tu**), L-methionine (**L-Met**) and guanosine-5'-monophosphate (**5'-GMP**) are hereby reported. We also explore the interactions of the complexes with the DNA/protein and their resultant cytotoxic effects in HeLa cell line.

6.2 Results and discussion

6.2.1 Synthesis of ligands and palladium complexes

The synthesis of ligands, **L_{13}**, and **L_{14}** was carried out by employing the previously described method [27], through the reaction of 2,6-dibromopyridine with the corresponding imidazoles under solvent free conditions at 150 °C (Sceheme 1). In contrast, **L_{15}** and **L_{16}** were prepared according to the well-established synthetic procedure [17], *via* the condensation reactions of pyridine bridged imidazolium dibromide derivatives with sulfur powder in the presence of K_2CO_3 (Scheme 6.1). Ligands **L_{13}**–**L_{16}** were obtained in moderate yields. The dicarbene complexes **PdL_{13}** and **PdL_{14}**, were obtained in the sequential one-pot reaction of $PdCl_2(NCMe)_2$, Ag_2O, $AgBF_4$ with the respective ligands **L_{13}** and **L_{14}** in MeCN at 50 °C as described in Scheme 6.1 (section 2.3). On the contrary, the reactions of **L_{15}** and **L_{16}** with the equimolar amounts of $[PdCl_2(NCMe)_2]$ in the presence of $NaBF_4$ in CH_2Cl_2 at room temperature produced the corresponding **PdL_{15}** and **PdL_{16}** (section 2.3).

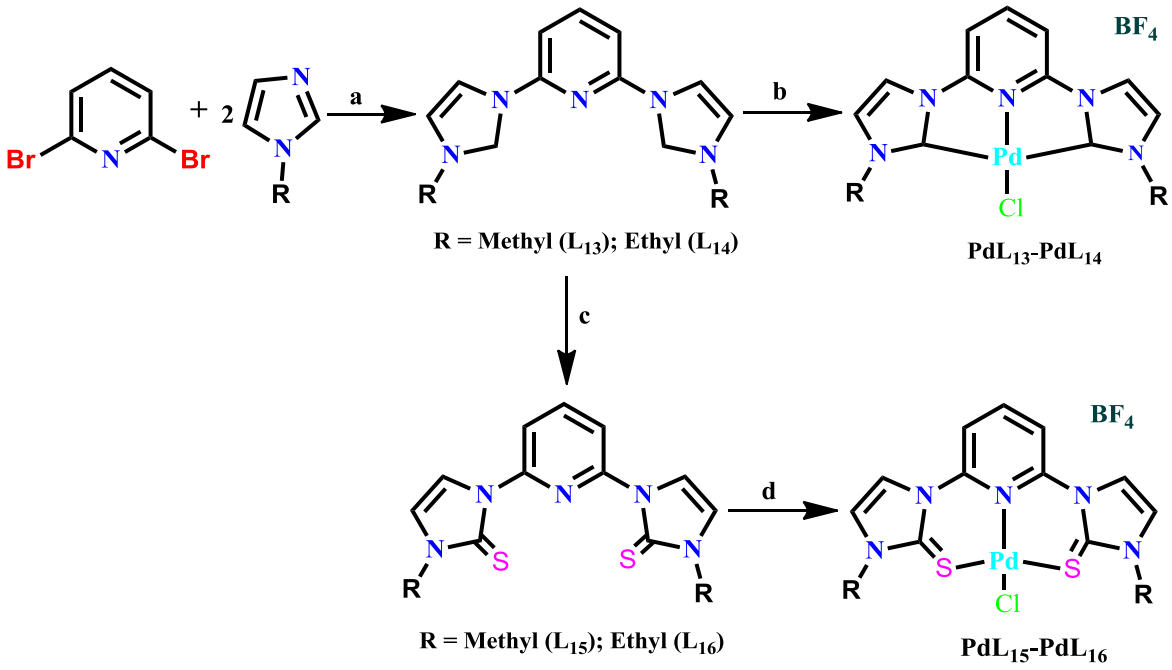

Scheme 6.1: Synthetic routes for the ligands and their respective Pd(II) complexes. *Reagents and conditions*; (**a**) neat conditions, 150 °C, 20 h; (**b**) Ag_2O, $PdCl_2(NCMe)_2$, $AgBF_4$, MeCN, 50 °C; (**c**) S_8 powder, K_2CO_3, MeOH, 8 h; (**d**) $PdCl_2(NCCH_3)_2$, $NaBF_4$, CH_2Cl_2, 12 h.

All ligands and complexes were stable towards air and moisture in the solid state, and demonstrate good solubility in common organic solvents. The compounds were characterised by ^{1}H, ^{13}C NMR spectroscopy, mass spectrometry, elemental analyses, and single crystal X-ray analyses (for **PdL$_{14}$**) to determine their formation. For instance, the ^{1}H NMR spectrum of **L$_{13}$** displays a singlet peak at δ 10.63 ppm, ascribed to CH proton, imidazolium group, and upon complexation (**PdL$_{13}$**) the peak disappears, (Figure 6.1), indicative of the coordination of the CH moiety to the Pd(II) atom. Likewise from ^{13}C NMR, the downfield shifts of the resonance of the carbene carbon at 145.20 ppm (**L$_{13}$**) to 166.35 pm (**PdL$_1$**) is consistent with the formation of the complex (Figure 6.2).

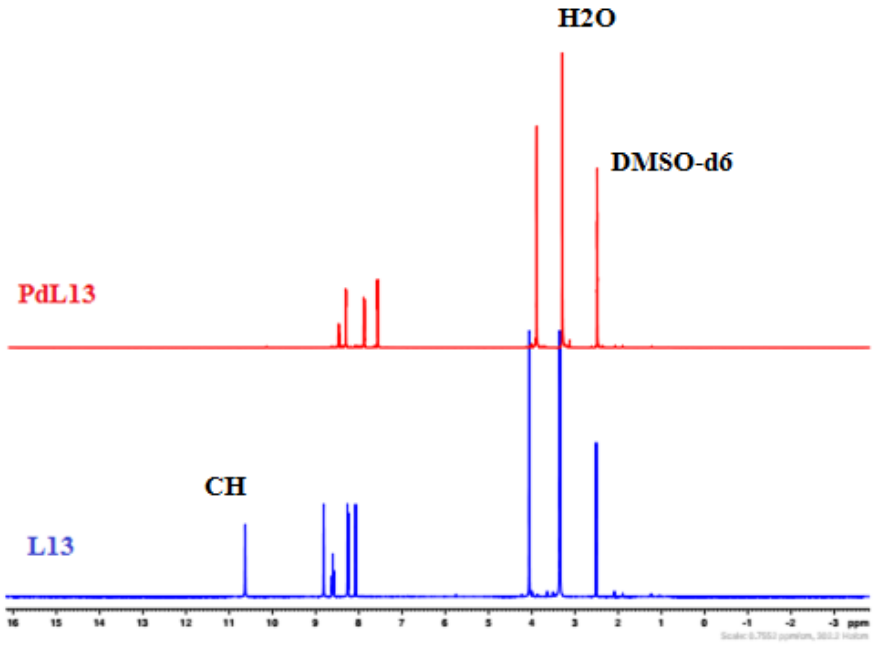

Figure 6.1: Overlays of ^{1}H NMR spectra of **L$_{13}$** in DMSO-d6, and the respective complex **PdL$_{13}$** showing disappearance of the CH protons at 10.63 ppm (**L$_{13}$**) upon complexation (**PdL$_{13}$**).

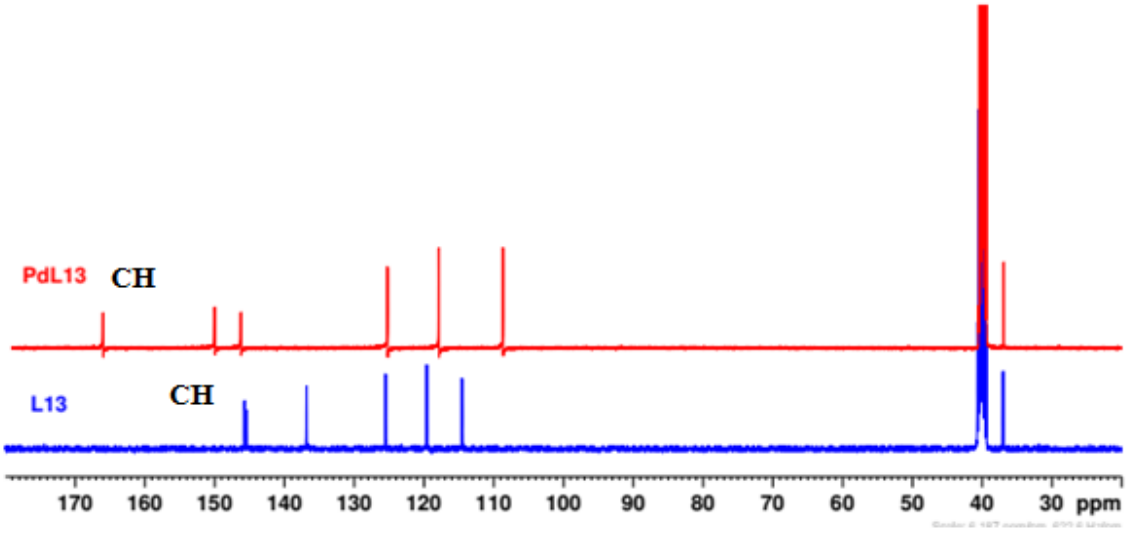

Figure 6.2: Overlays of ^{13}C NMR spectra of **L$_{13}$** in DMSO-d6, and the respective complex **PdL$_{13}$**, displaying downfield shifts of the resonance of the carbene carbon at 145.20 ppm (**L$_{13}$**) to 166.35 pm (**PdL$_{1}$**).

Similarly, the formation of the complexes were reliably determined by comparing their FT-IR spectra to their corresponding ligands. For instance, a shift of the absorption bands of of 1605 cm^{-1} (C=N, imidazole) and 1531 cm^{-1} (C=N, pyridine) in **L_{13}** to higher frequency values of 1619 and 1587 cm^{-1}, respectively **(PdL_{13})**, Figure 6.3 affirms the coordination of the Pd(II) ion to the nitrogen atoms of pyridine and the carbene in the imidazolium unit. The positive electron ionisation mass spectrometry (ESI-MS) further proved the formation of Pd-complexes. For example, the ESI-MS spectrum for **PdL_{13}** is in tandem with the calculated isotopic mass distributions (Figure 6.4). Elemental analyses data for all the complexes showed a close agreement with the theoretical calculations validating the proposed structures and also confirmed their purity.

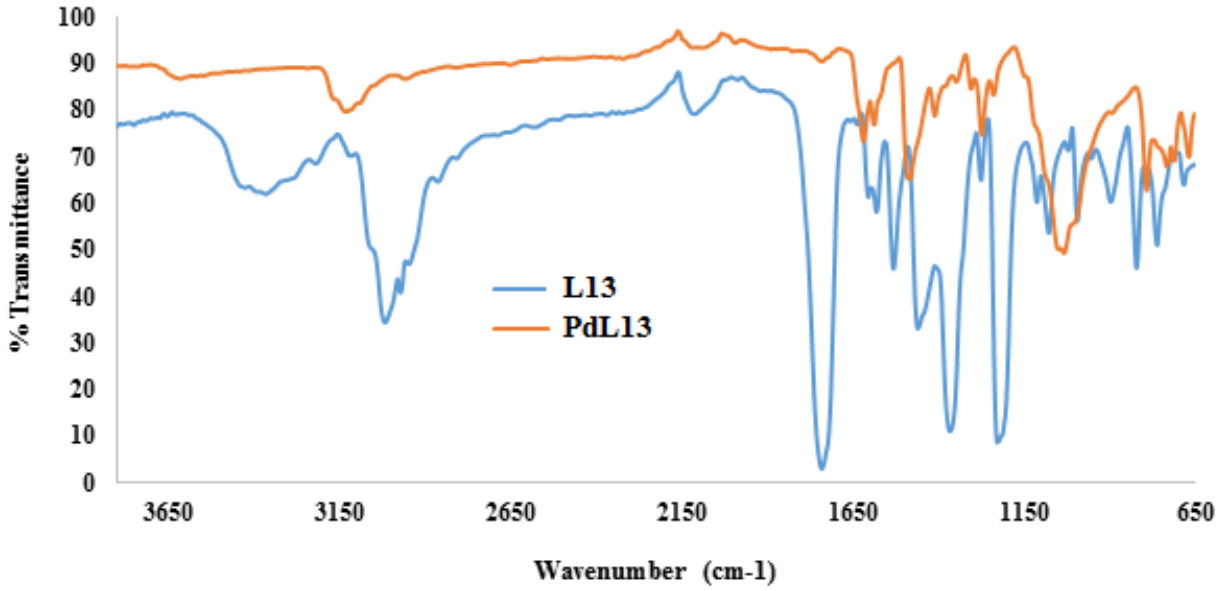

Figure 6.3: Overlays of FT-IR spectra of **L_{13}** and the respective complex **PdL_{13}**, indicating a shift of 1605 cm^{-1} υ (C=N, imidazole) and 1531 cm^{-1} υ (C=N, pyridine) (**L_{13}**) to 1619 and 1587 cm^{-1}, respectively upon complexation (**PdL_{13}**).

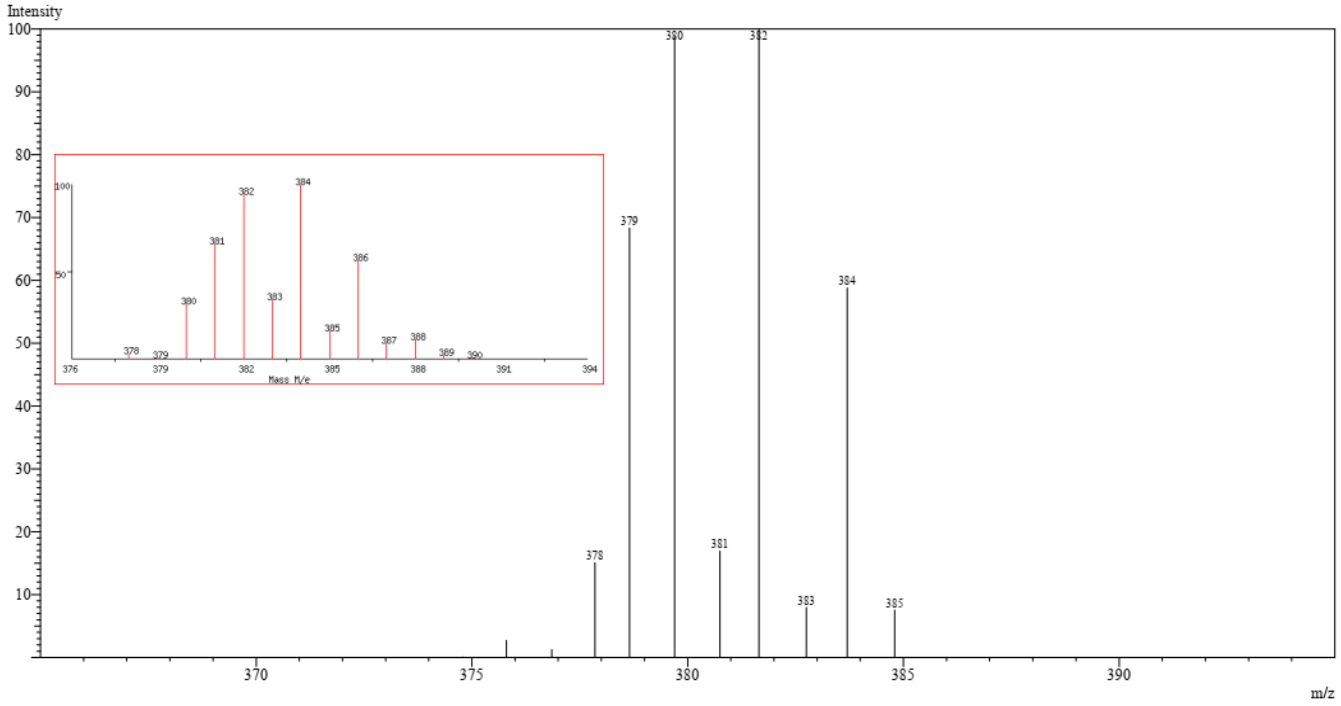

Figure 6.4: Expanded ESI mass spectrum of complex **PdL$_{13}$** with *m/z* at 382 (100%) in agreement with the exact mass of 382.01. The spectrum compare well with the calculated isotopic mass distribution (insert shows the mass spectrum of the calculated isotopic distribution).

6.2.2. X-ray molecular structure of complex PdL$_{14}$

Single crystals suitable for crystallographic diffraction of complex **PdL$_{14}$** were obtain by slow diffusion of diethyl ether/acetonitrile layered solutions. The solid-state molecular structure of complex **PdL$_{14}$** is shown in Figure 6.5, while crystallographic data, details of data collection and structural refinement parameters are summarised in Table 6.1.

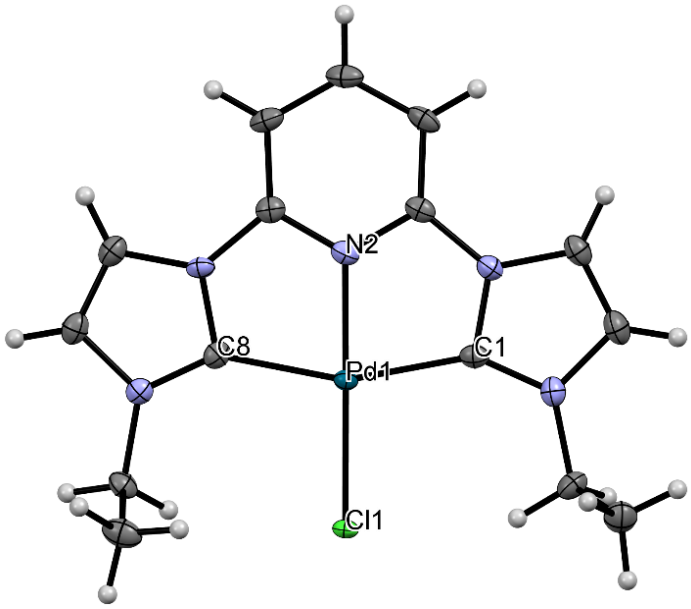

Figure 6.5: ORTEP diagram (50% thermal ellipsoids probability level) of **PdL$_{14}$**, hydrogen atoms are depicted as spheres of common arbitrary radius. The BF^-_4 counter-anion has been omitted for clarity. Selected bond lengths [Å] : Pd(1)-N(2), 1.966(3); Pd(1)-C(1), 2.032(3); Pd(1)-C(8), 2.035(3); Pd(1)-Cl(1), 2.3033(8). Selected bond angles [˚]: N(2)-Pd(1)-C(1), 79.46(12); N(2)-Pd(1)-C(8), 79.03(13); C(1)-Pd(1)-C(8), 158.50(14); N(2)-Pd(1)-Cl(1), 179.15(9); C(1)-Pd(1)-Cl(1), 100.91(10); C(8)-Pd(1)-Cl(1), 100.59(10).

Table 6.1: Crystal data and structure refinement for complex **PdL_{14}**

Parameters	**PdL_4**
Empirical formula	$C_{15}H_{17}BClF_4N_5Pd$
Formula weight	495.99
Temperature	100(2) K
Wavelength	0.71073 Å
Crystal system	Monoclinic
Space group	P 21/n
Unit cell dimensions	
	a = 7.5773(4) Å
	b = 24.1654(11) Å
	c = 10.3250(5) Å
	α = 90°; β =110.791(2)°; γ = 90°
Volume	1767.48(15) $Å^3$
Z	4
Density (calculated)	1.864 Mg/m^3
Absorption coefficient	1.252 mm^{-1}
F(000)	984
Crystal size	0.222 x 0.091 x 0.058 mm^3
Index ranges	-9<=h<=9, -30<=k<=30, -13<=l<=13
Reflections collected	27251
Independent reflections	3681 [R(int) = 0.0320]
Completeness to theta = 25.242°	98.4 %
Refinement method	Full-matrix least-squares on F^2

Complex **PdL$_{14}$** crystallised in the monoclinic space group, P 21/n. The solid-state molecular structure, reveal one tridentate ligand unit, and Cl atom to give a nominally square planar geometry. The dihedral angles N(2)-Pd(1)-C(1) of 79.46(12)° and N(2)-Pd(1)-C(8) of 79.03(13) ° deviate considerably from the expected 90° for a perfect square planar geometry. Similarly, bite angles C(1)-Pd(1)-C(8) of 158.50(14)° depart significantly from 180°, consistent with a distorted square planar geometry. Therefore, the geometry around the Pd(II) ion could best be described as pseudo square planar, consistent for Pd(II) complexes [28]. The average bond distance Pd-C_{av} (2.033Å) is within the range 1.996 ± 0.038 Å averaged for 15 related Pd structures [29]. The bond length Pd(1)-Cl(1) 2.303(8) Å compare reasonably with the mean of 2.365 ± 0.022 Å calculated from 14 similar structures [30].

6.2.3 DFT-computational optimisation, calculations and analysis

DFT calculations were carried out to obtain an in-depth understanding of the electronic and structural properties of Pd-ccomplexes. The modelled geometry structures, frontier orbital density distributions (HOMOs and LUMOs), and planarity of the complexes are given in Figure 6.6, while a summary of the selected geometrical data are provided in Table 6.2. Both the HOMO and LUMO orbitals of complexes **PdL$_{13}$** and **PdL$_{14}$** reveal that the electron density are centred primarily on the Pd(II) metal ions, chelating ligands, and partially on the chloro ligands. On the other hand, the HOMOs and LUMOs of **PdL$_{15}$** and **PdL$_{16}$** are significantly concentrated on the metal centres, imidazolyl units and the chlorine atoms. Notably, the significant distribution of the LUMOs on the Pd-metal centre, indicate the potential σ-donor ability of the chelating ligand. The consequence of this is the formation of a more electronically saturated Pd(II) metal centre, which stabilises the ground state, while destabilising the five-coordinate transition state. The modelled planarity structures of complexes reveal that **PdL$_{15}$** and **PdL$_{16}$** suffer distortion to accommodate steric repulsions, causing the twisting of the chelating ligands.

Geometry optimised structure	HOMO map	LUMO map	Planarity
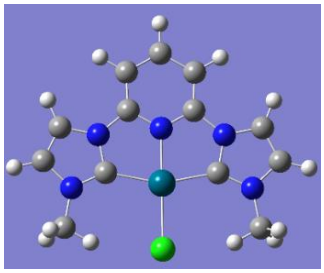	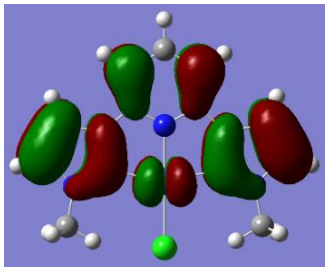	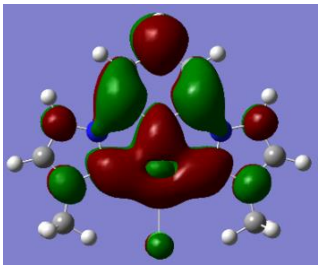	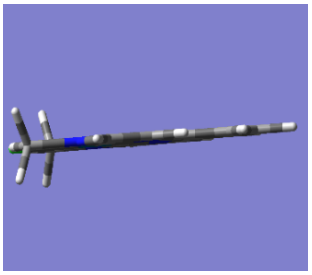
PdL_{13}			
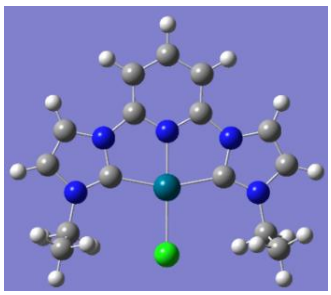	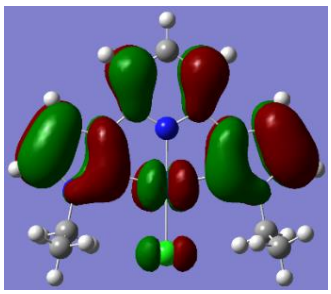	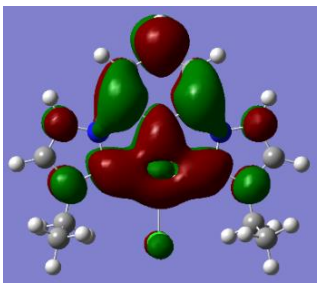	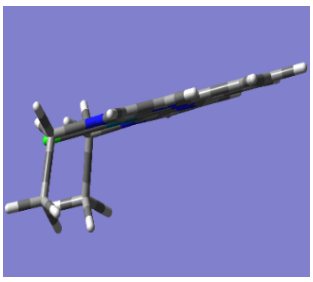
PdL_{14}			
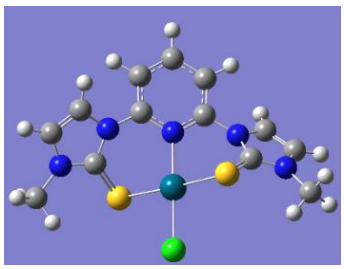	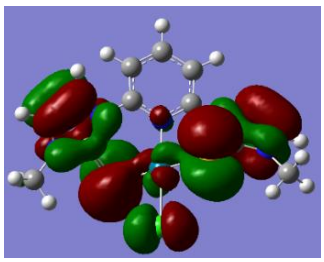	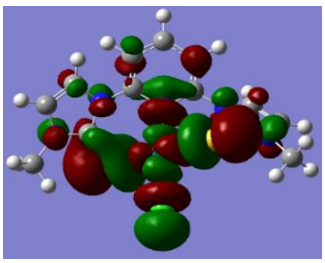	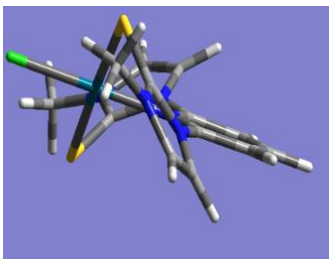
PdL_{15}			
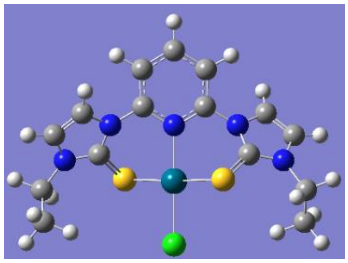	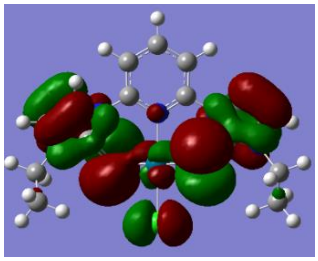	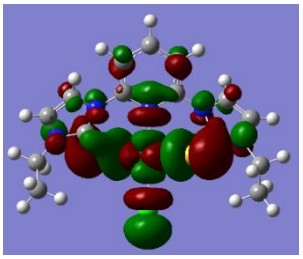	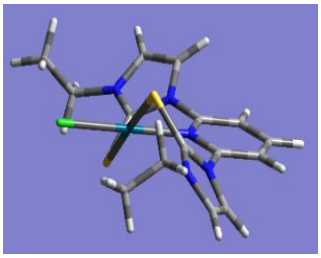
PdL_{16}			

Figure 6.6: DFT-optimised frontier orbital density distributions, and planarity for complexes **PdL_{13}-PdL_{16}**.

Table 6.2: Summary of selected DFT-calculated data for complexes, **$PdL1_3$-PdL_{16}**

Properties	**PdL_{13}**	**PdL_{14}**	**PdL_{15}**	**PdL_{16}**
NBO charge				
Pd^{2+}	0.276	0.262	-0.053	-0.061
Cis-C	0.164	0.171	-	-
Cis-S	-	-	0.126	0.124
Bond lengths (Å)				
Pd-N	2.007	2.007	2.111	2.110
Pd- C	2.065	2.063	-	-
Pd-S	-	-	2.447	2.450
Pd-Cl	2.414	2.410	2.400	2.399
Bond angles (º)				
C – Pd – C	158.504	158.563	-	
S – Pd – S	-	-	177.619	177.132
N – Pd – C	79.252	79.281	-	
N – Pd – S	-	-	88.812	88.565
MO energy (eV)				
$-E_{HOMO}$	7.0712	6.9462	6.6734	6.6007
$-E_{LUMO}$	2.7582	2.7492	3.3323	3.3427
$\Delta E_{LUMO–HOMO}$	4.3130	4.2970	3.3341	3.2580
Electrophilicity index (ω)	5.6003	5.4689	7.5067	7.5868
Dipole moment (*D*)	12.3536	12.9170	18.6181	18.6725

6.2.4 Kinetic and mechanistic study

6.2.4.1 Concentration effect

The reactions of the complexes towards the biological nucleophiles (*i.e*. **Tu**, **L-Met**, and **5'-GMP**) were followed spectrophotometrically by monitoring the changes in absorbance of the spectra at a suitable wavelength as a function of time. Typical kinetic trace recorded from stopped-flow spectrophotometer for the reaction of **PdL$_{13}$** with **Tu** is shown in Figure 6.7a. All kinetic traces were of excellent fit to a single-exponential decay function to generate the observed *pseudo*-first-order rate constants (k_{obs}) using equation (1), signifying that the reactions were first-order. The k_{obs} values obtained were plotted against the concentration of the entering nucleophiles [Nu]. Representative plots of k_{obs} against [Nu] obtained for **PdL$_{13}$** at 298 K is presented in Figure 6.7b. A linear dependence of k_{obs} on [Nu] with zero intercept was observed in all the plots, indicative of irreversible or non-solvotic pathways. Thus, the relationship between k_{obs} and [Nu] can be best described by equation (3). The slopes of the graph gave the second order rate constants (k_2), and the acquired values are provided in Table 6.3.

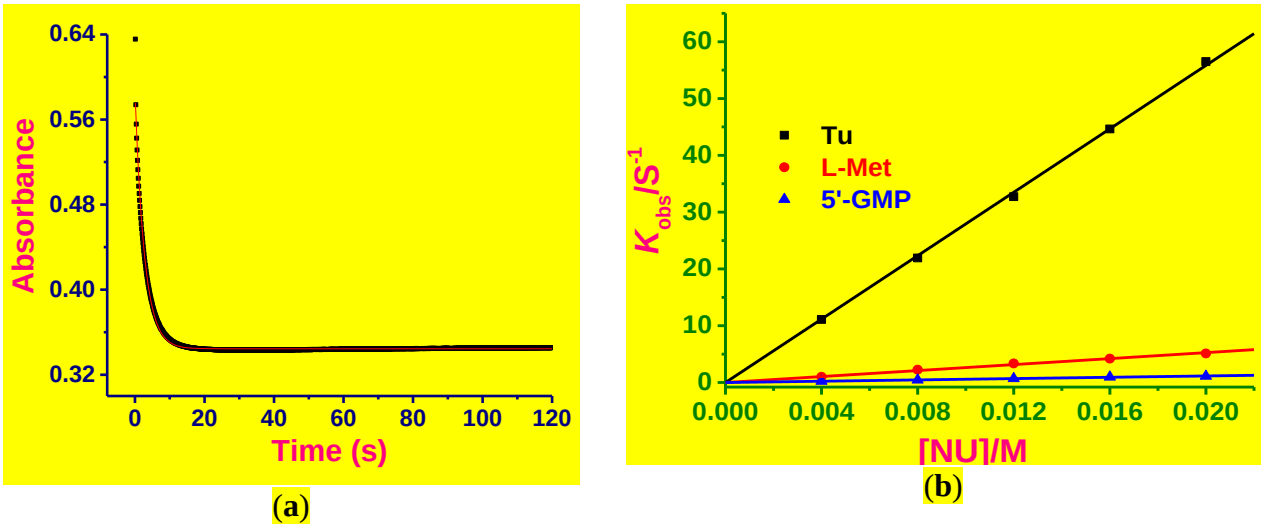

Figure 6.7: (**a**); Time resolved stopped-flow kinetic trace at 345 nm of **PdL$_{13}$**, at T = 298 K in aqua media, 50 µM Tris-HCl buffer (pH = 7.2), and 50 mM NaCl. (**b**); Concentration dependence of k_{obs} for chloride substitution of Cl ligand from **PdL$_{13}$**.

Table 6.3: Summary of the second order rate constants, k_2, at 298 K, and activation parameters, $\Delta H^{\neq}$, $\Delta S^{\neq}$ and $\Delta G^{\neq}_{25°C}$ for the substitution reactions of Pd(II) complexes with Nu.[a]

Complex	Nu	k_2/M^{-1} s^{-1}	$\Delta H^{\neq}$/ kJ mol^{-1}	$-\Delta S^{\neq}$/Jmol^{-1} K^{-1}	$\Delta G^{\neq}_{25°C}$/kJ mol^{-1}
	Tu	2791 ± 19	14 ± 1	132 ± 4	53 ± 3
PdL$_{13}$	**L-Met**	263 ± 5	18 ± 1	137 ± 3	59 ± 2
	5'-GMP	58 ± 1	26 ± 1	124 ± 4	63 ± 3
	Tu	2122 ± 13	15 ± 1	131 ± 3	54 ± 2
PdL$_{14}$	**L-Met**	204 ± 4	21 ± 1	132 ± 4	60 ± 3
	5'-GMP	44 ± 2	26 ± 1	125 ± 3	63 ± 2
	Tu	1315 ± 9	28 ± 1	90 ± 3	55 ± 2
PdL$_{15}$	**L-Met**	139 ± 3	41 ± 1	66 ± 3	61 ± 2
	5'-GMP	27 ± 2	44 ± 1	70 ± 3	65 ± 2
	Tu	930 ± 7	29 ± 2	89 ± 5	56 ± 4
PdL$_{16}$	**L-Met**	108 ± 4	40 ± 1	71 ± 3	61 ± 2
	5'-GMP	22 ± 2	44 ± 1	71 ± 3	65 ± 2

[a]Reactions performed in aqua media, 50 μM Tris-HCl buffer (pH = 7.2), and 50 mM NaCl

From the second-order rate constants values, k_2, provided in Table 6.3, the reactivity of the Pd-complexes increases marginally by factors ranging from 1.3 to 1.6. The order of the reactivity of the complexes decreases in the order; **PdL$_{13}$** > **PdL$_{14}$** > **PdL$_{15}$** > **PdL$_{16}$**. The observed reactivity trend can be accounted for in terms of both electronic and steric contributions of the spectator ligand(s). Notably, the lower reactivity of **PdL$_{14}$** in comparison to **PdL$_{13}$** is attributed to the superior positive σ-donation capability of the ethyl substituents (**PdL$_{14}$**) than the methyl group (**PdL$_{13}$**). The ethyl substituents on the ligand architecture enhances the σ-donation towards the Pd(II) ion. The net effect is the accumulation of electron density on the Pd metal centre, which hinders the incoming nucleophiles through electron repulsion. The reasoning is consistent with the raised E_{HOMO} of **PdL$_{14}$** in comparison to **PdL$_{13}$** (Table

6.2). This is also reflected by the positive NBO charges of Pd(II) ions which decrease from 0.276 (**PdL$_{13}$**) to 0.262 (**PdL$_{14}$**), Table 6.2. Similarly, the dampened reactivity of **PdL$_{16}$** in comparison to **PdL$_{15}$** is plausibly due to the presence of the high electron-rich ethyl substituents on the chelated spectator ligand, drive the *d*-orbitals higher in energy. The argument is well validated by the raised E_{HOMO} values which are ordered as; **PdL$_{15}$** (-6.6734 eV) < **PdL$_{16}$** (-6.6007 eV), Table 6.2.

The observed high reactivity of C^N^C (**PdL$_{13}$** and **PdL$_{14}$)** in comparison to S^N^S (**PdL$_{15}$** and **PdL$_{16}$**) is due to the rigidity of their ligand motifs, which are in a five-membered cluster. It should be mentioned that, five-membered chelated systems are more rigid than their six-membered counterparts. As depicted by the modelled structures **PdL$_{13}$** and **PdL$_{14}$** are rigid and planar (Figure 6.5), and the smaller dihedral angle N-Pd-C of 79.252 ˚ for **PdL$_{13}$** and 79.281˚for **PdL$_{14}$** (Table 6.2), result to steric strain within the chelate framework leading significantly to increased intrinsic reactivity. In contrast, the structures of **PdL$_{15}$** and **PdL$_{16}$** are twisted out of the mean plane (Figure 6.5), at dihedral angles, for instance N-Pd-S of 88.812 ˚ (**PdL$_{15}$**) and 88.565 ˚ (**PdL$_{16}$**), Table (6.2). The boat-shaped conformation of **PdL$_{15}$** and **PdL$_{16}$** (more flexible conformation) introduces steric effects and thereby impeding nucleophilic attack. In addition, the analysis of the of NBO charges on the Pd(II) depicts fairly unusual negative values of -0.053 for **PdL$_{15}$** and -0.061 for **PdL$_{16}$**, tenably due to the fact that S-atom is more polarisable than C-atom. Notably, the S-atom is larger and have more loosely held electrons than the C-atom, and thus is more willing to share the electron density with the Pd(II) ion through the σ-framework [31, 32].

The trend in the nucleophilicity of the entering ligands decreases in the form **Tu > L-Met > 5'-GMP** (Table 6.3), highlighting that the reactivity is controlled by both electronic and steric effects. Sulfur-donor nucleophiles (**Tu** and **L-Met**) show higher lability than the nitrogen -donor nucleophile (**5'-GMP**). The observation is attributable to the fact that Pd(II), a soft acid, has a higher affinity for sulfur

compounds (soft bases) [33]. The entering ligand, **Tu** exhbit the highest reactivity because it combines the properties of the thioethers (function as σ-donors and π-acceptors), and thiolates (acts as π-donors) [34]. In addition, the increased amine groups in **Tu** in relation to **L-Met** improves the nucleophilicity on the S-atom than the methyl substituent, due the positive inductive effect, leading to higher reactivity. The bulkiness of **5′-GMP** hinders it from competing with **Tu** (least sterically demanding) and **L-Met** (moderate steric demands).

6.2.4.2 Temperature effect and iso-kinetic relationship

To ascertain the mechanism of the substitution process followed by the complexes, the reaction temperatures were systematically varied from 298-318 K at intervals of 5 K. The enthalpy of activation ($\Delta H^{\neq}$), entropy of activation ($\Delta S^{\neq}$) and Gibbs free energy of activation ($\Delta G^{\neq}_{25°C}$) were computed using the Eyring equation (4). Representive Eyring plots obtained for **PdL$_{13}$** are given in Figure 6.8a. The calculated values of thermal parameters are depicted in Table 6.3. The higher reactivity of **PdL$_{13}$** and **PdL$_{14}$** in relation to **PdL$_{15}$** and **PdL$_{16}$** is facilitated by the small values of $\Delta H^{\neq}$ (Table 6.3), signifying low energy barrier that is associated with the process of the formation of bonds in the transition state. The small positive values $\Delta H^{\neq}$ and the large negative values $\Delta S^{\#}$ (Table 6.3) indicate an associative mechanism, where Pd-Cl bond breakage and Pd-nucleophile bonds formation are concerted [14]. The large sensitivity of the second order rate constants to the nucleophiles is consistent with an associative mode of substitution [35]. The magnitude of $\Delta G^{\neq}_{25°C}$ (obtained from equation 5) for the reactions of complexes **PdL$_{13}$-PdL$_{16}$** with the three biological nucleophiles are all comparable, indicating that the reactions follow the same mechanism (which is associative in this case) [36, 37].

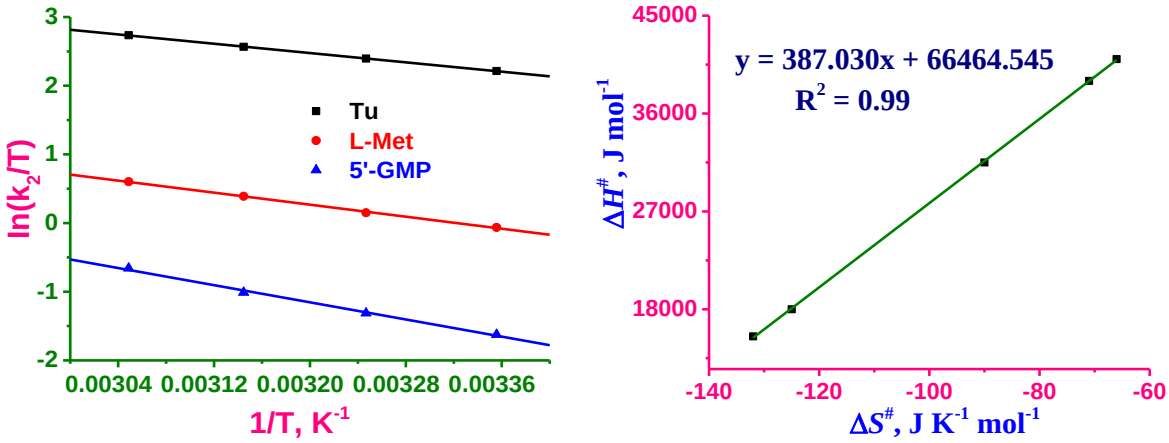

(**a**) (**b**)

Figure 6.8: **(a)**; Eyring plots for the reaction of **PdL$_{13}$** with the nucleophiles in aqua media, in 50 µM Tris-HCl buffer (pH = 7.2), and 50 mM NaCl and temperature range of 298-318 K. **(b)**; *Iso*-kinetic plots for ligand substitution reactions of complexes **PdL$_{13}$-PdL$_{16}$** with the biological nucleophiles.

Linear plots of $\Delta H^{\neq}$ and $\Delta S^{\#}$ for the kinetic reactions displayed the existence of a linear free energy relationship (LFER) between the two thermal parameters (Figure 6.8b). The *iso*-kinetic temperatures and Gibbs free energies ($\Delta G^{\neq}$) were respectively calculated from the slopes and intercepts of the plots, for all the substitution reactions. In the current study, the *iso*-kinetic temperature and $\Delta G^{\neq}$ were predicted at 387.03 K, and at 66464.54 kJ mol^{-1}, respectively. Similarly, LFER/isokinetic plots illustrate that the kinetic reactivity of the complexes followed the same mode of action (*i.e.* associative mechanism) [36, 37].

6.2.5 CT-DNA interactions studies

6.2.5.1 UV-Vis absorption spectral studies

Electronic absorption spectroscopy studies were performed to determine the mode and extent of binding of the Pd-complexes to CT-DNA. A typical absorption spectral titration curves of complex **PdL$_{13}$** in the absence and presence of DNA, at varying concentration is shown in Figure 6.9 (the time of equilibration

for Pd-CT-DNA being less than 30 s). The spectra of the complexes **PdL$_{13}$-PdL$_{16}$** displaced well-resolved bands in the range 250-300 nm, attributed to the intra-ligand charge transfer transitions of the type $\pi \rightarrow \pi^*$ [38]. Upon the addition of CT-DNA, the bands of complexes **PdL$_{13}$-PdL$_{16}$** demonstrated significant hypochromism accompanied with bathochromic shifts, indicating that the complexes are likely to bind *via* intercalation. The intrinsic binding constants (K_b) showing the binding strength of the complexes to the CT-DNA were determined from Wolfe-Shimer equation (6) and the results are provided in Table 6.4. The K_b values of $(31.24 \pm 0.81) \times 10^5$ (**PdL$_{13}$**), $(2.30 \pm 0.11) \times 10^5$ (**PdL$_{14}$**), $(2.12 \pm 0.13) \times 10^5$ (**PdL$_{15}$**), and $(1.54 \pm 0.13) \times 10^5$ M^{-1} (**PdL$_{16}$**), compare well with related Pd(II) complexes obtained in the literature [39-41]. Noteworthy, intercalative binding mode is largely sensitive to planarity of the chelating ligand(s) available for stacking, thus explaining the lower binding affinity for **PdL$_{15}$** and **PdL$_{16}$** (which suffer from distortion as a result of ring strain as depicted in the DFT Figure 6.8). The free energy (ΔG) of the complex-DNA adduct was evalaued using van't Hoff equation (7), and the results are presented in Table 6.4. The negative ΔG values of **PdL$_{13}$-PdL$_{16}$** highlighting the spontaneity of complex-DNA interaction [42, 43].

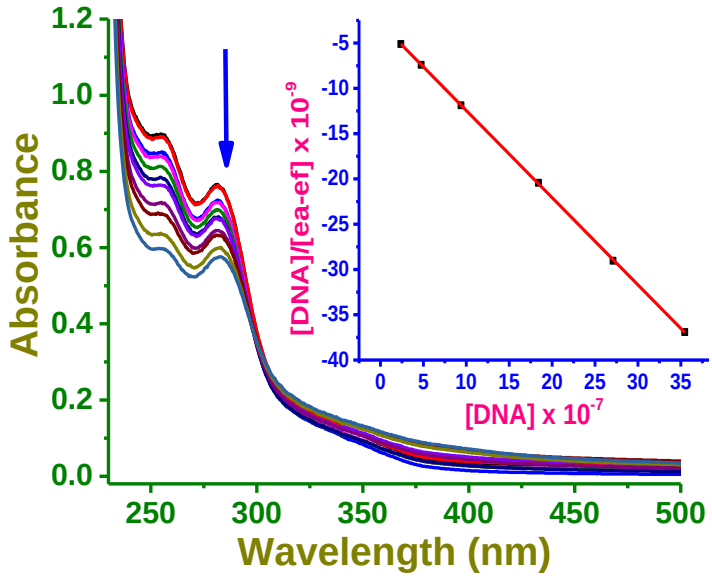

Figure 6.9: Absorption spectra of **PdL$_{13}$** in 50 μM Tris buffer consisting of 50 mM NaCl at pH = 7.2 in the absence and presence of increasing amounts CT-DNA (0-40 μM), at room temperature. The arrow shows absorbance changes with the increasing CT-DNA concentration. Inset: plot of [CT-DNA] versus [DNA]/(ε_a- ε_f).

6.2.5.2 Competitive fluorescence measurements for CT-DNA

With an aim to confirm the mode of CT-DNA interactions with complexes **PdL$_{13}$-PdL$_{16}$**, fluorescent-quenching experiments with EB-bound to DNA were performed. The molecular fluorophore EB emitted strong fluorescence at 598 nm, ascribed to the strong intercalation between adjacent DNA base pairs [44]. The incremental additions of **PdL$_{13}$-PdL$_{16}$** to EB-CT-DNA adduct caused appreciable decrease in the fluorescence intensity (35-45%), revealing intercalative mode of interaction [45, 46]. Representative emission titration spectrum of EB-bound to DNA in the absence and presence of complex **PdL$_{13}$** is given in Figure 6.10a. The Stern-Volmer quenching constant (K_{sv}) and bimolecular quenching rate constant (k_q), were calculated from the Stern-Volmer equation (8). Straight line Stern-Volmer plots are presented in Figure 6.10b for **PdL$_{13}$**, and the data are given in Table 6.4. The K_{sv} values of **PdL$_{13}$-PdL$_{16}$** (magnitude 10^3-10^4 M^{-1}), signifying that the studied complexes can displace bound EB from the CT-DNA *via* intercalative mode (Table 6.4) [10]. The values of apparent binding constant (K_{app}) obtained

from the equation (9) are presented in Table 6.5. The calculated K_{app} values (magnitude 10^8- 10^9 M^{-1}) are higher than the classical intercalators and metallointercalators binding constant (10^7 M^{-1}) [47], indicative of a strong intercalative interaction mode. The K_q values for the Pd-complexes found in the magnitude (10^{11}-10^{12} M^{-1} s^{-1}), are greater than most known dynamic flouresecent biopolymers (10^{10} M^{-1} s^{-1}), indicating a static quenching mechanism [41]. DNA binding constant, K_F and the number of binding sites per nucleotide, *n* were analysed from the Scatchard equation (10). Straight-line plots of **PdL$_{13}$** are presented in Figure 6.10c. The calculated K_F values (1.00-22.60) x 10^4 M^{-1}, signify strong intercalative mode of binding. The n values which are close to 1, show the presence of a single binding site in the CT-DNA for all the studied Pd-complexes. The results of the competitive flouresecence measurements are in excellent agreement with the data obtained form the UV-Vis studies, showing that studied Pd-complexes considerably interact with DNA intercalatively.The perturbation of the complexes on the base-stacking of CT-DNA follows the order; **PdL$_{13}$** > **PdL$_{14}$** > **PdL$_{15}$** > **PdL$_{16}$**, consistent with the substitution kinetics trend (Table 6.3).

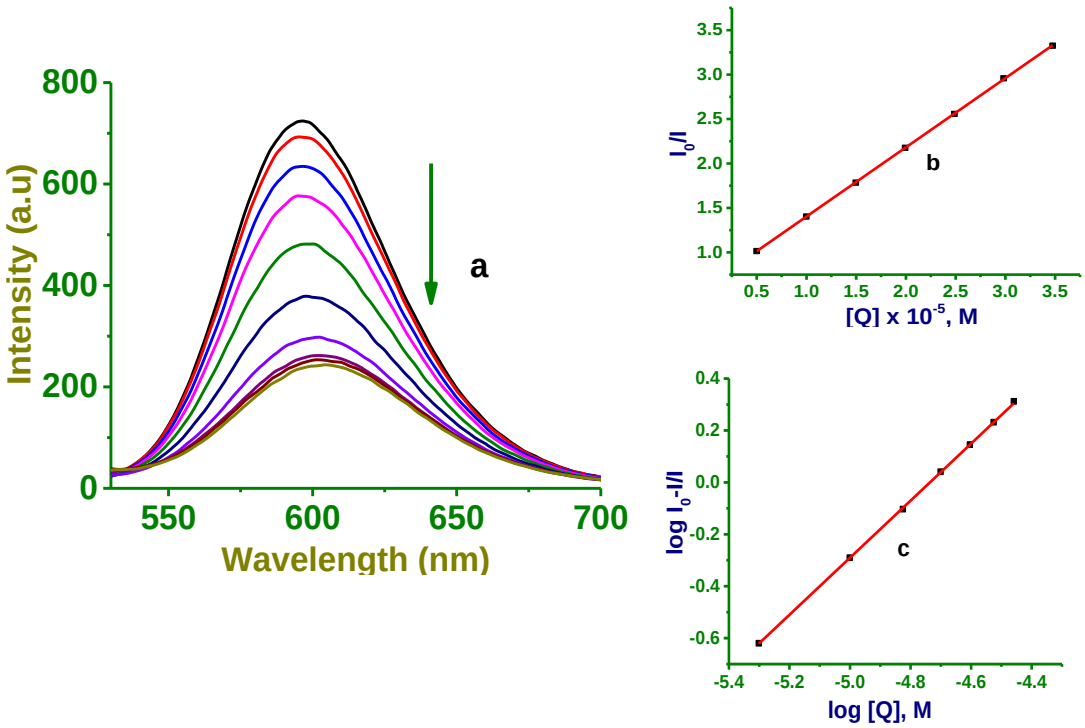

Figure 6.10: (**a**); The effect of addition of complex **PdL$_{13}$** on the emission intensity of EB bound to CT-DNA at varying concentration in 50 μM Tris buffer consisting of 50 mM NaCl at pH = 7.2, λem = 598 nm. The arrow shows the changes on addition of metal complex. **(b)**; Stern-Volmer plot of I_o/I versus [Q]. **(c)**; Scatchard plot of log[(I_o–I)/I] versus log[Q] for the titration of the complex with EB-DNA system.

Table 6.4: Binding constants and thermodynamic parameters for complex-CT-DNA systems

Complex	UV-Vis titration		EB fluorescence quenching titration				
	K_b (10^5 M^{-1})	ΔG/k J mol^{-1}	K_{sv} (10^4 M^{-1})	K_{app} (10^9 M^{-1})	k_q (10^{12} M^{-1} s^{-1})	K_F (10^5 M^{-1})	*n*
PdL13	31.24 ± 0.81	-37.05	7.79 ± 0.55	2.00 ± 0.23	3.39 ± 0.19	2.26 ± 0.17	1.13
PdL14	2.30 ± 0.11	-30.59	6.70 ± 0.39	1.68 ± 0.26	2.91 ± 0.19	1.20 ± 0.14	1.10
PdL15	2.12 ± 0.13	-30.39	4.80 ± 0.20	1.56 ± 0.08	2.08 ± 0.21	0.89 ± 0.06	0.79
PdL16	1.54 ± 0.13	-29.60	0.63 ± 0.04	0.30 ± 0.05	0.28 ± 0.01	0.10 ± 0.03	0.81

6.2.6 BSA interactions

6.2.6.1 Fluorescence quenching measurements

The intensity of the characteristic broad emission band at 281 nm shows notable decreasing trends with increasing concentration of Pd-complexes, confirmimg the interaction of the studied complexes with BSA. Figures 6.11a show fluorescence emission spectra for complex **PdL13**. The observed hypochromicity is indicative of the existence intercalative mode of interactions. The change in the emission intensity with the successive addition of the Pd-complexes fit well into the Stern–Volmer equation (K_{sv} and k_q) and Scatchard equations (K_F and n). Linear Stern-Volmer plots are depicted in Figures 6.11b for **PdL13**. Similarly, straight line Scatchard plots are presented in Figures 6.11c (**PdL13**). The values of k_q, K_{SV}, K_F, and n are provided in Table 6.5. The values of K_{SV} (8.78-25.53 x 10^4 M^{-1}) illustrate that the interactions of **PdL13-PdL16** with the protein *i.e*. BSA is not fully controlled by diffusion [48]. Similarly, the calculated k_q values (3.82-11.10 x 10^{13}, M^{-1} s^{-1}), are higher than the most known quenchers (10^{10} M^{-1} s^{-1}), approve static quenching mechanism [49]. Notably, the K_F values (1.10-10.01 x 10^3 M^{-1}) for **PdL13-PdL16** are within the optimum values of 10^3-10^6 M^{-1} [50], showing that the

complexes can easily be transported and released to the cancer cells. The computed values of n (≈ 1), reveal that only a single binding site of BSA is accessible for the interaction with the Pd-complexes. The BSA flouresecence quenching constants and binding constants (Table 6.5), show strong and fevourable binding of the complexes to the protein, and the order of binding is in agreement with the kinetics reactivity (Table 6.3).

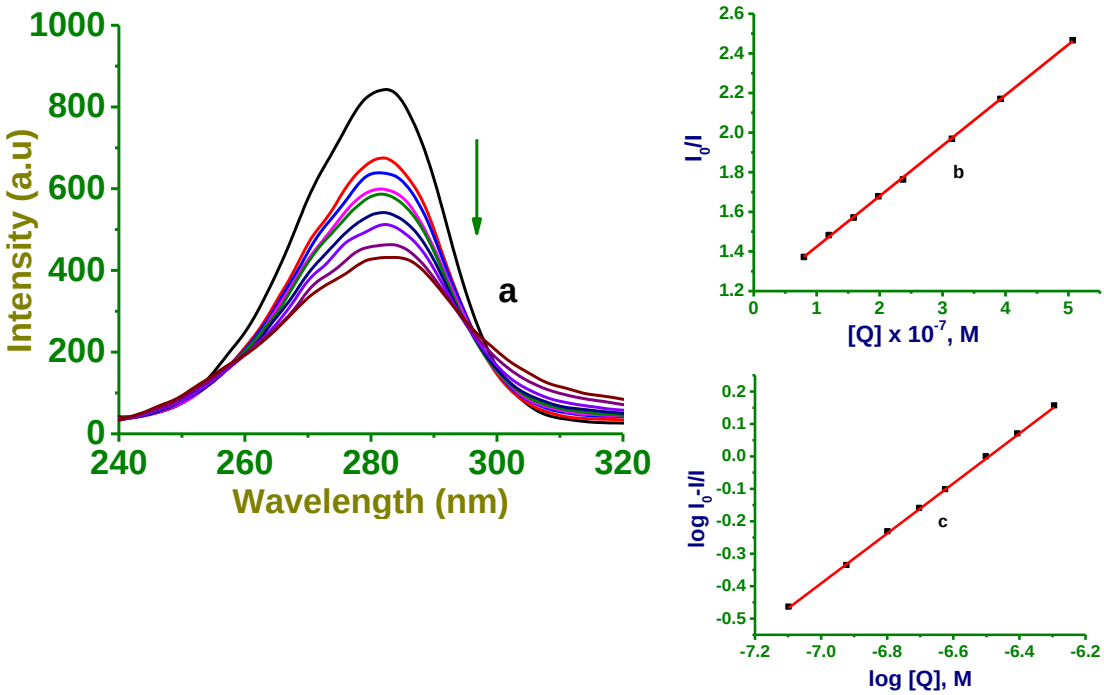

Figure 6.11: (a); Fluorescence emission spectrum of BSA (12 μM; λemi = 345 nm) in the presence of increasing amounts of **PdL$_{13}$**. The arrow shows the flouresecence quenching upon increasing the concentration of **PdL$_{13}$** (0-200 μM). (**b**): Stern-Volmer plot of I_o/I versus [Q] and (**c**): Scatchard plot of log[(I_o–I)/I] versus log[Q].

Table 6.5: The binding constant, quenching constants and number of binding sites for the Pd(II) complexes with BSA

Complex	K_{sv} (10^5 M^{-1})	k_q (10^{13} M^{-1} s^{-1})	K_F (10^3 M^{-1})	n
PdL_{13}	25.53 ± 0.92	11.10 ± 0.45	10.01 ± 0.38	0.77
PdL_{14}	16.11 ± 0.90	7.01± 0.36	5.86 ± 0.32	0.78
PdL_{15}	9.08 ± 0.31	3.95 ± 0.28	3.85 ± 0.30	0.84
PdL_{16}	8.78 ± 0.33	3.82 ± 0.26	1.10 ± 0.21	0.68

6.2.7 Cytotoxic activities of the complexes

The encouraging DNA and BSA binding affinities of complexes **PdL_{13}-PdL_{16}** prompted the need to further investigate their biological significance (antitumour activity). In this relevance, the cytotoxicity of the complexes against cervical cancer (HeLa) cell lines were assessed using MTT assay, with cisplatin as positive control (**PdL_{13}-PdL_{16}** being stable in the DMSO media). The effects of the complexes on cell viability were determined after the cells were exposed to them for 48 h. As depicted in Figure 6.12, each sample (6.25-100 µM) reduced the viability of HeLa cell lines in a concentration-dependent manner, signifying that the complexes produced a dose-response sensitive on the growing of HeLa cell lines. The *in vitro* cytotoxicity of the complexes are summarised in Table 6.6. From the results, the complexes did not show any appreciable cell viability compared to cisplatin, even with their increasing concentrations. These results necessitate the evaluation of the effects of the complexes on a wider panel of cancer cells, to determine the existence of differential cytotoxic sentivities of the complexes on a varity of different cells, in tandem with the number of studies indicating the resistant nature of HeLa. The lower activity of complexes **PdL_{13}-PdL_{16}** was presumably due their minimal

aromaticity, solubility in DMSO, lipophilicity and difficulty to penetrate the cells and attack survival machineries to cause cell death [19, 51, 52].

Table 6.6: Cytotoxic activity (% of negative control) of **PdL_{13}-PdL_{16}**, against HeLa cell line[a]

µM	**6.25**	**12.5**	**25**	**50**	**100**	**IC_{50}**
PdL_{13}	117.5 ± 33.8	130.6 ± 9.0	107.7 ± 32.2	102.1 ± 14.4	76.6 ± 9.5	264.5 ± 45.7
PdL_{14}	133.7 ± 6.8	127.6 ± 4.9	115.5 ± 5.5	99.9 ± 12.2	77.6 ± 15.8	179.3 ± 41.8
PdL_{15}	116.3 ± 0.9	122.4 ± 25.3	113.2 ± 26.21	96.0 ± 21.7	81.3 ± 19.19	338.4 ± 38.9
PdL_{16}	124.0 ± 7.8	132.1 ± 4.0	131.6 ± 25.2	95.1 ± 1.3	78.3 ± 3.9	208.2 ± 29.1
Cisplatin						11.4 ± 3.5

[a]The values (as % of negative control) were obtained using the MTT assay after 48 h drug exposure at different concentrations. The results are expressed as mean ± SD of at least two independent experiments. The SI values were not computed due to the inactivity of the complexes.

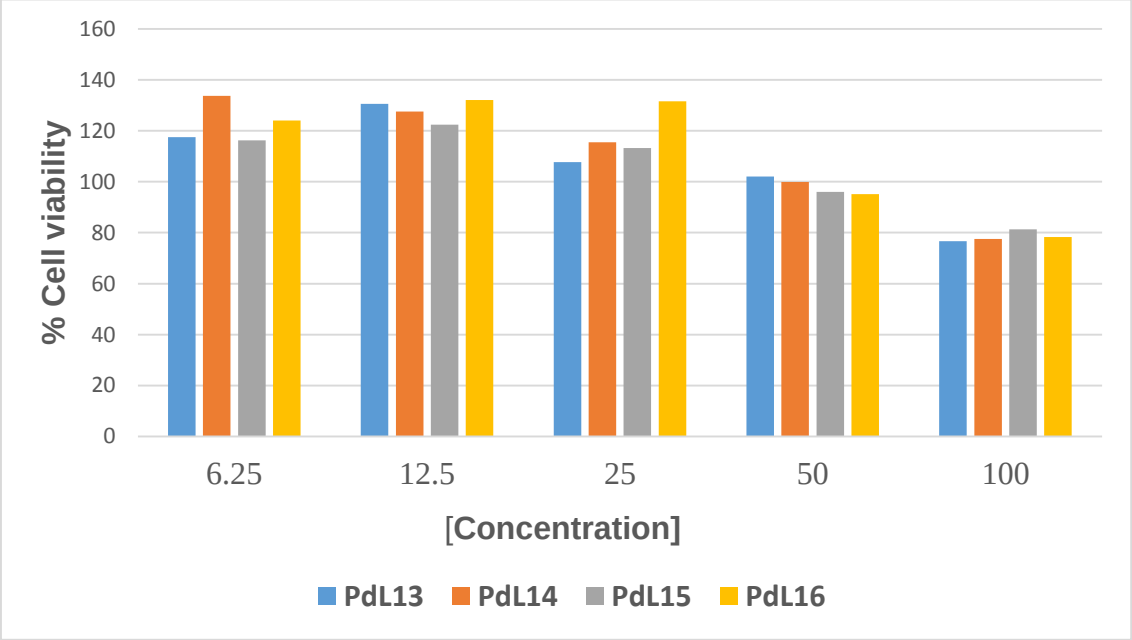

Figure 6.12: Effects of complexes **PdL_{13}-PdL_{16}** on HeLa cells after 48 h incubation. Each bar represents the mean ± SEM of triplicate viability values obtained as cellular (cytotoxic) response to treatment with the indicated concentration of the indicated complexes. Each data point represents an average of 2 or 3 independent experiments.

6.3 Conclusions

Palladium(II) complexes bearing CNC and SNS pincer-type ligands have been synthesised and structurally characterised successfully. The solid-state structure of complex **PdL$_{14}$** reveal a tridentate coordination mode of the ligand to afford a square planar complex. Kinetic reactivity of the Pd-complexes with the biological nucleophiles is controlled by both electronic and steric influence of the chelating ligand(s). DFT simlations of the complexes are in agreement with the observed kinetic trend. The values of thermal activation $\Delta H^{\neq}$, $\Delta S^{\neq}$ and $\Delta G^{\neq}_{25°C}$ reveal an associative mode of substitution reactions. Isokinetic linear relationships support a single reaction pathway for the complexes with the incoming ligands. The computed CT-DNA/BSA binding constants are comparable to most Pd(II) complexes in the literature, and the values indicate strong and favourable binding of the complexes to DNA/BSA. The spectral results show that intercalation binding mode and the order of binding matches kinetic reactivity order. Also, the spectral data show a single binding site of DNA/BSA accessible for the interactions with the metal complexes. Cytotoxic evaluations of complexes **PdL$_{13}$-PdL$_{16}$** on HeLa cell line reveal lower activity compared to cisplatin.

6.4 References

[1] Y. Wang, G.H. Robinson, Inorg. Chem. 50 (2011) 12326-12337.

[2] W.-G. Jia, Y.-B. Huang, G.-X. Jin, J. Organomet. Chem. 694 (2009) 4008-4013.

[3] S.T. Manjare, S. Sharma, H.B. Singh, R.J. Butcher, J. Organomet. Chem. 717 (2012) 61-74.

[4] A. Collado-Martinez, J. Bohnenberger, M.-J. Oliva-Madrid, P. Nun, D.B. Cordes, A.M. Slawin, S.P. Nolan, Eur. J. Inorg. Chem. (2016).

[5] G. Onar, C. Gürses, M.O. Karataş, S. Balcıoğlu, N. Akbay, N. Özdemir, B. Ateş, B. Alıcı, J. Organomet. Chem. 886 (2019) 48-56.

[6] S.Y. Hussaini, R.A. Haque, M.R. Razali, J. Organomet. Chem. 882 (2019) 96-111.

[7] A. Kumar, A. Naaz, A. Prakasham, M.K. Gangwar, R.J. Butcher, D. Panda, P. Ghosh, ACS omega 2 (2017) 4632-4646.

[8] S. Ostrowska, T. Scattolin, S.P. Nolan, Chem. Commun. 57 (2021) 4354-4375.

[9] Y.-F. Han, L. Zhang, L.-H. Weng, G.-X. Jin, J. Am. Chem. Soc. 136 (2014) 14608-14615.

[10] L. Zhang, T. Yan, Y.-F. Han, F.E. Hahn, G.-X. Jin, Dalton Trans. 44 (2015) 8797-8800.

[11] N. Ghavale, S.T. Manjare, H.B. Singh, R.J. Butcher, Dalton Trans. 44 (2015) 11893-11900.

[12] W.G. Jia, T.T. Du, L.L. Gao, J. Du, Appl. Organomet. Chem. (2020) e5651.

[13] K.M. Hindi, M.J. Panzner, C.A. Tessier, C.L. Cannon, W.J. Youngs, Chem. Rev. 109 (2009) 3859-3884.

[14] A.A. Seliman, M. Altaf, A.T. Onawole, S. Ahmad, M.Y. Ahmed, A.A. Al-Saadi, S. Altuwaijri, G. Bhatia, J. Singh, A.A. Isab, J. Organomet. Chem. 848 (2017) 175-183.

[15] M.Y. Jomaa, M. Altaf, S. Ahmad, A. Alhoshani, N. Baig, A.-N. Kawde, G. Bhatia, J. Singh, A.A. Isab, Polyhedron 141 (2018) 360-368.

[16] J.R. Miecznikowski, W. Lo, M.A. Lynn, S. Jain, L.C. Keilich, N.F. Kloczko, B.E. O'Loughlin, A.P. DiMarzio, K.M. Foley, G.P. Lisi, Inorg. Chim. Acta. 387 (2012) 25-36.

[17] W.-G. Jia, Y.-C. Dai, H.-N. Zhang, X. Lu, E.-H. Sheng, RSC Adv. 5 (2015) 29491-29496.

[18] V. Rani, H.B. Singh, R.J. Butcher, Eur. J. Inorg. Chem. 2017 (2017) 3720-3728.

[19] M.A. Bernd, E.B. Bauer, J. Oberkofler, A. Bauer, R.M. Reich, F.E. Kühn, Dalton Trans. 49 (2020) 14106-14114.

[20] J.-Y. Lee, J.-Y. Lee, Y.-Y. Chang, C.-H. Hu, N.M. Wang, H.M. Lee, Organometallics 34 (2015) 4359-4368.

[21] S. Akkoç, V. Kayser, İ.Ö. İlhan, D.E. Hibbs, Y. Gök, P.A. Williams, B. Hawkins, F. Lai, J. Organomet. Chem. 839 (2017) 98-107.

[22] M.Z. Ghdhayeb, R.A. Haque, S. Budagumpi, M.B.K. Ahamed, A.M.A. Majid, Polyhedron 121 (2017) 222-230.

[23] J.D. Atwood, Inorganic and organometallic reaction mechanisms, VCH Publishers, 1997.

[24] T.T.H. Fong, C.N. Lok, C.Y.S. Chung, Y.M.E. Fung, P.K. Chow, P.K. Wan, C.M. Che, Angew. Chem. Int. Ed. 55 (2016) 11935-11939.

[25] S. Ray, R. Mohan, J.K. Singh, M.K. Samantaray, M.M. Shaikh, D. Panda, P. Ghosh, J. Am. Chem. Soc. 129 (2007) 15042-15053.

[26] M.-L. Teyssot, A.-S. Jarrousse, M. Manin, A. Chevry, S. Roche, F. Norre, C. Beaudoin, L. Morel, D. Boyer, R. Mahiou, Dalton Trans. (2009) 6894-6902.

[27] J.C. Chen, I.J. Lin, J. Chem. Soc., Dalton Trans. (2000) 839-840.

[28] L. Yang, D.R. Powell, R.P. Houser, Dalton Trans. (2007) 955-964.

[29] C.R. Groom, I.J. Bruno, M.P. Lightfoot, S.C. Ward, Acta Crystallogr., Sect. B: Struct. Sci., Cryst. 72 (2016) 171-179.

[30] S.R.I. Cooper, CrystEngComm. 22 (2020) 7186.

[31] T. Chakraborty, K. Gazi, D.C. Ghosh, Mol. Phys. 108 (2010) 2081-2092.

[32] D.C. GHOSH, J Theor Comput Chem. 4 (2005) 21-33.

[33] S. Jovanović, K. Obrenčević, Ž.D. Bugarčić, I. Popović, J. Žakula, B. Petrović, Dalton Trans. 45 (2016) 12444-12457.

[34] S.G. Murray, F.R. Hartley, Chem. Rev. 81 (1981) 365-414.

[35] B. Petrović, Z.i.D. Bugarčić, A. Dees, I. Ivanović-Burmazović, F.W. Heinemann, R. Puchta, S.N. Steinmann, C. Corminboeuf, R. Van Eldik, Inorg. Chem. 51 (2012) 1516-1529.

[36] R. Bellam, D. Jaganyi, A. Mambanda, R. Robinson, New J. Chem. 42 (2018) 12557-12569.

[37] R. Bellam, D. Jaganyi, A. Mambanda, R. Robinson, M.D. BalaKumaran, RSC Adv. 9 (2019) 31877-31894.

[38] P. Sathyadevi, P. Krishnamoorthy, R.R. Butorac, A.H. Cowley, N.S. Bhuvanesh, N. Dharmaraj, Dalton Trans. 40 (2011) 9690-9702.

[39] A.A. Franich, M.D. Živković, D. Ćoćić, B. Petrović, M. Milovanović, A. Arsenijević, J. Milovanović, D. Arsenijević, B. Stojanović, M.I. Djuran, J. Biol. Inorg. Chem. 24 (2019) 1009-1022.

[40] K. Karami, N. Jamshidian, M. Zakariazadeh, Appl. Organomet. Chem. 33 (2019) e4728.

[41] I. Mitra, S. Mukherjee, B. Misini, P. Das, S. Dasgupta, W. Linert, S.C. Moi, New J. Chem. 42 (2018) 2574-2589.

[42] S. Mukherjee, I. Mitra, C. Fouzder, S. Mukherjee, S. Ghosh, U. Chatterji, S.C. Moi, J. Mol. Liq. 247 (2017) 126-140.

[43] K. Karami, M. Alinaghi, Z. Amirghofran, J. Lipkowski, Inorg. Chim. Acta. 471 (2018) 797-807.

[44] D. Ćoćić, S. Jovanović-Stević, R. Jelić, S. Matić, S. Popović, P. Djurdjević, D. Baskić, B. Petrović, Dalton Trans. 49 (2020) 14411-14431.

[45] A. Tarushi, K. Lafazanis, J. Kljun, I. Turel, A.A. Pantazaki, G. Psomas, D.P. Kessissoglou, J. Inorg. Biochem. 121 (2013) 53-65.

[46] E.S. Koumousi, M. Zampakou, C.P. Raptopoulou, V. Psycharis, C.M. Beavers, S.J. Teat, G. Psomas, T.C. Stamatatos, Inorg. Chem. 51 (2012) 7699-7710.

[47] M. Cory, D.D. McKee, J. Kagan, D. Henry, J.A. Miller, J. Am. Chem. Soc. 107 (1985) 2528-2536.

[48] M.M. Milutinović, A. Rilak, I. Bratsos, O. Klisurić, M. Vraneš, N. Gligorijević, S. Radulović, Ž.D. Bugarčić, J. Inorg. Biochem. 169 (2017) 1-12.

[49] D.M. Poloni, O. Dangles, J.A. Vinson, J. Agric. Food. Chem. 67 (2019) 9139-9147.

[50] T. Topală, A. Bodoki, L. Oprean, R. Oprean, Clujul medical. 87 (2014) 215.

[51] E. Ramachandran, P. Kalaivani, R. Prabhakaran, M. Zeller, J.H. Bartlett, P.O. Adero, T.R. Wagner, K. Natarajan, Inorg. Chim. Acta. 385 (2012) 94-99.

[52] A. Zamora, S.A. Pérez, M. Rothemund, V. Rodríguez, R. Schobert, C. Janiak, J. Ruiz, Chem. Eur. J. 23 (2017) 5614-5625.

CHAPTER 7

General concluding remarks and future prospects

7.1. General conclusions

In summary, the thesis examines the synthesis, structural characterisation, ligand substitution reactions and *in vitro* biological activities of a series of palladium(II) complexes of mixed-donor (N-; S-, O-, C) tridentate ligands. The study is crucial because it sheds some lights on the relationship on substitution kinetics patterns, DNA/BSA binding affinities and anti-tumour properties of metal-based anticancer drugs. The project unravel the role of kinetic reactivity on the rational design and development of potent anti-tumour drugs, with lower toxicological profile and suitable retention time in the blood plasma, and thus improving the future of chemotherapeutic protocols. In part, the work motivates and stimulates more studies on the correlation on ligand exchange kinetics, DNA/BSA interactions and cytotoxicity of metal-based complexes. Figure 7.1 shows selected Pd(II) complexes in each chapter, demonstrating highest and lowest cytotoxic effects, while Table 7.1 presents the results for correlative studies of substitution behaviours, DNA/BSA interactions and anti-tumour properties of the selected complexes. The structural elucidation of Pd(II) complexes was established by ^{1}H, ^{13}C NMR and IR spectroscopy, mass spectrometry, elemental analysis, and single crystal X-ray crystallography. The solid-state structures of the complexes confirmed the presence of one tridentate ligand unit, and Cl ligand around Pd(II) ion, giving distorted square planar complexes.

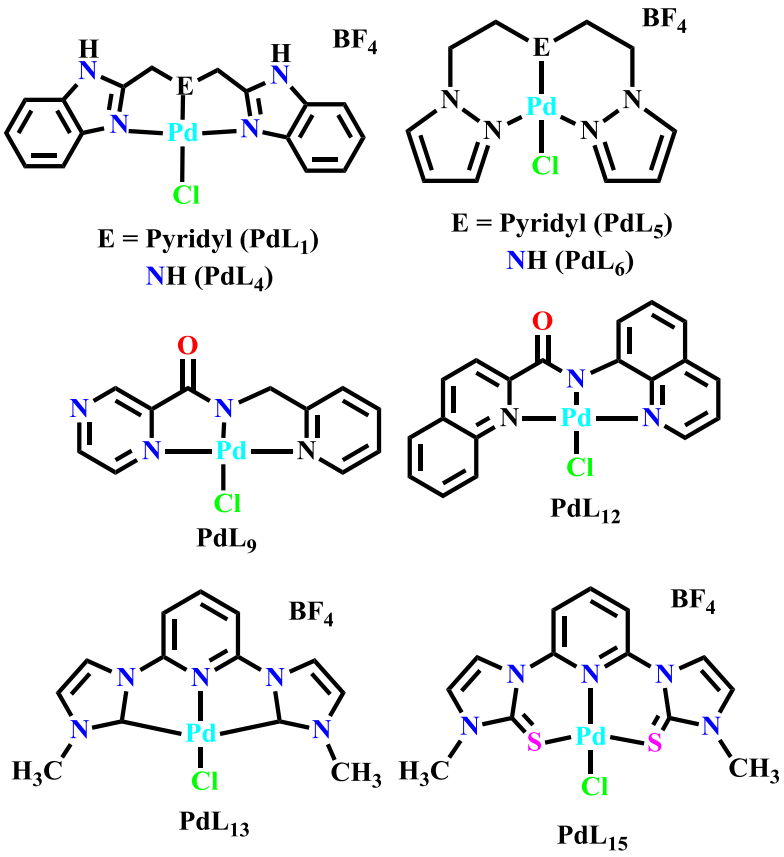

Figure 7.1: Selected Pd(II) complexes, displaying highest and lowest cytotoxic effects, with HeLa cells

Table 7.1: Representative correlative studies of substitution kinetics reactions (with **Tu** as the reference), DNA/BSA bindings and cytotoxic activities of Pd(II) complexes

Compound	Kinetics reactions (M^{-1} s^{-1})	DNA binding, K_b (M^{-1})	BSA binding, K (M^{-1})	Cytotoxicity (IC_{50}, μM),	SI	Chapter
PdL_1	(6.15 ± 0.08) x10^3	5.53 x 10^6		16.3	1.5	**3**
PdL_4	(1.07 ± 0.01) x10^3	5.3 x 10^5		73.6	2.4	
PdL_5	(5.95 ± 0.10) x10^2	(4.99 ± 0.50) x 10^5	(6.70 ± 0.11) x 10^6	No observed effect reached		**4**
PdL_6	(4.32 ± 0.04) x10^2	(3.66 ± 0.41) x 10^5	(3.24 ± 0.22) x 10^6	50% depression viability.		
PdL_9	(9.59 ± 0.02) x10^4	(11.01 ± 0.52) x 10^4	(12.25 ± 0.14) x 10^5	35.2	> 2	**5**
PdL_{12}	(1.01 ± 0.01) x10^4	(3.50 ± 0.02) x 10^3	(1.30 ± 0.01) x10^4	>100	-	
PdL_{13}	(2.79 ± 19) x10^3	(31.24 ± 0.81) x 10^5	(10.01 ± 0.38) x 10^3	No observed effect reached		**6**
PdL_{15}	(1.32 ± 9) x10^3	(2.12 ± 0.13) x 10^5	(3.85 ± 0.30) x 10^3	50% depression viability.		

K_b = DNA-binding constant; K = BSA association binding constant; IC_{50} = Half maximal inhibitory concentration, measures the inhibition strength of the complexes; SI = selectivity index, determines the level of toxicity of the compounds. Treatments viability of the compounds in **Chapters 3, 4** and **6** were followed up to 48 h, while those in **Chapter 5** were monitored for 24 h.

From Table 7.1, it is clear that substitution kinetics, DNA/BSA interactions and *in vitro* cytotoxic activities of Pd(II) complexes may be fine-tuned by varying the structure of the spectator ligand(s). Both electronic and steric parameters of the inert chelating ligands affect the kinetic reactivity and biological activities of the examined Pd(II) complexes. More interestingly, Table 7.1 reveal that π-acceptor ability of the ligand motifs, bis(benzazole)Pd(II) (**PdL_1-PdL_3**) carboxamide Pd(II) (**PdL_9-PdL_{11}**) lead to a significant increase in the rate of nucleophilic substitution (due to pi-back donation), resulting to better inhibitory effects. In contrast, σ-donor ligands bis-pyrazolyl Pd(II) (see **PdL_6-PdL_8**, **PdL_{12}**), CNC/SNS Pd(II) (**PdL_{13}-PdL_{16}**) are responsible for lower the reactivity of Pd(II) complexes (ascribed to positive inductive effects), and their minimal anti-neoplastic properties. Similarly, steric strain imposed by ring size effect of the chelating ligand architecture (see **PdL_{15}-PdL_{16}**) impede nucleophilic attack, causing reduced cytotoxic effects activities of the complexes. Also, the methylene linkers (*i.e.* in **PdL_4**, **PdL_5-**

PdL$_8$) distort the planarity of the complexes, resulting to reduced kinetic reactivity, DNA binding and cytotoxic effects of the complexes. In addition, the CH_2 linker destroys the aromaticity of the auxiliary ligands (minimising pi-conjugation) leading to the reduction of pi-back bonding [1]. Complexes **PdL$_1$-PdL$_3$** and **PdL$_{10}$-PdL$_{11}$** exhibit higher kinetic values and lower IC_{50} values courtesy of their planar aromatic spectator ligand(s), accounting for their slightly comparable IC_{50} values with cisplatin. Complexes with aromatic ligands are known to have better the lipophilicity, and cellular uptake, leading to better bioactivity efficacy [2-5].

The data in Table 7.1, indicate a strong positive relationship between kinetics of ligand exchange and DNA/BSA binding abilities of the complexes, more particularly within the individual chapters. Table 7.1 also reveals a rough correlation between substitution kinetics and anti-proliferative activities of Pd(II) complexes, **Chapter 3** (**PdL$_1$** and **PdL$_4$**) and **Chapter 5** (**PdL$_9$** and **PdL$_{12}$**). While in this thesis we have demonstrated that substitution kinetics could be used as a tool to predict and tailor DNA/BSA interactions and the resultant anti-tumour activities of metal-based drugs, care must taken to avoid misleading conslusion, as the cytotocxity of the metal-based drugs are likely to be controlled by other cellular factors.

7.2. Future prospects

Unlike what is common in most organic drugs, metal-based complexes may have similar structures but differ remarkably from each other in terms of biological activity. Thus making it difficult to use structure-activity relationship as a basis for designing active drugs. From this thesis, we do not have convincing data to authoritatively formulate rules to be fulfilled to get potent and selective metal-based compounds. However, from our results and findings pi-conjugation seems to have some influence on the anti-tumour properties of Pd(II) complexes. One such finding is of carboxamide Pd(II) (**Chapter 5**), which examines the role of pi-conjugation in developing active anti-tumour drugs. Planar and

aromatic systems display higher kinetic lability and better inhibitory effects than their counterparts. It is against this background that we propose to extend the study using planar aromatic carrier ligands. A proposed study is shown in Figures (7.2), with a terpy ligand head. Pd(II)/Pt(II) complexes of terpy ligands are well-known for their strong pi-acceptor properties, which reduce the electron cloud on the metal centre by facilitating back donation of electrons from the filled *dπ*-orbitals on metal ion into the vacant and low lying energy π* orbitals of the inert chelating ligand(s).

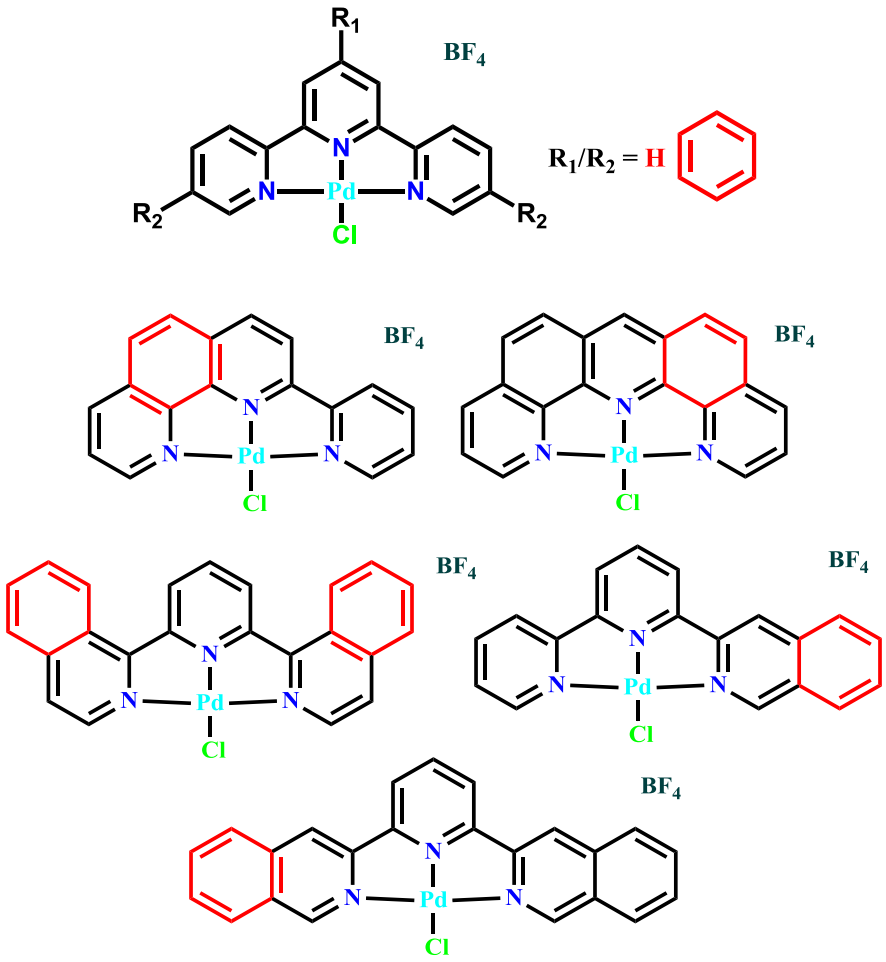

Figure 7.2: Influence of extended pi-conjugation on ligand substitution kinetics, DNA/BSA protein interactions, lipophilicity and *in vitro* cytotoxicity of Pd(II) polypridyl complexes

Even though the results presented in Table 7.1, appear to suggest that high kinetic reactivity favours promising anti-tumour activities and high selectivity, at this stage we are not able to establish the optimum substitution kinetics values for desirable cytotoxic profile of metal-based drugs, which largely depend on the metal centre. Therefore, another approach to extend this work is to use other bioactive metal centres including platinum, ruthenium, gold, and rhodium.

It is our hypothesis that to elucidate the possible preferential substitution kinetic values for enhanced potency, the mechanistic aspect involving the interaction of the drugs with the cancer cells needs to be fully understood. It seems very likely that most metal-based drugs have multi-target mode of action. Future studies may need to identify mechanism of action of the complexes as well as the applicable biological targets.

7.3 References

[1] D.O. Onunga, R. Bellam, G.K. Mutua, M. Sitati, M.D. BalaKumaran, D. Jaganyi, A. Mambanda, J. Inorg. Biochem. 213 (2020) 111261.

[2] P. Čanović, A.R. Simović, S. Radisavljević, I. Bratsos, N. Demitri, M. Mitrović, I. Zelen, Ž.D. Bugarčić, J. Biol. Inorg. Chem. 22 (2017) 1007-1028.

[3] I. Cassells, T. Stringer, A.T. Hutton, S. Prince, G.S. Smith, J. Biol. Inorg. Chem. 23 (2018) 763-774.

[4] Ö. Karaca, S.M. Meier-Menches, A. Casini, F.E. Kühn, Chem. Commun. 53 (2017) 8249-8260.

[5] B.J. Pages, K.B. Garbutcheon-Singh, J.R. Aldrich-Wright, Eur. J. Inorg. Chem. 2017 (2017) 1613-1624.